Geodätisch-geophysikalische Arbeiten in der Schweiz

(Fortsetzung der Publikationsreihe
«Astronomisch-geodätische Arbeiten in der Schweiz»)

herausgegeben von der

Schweizerischen Geodätischen Kommission
(Organ der Akademie der Naturwissenschaften Schweiz)

Siebenundsiebzigster Band
Volume 77

Trajectory Determination and Analysis in Sports by Satellite and Inertial Navigation

Adrian Wägli

2009

Adresse der Schweizerischen Geodätischen Kommission:

Institut für Geodäsie und Photogrammetrie
Eidg. Technische Hochschule Zürich
ETH Hönggerberg
CH-8093 Zürich, Switzerland

Internet: http://www.sgc.ethz.ch

ISBN 978-3-908440-21-5

Redaktion des 77. Bandes:
Dr. A. Wägli, J. Müller-Gantenbein, Prof. Dr. A. Geiger
Druck: Print-Atelier ADAG, Zürich

VORWORT

Neue miniaturisierte Messinstrumente eröffnen neue Möglichkeiten (und Herausforderungen) in der kinematischen Geodäsie. Wie die Erfinder der Trägheitsnavigation nicht davon zu träumen wagten, dass komplette IMUs (Inertial Measurement Units) nur noch wenige Kubikmillimeter gross sein könnten, dachten die Entwickler des Global Positioning System (GPS) nicht daran, Sportler mit kleinen Empfängern auszurüsten. Dank der Spannweite von zivilen Anwendungen konnte die Messgenauigkeit dieser ursprünglich militärischen Technologie um Grössenordnungen verbessert werden. Dies wird erreicht, indem zusätzliche Signale gemessen werden oder innovative Algorithmen vorgeschlagen werden.

Die Arbeit von Herrn Wägli gehört zur zweiten Kategorie. Sie präsentiert (mit aussergewöhnlicher Stringenz) innovative Algorithmen und neue Datenanalyse-Ansätze. Dank der Kombination von kleinen GPS-Empfängern mit miniaturisierten (und sehr unpräzisen) Inertialsensoren (vom Typ MEMS, Micro-electromechanical) entsteht ein überzeugendes Messinstrument, das die Trajektorie eines Skifahrers mit einer relativen Genauigkeit von 0.01% bestimmen kann. Die Mischung von hoher Präzision und kleiner Messeinheit erlaubt es, die Bewegungen des Athleten fast ständig nachzuverfolgen und aus den gemessenen Positionen, Geschwindigkeiten und Orientierungen Leistungsparameter ableiten zu können. Die Anwendung im Skisport ist aufgrund der hohen Dynmaik und dem reduzierten GPS-Signalempfang in den Bergen sehr anspruchsvoll. So ist nachvollziehbar, dass die Geräte auch in weniger schwierigen Umgebungen eingesetzt werden können. Gleichzeitig ist die Forschung auf einem Gebiet, wie dem in der Schweiz so populären Skisport, sehr motivierend.

In seiner Arbeit beweist Adrian Wägli als Erster, dass eine Orientierungs-Genauigkeit von einem Grad (RMS) dank der Anordnung mehrerer redundanter MEMS-IMUs erreicht werden kann. Ebenso kann Dezimeter-Positionsgenauigkeit während 30 Sekunden ohne den Empfang von GPS-Signalen und trotz hoher Dynamik erhalten bleiben. Des Weiteren wurden eine Vielzahl neuer Algorithmen und Software-Moduln für die praktische Anwendung sowie innovative Konzepte für die kinematische Positionierung und Navigation entworfen. Die ansprechende Kombination von Theorie und Praxis wird ein breites Leserspektrum ansprechen.

Die SGK bedankt sich bei der Akademie der Naturwissenschaften Schweiz (SCNAT) für die Übernahme der Druckkosten.

Dr. Jan Skaloud, MER
Institut für Topometrie
EPF Lausanne

Prof. Dr. A.Geiger
ETH Zürich
Präsident der SGK

PREFACE

La disponibilité de nouveaux dispositifs de mesure offre de nouvelles possibilités (et défis) dans la géodésie cinématique. Comme les inventeurs de la navigation inertielle n'ont jamais imaginé que des centrales inertielles (IMU - Inertial Measurement Units) puissent atteindre la taille de quelques millimètres cubes, les concepteurs du Global Positioning System (GPS) ne pensaient jamais équiper des sportifs de récepteurs miniaturisés. La variété d'applications civiles améliore de manière considérable la précision de mesure de cette technologie d'origine militaire. Ceci peut être atteint grâce à des signaux secondaires ou en proposant des algorithmes innovants.

Le travail d'Adrian Wägli appartient à la dernière catégorie en présentant (avec une rigueur exceptionnelle) des algorithmes et approches de traitement de données innovants. Ainsi, des signaux de récepteurs GPS bas-de-gamme et de capteurs inertiels miniaturisés (de type MEMS, Micro-electromechanical, et donc très imprécis) sont intégrés dans un instrument de mesure qui est capable de déterminer la trajectoire d'un skieur avec une précision de 0.01%. L'amalgame de haute précision et petite instrumentation permet de suivre les mouvements d'un athlète en permanence (100 fois par seconde). Des paramètres de performance des athlètes peuvent être déduits grâce à cette observation pratiquement continue de positions, vitesses et orientations. L'application de cette technologie dans des disciplines telles le ski alpin est très exigeante en raison de la haute dynamique et de la réception satellitaire réduite en raison du relief. Mais, comme la méthode a fait ses preuves dans un milieu aussi exigeant, elle devrait être utilisable dans des conditions plus favorables. En même temps, la recherche dans ce domaine est très motivante comme elle est en relation avec un sport aussi populaire.

Dans son travail, Adrian Wägli démontre pour la première fois qu'une précision d'orientation supérieure à 1 degré RMS peut être atteinte grâce à une configuration de capteurs MEMS-IMU redondants. De plus, le positionnement autonome d'une précision décimétrique peut être maintenu malgré des pertes du signal GPS et des hautes dynamiques pendant des durées allant jusqu'à 30 secondes. La thèse offre de nombreux algorithmes et modules de logiciels pour des applications réels ainsi que des concepts novateurs applicables dans d'autres domaines de la navigation et du positionnement cinématique. La combinaison de théorie et d'application pratique est bien présentée et va enchanter une large gamme de lecteurs.

La Commission Suisse de Géodésie (CGS) est reconnaissante envers l'Académie Suisse des Sciences Naturelles (ASSN) pour avoir pris à sa charge les coûts d'impression du présent manuscrit.

Dr. Jan Skaloud, MER
Laboratoire de Topométrie
EPF Lausanne

Prof. Dr. A.Geiger
ETH Zürich
Président de la CGS

FOREWORD

The abundance and availability of small positioning devices offers new opportunities (and challenges) for the art and science of Kinematic Geodesy. Certainly, as the inventors of inertial navigation never dreamed of a full Inertial Measurement Units (IMUs) occupying space of few cubic millimeters, the designers of the Global Positioning System (GPS) never thought of placing miniature receivers on human beings. Yet, it is the variety of civil application that improves the measurement accuracy of the originally military technology by an order (or several orders) of magnitude. This can be achieved either by exploiting secondary signals or by proposing innovative algorithms.

The research of Adrian Wägli belongs to the latter category as it presents (with an excellent rigor) innovative algorithms and data processing approaches which turn signals from small GPS receivers and miniature but very imprecise Micro-electromechanical (MEMS)-IMU into a convincing measurement instrument capable of tracking the skier's 2-G turn with 0.01% accuracy. The amalgam of high precision and small instrumentation then allows tracing movement of athletes not once in a while, but continuously at 100 times per second. Thus, through the practically continuous measurements of 3D position, velocity and orientation, the sportsmen's performance parameters can be deduced. Using it in sports like alpine skiing is very challenging task due to the encountered dynamic and the mountain surroundings that block the reception of satellite signals. Therefore, if the technology finds its place in such relatively hostile conditions, it can be surely used for other purposes in more benign environment. At the same time it represents a very motivating factor for the research undertaken at the country to which such sport belongs.

In his work, Adrian Wägli demonstrates for the first time that redundant configuration of low-cost MEMS-IMUs allows determining orientation better than 1 degree RMS and that the autonomous positioning of decimeter accuracy is feasible with these sensors up to 30-second long outages of GPS signals even in high dynamic. Although the thesis is application-driven, i.e. the work results in several algorithms and software modules applicable to real scenarios; it contains, at the same time, a number of novel concepts applicable to other domains of navigation and kinematic positioning. The nicely presented combination of theory and practice will therefore satisfy a wide spectrum of readers.

The SGC is grateful to the Swiss Academy of Sciences (SCNAT) for covering the printing costs of this volume.

Dr. Jan Skaloud, MER
Institute of Topometry
EPF Lausanne

Prof. Dr. A. Geiger
ETH Zürich
President of SGC

Contents

List of Figures

List of Tables

Notation and Abbreviations

Notation

Convention

Vectors are represented by lower-case bold letters, matrices by capital bold letters.

A superscript in a vector indicates a particular frame in which the vector is represented.

Rotation matrices between coordinate systems are defined by a subscript and a superscript denoting the two coordinate systems, e.g. $\mathbf{R}_b^n$ transforms from body frame b to the navigation frame n.

Angular velocity between two coordinate systems may be expressed either by an angular velocity vector, e.g. $\boldsymbol{\omega}_{ib}^b$ describes a rotation between the inertial and body frames expressed in the body frame, or by the corresponding skew-symmetric matrix form:

$$\boldsymbol{\Omega}_{ib}^b = \left[\boldsymbol{\omega}_{ib}^b\right] \times = \begin{bmatrix} 0 & -\omega_Z & \omega_Y \\ \omega_Z & 0 & -\omega_X \\ -\omega_Y & \omega_X & 0 \end{bmatrix}$$

Coordinate Frames

The local-level frame (NED) has been selected as navigation frame (index n). By convention the north axis is labeled x, the east y and the down z. The body frame is indicated by b, the inertial frame by i, whereas the Earth centered Earth fixed (ECEF) reference frame is indexed by e.

Position

$$\mathbf{r}^n = \begin{bmatrix} \varphi \\ \lambda \\ h \end{bmatrix}$$

where φ represents the latitude, λ the longitude and h the altitude.

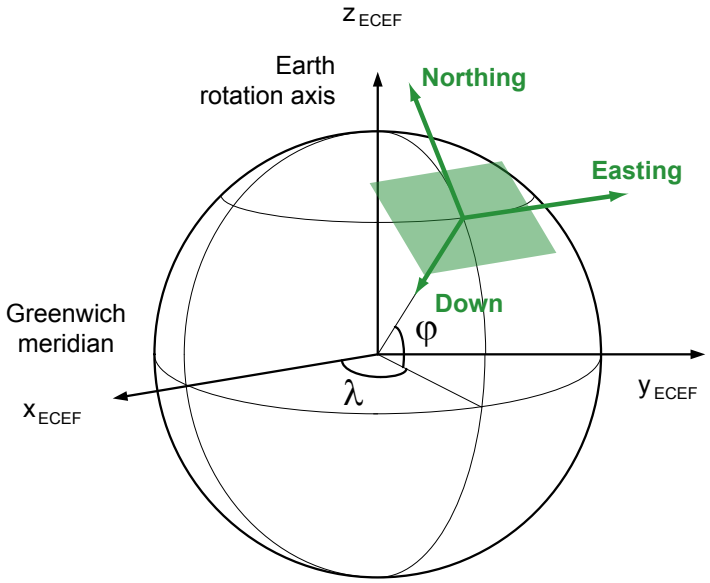

Reference frame notation and definition.

Velocity

$$\mathbf{v}^n = \begin{bmatrix} v_N \\ v_E \\ v_D \end{bmatrix} = \begin{bmatrix} (R+h)\dot{\varphi} \\ (R+h)\cos\varphi\dot{\lambda} \\ -\dot{h} \end{bmatrix}$$

$$\begin{bmatrix} \dot{\varphi} \\ \dot{\lambda} \\ \dot{h} \end{bmatrix} = \begin{bmatrix} \frac{v_N}{R+h} \\ \frac{v_E}{(R+h)\cos\varphi} \\ -v_D \end{bmatrix}$$

Rotation

$$\begin{aligned} \mathbf{x}^b &= \mathbf{R}_n^b \cdot \mathbf{x}^n \\ \mathbf{R}_n^b &= \mathbf{R}_1(\phi) \cdot \mathbf{R}_2(\theta) \cdot \mathbf{R}_3(\psi) \end{aligned}$$

where ϕ represents the roll angle, θ the pitch angle and ψ the heading angle.

$$\begin{aligned} \mathbf{R}_1(\phi) &= \begin{bmatrix} 1 & 0 & 0 \\ 0 & \cos(\phi) & \sin(\phi) \\ 0 & -\sin(\phi) & \cos(\phi) \end{bmatrix} \\ \mathbf{R}_2(\theta) &= \begin{bmatrix} \cos(\theta) & 0 & -\sin(\theta) \\ 0 & 1 & 0 \\ \sin(\theta) & 0 & \cos(\theta) \end{bmatrix} \\ \mathbf{R}_3(\psi) &= \begin{bmatrix} \cos(\psi) & \sin(\psi) & 0 \\ -\sin(\psi) & \cos(\psi) & 0 \\ 0 & 0 & 1 \end{bmatrix} \end{aligned}$$

Gravity

$$\mathbf{g} = \begin{bmatrix} 0 \\ 0 \\ g_0(\varphi, h) \end{bmatrix} \frac{\mathrm{m}}{\mathrm{s}^2}$$

where g_0 is the normal gravity. The anomalous gravity field (i.e. gravity anomaly and the deflections of the vertical) can be safely neglected in this research.

$$g_0(\varphi, h) = \frac{a \cdot g_E \cdot \cos^2\varphi + b \cdot g_P \cdot \sin^2\varphi}{\sqrt{a^2\cos^2\varphi + b^2\sin^2\varphi}} \cdot [1 - \frac{2}{a}(1 + f + m - 2f\sin^2\varphi)h + \frac{3}{a^2}h^2]$$

with

$$m = \frac{a^2 \cdot b \cdot \Omega_E^2}{G \cdot M_E}$$

and

$g_E = 9.7803253359$ m/s^2	the normal gravity at the equator
$g_P = 9.8321849378$ m/s^2	the normal gravity at the pole
$G \cdot M_E = 3.986004418 \times 10^{14}$ m^3/s^2	the gravitational constant
$\Omega_E = 7.292115 \cdot 10^{-5}$ rad/s	the Earth rotation rate
$a = 6378137$ m	the semi-major axis of WGS84 ellipsoid
$b = (1 - f)a$	the semi-minor axis of the WGS84 ellipsoid
$f = 1/298.257223563$	the flattening factor of WGS84 ellipsoid

Coriolis Terms

$$\begin{aligned} \boldsymbol{\omega}_{ie}^n &= \begin{bmatrix} \Omega_E\cos\varphi \\ 0 \\ -\Omega_E\sin\varphi \end{bmatrix} \\ \boldsymbol{\omega}_{en}^n &= \begin{bmatrix} \dot{\lambda}\cos\varphi \\ -\dot{\varphi} \\ -\dot{\lambda}\sin\varphi \end{bmatrix} \\ \boldsymbol{\omega}_{in}^n &= \boldsymbol{\omega}_{ie}^n + \boldsymbol{\omega}_{en}^n \end{aligned}$$

Earth's angular velocity $\boldsymbol{\omega}_{ie}^e$:

$$\boldsymbol{\omega}_{ie}^e = \begin{bmatrix} 0 \\ 0 \\ \Omega_E \end{bmatrix} = \begin{bmatrix} 0 \\ 0 \\ 7.292115 \cdot 10^{-5} \end{bmatrix} \frac{\mathrm{rad}}{\mathrm{s}}$$

Abbreviations

AI	Artificial Intelligence
AKF	Adaptive Kalman Filter
ANN	Artificial Neural Networks
ANFIS	Adaptive Neuro-Fuzzy Interference System
ARMA	Auto-Regressive and Moving Average
BOC	Binary Offset Carrier modulation
BPSK	Binary Phase-Shift Keying
CG	Center of gravity
DOP	Dilution of Precision
EGNOS	European Geostationary Navigation Overlay Service
EKF	Extended Kalman Filter
FDI	Fault Detection and Isolation
FES	Fuzzy Expert System
GNSS	Global Navigation Satellite System
GPS	Global Positioning System
GPRS	General Packet Radio Service
GSM	Global System for Mobile communication
IMU	Inertial Measurement Unit
INS	Inertial Navigation System
IrDA	Infrared Data Association
ISM	Industrial, Scientific and Medical radio bands
KF	Kalman Filter
LDA	Linear Discriminant Analysis
LEO	Low Earth Orbit
MEMS	Micro-Electro-Mechanical System
MSAS	Multi-transport Satellite Based Augmentation System
PCA	Principal Component Analysis
PDF	Probability Density Function
PDM	Point Distribution Model
PDOP	Position Dilution Of Precision
PF	Particle Filter
PPP	Precise Point Positioning
PRN	Pseudo Random Noise

QUEST	QUaternion ESTimation
QZSS	Quasi-Zenith Satellite System
RFID	Radio Frequency IDentification
RMS	Root Mean Square
RMSE	Root Mean Square Error
RTCM	Radio Technical Commission for Maritime Services
RTK	Real-Time Kinematic
RTS	Rauch-Tung-Striebel algorithm
SBAS	Space Based Augmentation System
SPKF	Sigma Point Kalman Filter
SP	Sigma Point
SPP	Single Point Positioning
SRIMU	Skew Redundant IMUs
Std	Standard deviation
SV	Space Vehicle (used as abbreviation for the number of visible satellites)
UERE	User Equivalent Range Error
UT	Unscented Transformation
UKF	Unscented Kalman Filter
UMTS	Universal Mobile Telecommunications System
UWB	Ultra-Wide Band
WAAS	Wide Area Augmentation System
WLAN	Wireless Local Area Networks

Chapter 1

Introduction

1.1 Context

Spectators of downhill skiing competitions know this confusion: An athlete seems fast, his carving technique seems perfect, but his timing splits are substandard. On the contrary, the descents of other skiers seem turbulent, their styles hazardous, but they are fast. Even professional commentators on TV are sometimes misled in their evaluation based on video sequences, which then amuses the audience. Wrong evaluations may also occur during training sessions and in other sport disciplines. In default of appropriate measurement tools, athletes and coaches largely characterize performances based on their experience and feeling. Their evaluation could be refined with complementary methods offering precise measurements of positions, velocities and orientations [169].

The lack of objectivity in sport performance assessment is not the only motivation for the development of new analysis systems. Firstly, the differences of skills between competitors tend to diminish in many sports. The demands on material as well as the physical and mental pressure on the athletes are tremendous. Consequently, the evaluation of trainings and competitions has become a key factor of success. Secondly, the athletes' performances are nowadays mainly analyzed by chronometry or video recordings. Material development and testing is based on repeated measurements with timing cells or wind tunnels. Unfortunately, these techniques provide few quantitative variables. Furthermore, they are limited by meteorological conditions and by the difficulty of replicating postures and movements across trials.

Satellite-based positioning and inertial navigation systems are interesting alternatives for trajectory evaluation in sports. Many GPS (Global Positioning System) receivers are proposed for leisure-time sport activities (e.g. *FRWD* [46], *Garmin* [52], *Polar* [139]). Such tools allow evaluating performance parameters like distances or velocity and height profiles. More precise satellite positioning systems have been employed for professional performance assessments in winter sports [171, 31, 10], car racing [75] and rowing [233, 234, 11]. However, the athletes' environments are often partially composed of areas that may block or attenuate satellite signals. To overcome this difficulty, Inertial Measurement Units (IMUs) are integrated with GPS, which also enables an accurate determination of accelerations and orientations. Conventional GPS/INS (Inertial Navigation System) equipment, consisting of dual-frequency GPS

receivers and tactical-grade INS, provides high accuracies (cm for position, cm/s for velocity and 1/100 deg for orientation). In the context of sport applications such equipment is not suitable because it is heavy (a few kg) and expensive ($>$ €40'000). In recent years however, Micro-Electro-Mechanical System (MEMS) IMUs as well as low-cost L1 GPS receivers entered the "navigation world" [95, 96, 36, 57].

MEMS-IMUs present a great potential for sport applications because of their low price and small size. However, their use in positioning is still in its early stages. Given the context of high dynamics in sports and the poor quality of inexpensive MEMS sensors, the feasibility of integration of inertial MEMS with GPS has to be verified - especially considering the magnitude and change of their systematic errors and their sensitivity to temperature changes. Reference [172] suggested an approach based on a black-box error model. A well-tuned model was identified as suitable for analyzing particular characteristics of the performance, but required a certain level of a priori knowledge of the underlying dynamics. Study [171] tested the synergy of integrating a digital magnetic compass with GPS using a recursive QUEST (QUaternion ESTimation) algorithm. This approach required accelerations differentiated from GPS measurement to the orientation computation and thus meant that the derived inertial accelerations were not independent of GPS. Nonetheless, the results were sufficiently encouraging for further consideration of MEMS-type sensors in sports.

This research is part of a technology transfer to the start-up enterprise *TracEdge* based at Grenoble, France. The goal of this collaboration is the development of innovative solutions for the performance assessment of outdoor sport disciplines with velocities ranging from $3 - 300$ km/h.

1.2 Particularities Related to Sport Applications

When developing a GPS/INS system for performance analysis of outdoor sports, the following issues need to be considered.

- **Human aspect.** Coaches, athletes and manufacturers are often not familiar with emerging technologies and have problems to identify their benefits [108], especially if new approaches modify established routines and work practices. However, innovation is not thought to replace their expertise, but to provide additional, relevant data that can help explain their (subjective) interpretation.

- **Application to numerous disciplines.** Sensors and data processing algorithms ideally cope with a large variety of dynamics (amplitude of motion, vibrations). It has to be modular to be able to satisfy the accuracy requirements of many disciplines.

- **Discontinuous availability of satellite signals.** Outdoor sports do not necessarily guarantee an open sky for satellite reception. Hence, using inertial sensors may help bridging gaps of satellite reception to ensure the continuity of performance evaluation and allows observing other performance-relevant parameters (e.g. orientation, acceleration).

- **Physical characteristics of the sensors.** Building a wearable system requires the use of miniaturized and low-power components. In addition, the placement of the sensors shall neither constrict the athletes' movements, nor be a risk of injury.
- **Limited infrastructure.** Most of the "traditional" trajectory assessment tools require considerable ground infrastructure. Furthermore, performance evaluation is sometimes time-consuming and results become available only weeks after measurement campaigns. The obvious benefit of a GPS/INS system is its (global) availability and its fast setup. Hence, the setting up of external material, like timing cells, video cameras or RFID tags, can be avoided.

1.3 Objectives

The research focuses on the development of innovative algorithms for the trajectory analysis in sports. The main objectives are:

1. **Elaborate innovative algorithms integrating low-cost satellite navigation and inertial measurements.** As the cost and ergonomic factors favor the use of MEMS-type inertial sensors and low-cost single-frequency GPS receivers, strategies to mitigate the effects of their large systematic errors must be developed.
2. **Define a methodology for trajectory analysis in sports.** Convenient representation as well as rigorous analysis and comparison of the athletic performance requires effective modeling algorithms that consider the degree of accuracy of trajectory reconstruction.
3. **Demonstrate and assess the system performance with experiments in sports.** The objective is to prove the feasibility of the integration, demonstrating the accuracy of the system and point out improvements for performance analysis in sports with respect to existing methods.

1.4 Methodology

Fig. 1.1 summarizes the methodology for performance evaluation in sports based on GPS/INS systems. The multi-disciplinary character of the present study defines the various fields that need to be investigated. The research can be broken down into six chapters:

Sport performance parameter and accuracy requirements. This study first aims at understanding how athletes, coaches, testers and equipment developers evaluate sport performances (Chapter 2). Different categories of sport applications are identified where GPS/INS systems can bring benefits. Then, their accuracy requirements are defined. Finally, an overview on current trajectory analysis techniques is given and the sensors that are appropriate for this research are chosen.

Measurements, models and estimation methods. The efforts described here begin with the research into the usual approach to GPS/INS integration in which the prevailing systematic inertial effects are estimated by external GPS measurements. Chapter 3 proposes

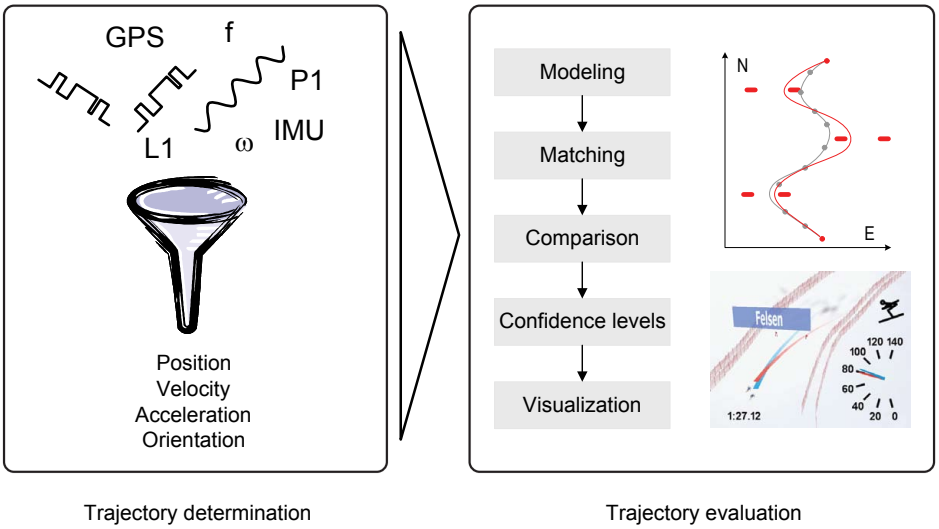

FIG. 1.1: Methodology for performance evaluation in sports.

application specific approximations and quantifies the expected measurement inaccuracies. Then, the processing and estimation algorithms are introduced that transform the measurements into the desired trajectory parameters.

System performance. Chapter 4 assesses the navigation performance of different system setups and integration strategies with respect to reference trajectories. The loosely and closely coupled GPS/INS integration schemes are investigated simultaneously. Moreover, extended and unscented Kalman filtering are compared. Lastly, the problem of orientation initialization and the benefits of magnetic MEMS-type sensors for the navigation solution are evaluated.

Advanced modeling and estimation methods. The characteristics of the MEMS-IMU sensors induce particular investigations with respect to their error model and the possibility of using numerous sensors to enhance the orientation determination.

- **Inertial error modeling.** The MEMS-type inertial sensors are prone to large systematic errors (e.g. biases, scale factors, drifts) which need to be compensated during the navigation. A simplified error model is proposed in this research which is validated by comparisons with higher-quality reference signals and evaluations in the navigation domain (chapter 5).
- **Redundant MEMS-IMUs.** Different strategies to integrate redundant MEMS-IMUs are presented in chapter 6. The navigation performance enhancement is assessed as a function of the geometrical arrangement of the sensors and the integration method. In addition, direct noise estimation, fault detection, and sensor calibration during uniform motion and static initialization are investigated.

Applications to sports. Before being employed and accepted by the end users, the superiority of any new development has to be demonstrated. This shall be achieved through testing in winter and motor sports (chapter 7). Firstly, a methodology for trajectory reconstruction and comparison is presented. Thereby, special emphasis is put on the accuracy of the estimated

parameters which determines whether the observed performance differences are statistically meaningful. Secondly, two applications of trajectory analysis that are particularly in demand are highlighted.

- Trajectory-derived chronometry. Traditionally, splits are measured based on timing cells. GPS/INS derived trajectories allow computing intermediate splits on variable sections.
- Orientation-related assessments. The orientation of sport equipment with respect to the direction of motion is an important parameter for equipment development or technique analysis. Two examples are presented in this chapter: the derivation of edging and skidding angles in skiing, as well as the derivation of lateral tire slipping in motorcycling.

Chapter 2

From Sports to Navigation

This research aims at measuring and comparing trajectories of outdoor sport disciplines by combination of satellite positioning and inertial navigation. Before explaining certain choices of algorithms and sensors, it is necessary to understand the accuracy requirements of the considered sport applications and disciplines. What accuracies are needed and are they technically feasible and economically efficient? What level of accuracy offer current trajectory determination methods? And, which are their limitations? The present chapter aims to answer the above questions and to define the objectives for the subsequent developments.

2.1 Criteria of Sport Applications

A certain number of requirements and expectations have to be respected when designing an innovative tool for performance assessment in sport.

- **Accuracy.** The system needs to satisfy the accuracy criteria demanded by the sport professionals. Often, such requirements are intuitively overestimated.
- **Safe and not handicapping for the athlete.** Fortunately, the safety is a major concern of athletes and developers. Indeed, a system carried by an athlete should not affect his performance nor present a risk for injury, e.g. in case of a crash.
- **Cost.** To address a large number of customers, the system needs to be affordable. Targeted are sport professionals and confirmed amateurs who buy heart rate monitors to follow their performance and who might invest up to €500 to analyze their trajectory. Hence, low-cost sensors are to be used with the option to employ higher-end devices for few cases with increased accuracy requirements and larger budgets.
- **Fast setup and processing.** Developers and coaches often lack the knowledge about emerging technologies. In addition, sport professionals like to be independent of external analysts, either because they do not want to share confidential information or because of economic restrictions. Thus, a blackbox-like system with minimum user interaction is preferred. Ideally, the data is processed automatically and transfered to a computer for performance analysis directly after the effort. Also, the algorithms and sensors shall be applicable to a wide range of dynamics.

- **Straightforward to interpret.** Unlike position, velocity and orientation profiles are more difficult to interpret. Experience reveals that they are often in conflict with the intuitive feeling of testers and trainers. Therefore, good visualization of the data is of utmost importance. Also, it is important to provide athletes and coaches with performance representations which are familiar to them. Finally, each technology has its limits and therefore features like accuracy indicators can help in gaining confidence into the tool. In addition, it is practical to associate other performance parameters (e.g. heart rates, rotations per minute of an engine) with the trajectory.

2.1.1 Accuracy Requirements

Trajectories can be analyzed in terms of position, velocity, acceleration and orientation in relation of the sensors' placement. On the other hand, some part of the sport community is interested also in the motion analysis of segments of the human, the orientation of the equipment [219, 218] or in the run-to-run comparison of other performance criteria [221]. Other deduced parameters of interest are:

- The distance covered by athletes and average velocities. These can be derived from position or integrated from velocities, respectively [156].
- Slipping angles which can be derived from the difference between the direction of motion and the orientation of a body segment or the equipment [75, 221].
- Energy transfer factors [189] combining altitude (potential energy $\mathbf{E}_{potential}$), velocity (kinetic energy $\mathbf{E}_{kinetic}$, friction $\mathbf{F}_f$ and drag $\mathbf{F}_d$) as:

$$\Delta\mathbf{E}_{potential} = \Delta\mathbf{E}_{kinetic} + \int (\mathbf{F}_f + \mathbf{F}_d) d\mathbf{s} \tag{2.1.1}$$

Tab. 2.1 summarizes requirements in terms of timing, position, velocity, and orientation accuracy of sports applications to performance evaluation techniques based on experience and evaluated through error propagation. Three categories were identified that possess distinct performance criteria: trajectory comparison, material testing and development, as well as motion analysis and rehabilitation.

Experience shows that sport professionals tend to overestimate the need in position accuracy. The cm to dm level positioning is crucial only for a few applications, namely those related to timing (material testing) and disciplines where small trajectory differences can be important (e.g. slalom in alpine skiing).

Also, there is often confusion about the needs in terms of absolute and relative accuracies. For instance, in many disciplines the trajectory shape (meaning high relative accuracy) is of higher importance than the absolute positioning accuracy. This is true also for energy transfer computations where relative changes of altitude, velocity and acceleration are more interesting than absolute values [107].

Measuring body motion is a more complex issue and the subject of many research projects [99, 100, 146, 14, 236, 56]. At EPFL, the Sport and REhabilitation program (SRE) aims at

TAB. 2.1: Accuracy requirements for trajectory determination in sports.

Field of use	Accuracy						Remarks
	Timing	Position	Velocity	Acceleration	Orientation	Sampling frequency	
Trajectory comparison							
- Post-mission		< 0.5 m	< 1 km/h		1-2 deg	1-5 Hz	Few applications require dm-accuracy (e.g. slalom in skiing), relative position accuracy is more important than absolute
- Real-time (e.g. TV broadcasting)		1-10 m	1-2 km/h	± 1 g			Includes trajectory matching and comparison algorithms
- Chronometry	1/100 s	20 cm at 80 km/h	< 1 km/h			max. 5 Hz	GPS or GPS/INS derived chronometry depends on the athlete's velocity and the position accuracy
Material testing and development							
- Tire development, ski testing		< 0.2 m	1-2 km/h		1-2 deg	1 Hz	Position and velocity of the ski are required, no crossing of the ski
- Vibrations						400 Hz	Max. vibrations in motor sports at 200 Hz, muscles absorb vibrations down to 20 Hz
- Gliding and aerodynamic properties (suit, ski)	1/100 s	20 cm at 80 km/h	< 1 km/h			1 Hz	Closely related to the timing accuracy, trajectory modeling
Motion analysis and rehabilitation							
- Evaluation of the athlete's motion					2 deg	50 Hz	Orientation of the body segments
- Energy transfer		CG: 10 cm	CG: 1-2 km/h			50 Hz	Qualitatively accurate data more important than quantitatively

reconstructing the movements of the human skeleton. It strives at providing athletes quantitative information about their rehabilitation process to avoid too intensive training or premature return to competition (with the risk of re-injury). However, presenting the algorithms and sensors applied for the reconstruction of full body motion is beyond the scope of this research.

2.2 Methods for Trajectory Determination

Every discipline of sports has its own techniques for performance analysis. The requirements for such evaluation methods are discipline specific and depend on its dynamics, ergonomic requirements and cost. For disciplines in motion over longer sections, the investigation of the trajectory is of utmost importance. This section and TAB. 2.2 present an overview on methods for trajectory determination.

TAB. 2.2: Current approaches for trajectory determination in sport.

	Position	Velocity	Acceleration	Orientation
Imagery				
- Single camera	Qualitative	Qualitative		Qualitative
- Stereo camera system	✓	✓	✓	✓
Positioning systems				
- GPS	✓	✓	Derived	
- INS	Relative changes	Relative changes	✓	✓
- GPS/INS	✓	✓	✓	✓
- UWB/WLAN	✓			
Other methods				
- Optical sensors		✓	Derived	✓
- Splits		Average speed		

2.2.1 Imagery

Optical methods employing single cameras and stereo-camera systems can be employed for trajectory analysis [25].

Single cameras provide qualitative information about the position and motion of an athlete. A powerful tool using single cameras has been developed by *Dartfish* (FIG. 2.1, [27]): the system detects common features in the images taken from two successive athletes (invariant image retrieval) and then superimposes the trajectory of the athletes [30]. However, as no quantitative data can be extracted, the conclusions about the sport performance are essentially based on relative comparisons and their interpretation depends on experience. *Cliqang* [8] and *3CA-Concept* are other examples of such 2D systems.

Stereo-camera systems in stereo-configuration are able to provide highly accurate, quantitative information about the 3D trajectory and motion of athletes. Three groups of systems can be distinguished.

- Systems with active markers that are identified electronically by the cameras. The active markers are often infra-red LEDs. An example is the *Codamotion* system [19].
- Passive marker systems using either optical or infra-red cameras. In the former approach, the points of each marker need to be edited manually, at least in the first frames (e.g. *Ariel APAS*). In infra-red systems, only the markers are visible on the image and are identified in 3D. Unfortunately, such systems are limited outdoors because of the interference with the background illumination. Examples are the *Vicon* system [210], *BTS ElitePlus* or *Peak Performance Motus*.
- Markerless motion capture systems with volume models fitted to the athlete [24]. An example is the *organicmotion* system [127].

The accuracy provided by multi-cameras systems depends essentially on the volume in which the motion is to be analyzed with respect to the geometry of the configuration. Their performance also depends on the calibration of the system, often realized with a calibration grid that is visible by all the cameras. Very high position accuracy (mm) can be reached for volumes up to a few m^3 while the accuracy degrades rapidly with increasing range. However, orientation accuracies are limited to 5 deg [143, 211].

FIG. 2.1: Trajectory visualization with *Dartfish Stromotion* [27].

Generally, all video systems require a large infrastructure, take long to setup (e.g. synchronization of cameras, determination of the cameras' position and exterior orientation) and are not adapted for every day use as well as for training purposes. In addition, these methods appear vulnerable to meteorological conditions. On the other hand, they may provide complex information about the athletes' movement and are therefore widely used for motion analysis and energy transfer studies.

2.2.2 Satellite and Inertial Navigation

Satellite-based positioning fulfills some of the criteria presented in TAB. 2.1. It has already proven its effectiveness for performance assessment, tracking of athletes and even rule compliance in disciplines like:

- Motor sports (e.g. car racing [75]).
- Water sports (e.g. rowing [233, 234, 11], windsurfing [58], kitesurfing [16], sailing [178]).
- Aeronautic sports (e.g. paragliding [59], ballooning [43]).
- Winter sports (e.g. alpine skiing [171, 31], ski jumping [10]).

Satellite navigation is also employed for the tracking of athletes during competitions [200, 179, 98, 199, 178]. Unfortunately, the athlete's environment is quickly alternating between open spaces and areas that are adverse to the reception of satellite signals (sudden satellite masking). Hence, continuous observation of the athlete's performance is not ensured for most disciplines. Considering the ergonomic requirements placed on the equipment, today's technological limits in GPS positioning are quickly reached or even exceeded [88, 106]. On the other hand, dual-frequency GPS receivers are restricted to few sports applications with higher accuracy needs because of their larger size and cost. In addition, many sports professionals are interested not only in position and velocity determination but also in orientation and acceleration. These quantities can not be observed directly with GPS. Indeed, orientations can only be computed based on multi-antenna systems. Accelerations cannot be observed, but approximated through numerical derivation [15, 171].

Inertial navigation systems (INS) provide standalone navigation. They allow determining orientations, accelerations and velocity and position changes at very high rates. However, even in higher-grade instruments, the effects of uncompensated systematic effects accumulate and the system's accuracy degrades rapidly with time. Because of their size and cost, high-grade INS are difficult or even impossible to use for performance evaluation in sports. On the other hand, low-cost, MEMS-type (Micro-Electro-Mechanical System) IMUs (Inertial Measurement Units) do not allow standalone navigation because their systematic errors are too large.

By combining satellite and inertial navigation, the drawbacks of each method are successfully canceled (Tab. 2.3). Indeed, satellite outages are potentially bridged by inertial measurements, while a part of the systematic inertial errors are calibrated when satellite positioning is available. The combination of the high short-term (relative) accuracy of the INS and long-term (absolute) accuracy of GPS results smears the variation in positioning performances and provides data at high rate including good orientation estimates.

2.2.3 Alternative Techniques Based on Position Fixing

Unlike satellite navigation, radio technologies like Ultra-Wide Band (UWB, [124, 126, 125, 119]) or Wireless Local Area Networks (WLAN, [86]) can be employed for positioning. They perform well indoors while their employment is rather difficult (i.e. due to heavy infrastructure, short range). Multipath and shadowing of the human body limit the use of such systems for performance evaluation of athletes [137].

2.2.4 Complementary Methods to Trajectory Determination

Timing cells are often used to measure intermediate splits. The method is widely employed for (average) performance assessment of athletes, material testing and ranking in competitions. However, no feedback about the instantaneous performance can be obtained.

TAB. 2.3: The characteristics of satellite and inertial methods for trajectory determination.

INS	GPS		GPS/INS
Autonomous	Dependent on satellite reception		Needs periodic satellite reception for initialization and the calibration of inertial sensor errors
No signal outages	Subject to loss of lock and cycle slips		Bridging of GPS outages
High short-term accuracy for position and velocity	High long-term accuracy for position and velocity	⇒	High position and velocity accuracy
Accurate orientation information	No orientation information		Precise orientation determination
Accurate acceleration information	Acceleration not reliable		Precise acceleration determination
Accuracy degrading with time	Uniform accuracy over time		Uniform accuracy over time
High data rate	Low data rate		High data rate

Other (optical) sensors were developed to provide partial information about a trajectory. Speed sensors are available for a wide range of applications. In motor sports, optical speed sensors provide information about the rotation rate of wheels which translates the power of the engine (FIG. 2.2, left). Optic odometers can be employed to assess the instantaneous velocity of a vehicle. A similar sensor is being developed in alpine skiing (FIG. 2.2, right): optical technology provides information about the instantaneous lateral and longitudinal velocity of a ski which allows the approximate derivation of sliding and edging angles [212]. Alternatively, speed can be determined with radar sensors by measuring the frequency shift caused by the Doppler effect (e.g. in alpine skiing [109]). Instantaneous speed at particular spots or velocity profiles on straightaways can be tracked by external radar installations [226].

FIG. 2.2: Speed measurement in motorcycling (left, [151]) and in alpine skiing (right, [212]).

2.2.5 Summary

None of the previously presented methods is a "universal" tool for performance assessment in sports. Indeed, every technique has its advantages and drawbacks. In terms of the offered accuracies and frequencies of observed parameters, GPS/INS derived trajectories provide certainly the most attractive alternative that is superior to other methods also at the rapidity of assessment. However, it cannot restore the athletes' feeling as the qualitative comparison based on images is lost. Hence, the presented methods are complementary and should be selected according to the needs.

2.3 Instrumentation for Satellite and Inertial Navigation

This section aims to identify the interesting setups of satellite and inertial navigation with respect to performance assessment in sports. The analysis is based on currently available infrastructure and commercially available hardware while discussing their suitability for sport applications.

2.3.1 Overview on GNSS and Processing Methods

GNSS - Today and tomorrow

Currently, two Global Navigation Satellite Systems (GNSS) are operational while the deployment of others is in preparation (Fig. 2.3). The operational systems consists of the American NAVSTAR-GPS and the Russian GLONASS (GLObal NAvigation Satellite System). Furthermore, four civil Satellite Based Augmentation Systems (SBAS) are operational or being developed to overcome the lack of accuracy, integrity, continuity and availability of the existing GNSS (Fig. 2.3):

- The American Wide Area Augmentation System (WAAS) covering North America.
- The European contribution EGNOS (European Geostationary Navigation Overlay Service).
- The Japanese SBAS called Multi-functional Transport SATellites (MTSAT) Satellite-based Augmentation System (MSAS).
- The Indian GPS/GLONASS And Geo-stationary Augmented Navigation (GAGAN).

In the past 5 years, the GLONASS constellation was composed of $8 - 18$ satellites, with some satellites in maintenance and thus not available for navigation. Recurrent promises with respect to the completion and modernization of GLONASS have been made [140, 87], and the complete constellation is most likely to be reached within a few years [142, 141]. Unlike GLONASS, all GPS satellites transmit with the same carrier frequency [132, 94]. The GPS receivers are therefore electronically less complex and less expensive thanks to their wider distribution. Some manufacturers combine GPS and GLONASS which increases the

availability of satellite signals in topographically difficult terrain [79]. However, the current pricing and processing complexity makes this option so far unattractive for sport applications. Thus, for this work, only GPS and its augmentations are considered.

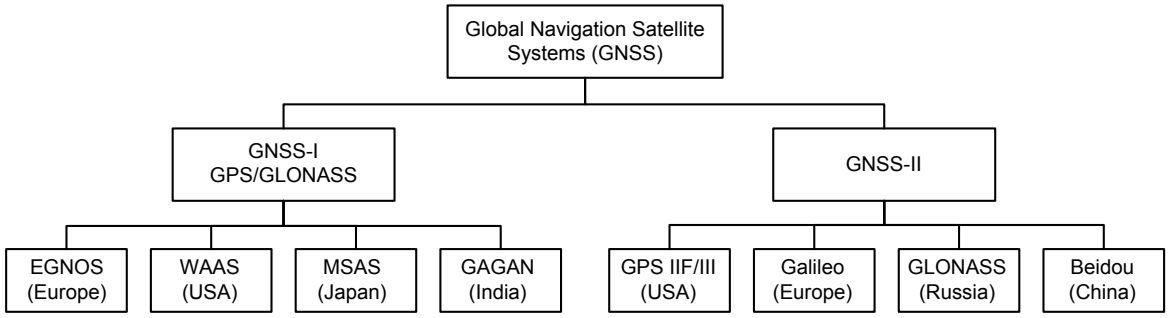

FIG. 2.3: Overview of Global Navigation Satellite Systems.

The second generation of GNSS (GNSS-II, FIG. 2.3) will consist at least of three global and several regional satellite navigation systems.

- **The modernized GPS**. The enhancements will affect the signal structure (new signals, state-of-the-art modulations) and the ground segment [38, 181, 69, 162, 68, 213, 18]. The new signals will be entirely available after 2015 (satellites are replaced by failure).

- **The modernized GLONASS**. The frequency band will be narrowed, additional navigation data will be transmitted (integrity information, timing difference GPS-GLONASS) and the satellite clocks are promised to become more stable [141, 142, 237]. A second and a third civil frequency will be added, as well as a new search and rescue service. In 2010, the constellation is promised to be composed of 24 satellites [142, 140, 87].

- The European GNSS called **Galileo**. It will offer modern signals [71, 80, 162], interoperability with GPS on L1 [201] and innovative value-added services, e.g. for safety of life applications, [70, 120, 33, 34]. The system is planned to become active in 2010-2012, with a delay of 2-3 years with respect to the initial plans [69, 50, 51].

- Regional satellite navigation systems like China's Compass (Beidou 2) satellite system or the Japanese Quasi-Zenith Satellite System (QZSS).

The above mentioned systems will not be available before the end of the thesis and are therefore not further considered in this research. However, it is important to underline the two main benefits that are expected for sport applications when they emerge [55].

- Thanks to the interoperability of GPS and Galileo on certain frequencies (and in particular L1), the number of available satellites will be doubled. In addition, a combined L1 GPS/Galileo receiver will not be significantly more expensive than the receiver of one system. Having access to two independent GNSS systems generates essentially availability and reliability advantages as discussed in many studies [123, 150, 148, 149].

- The modern signals will permit a more robust tracking and improve the multipath rejection. Indeed, the multipath performance of the modulations proposed by Galileo (BOC) is generally improved compared to existing GPS signals [70]. Their tracking accuracy is enhanced, thanks to the possibility to transmit side-lobes and because the BOC signals have lower correlation losses.

GPS signal structure

Based on a fundamental frequency, GPS satellites generate two frequencies L1 (1575.42 MHz) and L2 (1227.60 MHz, Fig. 2.4). Newer generations of satellites (will) emit additional signals (L2C since block IIR-M, L5 starting with block IIF). However, they are not yet available for the entire constellation and are therefore not considered in this research. L1 and L2 are modulated by phase which allows emitting:

- a data code (satellite ephemeris, coefficients of the ionospheric model, clock parameters and satellite health).
- pseudo-random codes (Pseudo Random Noise PRN).

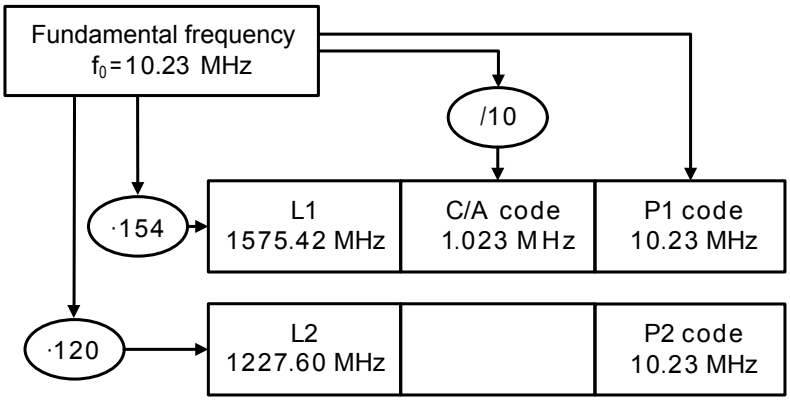

Fig. 2.4: GPS signal structure without message.

The coarse/acquisition (C/A) code is modulated on L1 and is available to all users. The precise P code is modulated on L1 and L2 (P1 and P2) and is reserved to the American military and its allies. The "protection" is created by adding a W code to the P codes which creates the so-called Y code (anti-spoofing). Generally, the unauthorized users are not able to measure P codes. However, the GPS receiver manufacturers have invented signal treatment techniques that allow either elimination or reconstitution of the Y code by squaring the signal, cross correlation or Z technology [12].

GPS methods

Fig. 2.5 gives an overview of current GPS positioning techniques that are of interest for applications in sports.

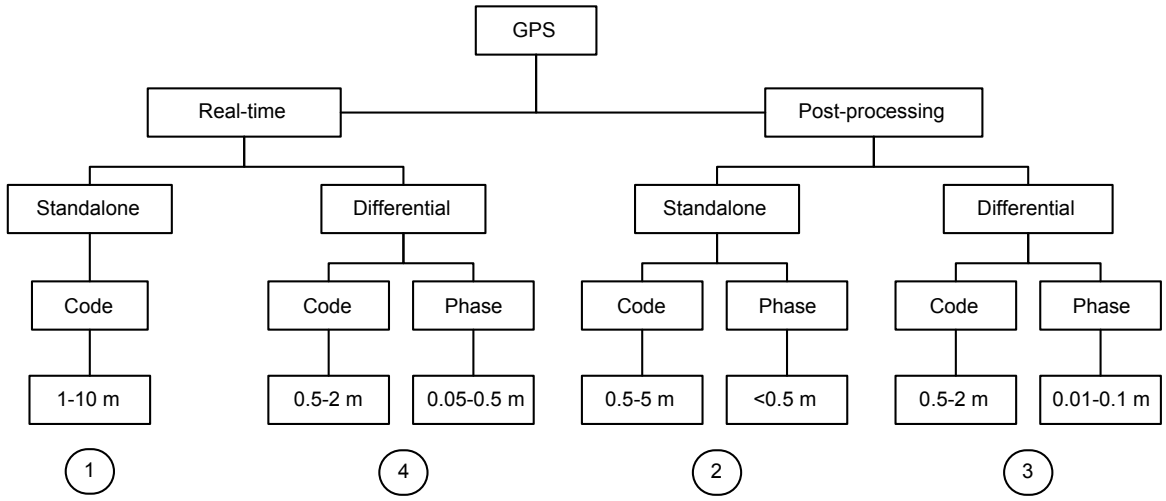

FIG. 2.5: Current GPS methods. "Code" indicates the use of carrier-phase smoothed pseudoranges. "Phase" refers to methods where carrier-phase ambiguities are estimated.

- Single Point Positioning (SPP) is the most commonly used method real-time positioning method. It is based on a single antenna that is mounted on an athlete (absolute GPS positioning, ① in FIG. 2.5). Ideally, this solution integrates phase-smoothed code measurements and a space based augmentation system SBAS. This approach results in a position accuracy of 1-4 m [214, 216, 72, 195, 9, 136]. However, SBAS do not yet cover the entire globe. In addition, the correction signal must be received from a geostationary satellite that may be low at the horizon (around 30 deg for Swiss latitudes) or by a terrestrial communication link [196].

- Precise Point Positioning (PPP, ② in FIG. 2.5) uses single- or dual-frequency measurements as well as orbit and clock corrections (near real-time publication of precise GPS ephemeris data) to achieve submetric or even decimetric position accuracy [152, 165, 167]. This technique is available world-wide without the need for local augmentation. However, PPP requires continuous signal tracking which is difficult to achieve in dynamic land applications. Additionally, the conversion rate exceeds the duration of some sport events. However, it can provide sufficiently accurate results for disciplines with low dynamics and long duration, e.g. golf [176].

- Dual-frequency carrier-phase measurements offer cm to dm accuracy in dynamic sport applications [171, 169]. Post-processing algorithms (③ in FIG. 2.5) do not require direct communication links between the reference station and rover. Thus, users do not have to bother about the setup of real-time communication devices and the initialization of GPS receivers. The main drawback of the post-processing approach is the uncertainty of system performance during data collection, i.e. undetected sensor failure, varying data quality [154]. Unlike real-time applications, the post-processing algorithms may recover ambiguities through backward processing, permit backward smoothing and allow estimating sophisticated clock and atmosphere models which increases their accuracy.

- Real-time differential applications (④ in Fig. 2.5) require continuous data exchange between GPS reference and rover stations. Therefore, additional devices need to be setup and communication links maintained [168, 169]. The advantage is in providing a positioning solution without the need of subsequent data downloading, conversions and computations by the user. Reduced positioning performance can be detected instantaneously.

GPS receivers

GPS receivers can be classified according to the number of tracked signals. Dual-frequency GPS receivers provide highly accurate results, but are only affordable for few sport disciplines with higher accuracy requirements (Fig. 2.6). The size of dual-frequency receivers has been reduced tremendously and the receiver boards have now acceptable dimensions for sport applications. Single-frequency receivers are less accurate, but have a more favorable pricing. Single-frequency geodetic and low-cost receivers are distinguished. Fig. 2.7 illustrates receivers of each category. This study aims at exploiting L1 only receivers, and particularly low-cost receivers, for performance assessment in sport.

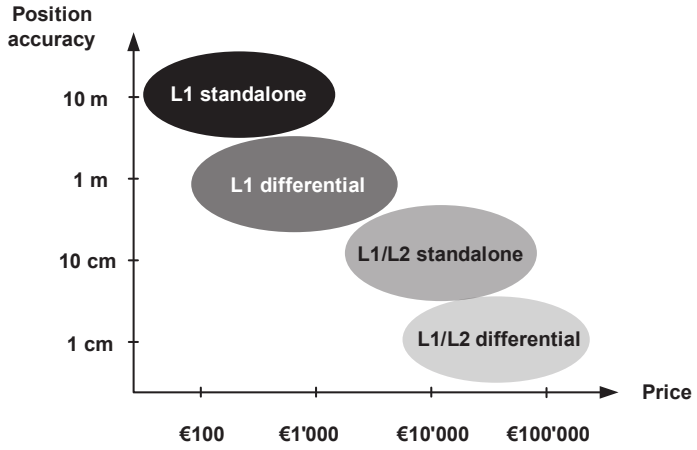

Fig. 2.6: Accuracy-price trade-off between different satellite navigation techniques.

Fig. 2.7: Not to scale: *Javad LGG100* (dual-frequency GPS and GLONASS receiver, left), *Thales DG16* (geodetic, single-frequency GPS receiver, middle) and *u-blox LEA-5T* (low-cost, single-frequency GPS receiver with access to raw data, right).

GPS antenna considerations

The quality and placement of the GPS antenna and the connection to the GPS receiver is particularly important. Indeed, injudicious placement or power losses due to antennas and cabling, that do not amplify the signal as expected by the receiver, alter the quality of the resulting positioning. Furthermore, the vertical response pattern and the phase center stability impact the quality of the received signal [138]. In addition, the physical size of a GPS antenna is limited by the wavelength of the signal [182]. Falling below these physical constraints will result in performance losses as well. Globally, patch and helix antennas can be distinguished (Fig. 2.8). The latter are able to acquire GPS signals in wider angle. Hence, they can be oriented randomly by the users which is an undeniable advantage in sports.

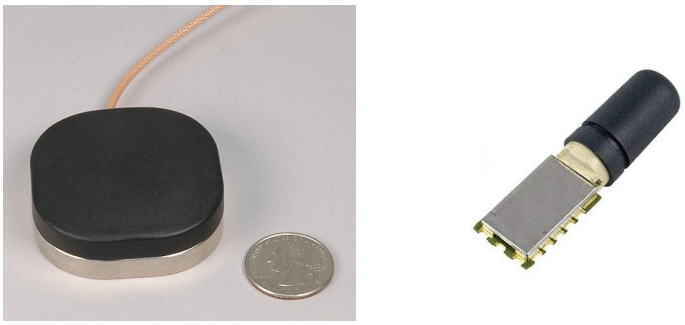

Fig. 2.8: Not to scale: *Antcom L1/L2 Low Profile*(Dual-frequency GPS antenna, left) and *Sarantel GeoHelix-S* (single-frequency GPS antenna, right).

2.3.2 Inertial Measurement Units

Gyroscope technology

Gyroscopes are angular rate sensors. They generally represent the most expensive part of an INS and their performance is usually limiting the overall navigation performance. The design of gyros can be subdivided in five major groups according to the underlying physical principles [160, 170]. The conservation of the angular momentum leads to the design of rigid **rotor gyros** which were successfully implemented on gimbaled platforms. **Optical gyros** use the Sagnac effect, i.e. the relativistic principle that speed of light is conserved in rotating bodies. They are currently employed in most applications of autonomous navigation [191]. **Vibratory gyros** make use of the principle that a vibrating object tends to keep vibrating in the same plane, while the rotation of its support induces a Coriolis effect. **Coriolis sensors** are also based on accelerometer technology. The angular rates are sensed either from a single rotating accelerometer or a pair of accelerometers to which a high frequency acceleration has been applied. This technique is the major design concept in MEMS devices [47]. There are also other approaches like glass resonators or based on **atomic interferometry** exploring the preservation of mass in internal atomic structures. The latter technology has the potential to become extremely sensitive.

Accelerometer technology

Accelerometers measure specific forces. Three major groups of accelerometers can be distinguished [160, 170]. **Force-rebalance sensors** measure the electrical current (which is proportional to the force) needed to restrain a mass at a zeros point. **Vibratory accelerometers** sense frequency differences in a vibrating system as a measure of acceleration. These sensors are often fabricated using MEMS technology. A new development aims at producing high performance accelerometers involving MEMS technology and **electrostatic levitation** [192].

Sensor quality

The previous sections have illustrated the wide range of available sensors. Accordingly, the spectrum of achievable accuracies spans several orders of magnitude between the classes and also within them. Nevertheless, the suitability of gyroscopes and accelerometers for a particular application concerns not only their stability but also other factors such as sensor's dynamic range or its sensitiveness to the environment in which it will operate (e.g. shock, vibrations, temperature change, acceleration) [170].

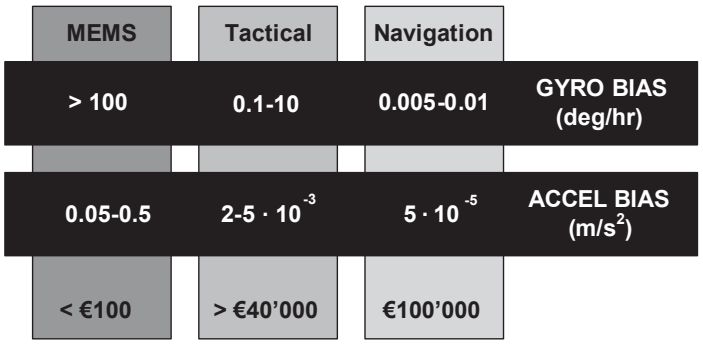

Fig. 2.9: Accuracy-price trade-off for MEMS-type, tactical-grade and navigation-grade IMUs.

Fig. 2.9 presents an overview of accuracies and cost for the three major groups of IMUs. Tab. 3.1 details the error budget for the three categories. The pricing, but also the size and weight of the sensors limit the use of inertial navigation for many sports to MEMS technology. Investigating the application of this technology to sports with respect to the mitigation of their large errors is a major objective of this research.

2.3.3 Other Aspects Related to System Architecture

A tool for trajectory assessment in sports should also include interfaces to other sensors related to the physical performance (e.g. VO2, heart rate) or the sport equipment (e.g. strain gauges, torque sensor). Furthermore, data transmission must be foreseen, either for real-time data exchange (RTK, real-time following of the athletes position) or subsequent data download. Besides the requirement listed in Tab. 2.1, limitations for weight and form of the sensors are

specific to each discipline and need to be considered in the system design. This requires the use of low-power components to reduce battery weight (e.g. asynchronous electronic components [190]).

Communication link

A further objective of this research is to make the comparison of the athletes' performance accessible to the spectators and coaches and to bring it as close to real-time as possible. Thus, the possibilities of advising athletes in real-time are addressed. Considering GNSS in differential mode, such approach requires the implementation of a reliable and flexible communication architecture between sensors placed on athletes (GPS rovers), the GPS master station and a central server where the performance is monitored, visualized or distributed.

Tab. 2.4 presents a list of currently exploited communication technologies. The choice of the technology depends on:

- Availability of the communication network at the training and competition sites with sufficient bandwidth (the required bandwidth is approximately 15 kbps, [169]).
- Robustness of the communication link.
- Power consumption.
- Negligible interferences with GPS.

Radio transmission is the traditional communication link for GPS RTK (Real-Time Kinematic). Unfortunately, the technique is sensitive to interferences and has reduced range with low power transmitters (especially in mountainous regions). Some ISM frequencies (Industrial, Scientific and Medical radio bands) like 868 MHz provide proprietary data transmission for low data rates over small baselines (< 10 km) and with small power consumption. Furthermore, wireless mesh architecture provide high bandwidth for a network of a specific coverage area.

GSM (Global System for Mobile communication) transmission enables a bidirectional point-to-point communication on a reserved channel. This complicates the transmission of GPS corrections to multiple stations. In addition, the communication channel is often overloaded and the connecting time is rather long [168]. On the other hand, GPRS (General Packet Radio Service) allows the distribution of GPS corrections by the Internet and has a higher (theoretical) bandwidth than GSM. Regrettably, GPRS does not provide a reserved communication channel. Indeed, the available bandwidth and the availability of the network depends on the network utilization. Moreover, some hardware problems with GPRS modules were reported [92]. UMTS (Universal Mobile Telecommunications System) provides a larger bandwidth and was designed for "highspeed" data download. However, UMTS is less favorable than GPRS for continuous data transmission and small delays are encountered because of the negotiation procedure between modem and service provider.

Satellite based communication (SatCom) systems based on LEO (Low Earth Orbit) satellites provide larger coverage than terrestrial communication networks but still suffer from reduced

bandwidth (lower than 9,6 kbps). Cost and power consumption of SatCom modems is approximately ten times higher than for GPRS modems. Broadband SatCom links are not yet miniaturized for outdoor activities.

Wireless communication based on Bluetooth (802.15-1), Zigbee (802.15-4), WLAN (802.11), IrDA (Infrared Data Association) or UWB are sensitive to interferences and have reduced range (less than 300 m, except with directional transmission).

It follows from the discussion that radio transmission networks are the favorite communication link for local sport applications. It is proprietary, provides sufficient bandwidth and has limited cost. Furthermore, the mesh network structure is suitable for the small range of L1-RTK. Indeed, as the ionospheric modeling is limited by the missing L2 frequency, the transmitted corrections are valid only for short ranges (< 1 km, Fig. 2.10).

Tab. 2.4: Appropriateness of communication links for sport applications.

	Radio	GSM	GPRS/UMTS	SatCom	802.1x
Proprietary	+	+	−	+	+/−
Data rate	+	−	+	−	+
Availability	+	−	−	+	−−
Coverage	+/−	+	+	+	−−
Cost	+	−	−	−	+
Power consumption	+	+/−	+/−	+/−	+

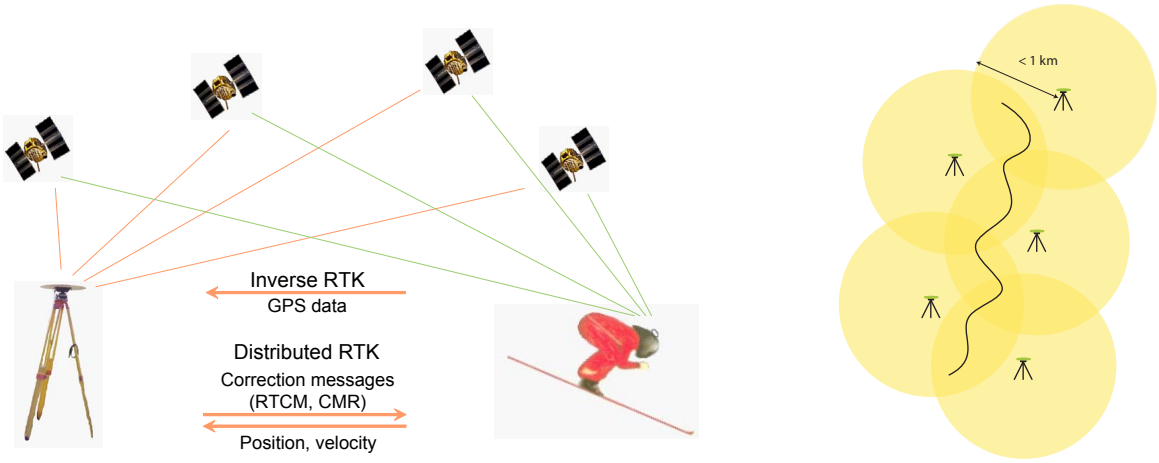

Fig. 2.10: Communication and RTK infrastructure.

Transmitted data

The communication architecture can be imagined in two ways (Fig. 2.10).

- With inverse RTK, the raw GPS measurements are sent to the master station where they are processed with the reference data to compute the athlete's position. As no

differential processing on the athlete is required, the computation power of the device carried by the athlete is significantly reduced. The advantage is the one-directional communication, as well as the employment of cheaper non-RTK capable GPS receivers. However, the purchase or development of inverse RTK software is required.

- Distributed RTK is an approach proposed by reference [169]. Distributed RTK benefits from the GPS software integrated in the receiver carried by the athlete which requires RTK-enabled GPS receivers. The resulting position and velocity is transmitted back to the base station. The computational load is distributed to the numerous rovers, but the communication link has to be bi-directional.

In real-time applications, the continuity of the communication link is an important issue. Its interruption can be handled by implementing a delayed buffer [92]: When no communication link is available, the data is stored on the rover. As soon as a communication link is established, the buffered data is transmitted to a central computer for performance analysis.

Chapter 3

Measurements, Models and Estimation Methods

To determine the trajectory of an athlete based on satellite and inertial positioning, it is necessary to model various physical observations. The efforts described here began with research into the usual approach to GPS/INS integration in which the prevailing systematic effects are estimated by external measurement of positions and velocities. The first part of this chapter presents inertial and satellite measurements and their corresponding error models. In the second part, different sensor fusion algorithms are compared in order to identify the most appropriate methods. Finally, the GPS/INS integration algorithms are developed.

3.1 Inertial Measurement Model

3.1.1 Generalized Error Model for Inertial Observations

Accelerometers and gyroscopes are mounted together on platforms. Typically, three orthogonal sensors of both types are used (orthogonal triads), establishing an Inertial Measurement Unit (IMU). The gyroscopes sense angular velocity $\boldsymbol{\omega}_{ib}^{b}$ between the body frame and the inertial frame. The accelerometers measure specific force $\mathbf{f}^{b}$ (i.e. force per unit mass) along the axes of the body frame.

Inertial measurements are always affected by random and systematic errors with varying magnitude according to the sensor's quality. The following generalized error model can be formulated [191, 64, 130, 131].

$$\hat{\boldsymbol{\ell}} = \mathbf{M}_{\ell} \cdot (\mathbf{S}_{\ell} \cdot \boldsymbol{\ell} + \mathbf{b}_{\ell}) + \mathbf{w}_{\ell} \tag{3.1.1}$$

where $\hat{\boldsymbol{\ell}}$ represents the estimated measurement, $\boldsymbol{\ell}$ the nominal observation and $\mathbf{M}_{\ell}$ the misalignment matrix. The diagonal matrix $\mathbf{S}_{\ell}$ contains the scale factors, $\mathbf{b}_{\ell}$ is the bias and $\mathbf{w}_{\ell}$ the measurement white noise vector. Tab. 3.1 indicates typical errors for three categories of IMU sensors.

TAB. 3.1: Typical errors of accelerometers and gyroscopes.

	Navigation-grade	Tactical-grade	MEMS-type
Accelerometer			
Bias [m/s^2]	$5 \cdot 10^{-5}$	$2 \cdot 5^{-3}$	$0.05 - 0.5$
Scale factor [ppm]	$25 - 50$	300	$30'000$
Misalignment [arcsec]	5	60	3600
White noise [m/s$^2/\sqrt{\text{Hz}}$]	$5 \cdot 10^{-5}$	$5 \cdot 10^{-4}$	$0.02 - 0.2$
Gyroscope			
Bias [deg/h]	$0.005 - 0.01$	$0.1 - 10$	> 100
Scale factor [ppm]	1	100	$150'000$
Misalignment [arcsec]	2	60	3600
White noise [deg/h/$\sqrt{\text{Hz}}$]	0.001	0.002	0.5

The misalignment matrix $\mathbf{M}_\ell$ is defined as:

$$\mathbf{M}_\ell = \begin{bmatrix} 1 & -y_z & z_y \\ x_z & 1 & -z_x \\ -x_y & y_x & 1 \end{bmatrix} \tag{3.1.2}$$

where x_y, x_z, y_x, y_z, z_y and z_x are the non-orthogonality of the sensor axes defining the body frame.

The scale factor matrix is defined as:

$$\mathbf{S}_\ell = \mathbf{I} + \mathbf{S}_\ell^C + \mathbf{S}_\ell^{RC} + \mathbf{S}_\ell^{GM} + \mathbf{S}_\ell^{RW} \tag{3.1.3}$$

where $\mathbf{S}_\ell^C$ are the constant components of the scale factors, $\mathbf{S}_\ell^{RC}$ are random constants vectors defined by the stochastic processes: $\mathbf{S}_\ell^{RC} = G(\mu, \sigma)$, G being a standard Gaussian process with $\dot{\mathbf{S}}_\ell^{RC}(t) = 0$. $\mathbf{S}_\ell^{GM}$ are first-order Gauss-Markov stochastic processes defined as:

$$\dot{\mathbf{S}}_\ell^{GM}(t) = -\beta \cdot \mathbf{S}_\ell^{GM}(t) + \mathbf{w}_k(t) \tag{3.1.4}$$

where $\beta = 1/T$ is the inverse of the correlation time T and $\mathbf{w}_k$ a zero-mean Gaussian white-noise process. $\mathbf{S}_\ell^{RW}$ is a random walk stochastic process defined by:

$$\dot{\mathbf{S}}_\ell^{RW}(t) = \mathbf{w}_k(t) \tag{3.1.5}$$

The bias is defined as:

$$\mathbf{b}_\ell = \mathbf{b}_\ell^C + \mathbf{b}_\ell^{RC} + \mathbf{b}_\ell^{GM} + \mathbf{b}_\ell^{RW} + \mathbf{b}_\ell^{BI} + \mathbf{b}_\ell^{GS} \cdot \hat{\mathbf{f}} \tag{3.1.6}$$

where $\mathbf{b}_\ell^C$ are the constant components of the bias, $\mathbf{b}_\ell^{RC}$ are random constants stochastic processes, $\mathbf{b}_\ell^{GM}$ are first-order Gauss-Markov stochastic processes and $\mathbf{b}_\ell^{RW}$ are random walk stochastic processes (defined as previously for the scale factors). $\mathbf{b}_\ell^{BI}$ are the bias instabilities

investigated by [64, 130, 131]. Finally, the term $\mathbf{b}_\ell^{GS}$ is a gravity sensitivity parameter which has to be added to the specific force measurements of some accelerometers.

The white noise processes $\mathbf{w}_\ell$ are defined as:

$$\mathbf{w}_\ell(t) = \sigma_\ell \cdot \mathbf{w}_k(t) \tag{3.1.7}$$

where σ_ℓ is the standard deviation of the white noise processes.

Even though the numerous error terms can be modeled, their estimation during the navigation processing depends on the dynamics and the type of external measurements. Eventually, some parameters are sufficiently stable and can be determined by long-term (static or dynamic) experiments. Measurement biases $\mathbf{b}$ are the result of manufacturing imperfections that tend to vary with the change of environmental conditions. Scale factors $\mathbf{S}$ are sometimes determined under lab conditions, but become variable under high dynamics [193]. Misalignments $\mathbf{M}$ result from the non-orthogonality of the axes that define the body coordinate frame. In kinematic applications, this effect becomes less significant if frequent maneuvers are performed and can be assigned to the random error term. However, parameters calibrated under laboratory conditions are rarely completely stable, even for higher-grade IMUs. Furthermore, note that some of the previously described error contributions are physically irrelevant for some sensors (e.g. ring-laser gyroscopes do not require the estimation of g-sensitivity and scale-factors which are often negligible).

3.1.2 Simplified Error Model for Inertial Observations

Judging that the misalignments, scale factors and constant error terms cannot be decorrelated efficiently given the complexity of the MEMS sensors, the generalized error model is simplified. Indeed, only a bias term is considered and its associated errors are modeled as first order Gauss Markov processes [221, 220, 194].

$$\begin{aligned} \hat{\boldsymbol{\ell}} &= \boldsymbol{\ell} + \mathbf{b}_\ell + \mathbf{w}_\ell \\ \dot{\mathbf{b}}_\ell &= -\beta_\ell \cdot \mathbf{b}_\ell + \sqrt{2\sigma_\ell^2 \beta_\ell}\ \mathbf{w}_\ell \end{aligned} \tag{3.1.8}$$

where $\hat{\boldsymbol{\ell}}$ is the estimated measurement, $\boldsymbol{\ell}$ the nominal observation, $\mathbf{b}_\ell$ the bias term, $\mathbf{w}_\ell$ the measurement noise and $\beta_\ell = 1/T$ the inverse of the correlation time T. This process permits to estimate a wide range of error behaviors as a function of β, from random constants to random walks.

In chapter 5, it will be experimentally proven that this simplified error model is justified considering the error characteristics of MEMS-type sensors, typical dynamics in sport applications and the often short integration intervals.

3.2 Magnetic Measurements

Some MEMS-type IMUs on the market (e.g. *Microstrain 3DM-G*, *Xsens MTi*) contain also a triad of magnetometers. These sensors measure the amplitude of the magnetic field along

their axis. FIG. 3.1 describes the components of Earth magnetic field and the magnetic measurements.

The azimuth α is the angle between magnetic north and the x-axes of a triple-axis magnetic sensor in NED configuration (equation 3.2.1). Magnetic north is the direction of the horizontal component H_h of the magnetic field of the Earth $\mathbf{H}_e$ which is the component perpendicular to the gravity vector. The azimuth needs to be corrected for the magnetic declination λ to derive the orientation with respect to the geographic north which is defined by the Earth's axis of rotation. The magnetic declination is varying as a function of the position on the globe and time. It can be retrieved from global or local models, e.g. the World Magnetic Model (WMM) produced by the United States National Geospatial-Intelligence Agency (NGA) [122]. The magnetic inclination δ is the angle of the magnetic vector to the horizontal plane (equation 3.2.2).

$$\alpha = \arctan\left(\frac{-H_y}{H_x}\right) \tag{3.2.1}$$

$$\mathbf{H}_e = H_h \begin{bmatrix} \cos(\alpha) \\ -\sin(\alpha) \\ \tan(\delta) \end{bmatrix} = \begin{bmatrix} H_x \\ H_y \\ H_z \end{bmatrix} \tag{3.2.2}$$

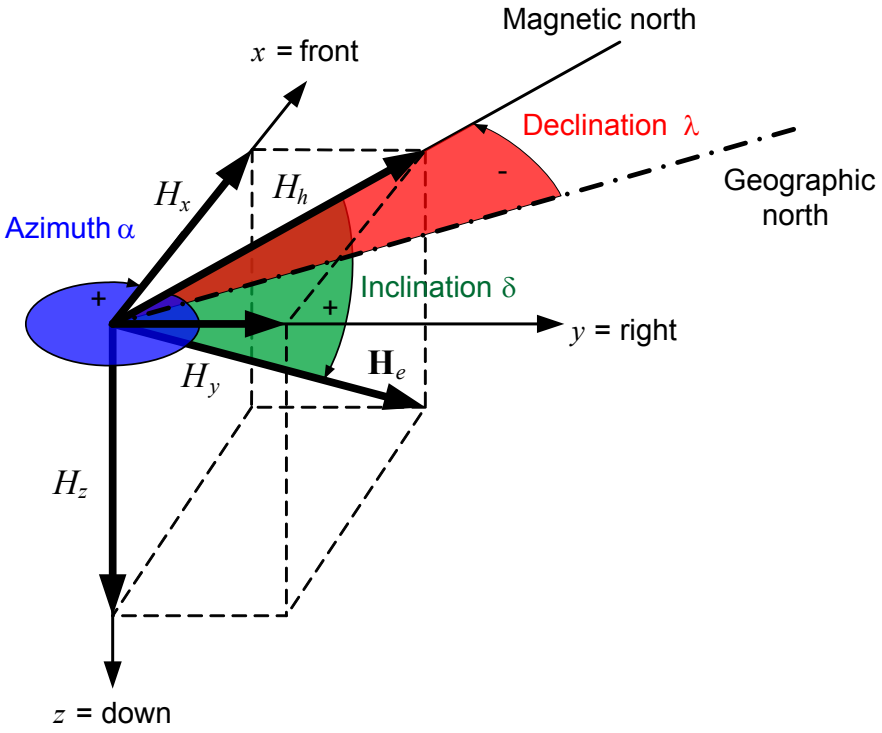

FIG. 3.1: Representation of the magnetic field of the Earth on the northern hemisphere.

Unfortunately, the Earth magnetic field measurement is disturbed by parasite magnetic fields. The perturbations can be natural or caused by man-worn objects. Soft perturbations may be caused by ferrous materials that influence the direction of the Earth magnetic field. Hard

magnetic disturbances (i.e. sign flipping or complete overmasking) may be caused by magnetic objects like electrical lines or electronic equipment. These perturbations may vary much faster in time, e.g. during the communication setup of a telecommunication link. Generally, rotation and translation parameters are estimated to model the weak magnetic disturbances [90]. In this research, a simplified model is considered estimating only a bias term.

$$\hat{\mathbf{h}} = \mathbf{h} + \mathbf{d}_m + \mathbf{w}_m \tag{3.2.3}$$

where $\hat{\mathbf{h}}$ is the estimated magnetic field measurement, $\mathbf{h}$ the measured magnetic field, $\mathbf{d}_m$ the magnetic disturbance and $\mathbf{w}_m$ the measurement noise. The magnetic disturbance is modeled as a first order Gauss-Markov process.

$$\dot{\mathbf{d}}_m = -\beta_{d_m}\mathbf{d}_m + \sqrt{2\sigma_{d_m}^2\beta_{d_m}}\ \mathbf{w}_{d_m} \tag{3.2.4}$$

3.3 GPS Observations

The GPS signals and methods were introduced in section 2.3.1. This section details how these signals are acquired and modeled for positioning.

3.3.1 Code Measurements

Measuring pseudoranges requires knowledge about the PRN codes. By comparing the signal from the satellite against its copy, the receiver determines a time shift and deduces the pseudorange between the receiver and the satellite.

$$\rho_r^s = c \cdot (t_r - t^s) \tag{3.3.1}$$

where ρ_r^s is the range between satellite s and receiver r, c the speed of light, t_r the time of signal reception registered by the receiver clock, and t^s the time of transmission of the signal, both expressed in the GPS reference time.

This measurement of range ρ_r^s is subject to numerous errors that need to be modeled and eliminated in the positioning algorithm.

$$p_{Li,r}^s - v_r^s = \rho_r^s + d\rho_r^s + c \cdot (dt_r - dt^s(t-\tau)) + T_r^s + I_{Li,r}^s + M_{pi,r}^s + c \cdot (b_{Li}^s + b_{Li,r}) \tag{3.3.2}$$

where $p_{Li,r}^s$ is the observed pseudorange on Li (L1 or L2) at time t, ρ_r^s the true distance between the receiver r and the satellite s, $d\rho_r^s$ the radial orbital error at transmit time, dt_r the receiver clock error, and $dt^s(t-\tau)$ the satellite clock error considering the propagation time τ of the GPS signal ($\tau = \rho/c$). T_r^s is the tropospheric delay, while $I_{Li,r}^s$ are the ionospheric delays on Li. $M_{pi,r}^s$ is the multipath error, b_{Li}^s as well as $b_{Li,r}$ are hardware delays and v_r^s the residual error.

The clock errors of the receiver and of the satellite are equal on both frequencies because they are generated by the same oscillators. The troposphere is a diffracting medium. Indeed, the speed and refraction index do not depend on the wavelength of the signal. Hence, the

tropospheric error is of the same amplitude for both frequencies. The ionosphere is dispersive and the ionospheric error I_{L1} is related to I_{L2} through the following expression [183, 214].

$$I_{L2} = \frac{f_{L1}^2}{f_{L2}^2} \cdot I_{L1} \tag{3.3.3}$$

Multipath errors $M_{Li,r}^s$ are systematic errors if short observation periods are considered (up to a few minutes), but may also be interpreted as noise for longer observation periods. Antenna eccentricities are neglected in this research (max. $1-2$ mm) and are not taken into account in equation 3.3.2.

Tab. 3.2 indicates the importance of the different error contributions of pseudorange measurements [132]. Even though the satellite clocks have improved [118, 117], that more precise ephemeris are available [26] and that the evolution of receiver electronics has lowered measurement noise [91], the overall error budget remains representative.

Tab. 3.2: GPS error sources of pseudorange measurements (1σ) [132].

Error source	Standard GPS [m]	Differential GPS [m]
Ephemeris	2.1	0.0
Satellite clock	2.1	0.7
Ionosphere	4.0	0.5
Troposphere	0.7	0.5
Multipath	1.4	1.4
Receiver measurement	0.5	0.2
Reference station	-	0.4

3.3.2 Carrier-Phase Measurements

In carrier-phase measurements, the distance between satellite and receiver is composed of an integer number of unknown cycles and of the fractional phase measurement. The receiver counts the changes in number of cycles generated through the motion of the satellite.

$$\rho_r^s = N_{Li,r}^s \cdot \lambda_{Li} + \phi_{Li,r}^s \cdot \lambda_{Li} \tag{3.3.4}$$

where ρ_r^s represents the distance between satellite and receiver, $N_{Li,r}^s$ an unknown number of cycles (carrier-phase ambiguity), $\phi_{Li,r}^s$ the phase measurement and λ_{Li} the wavelength.

Accounting for the various error sources in the distance measurements, the carrier-phase measurements can be modeled by:

$$Li_r^s - v_r^s = \lambda_{Li}\cdot\phi_{Li,r}^s - v_r^s = \rho_r^s + d\rho_r^s + c\cdot(dt_r - dt^s(t-\tau)) + T_r^s - I_{Li,r}^s + M_{Li,r}^s + \lambda_{Li}\cdot B_{Li,r}^s \tag{3.3.5}$$

with $\lambda_{Li} \cdot B_{Li,r}^s = \lambda_{Li} \cdot (N_{Li,r}^s + \delta N_{Li,r}^s) + c \cdot (b_{Li}^s + b_{Li,r})$.

The term $\lambda_{Li} \cdot B_{Li,r}^s$ includes the integer ambiguity $N_{Li,r}^s$ and the "phase windup" effect $\delta N_{Li,r}^s$ [155]. The ambiguity $N_{Li,r}^s$ cannot be separated from hardware errors b_{Li}^s and $b_{Li,r}$.

Hence, $B^s_{Li,r}$ must be considered as a real value rather than an integer. However, while the phase windup phenomena is important for geodetic applications, it can be attributed to measurement noise in this research.

Comparing equations 3.3.2-3.3.4 shows that the code measurements are delayed by the same amount as the carrier-phase measurements are advanced by the ionosphere (I_{L1} and I_{L2}).

3.3.3 Carrier-Phase Smoothing

If continuous code and carrier-phase measurements are available, the former can be smoothed by the carrier-phase [155].

$$\tilde{p}^s_{Li,r}(t) = \bar{p}^s_{Li,r} + \Delta Li^s_r(t) + 2\frac{f^2_{L1}}{f^2_{L1} - f^2_{L2}} \cdot (\Delta L1^s_r(t) - \Delta L2^s_r(t)) \tag{3.3.6}$$

with

$$\Delta Li^s_r(t) = Li^s_r(t) - \bar{Li}^s_r \tag{3.3.7}$$

where $\tilde{p}^s_{Li,r}(t)$ are the carrier-phase smoothed code measurements at time t, $Li^s_r(t)$ the carrier-phase measurements at time t expressed in meters. $\bar{p}^s_{Li,r}$ and $\bar{Li}$ are the average pseudorange and carrier-phase measurements over n epochs without cycle slip. The measurement noise is reduced by a factor $\sqrt{n}$ [155].

For single-frequency measurements, carrier-phase smoothing can be performed as described by [67, 94, 62]:

$$\tilde{p}^s_{L1,r}(t) = \frac{1}{n}p^s_{L1,r} + \frac{n-1}{n} \cdot (\bar{p}^s_{L1,r}(t-1) + (L1^s_r(t) - L1^s_r(t-1))) \tag{3.3.8}$$

3.3.4 Doppler Measurements

The frequency of the received GPS signal differs from the frequency transmitted by the satellite. This frequency offset is partly due to the Doppler effect which is caused by the relative motion of the transmitting satellite with respect to the receiver. The Doppler shift $D^s_{Li,r}$ can be expressed by the following dot product [132, 93]:

$$D^s_{Li,r} = -\frac{\mathbf{v}^s - \mathbf{v}_r}{c} \bullet \frac{\mathbf{r}^s - \mathbf{r}_r}{\|\mathbf{r}^s - \mathbf{r}_r\|} \cdot Li^s_r \tag{3.3.9}$$

where $\mathbf{v}^s$ is the satellite velocity, $\mathbf{v}_r$ the receiver velocity, c the speed of light, $\mathbf{r}^s$ the satellite position and $\mathbf{r}_r$ the receiver position.

The Doppler shift can be converted to a pseudorange rate observation by the following expression [132, 93]:

$$\dot{p}^s_{Li,r} - v^s_r = \dot{\rho}^s_r + c \cdot \dot{dt}_r \tag{3.3.10}$$

where $\dot{p}^s_{Li,r}$ is the pseudorange rate observation, $\dot{\rho}^s_r$ the true pseudorange rate, $\dot{dt}_r$ is the receiver clock drift to the delta range measurement and v^s_r the residual error.

3.3.5 Differential GPS

Differential GPS (DGPS) permits reducing the systematic errors in satellite positioning (Tab. 3.2) by comparison of the observations between GPS receivers in vicinity, i.e. a static GPS receiver (master m) and a mobile GPS receiver (rover r). For single-frequency measurements, this hypothesis is valid for distances up to approximately $3-5$ km [94]. Assuming that two receivers are affected by the same atmospheric errors, the latter can be eliminated from equations 3.3.5-3.3.2 together with the satellite clock errors $\Delta t^s(t-\tau)$ and the orbital errors $d\rho$. The so-called single differences lead to the following expressions:

$$\begin{aligned}
\Delta p^s_{Li,mr} - v^s_{mr} &= \Delta\rho^s_{mr} + c\cdot\Delta dt_{mr} + \Delta M^s_{pi,mr} + c\cdot\Delta b_{Li,mr} \\
\Delta Li^s_{mr} \; - v^s_{mr} &= \Delta\rho^s_{mr} + c\cdot\Delta dt_{mr} + \Delta M^s_{Li,mr} + \lambda_{Li}\cdot\Delta B^s_{Li,mr} \\
\Delta \dot{p}^s_{Li,mr} - v^s_{mr} &= \Delta\dot{\rho}^s_{mr} + c\cdot\Delta\dot{dt}_{mr}
\end{aligned} \tag{3.3.11}$$

where single difference operator Δ of quantity x is defined as:

$$\Delta x^s_{mr} = x^s_m - x^s_r \tag{3.3.12}$$

The unknowns related to the GPS receivers, i.e. single-differenced receiver clock error Δdt_{mr}, receiver clock drift $\Delta\dot{dt}_{mr}$, hardware error $\Delta b_{Li,mr}$, can be eliminated by differentiating between satellites (double-differences):

$$\begin{aligned}
\nabla\Delta p^{zs}_{Li,mr} - v^{zs}_{mr} &= \nabla\Delta\rho^{zs}_{mr} + \nabla\Delta M^{zs}_{pi,mr} \\
\nabla\Delta Li^{zs}_{mr} \; - v^{zs}_{mr} &= \nabla\Delta\rho^{zs}_{mr} + \nabla\Delta M^{zs}_{Li,r} \; + \lambda_{Li}\cdot\nabla\Delta B^{zs}_{mr} \\
\nabla\Delta \dot{p}^{zs}_{Li,mr} - v^{zs}_{mr} &= \nabla\Delta\dot{\rho}^{zs}_{mr}
\end{aligned} \tag{3.3.13}$$

where z indicates the reference satellite and where double difference operator ∇ of quantity x is defined as:

$$\begin{aligned}
\nabla\Delta x^{zs}_{mr} &= \Delta x^z_{mr} \qquad - \Delta x^s_{mr} \\
&= (x^z_m - x^z_r) - (x^s_m - x^s_r)
\end{aligned} \tag{3.3.14}$$

3.4 GPS/INS Sensor Fusion

3.4.1 Integration Constraints

To combine the satellite and inertial measurements, the two systems need to be time synchronized and the observation of one system needs to be identified in the second. Different scenarios can be envisaged.

- A mathematical relation between the sensor placement can be expressed.
  - If GPS antenna and IMU are rigidly fixed with respect to each other, GPS coordinates, velocities or raw GPS measurements (pseudoranges, carrier-phase measurements) can be employed to calibrate the inertial sensors (section 3.4.3).

  - More sophisticated constraints can be expressed when reconstructing general complex movements. For instance, by introducing constraints related to the human skeleton, the body motion can be reconstructed with inertial sensors distributed on the appropriate body parts [14].

- Non-holonomic constraints can be imposed to particular dynamics, e.g.:
  - The zero velocity updates (ZUPTs) are used when the IMU is stationary and free from vibrations, which is very often the case at the beginning or at the end of a sport performance. Then, the external velocity measurements can be considered as zero.
  - For car navigation, the lateral and vertical velocities are zero if the vehicle is not skidding [57, 166, 186, 229].
  - In many sports, athletes experience zero lateral acceleration when they change from a left to a right turn (e.g. motor cycling, alpine skiing). This information could be deduced from a GPS derived trajectory (i.e. change in sign of the curvature).

- Eventually, additional information can be integrated.
  - Magnetometers measure the Earth magnetic field and potentially improve the orientation estimation.
  - Employing an array of GPS antennas provides external attitude observations. However, such setups are impractical for sport applications.
  - Redundant inertial sensors can improve the navigation performance on many levels and are discussed in chapter 6.
  - Other external measurements may be introduced to the GPS/INS algorithm to improve the navigation solution. This may include punctual velocity measurements (e.g. measured by radar) or position updates (e.g. determined by Radio Frequency IDentification (RFID) tags or special setups for the determination of the GPS antenna position as described by [10]).

Non-holonomic constraints are specific to the dynamics and cannot be generalized easily for other disciplines. Therefore, with the exception of ZUPTs, these constraints are not further investigated in this research. For the same reasons, additional (external) information than those provided by GPS, redundant IMUs and magnetometers are not considered in this work. However, the geometric relation between the placement of the GPS antenna and the inertial sensor will be exploited.

3.4.2 Integration Strategy Trade-offs

Extended Kalman Filtering (EKF) is widely used in GPS/INS integration. Although it has proven its effectiveness with higher-grade inertial sensors, its dependency on correct (physical) models, the underlying Gaussian assumption and linearization may limit its use when working with MEMS-type sensors. The linearization dependency might be a limiting factor (e.g. for filter convergence) in sports because of the high dynamics endured in some disciplines. Therefore, this section discusses alternative integration strategies with respect to their operation in sport applications (Tab. 3.3).

Linearization dependency

In conventional GPS/INS integration, the state distribution of the EKF is approximated by a Gaussian random variable which is then propagated analytically through the (first-order) linearization of the non-linear system. In contrast, Particle Filters (PF) and Sigma-Point KF (SPKF) propagate the state covariance according to the non-linear model (for the SPKF at least to the second-order). Hence, the prediction mode can be improved. Unlike EKF and SPKF, PFs make no assumption on the probability density function (PDF) and might reveal a superior numerical accuracy to other filtering methods. Hence, PFs give an approximate solution to an exact model, rather than an optimal solution to an approximate model as the EKF does [65]. However, they are computationally expensive for high-dimensional systems with large sampling rates.

The derivation of Jacobians for system and measurement models required in EKF is nontrivial and may lead to implementation difficulties. Furthermore, EKF only tolerates small errors. Otherwise, the first-order approximations may cause biased solutions and inconsistency of the covariance update which can lead to filter instability. Second order filters may improve filter stability, but the calculation of the second order derivatives (Hessians) is nontrivial and computationally expensive [202]. Iterative versions of KF as well require high computation power and are therefore not retained.

Model and prior knowledge dependency

The KFs are based on simplified, physically meaningful error models which are established according to prior knowledge and experience. Artificial Intelligence (AI), on the other hand, may be appropriate when the uncertainty in model structure is large, complex or varies in time, as it can be the case for MEMS-type sensors. Therefore, many AI-based algorithms (Artificial Neural Networks [17], neuro-fuzzy KF [1], Adaptive Neuro-Fuzzy Inference System [115]) have been developed which have sometimes shown improved error behavior compared to other filtering methods under steady conditions. On the other hand, it is questionable whether empirical models applied in AI are better suited to decorrelate signals from errors especially in cases where the varying dynamics make training sequences short and thus less appropriate. Additionally, AI methods do not use any statistical information as input, nor do they output statistics associated with the solution, unless methods of cross-validation are applied [115]. Thus, AI-based methods are not very suitable for trajectory smoothing and therefore appear less appropriate for applications that require the estimation of realistic confidence levels.

Sensor dependency and parameter tuning

Tuning the measurement covariance matrix $\mathbf{R}$ and the system noise matrix $\mathbf{Q}$ of the EKF can be time consuming and requires experience and background in both, satellite and inertial navigation. The stochastic parameters may significantly vary even for sensors of similar quality. On the contrary, model-less algorithms based on AI can perform the self-following and tuning under steady dynamics. Unfortunately, this assumption cannot be satisfied in sports, where rapid filter convergence is a major criterion. In addition, adaptive KF [230, 73] are not retained because of the mentioned difficulty to tune the statistical models over short time periods and because of the increased demand in computational power.

Computational cost and convergence

A comparison of the compared integration methods is given in Tab. 3.3. PF are computationally expensive because of the large number of particles that need to be propagated. Their computational demands are prohibitive for high-dimensional systems and short integration times, especially in the perspective of implementing the filter in real-time. On the other hand, references [202, 205, 166, 96] report that the computational complexity of SPKF is equivalent to EKF ($O(n^3)$). Furthermore, the same sources mention the faster convergence of the SPKF states compared to the EKF. Therefore, and with respect to the other criteria of Tab. 3.3, SPKF seems to be an appropriate alternative to EKF for sport applications. Hence, both, the EKF and SPKF, were implemented and will be presented simultaneously. Section 4.3 compares their performance in sport applications.

Tab. 3.3: Comparison of different GPS/INS integration strategies for sport applications.

	EKF	**PF**	**SPKF**	**AI**	Importance for sport applications
Linearization dependency	−	+	+	+	medium
Model dependency	−	−	−	+	medium
Prior knowledge dependency	−	−	−	+	medium
Sensor dependency	−	−	−	+	low
Parameter tuning/training	human	human	human	self	low
Computational cost	+	−	+	−	medium
Convergence	+	+/−	+	−	high
Appropriateness for sports	+	−	+	−	

3.4.3 Kalman Filtering

The following sections present the general principles of Kalman filtering and highlight the differences between EKF and SPKF. The algorithms are detailed in Appendices A and B. Later, section 3.6 develops the implementation of the two filters for GPS/INS integration.

General structure of the algorithm

Kalman filtering consists of 3 steps (Fig. 3.2).

- During the **initialization** step, the state vector and the corresponding covariance matrix are initialized. In the GPS/INS application, this consists of the computation or introduction of an initial orientation and eventually the estimation of initial sensor biases. Initial position and velocity are usually taken from the GPS measurements.
- Then, the state vector and covariance matrix are propagated in time based on a **prediction** model as long as no external measurements are available for updates. In the depicted example, the position state is propagated through distance and direction measurements. The covariance increases in time along the trajectory.

- As soon as external measurements become available, the state vector and covariance are **updated**. In the example, the position measurement improves the position estimation based on the extrapolation with distance and direction measurements. Generally, the accuracy of the state vector is improved, i.e. the updated position is closer to the reference trajectory.

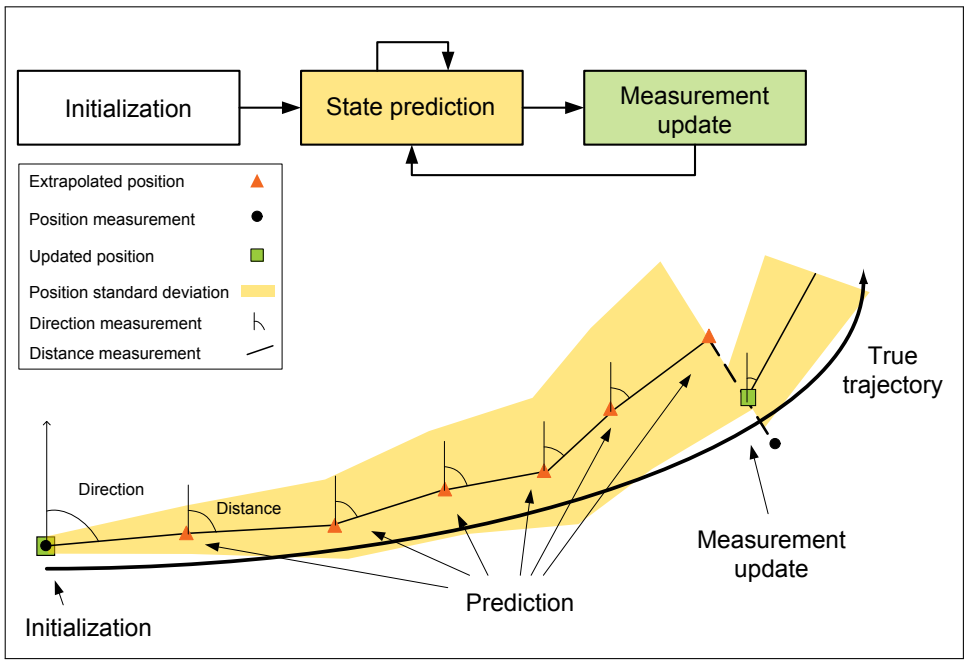

FIG. 3.2: Principle of Kalman filtering.

State propagation

The state propagation is based on a motion model which is normally expressed as a system of non-linear equations. The following section and FIG. 3.3 describes how this motion model is applied in the EKF and the SPKF.

The EKF is an adaptation of the KF to non-linear functions that are approximated by linearization. The state is propagated based on motion model constituted of equations $\mathbf{f}$. Meanwhile, the covariance matrix is predicted based on the transition matrix $\mathbf{\Phi}$ which is obtained from the linearization of $\mathbf{f}$. Hence, in the case of strong dynamics and reduced sampling rate, this first-order approximation of $\mathbf{\Phi}$ may be inaccurate.

The SPKF gets rid of the linearization of the motion model through the (non-linear and hence accurate) propagation of a set of Sigma Points (SP) that represent the statistical properties (average and covariance) of the state vector. The predicted state and corresponding covariance are derived from a weighted average of the propagated sigma points (associated weights w_i^m and w_i^c, developed in Appendix B.1).

In SPKF, the variance of the state is represented by a set of SPs whose propagation in time follow the same non-linear function as the mean value. The SPs, as well as their weights,

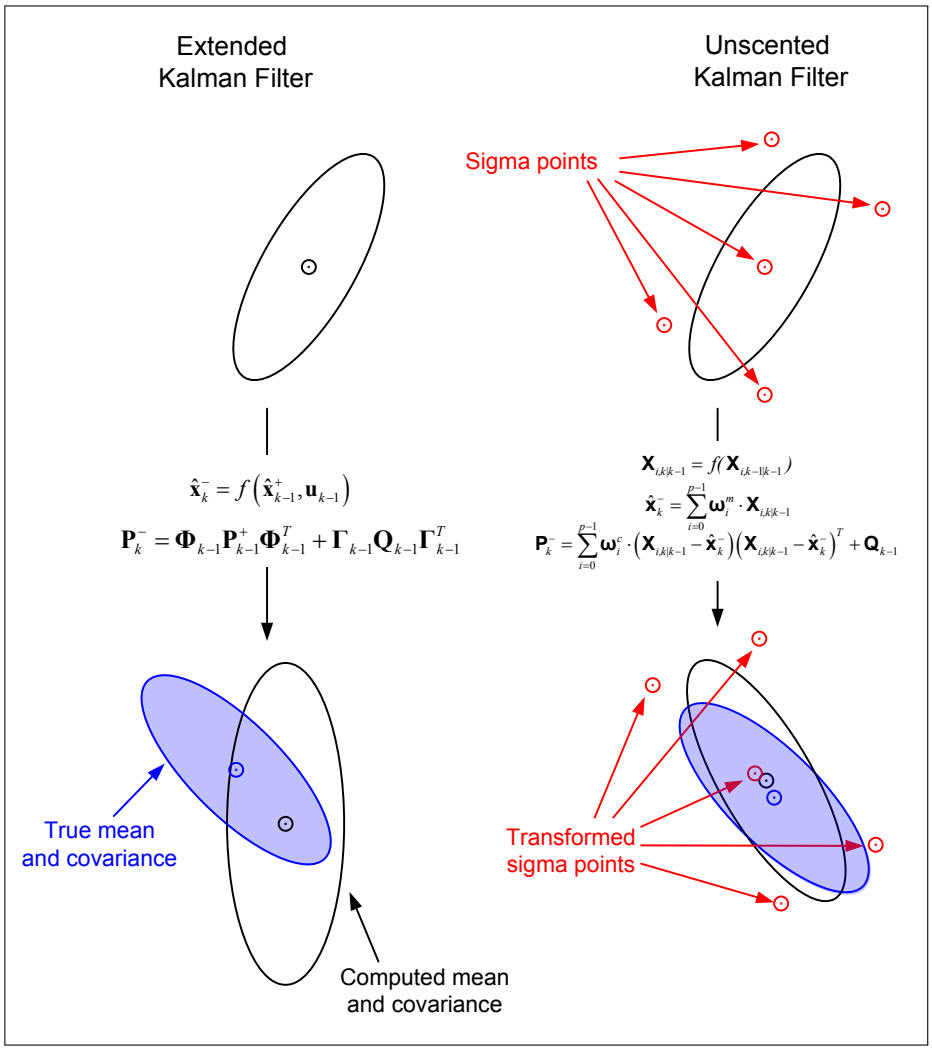

FIG. 3.3: Comparison of the state and covariance propagation based on EKF and UKF with a 2D example [204].

can be chosen in various ways. The main approaches are the Central Difference Filter (CDF) and the Unscented Kalman Filter (UKF). The difference between the two methods lies in the approximation of the posterior covariance term. The CDF has a smaller absolute error in the fourth order term and also guarantees positive semi-definiteness of the posterior covariance [204]. In contrast, the UKF can handle the non-positive semi-definiteness with two scaling parameters (α and β, [204]).

Because of the simplicity and limited computational cost, a Square-Root (SR) version of the UKF with non-additive error model has been implemented for this usage. This method is an adaptation of the SR-UKF [202] and the scaled unscented transformation exploited for the spreading of the SPs [84]. The proposed algorithm chooses $n + 2$ SP (n being the number of states) that match the first two moments while minimizing the third order moments (called spherical simplex SP [83]). The algorithm of the SR-UKF is described in detail in Appendix B.1.

Update stage

The update stage in Kalman filtering is composed of three steps (Appendices A and B.4). Firstly, the gain matrix is computed. It is based on the predicted state and the measurement covariance. Secondly, the state vector is updated: It is corrected by the gain and the difference between the predicted and measured observations. Finally, the predicted state covariance matrix is updated based on the measurement covariance and filter gain.

Unlike the EKF, the UKF does not require the calculation of partial derivatives of the measurement model with respect to the state variables. Furthermore, it does not require any matrix inversion which may improve the stability of the filter.

Comparison of EKF and UKF

Tab. 3.4 summarizes the important differences between the EKF and UKF. The EKF requires the derivation of the motion and the measurement model. Both derivations are sometimes not trivial and may be source of errors, especially during model testing. Unlike the EKF, the UKF does not propagate the covariance linearly, but the linearization is based on a second-order approximation. Therefore, the EKF is limited depending on the dynamics, the sampling rate and the corresponding prediction times [22] and might cause the divergence (or slower convergence) of the filter. Both filters assume a Gaussian distribution for the underlying probability density function and have the same computation complexity ($O(n^3)$, [204]).

Tab. 3.4: Comparison of the characteristics of the EKF and UKF [84, 204].

	EKF	**UKF**
State propagation	Non-linear	Second-order approximation minimizing the third order
Covariance propagation	Linear approximation	Second-order approximation minimizing the third order
Implementation	Motion and measurement model derivatives → Implementation difficulties and error source	No linearization, rapid implementation even for complex models and model evaluation
Convergence	Filter stability limited by the dynamics and the sampling rate (linear motion during the integration interval)	Stable, faster convergence under higher dynamics
Computation complexity	$O(n^3)$	$O(n^3)$
Probability density	Gaussian	Gaussian

3.4.4 Optimal Smoothing

In post-processing, the navigation performance can be improved through the appropriate selection of the processing direction. Indeed, the visibility of satellites often varies along the tracks. Furthermore, favorable situations for sensor calibration (static periods, large dynamics)

may be located at either end of the trajectories. In addition, the navigation performance can be improved by smoothing which is the combination of results obtained by processing the trajectories in forward and/or backward direction.

The following fixed-interval smoothing algorithm combines forward and backward filtered data sets in the least squares sense [103, 166]. It can be implemented for the EKF and the UKF.

$$\begin{aligned} \mathbf{P}_s &= (\mathbf{P}_f^{-1} + \mathbf{P}_b^{-1})^{-1} \\ \mathbf{x}_s &= \mathbf{x}_f^+ + \mathbf{P}_s \mathbf{P}_b^{-1} (\mathbf{x}_b^+ - \mathbf{x}_f^+) \end{aligned} \tag{3.4.1}$$

where $\mathbf{x}$ is the predicted (superscript $-$) or adjusted (superscript $+$) state vector with corresponding covariance matrix $\mathbf{P}$. Indexes f, b and s indicate forward or backward processed and smoothed states or covariances.

If the data are processed in one direction (forward or backward), the Rauch-Tung-Striebel (RTS) algorithm [54] can be applied. However, it requires knowledge about the $\mathbf{\Phi}$ matrix and is thus reserved to EKF.

$$\begin{aligned} \mathbf{x}_{s,k} &= \mathbf{x}_k^+ + \mathbf{J}_k \cdot (\mathbf{x}_{s,k+1} - \mathbf{x}_{k+1}^-) \\ \mathbf{P}_{s,k} &= \mathbf{P}_k^+ + \mathbf{J}_k \cdot (\mathbf{P}_{s,k+1} - \mathbf{P}_{k+1}^-) \cdot \mathbf{J}_k^T \end{aligned} \tag{3.4.2}$$

with

$$\mathbf{J}_k = \mathbf{P}_k^+ \cdot \mathbf{\Phi}_k^T \cdot (\mathbf{P}_{k+1}^-)^{-1} \tag{3.4.3}$$

where index k and $k+1$ indicate two successive measurement epochs.

3.5 Implementation of GPS Processing

3.5.1 Definition of the State Vector

For the GPS processing, the state vector contains the correction terms of the position and velocity parameters, as defined by:

$$\delta\mathbf{x} = \begin{bmatrix} \delta\varphi \\ \delta\lambda \\ \delta h \\ \delta v_N \\ \delta v_E \\ \delta v_D \end{bmatrix} \tag{3.5.1}$$

where

- the position errors ($\delta\mathbf{r}^n$) are defined by equation C.1.6.
- the velocity errors ($\delta\mathbf{v}^n$) are defined by relation $\delta\dot{\mathbf{v}}^n = \mathbf{0}_{3\times1}$.

In this research, double-differenced, phase-smoothed GPS code and Doppler measurements are employed. However, if single-differenced GPS measurements are to be exploited, the time difference between the master and rover receiver $\Delta\delta t_{mr}$ would need to be evaluated and hence to be added to the state vector. If carrier-phase measurements are used directly, the state vector is augmented by the ambiguity term N for each visible satellite. Thus, its size becomes variable.

3.5.2 Initialization

The initial position and velocity are determined by parametric adjustments of the double-differenced, phase-smoothed GPS code and Doppler measurements based on the first and third relation of equations 3.3.13.

3.5.3 State Propagation

For the state propagation in GPS processing, a constant velocity model is implemented. Models based on more sophisticated state prediction may improve the navigation solution, but have not been investigated in this research.

$$\begin{aligned}(\mathbf{v}^n)_{k+1} &= (\mathbf{v}^n)_k \\ (\mathbf{r}_e^n)_{k+1} &= (\mathbf{r}_e^n)_k + \mathbf{D^{-1}} \cdot (\mathbf{v}^n)_k \cdot \Delta t\end{aligned} \tag{3.5.2}$$

where $\mathbf{D}$ is defined as:

$$\mathbf{D}^{-1} = \begin{bmatrix} \frac{1}{M+h} & 0 & 0 \\ 0 & \frac{1}{(N+h)\cos\varphi} & 0 \\ 0 & 0 & -1 \end{bmatrix} \approx \begin{bmatrix} \frac{1}{R+h} & 0 & 0 \\ 0 & \frac{1}{(R+h)\cos\varphi} & 0 \\ 0 & 0 & -1 \end{bmatrix} \tag{3.5.3}$$

M and N are the principal ellipsoidal radii of curvature. They can be replaced by the average radii of curvature $R = \sqrt{M \cdot N}$. In some sport applications, the displacements are generally restricted to a few kilometers. There, R can be approximated based on the initial position.

$$\begin{aligned}M &= \frac{a(1-e^2)}{(1-e^2\sin^2\varphi)^{(\frac{3}{2})}} \\ N &= \frac{a}{(1-e^2\sin^2\varphi)^{(\frac{1}{2})}}\end{aligned} \tag{3.5.4}$$

M and N depend on the ellipsoidal latitude φ. Linearizing $v_N = (M+h)\cdot\dot{\varphi}$ leads to:

$$\delta v_N = (\delta M + \delta h)\cdot\dot{\varphi} + (M+h)\cdot\delta\dot{\varphi} \tag{3.5.5}$$

where

$$\delta M = -3Me^2\sin\varphi\cos\varphi\delta\varphi \tag{3.5.6}$$

As $\delta M << \delta h$, the dependence of M on φ can be neglected in this work. A similar demonstration can be made for N. The algorithm can be simplified by choosing a mean Earth radius, e.g. $R = 6378$ km.

3.5.4 Measurement Updates

GPS double-differenced pseudorange measurements

Double-differenced carrier-phase smoothed L1 pseudorange measurements are introduced at the update stage. Review the first expression of equations 3.3.13:

$$\nabla\Delta p_{mr}^{zs} - v_{mr}^{zs} = \nabla\Delta\rho_{mr}^{zs-} + \nabla\Delta M_{mr}^{zs} \tag{3.5.7}$$

where

$$\begin{aligned} \nabla\Delta p_{m,r}^{zs} &= (p_m^z - p_r^z) \quad - (p_m^s - p_r^s) \\ \nabla\Delta\rho_{m,r}^{zs-} &= (\rho_m^{z-} - \rho_r^{z-}) - (\rho_m^{s-} - \rho_r^{s-}) \end{aligned} \tag{3.5.8}$$

where ρ_r^{s-} is the predicted pseudorange between GPS receiver r and satellite s.

Multipath can be identified by evaluating the difference $\rho_r^{s-} - p_r^s$. If this is the case, the affected observation can be removed. More complex multipath mitigation methods can be found in the literature [53, 231, 13, 206]. However, their evaluation is beyond the scope of this research. Appendix C.3.2 presents the linearization of equation 3.5.7 for the EKF updates.

GPS double-differenced Doppler measurements

Unlike carrier-phase measurements, Doppler measurements are unambiguous and thus theoretically insensitive to cycles slips. For GPS processing, double-differenced L1 Doppler measurements are introduced at the update stage based on the third expression of equations 3.3.13:

$$\nabla\Delta\dot{p}_{mr}^{zs} - v_{mr}^{zs} = \nabla\Delta\dot{\rho}_{mr}^{zs-} \tag{3.5.9}$$

where

$$\begin{aligned} \nabla\Delta\dot{p}_{mr}^{zs} &= (\dot{p}_m^z - \dot{p}_r^z) \quad - (\dot{p}_m^s - \dot{p}_r^s) \\ \nabla\Delta\dot{\rho}_{m,r}^{zs-} &= (\dot{\rho}_m^{z-} - \dot{\rho}_r^{z-}) - (\dot{\rho}_m^{s-} - \dot{\rho}_r^{s-}) \end{aligned} \tag{3.5.10}$$

with

$$\dot{\rho}_r^{s-} = (\mathbf{v}^s - \mathbf{v}_r) \bullet \frac{\mathbf{r}^s - \mathbf{r}_r}{\|\mathbf{r}^s - \mathbf{r}_r\|}. \tag{3.5.11}$$

Appendix C.3.2 presents the derivation of equation 3.5.9 for EKF.

3.6 Implementation of GPS/INS Integration

3.6.1 Definition of the State Vector

In this research, the local-level frame has been chosen as navigation frame. The advantage of the local-level frame is that its axis are aligned to the local east, north and down directions. As

the definition of the local-level frame is based on the vertical to the reference ellipsoid, geodetic coordinate differences result from the integration which makes the state interpretation straightforward.

The state vector contains the correction terms of the navigation parameters as well as the significant part of the systematic errors of the inertial and magnetic measurements (sections 3.1 and 3.2), as defined by:

$$\delta\mathbf{x} = \begin{bmatrix} \delta\varphi \\ \delta\lambda \\ \delta h \\ \delta v_N \\ \delta v_E \\ \delta v_D \\ \delta\epsilon_N \\ \delta\epsilon_E \\ \delta\epsilon_D \\ \delta b_{f_x} \\ \delta b_{f_y} \\ \delta b_{f_z} \\ \delta b_{\omega_x} \\ \delta b_{\omega_y} \\ \delta b_{\omega_z} \\ \delta d_{m_x} \\ \delta d_{m_y} \\ \delta d_{m_z} \end{bmatrix} \tag{3.6.1}$$

where

- the position errors ($\delta\mathbf{r}^n$) are defined by equation C.1.6.
- the velocity errors ($\delta\mathbf{v}^n$) are defined by equation C.1.13.
- the orientation errors ($\delta\boldsymbol{\epsilon}^n$) are defined by equation C.1.20.
- the accelerometer biases ($\delta\mathbf{b}_{f^b}$) are defined by equation 3.1.8.
- the gyroscope biases ($\delta\mathbf{b}_\omega$) are defined by equation 3.1.8.
- the magnetic disturbance ($\delta\mathbf{d}_m$) are defined by equation 3.2.4. The magnetic disturbance terms are normalized to limit numerical instabilities.

Employing double-differenced, phase-smoothed GPS code and Doppler measurements, the state vector is the same in the loosely and in the closely coupled approach (section 3.6.4). Therefore, neither time differences between the master and rover receiver $\Delta\delta t_{mr}$, nor ambiguity terms N for each visible satellite need to be estimated.

Acceleration terms are not included in the state vector. Indeed, accelerations derived from GPS measurements are fully correlated to the velocities which leads to a lack of observability.

3.6.2 Initialization

Position and velocity states are initialized by GPS measurements. Alternatively, if the athlete is not moving, the initial coordinates can be introduced manually. The coarse alignment method applied in conventional GPS/INS integration considers two pairs of vectors which are both available in the local-level frame (n), which is also the navigation frame, and the body-frame (b). The local-level projection of these two vectors is known from the model of the Earth (gravity and Earth rotation) while the body frame projections are obtained from the sensor measurements (specific force and angular rate). Unfortunately, the error characteristics of the MEMS gyroscopes (noise level > 0.1 deg/s/$\sqrt{\text{Hz}}$, systematic errors of several deg/s) do not allow sensing the Earth's rotation rate. Hence, the conventional alignment methods cannot be employed. Therefore, two alternative approaches exploiting MEMS magnetometers are envisaged: A modified coarse alignment and a quaternion based algorithm. Both will be presented in the sequel.

Modified coarse alignment method

The MEMS magnetic measurements and the a priori known magnetic field of the Earth offer a pair of vectors that replace the gyroscope measurements. The orientation of a rigid body $\mathbf{R}_n^b$ can be determined from the following relation:

$$\left[\begin{array}{ccc} -\mathbf{f}^b & \mathbf{m}^b & -\mathbf{f}^b \times \mathbf{m}^b \end{array} \right] = \mathbf{R}_n^b \left[\begin{array}{ccc} \bar{\mathbf{g}}^n & \mathbf{m}^n & \bar{\mathbf{g}}^n \times \mathbf{m}^n \end{array} \right] \tag{3.6.2}$$

where $\mathbf{f}^b$ is the specific force measurement, $\bar{\mathbf{g}}^n$ the normal gravity vector, $\mathbf{m}^b$ the magnetic observation and $\mathbf{m}^n$ the Earth magnetic field deduced from any global or local reference model (e.g. the World Magnetic Model of [122]). $\mathbf{f}^b$ and $\mathbf{m}^b$ can be averaged over a period during which the sensor does not move.

In the coarse alignment algorithm the rotation matrix must be converted to quaternion form. This step is potentially unstable. Indeed, in the cases where the trace of the rotation matrix equals -1 and the off-diagonal terms are skew-symmetric, a zero quaternion is generated.

Quaternion estimation algorithm

Exploiting again the Earth's gravity and magnetic fields, the initial orientation can also be found based on weighted (w_k) observations and their external reference expressed as unit vectors (Wahba's problem [223]):

$$J(\mathbf{q}_n^b) = \frac{1}{m} \sum_{i=1}^{m} w_k (\mathbf{b}_i - \mathbf{R}_n^b \mathbf{n}_i)^2 \tag{3.6.3}$$

where J is a cost function, $m = 2$ represents the number of used sensors (magnetometers and accelerometers) and $\mathbf{q}_n^b$ the orientation expressed as quaternion (equation 3.6.4). $\mathbf{b}_i$ is a measurement in the body frame (magnetic observation $\mathbf{m}^b$ or specific force $\mathbf{f}^b$) and $\mathbf{n}_i$ the corresponding reference value (magnetic field $\mathbf{m}^n$ and normal gravity $\bar{\mathbf{g}}^n$).

In this work, the orientation is preferably expressed in quaternion form [191]. Quaternions are a four-parameter attitude representation method based on Euler's theorem which states that a transformation from one coordinate frame to another can be performed by a single rotation of a given magnitude about a vector. The four elements of the quaternion $\mathbf{q}$ are functions of the vector $\mathbf{u}$ and the magnitude of rotation u:

$$\mathbf{q} = \begin{bmatrix} \cos\left(\frac{u}{2}\right) \\ \frac{u_x}{2}\sin\left(\frac{u}{2}\right) \\ \frac{u_y}{2}\sin\left(\frac{u}{2}\right) \\ \frac{u_z}{2}\sin\left(\frac{u}{2}\right) \end{bmatrix} \tag{3.6.4}$$

where u_x, u_y and u_z are the components of the vector $\mathbf{u}$ with magnitude $u = \sqrt{u_x^2 + u_y^2 + u_z^2}$.

An elegant solution for quaternion based algorithms is referred to as the QUEST (QUaternion ESTimation) algorithm [159]. The orientation can be found unambiguously when minimizing expression

$$J(\mathbf{q}_n^b) = \frac{1}{2}\sum_{i=1}^{2} w_k(\mathbf{b}_i - \mathbf{R}_n^b \mathbf{n}_i)^2 \tag{3.6.5}$$

with the condition $(\mathbf{q}_n^b)^T \cdot \mathbf{q}_n^b = 1$.

In contrast to the coarse alignment algorithm, the QUEST algorithm directly provides a quaternion which is employed in the strapdown navigation without further transformation.

Adaptation for dynamic initialization

If the initialization is to be performed under dynamic conditions, the specific force measurement needs to be corrected for the kinematic acceleration. This acceleration can be derived from GPS measurements in the navigation frame and fed back to the coarse alignment or to the QUEST algorithm:

$$\mathbf{f}^n = \mathbf{a}^n + (\boldsymbol{\omega}_{in}^n + \boldsymbol{\omega}_{ie}^n) \times \mathbf{v}^n - \mathbf{g}^n \tag{3.6.6}$$

where $\mathbf{a}^n$ and $\mathbf{v}^n$ are the acceleration and velocity vectors derived from GPS respectively [171, 15]. Furthermore, the gyroscope measurement can be accounted for between epochs by means of the elegant recursive QUEST (REQUEST) algorithm [7, 95].

3.6.3 Strapdown Inertial Navigation

Inertial navigation is unique among navigation technologies because of its autonomous character. As inertial sensors operate without reference to external signals, they are not affected by atmospheric conditions, line-of-sight obstructions or other obstacles inherent to other navigation systems based on position fixing (e.g. indoor, underground).

Orientation prediction

The orientation of the inertial sensor with respect to the navigation frame at time k $(\mathbf{q}_b^n)_{k|k}$ can be propagated to time $k+1$ by applying [193]:

$$(\mathbf{q}_b^n)_{k+1|k+1} = (\mathbf{q}_n^n)_{k+1|k} \cdot (\mathbf{q}_b^n)_{k|k} \cdot (\mathbf{q}_b^b)_{k|k+1} \tag{3.6.7}$$

The quaternion $\mathbf{q}_b^b$ expresses the rotation of the body frame (index b) between two successive epochs which is derived from the gyroscopes. It can be defined as a function of the rotation vector $\mathbf{u}_b^b$:

$$(\mathbf{q}_b^b)_{k|k+1} = \begin{bmatrix} \cos(\frac{\|\mathbf{u}_b^b\|}{2}) \\ \frac{\mathbf{u}_b^b}{\|\mathbf{u}_b^b\|} \sin(\frac{\|\mathbf{u}_b^b\|}{2}) \end{bmatrix} \tag{3.6.8}$$

where $\dot{\mathbf{u}}_b^b \approx \boldsymbol{\omega}_{ib}^b$ are the rotation rates measured by the gyroscopes. This leads to:

$$\mathbf{u}_b^b = \int_{t_k}^{t_{k+1}} \dot{\mathbf{u}}_b^b \, dt \approx (\boldsymbol{\omega}_{ib}^b)_k \cdot (t_{k+1} - t_k) \tag{3.6.9}$$

The rotation quaternion $(\mathbf{q}_n^n)_{k+1|k}$ describes the relative motion of the navigation frame (index n) at instant t_k with respect to instant t_{k+1}. It is opposite in phase to the rotation vector $\mathbf{u}_n^n$. This is taken into account by the negative sign of $\mathbf{u}_n^n$ in equation 3.6.10:

$$(\mathbf{q}_n^n)_{k+1|k} = \begin{bmatrix} \cos(\frac{\|\mathbf{u}_n^n\|}{2}) \\ -\frac{\mathbf{u}_n^n}{\|\mathbf{u}_n^n\|} \sin(\frac{\|\mathbf{u}_n^n\|}{2}) \end{bmatrix} \tag{3.6.10}$$

where

$$\mathbf{u}_n^n \approx \boldsymbol{\omega}_{in}^n \cdot \Delta t \tag{3.6.11}$$

This algorithm propagates $\mathbf{q}_b^n$, $\mathbf{q}_b^b$ and $\mathbf{q}_n^n$ at equal rates. Reference [153] describes a more general algorithm where $\mathbf{q}_b^n$ is not necessarily propagated at the same frequency as the body frame rotation $\boldsymbol{\omega}_{ib}^b$ or the navigation-frame rotation $\boldsymbol{\omega}_{in}^n$. The suggested algorithm has not been tested, although its application reduces the number of mathematical operations without affecting the numerical precision.

Velocity prediction

Once the orientation of the sensors at time t_{k+1} is known, the velocity can be integrated from the specific force measurements $\mathbf{f}^b$:

$$(\mathbf{v}^n)_{k+1} = (\mathbf{v}^n)_k + (\Delta\mathbf{v}_{g/cor}^n)_{k+1} + (\Delta\mathbf{v}_f^n)_{k+1} \tag{3.6.12}$$

where

$$\begin{aligned}(\Delta\mathbf{v}^n_{g/cor})_{k+1} &= \int_{t_k}^{t_{k+1}} \mathbf{g}^n - (2\cdot\boldsymbol{\omega}^n_{ie}+\boldsymbol{\omega}^n_{en})\times\mathbf{v}^n\ dt \\ &\approx [(\mathbf{g}^n)_k - (2\cdot(\boldsymbol{\omega}^n_{ie})_k + (\boldsymbol{\omega}^n_{en})_k)\times(\mathbf{v}^n)_k]\cdot(t_{k+1}-t_k)\end{aligned} \tag{3.6.13}$$

and

$$\begin{aligned}(\Delta\mathbf{v}^n_f)_{k+1} &= \int_{t_k}^{t_{k+1}} \mathbf{R}^n_b\mathbf{f}^b dt \\ &\approx (\mathbf{R}^n_b)_{k+1|k}\cdot\mathbf{f}^b dt = (\mathbf{R}^n_b)_{k+1|k}\cdot\mathbf{f}^b\cdot\Delta t\end{aligned} \tag{3.6.14}$$

$\mathbf{v}^n$ represents the velocity with respect to the navigation frame n, $\boldsymbol{\omega}^n_{ie}$ the rotation rate of the Earth expressed in the navigation frame, $\boldsymbol{\omega}^n_{en}$ the rotation rate of the local geographic frame with respect to the Earth fixed frame. $(\mathbf{R}^n_b)_{k+1/k}$ is the matrix expression of $(\mathbf{q}^n_b)_{k+1/k}$ which can be derived from equation 3.6.7:

$$(\mathbf{q}^n_b)_{k+1|k} = (\mathbf{q}^n_n)_{k+1|k}\cdot(\mathbf{q}^n_b)_{k|k} \tag{3.6.15}$$

The accelerations $\mathbf{a}^n$ are extracted from equations 3.6.13-3.6.14.

$$(\mathbf{a}^n)_{k+1} = (\mathbf{R}^n_b)_{k+1|k}(f^b)_k + \mathbf{g}^n \tag{3.6.16}$$

Position prediction

The position term $\mathbf{r}^n$ can be predicted as follows:

$$(\mathbf{r}^n)_{k+1} = (\mathbf{r}^n)_k + \frac{1}{2}\cdot\mathbf{D}^{-1}((\mathbf{v}^n)_{k+1}+(\mathbf{v}^n)_k)\cdot(t_{k+1}-t_k) \tag{3.6.17}$$

where $\mathbf{D}$ is defined by equation 3.5.3.

Higher-order extrapolations could be applied to $\mathbf{r}^n$ and $\mathbf{v}^n$ for very high dynamics, e.g. by extrapolating the previous states by $\frac{1}{2}\Delta t$ [193]:

$$x_{k+\frac{1}{2}} = \frac{3}{2}x_k - \frac{1}{2}x_{k-1} \tag{3.6.18}$$

This extrapolation can be applied to $\mathbf{r}^n$ and $\mathbf{v}^n$ before the state propagation. This guarantees that all derived variables (e.g. $\boldsymbol{\omega}^n_{in}$) are predicted automatically according to the same extrapolation scheme. The extrapolation has been tested in skiing and motorcycle experiments and did not result in improved navigation accuracy. It seems that the dynamics encountered in theses applications as well as the sampling frequencies and sampling regularity of the sensors do not justify the increased computational effort. However, as the sampling frequency of MEMS-type sensors is not stable, robust integrators could improve the navigation performance [147].

Propagation of the inertial error states

The states representing the inertial sensor errors (gyroscope, accelerometer and magnetometer biases) are modeled as first order Gauss-Markov processes. Hence, their propagation can be expressed as:

$$\begin{aligned}(\mathbf{b}_{\omega_{ib}^b})_{k+1} &= (1-\beta_{b_\omega}(t_{k+1}-t_k))(\mathbf{b}_\omega)_k \\ (\mathbf{b}_{f_b})_{k+1} &= (1-\beta_{b_{f_b}}(t_{k+1}-t_k))(\mathbf{b}_{f_b})_k \\ (\mathbf{d}_m)_{k+1} &= (1-\beta_{d_m}(t_{k+1}-t_k))(\mathbf{d}_m)_k\end{aligned} \tag{3.6.19}$$

Backward state propagation

The backward mechanization equations can be easily derived from equations 3.6.7 (orientation prediction), 3.6.12 (velocity prediction) and 3.6.17 (position prediction) and 3.6.19 (extra states prediction). The change in sign of Δt switches the mentioned equations to backward mode. Only in equation C.2.22, the absolute value $|\Delta t|$ has to be applied.

3.6.4 Measurement Updates

In the **loosely coupled approach** (Fig. 3.4), GPS coordinates and velocities are fed to the filter as external aiding to the INS measurements. In addition, magnetometer measurements are introduced at the update stage. In the **closely coupled approach** (Fig. 3.5), the double-differenced carrier-phase smoothed GPS pseudorange and Doppler measurements are integrated with the INS measurements. Again, the magnetometer measurements are introduced as external aiding.

Closely coupled methods allow integrating GPS and inertial measurements even if the number of observed satellites drops below four [187, 224]. In this approach, GPS data from individual satellites can be used or rejected at the measurement update of the Kalman filter. According to [161, 225], the closely coupled approach is more robust for an incomplete constellation (and especially for very poor geometry with $PDOP > 50$) and it offers superior performance compared to loosely coupled systems under these circumstances. When the number of satellites falls below three, the positioning accuracy deteriorates rapidly and is dominated by the errors of inertial navigation. Study [187] has reported in simulations that for partial GPS outages lasting 20 s, the horizontal position error was improved by a factor of 15 when only two GPS satellites were visible. However, when the satellite geometry was reasonable (i.e. > 4 SVs), the closely coupled approach did not show significantly better performance than the loosely coupled [161].

GPS coordinate

To integrate GPS coordinates with IMU measurements, the coordinates of the GPS antenna can be expressed with respect to the IMU navigation center taking into account the lever-arm vector $\mathbf{o}^b$.

$$\mathbf{o}^n = \mathbf{R}_b^n \cdot \mathbf{o}^b = \begin{bmatrix} o_N & o_E & o_D \end{bmatrix}^T \tag{3.6.20}$$

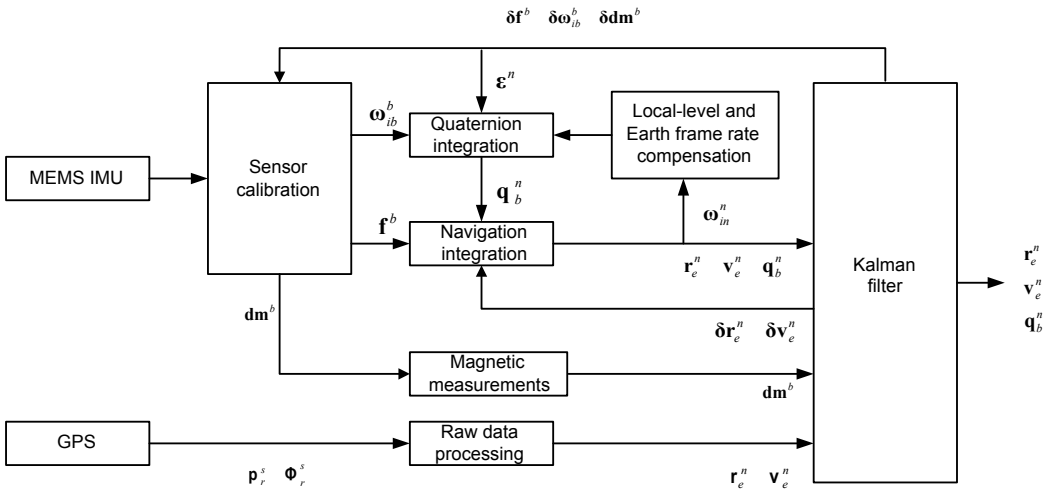

FIG. 3.4: Flow chart of the loosely coupled GPS/INS integration.

Accounting for this lever-arm, the GPS coordinate measurement model can be expressed as follows:

$$h_r(\hat{\mathbf{x}}_k^-) = \mathbf{r}_{IMU}^n + \mathbf{D}^{-1}\mathbf{R}_b^n \cdot \mathbf{o}^b + \mathbf{w}_r \tag{3.6.21}$$

where $\mathbf{w}_r$ is the position measurement noise. Appendix C.3.1 presents the derivative of equation 3.6.21 for the EKF.

GPS velocity

Differentiating expression 3.6.21, the GPS velocity measurement model can be expressed as follows:

$$h_v(\hat{\mathbf{x}}_k^-) = \mathbf{v}_{IMU}^n + \delta\mathbf{R}_b^n\mathbf{o}^b \tag{3.6.22}$$

Knowing that $\delta\mathbf{R}_b^n = [\boldsymbol{\omega}_{nb}^n\times]\mathbf{R}_b^n$, the expression transforms to:

$$h_v(\hat{\mathbf{x}}_k^-) = \mathbf{v}_{IMU}^n + \boldsymbol{\omega}_{nb}^n \times \mathbf{R}_b^n\mathbf{o}^b + \mathbf{w}_v \tag{3.6.23}$$

The derivative of equation 3.6.23 for the EKF is given in Appendix C.3.1.

GPS double-differenced pseudorange measurements

In the closely coupled approach, the double-differenced, phase-smoothed GPS code are introduced as external aiding to the INS measurements (equation 3.5.7):

$$\nabla\Delta p_{mr}^{zs} - v_{mr}^{zs} = \nabla\Delta\rho_{mr}^{zs-} + \nabla\Delta M_{mr}^{zs} \tag{3.6.24}$$

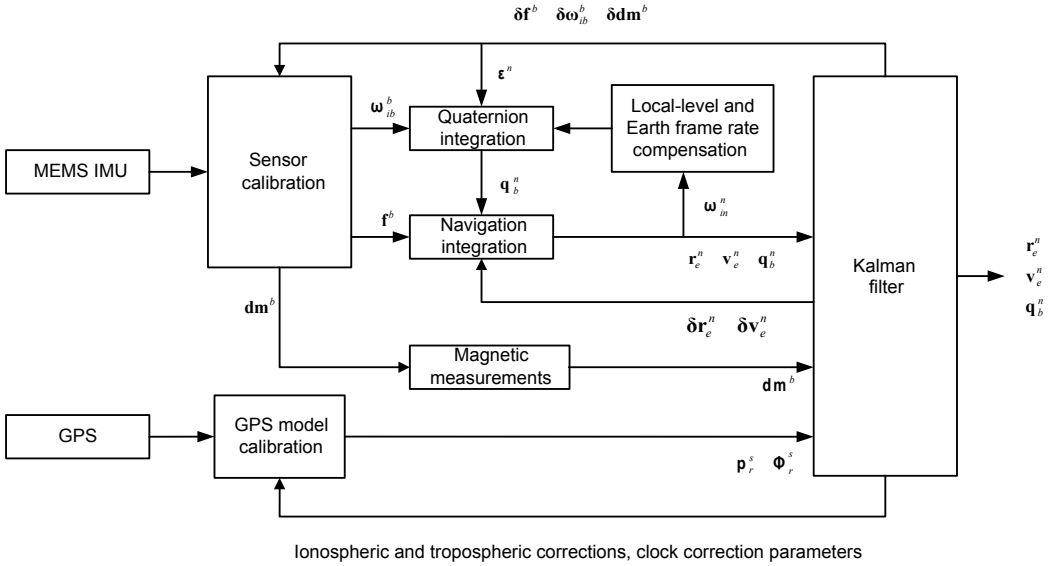

FIG. 3.5: Flow chart of the closely coupled GPS/INS integration.

The predicted pseudorange ρ_r^{s-} between GPS receiver r and satellite s can be derived from the satellite's position $\mathbf{r}^s$ and the predicted position of the GPS antenna considering the lever arm $\mathbf{o}^b$ between GPS antenna and the IMU position $\mathbf{r}^n$:

$$\rho_r^{s-} = \sqrt{(g(\mathbf{r}^s) - g(\mathbf{r}^n + \mathbf{D}^{-1}\mathbf{R}_b^n\mathbf{o}^b)^T \cdot (g(\mathbf{r}^s) - g(\mathbf{r}^n + \mathbf{D}^{-1}\mathbf{R}_b^n\mathbf{o}^b)} \tag{3.6.25}$$

where g is the function that converts geographic to Cartesian coordinates.

Appendix C.3.2 presents the linearization of equation 3.3.13 for the EKF updates.

GPS double-differenced Doppler measurements

In the closely coupled approach, double-differenced L1 Doppler measurements are introduced as external aiding to the INS measurements (equation 3.5.9):

$$\nabla\Delta\dot{p}_{mr}^{zs} - v_{mr}^{zs} = \nabla\Delta\dot{\rho}_{mr}^{zs} \tag{3.6.26}$$

Appendix C.3.2 presents the derivation of equation 3.3.13 for EKF.

Magnetic measurements

The measurements of the magnetic compass can be integrated based on the following relation [194]:

$$h_m(\hat{\mathbf{x}}_k^-) = \mathbf{R}_n^b[\mathbf{h}^n] \times \boldsymbol{\epsilon}^n - \mathbf{d}_m + \mathbf{w}_m \tag{3.6.27}$$

where $\boldsymbol{\epsilon}^n$ are the misalignment errors defined by relation C.1.10.

Chapter 4

GPS/MEMS-IMU System Performance

This chapter describes the navigation performance of MEMS-IMUs integrated with GPS. Firstly, the performance of satellite positioning with GPS receivers of different quality is assessed based on experiments in sports. The same GPS data is then integrated with the MEMS-IMUs based on the previously described loosely and closely coupled integration schemes. The integration performance is interpreted for complete and partial (< 4 SV) satellite constellations. Then, the benefits of RTS smoothing, magnetic measurements and UKF are analyzed. Finally, the initial alignment methods are evaluated.

4.1 Experimental Setup

Throughout the system evaluation, the findings are supported by experiments. These experiments come from racing environments where references of superior accuracy are provided in both the measurement and the navigation domains.

Downhill skiing is an ideal discipline for testing of the proposed integration methods because of the important dynamics encountered and due to the difficult satellite reception imposed by the mountainous environments. To investigate the navigation performance of the low-cost L1 GPS/MEMS-IMU setup, the instruments were mounted in a backpack (Fig. 4.2) together with a reference system, comprising a dual-frequency GPS receiver (*Javad Legacy*) and a tactical-grade IMU (*Litton LN200*). Three orthogonally placed MEMS sensors (*Xsens MTi*) were fixed rigidly to the reference IMU with a constant lever arm together with a low-cost GPS receiver (*u-blox AEK4*). A dozen of downhill runs of approximately one minute duration were performed by a professional skier. Each run was preceded by a static initialization phase of $2 - 3$ min (Fig. 4.1, left).

A slope at Plaine-Joux (France) has been chosen because its south-facing slope offers good satellite reception and almost no satellite masking above 20 deg. The reference GPS receivers (*Topcon Maxor-660T* and *u-blox AEK4*) were placed at the start. This limited the distance between the reference and the rover GPS receiver to 500 m. The velocity profile of a typical run is given in Fig. 4.1 (right). On the average, 6 satellites were visible during the downhill

runs. The PDOP (Position Dilution Of Precision) values were varying between 1.1 and 1.9, which is an optimal scenario.

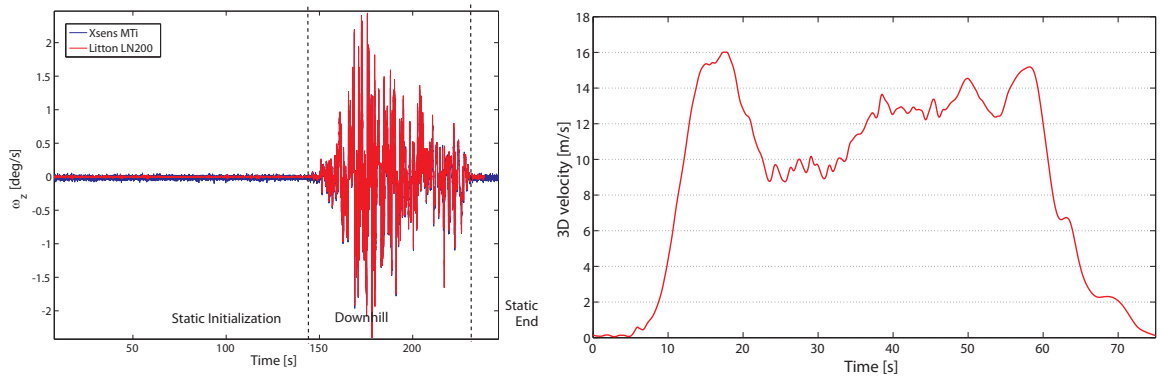

FIG. 4.1: Angular rotation rate around the z-axis (left) and velocity profile (right)

The gates were determined by post-processing of static, dual-frequency GPS measurements. Their position accuracy is estimated at 2 cm (position) and 5 cm (altitude).

Unless otherwise specified, the results presented in the sequel refer to the skiing experiment. However, other experiments with varying setups have been conducted with (parts of) the equipment presented above, in other disciplines and under different dynamics, e.g. motorcycling (FIG. 4.2).

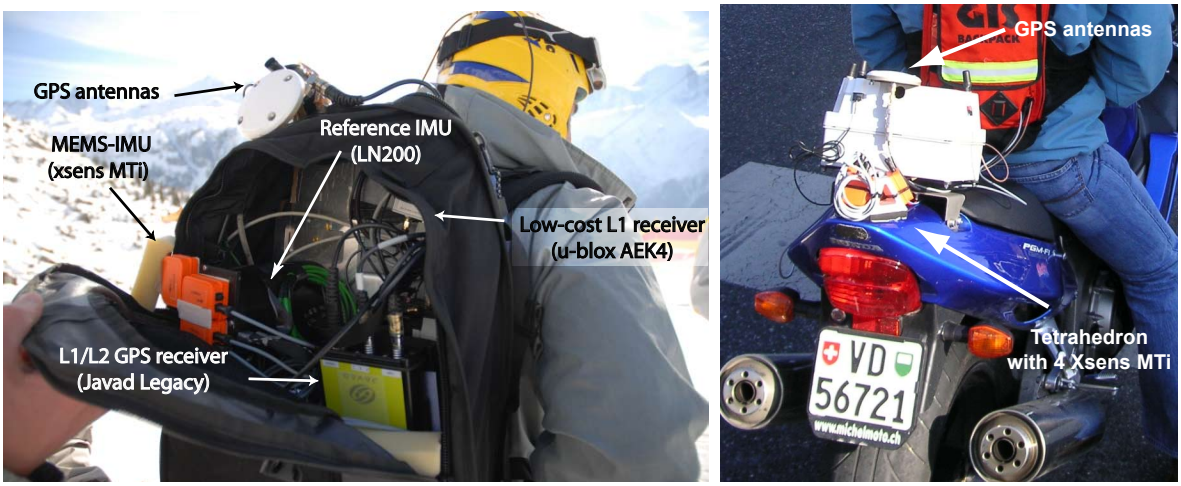

FIG. 4.2: Experimental setup mounted on a professional skier and on a motorcycle.

4.2 GPS/MEMS-IMU Performance

The integration strategy is investigated in three steps. Firstly, the accuracy provided by different GPS receivers is assessed, i.e. geodetic receivers with fixed/float carrier-phase ambiguities and low-cost receivers with smoothed carrier-phase measurements. Secondly, the MEMS-IMU

measurements (100 Hz) were integrated with GPS updates (1 Hz) based on the loosely and closely coupled integration approaches. Again, the performance of distinctive GPS algorithms and L1 measurements with different quality is evaluated. The third part refines the assessment of the performance provided by the two integration strategies. Here, the GPS data sets are resampled by removing satellite measurements over a different time intervals ($5 - 40$ s). It is important to stress that an outage of 40 s corresponds to two thirds of the run with only 10 s of satellite data remaining after the start and before the arrival. The SVs with small elevation were removed first, which corresponds to artificially increasing the surrounding topography leading to artificially reduced satellite constellations. All comparisons were performed for 6 independent downhill runs.

4.2.1 Satellite Navigation

The performance of different solutions is assessed with respect to the reference solution provided by the dual-frequency GPS/INS (*Litton LN200*) trajectory processed by commercial software packages [116, 4]. Fig. 4.3 and Tab. D.1 summarize the root mean square errors (RMSE) of GPS solutions based on different processing schemes and receivers. A commercial software package [116] succeeded in fixing the carrier-phase ambiguities with the dual-frequency GPS receiver during 95% of the time. However, their resolution becomes difficult with (geodetic and low-cost) single-frequency GPS receivers. Therefore, two alternative approaches were investigated: Estimating float ambiguities with a commercial software package [116] ("float") or employing carrier-phase smoothed pseudoranges ("smoothed p") based on the algorithm presented in section 3.5.

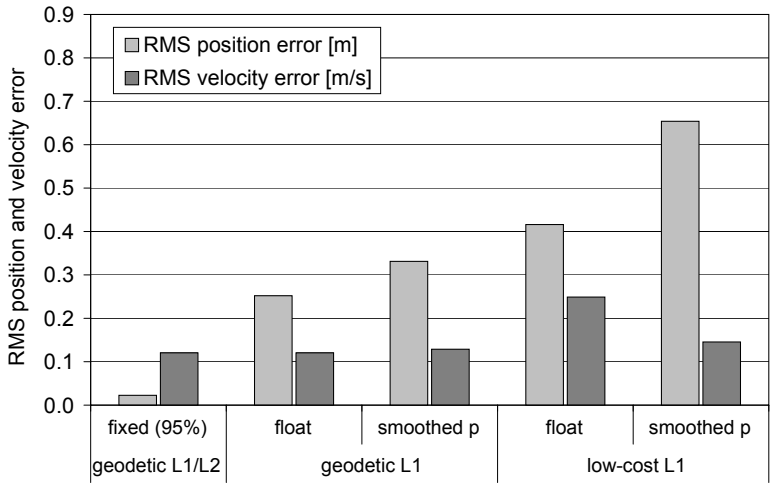

Fig. 4.3: 3D position and velocity RMSE of differential GPS solutions for 6 downhill runs (approximately 150000 samples) as a function of the GPS receiver hardware (geodetic L1 and L1/L2, low-cost L1) and the ambiguity resolution approach (fixed and float ambiguities, carrier-phase smoothed pseudoranges).

The L1/L2 solution presents an average position accuracy below decimeter level despite the difficulty in maintaining fixed ambiguities because of the rapidly changing signal reception

due to the mountainous environment. Indeed, the ambiguities remain float on certain portions of the track. The position accuracy decreases for the single-frequency solutions to a level of 30 cm using the same receiver and to half-meter level using the low-cost receiver. The accuracy is clearly improved when float ambiguities are estimated instead of using carrier-phase smoothed pseudoranges (improvement of $30 - 50\%$). Except in the case of the low-cost receiver, there is no significant accuracy difference between the horizontal and vertical components. In the velocity domain however, the accuracy differences are much smaller between the GPS solutions. Indeed, the velocity computation is independant of the ambiguity resolution and uses the same observations (Doppler measurements). It is more surprising that the quality of the GPS receiver does not significantly improve the velocity estimation. Except the solution with the low-cost receiver and float ambiguities all solutions provide dm/s accuracy. The larger velocity error in this case is probably originated by differing filter settings in the GPS processor, i.e. a commercial software [116] where not all parameters can be controlled.

4.2.2 GPS/MEMS-IMU Integration

The L1 GPS observations from geodetic and low-cost receivers were integrated with MEMS-IMU measurements based on the loosely and closely coupled integration schemes presented in section 3.6.4 and compared to the reference solution. Fig. 4.4 and Fig. 4.5 summarize the RMSE of the GPS/INS solutions for 6 downhill runs.

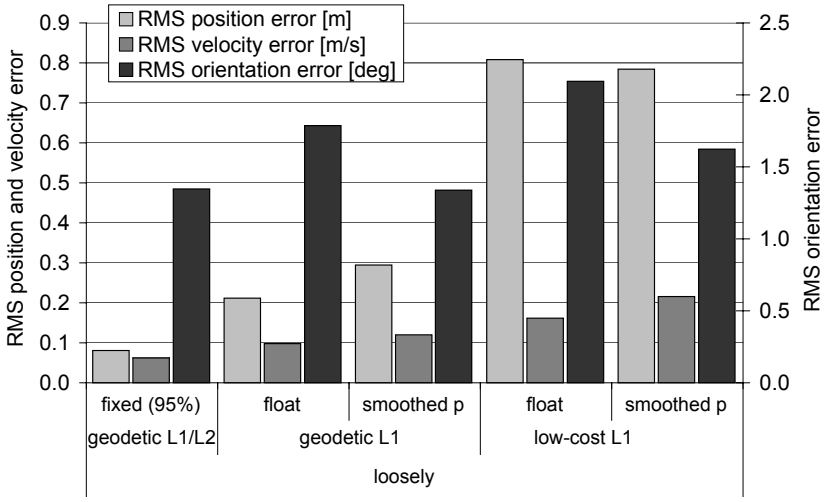

Fig. 4.4: 3D position, velocity and orientation RMSE of 6 downhill runs based (approximately 150000 samples) on the loosely coupled approach.

Fig. 4.4 illustrates the position, velocity and orientation RMSE in the loosely coupled approach (Tab. D.2). The position accuracy is mainly driven by the accuracy of differential GPS (with floating ambiguities or carrier-phase smoothed pseudo-range measurements) and thus corresponds to the values presented in Fig. 4.3 and Tab. D.1. Except for the low-cost receiver, there is no significant accuracy difference between the horizontal and vertical components. The integration of the MEMS-IMU measurements hardly affects the velocity accuracy. The obtained orientation performance is comparable in all approaches. Roll and pitch errors range from $0.5 - 1.5$ deg on average, while heading errors are slightly larger ($1 - 3$ deg).

This can be explained by the limited observability of the heading angle (section 6.6.4). The presented navigation performance is confirmed by independent findings where comparable accuracy levels were reached [57, 96, 36].

Fig. 4.5 summarizes the difference between loosely and closely coupled integrations schemes (Tab. D.3). The discrepancies are negligible and may originate from the filter settings in the GPS processing.

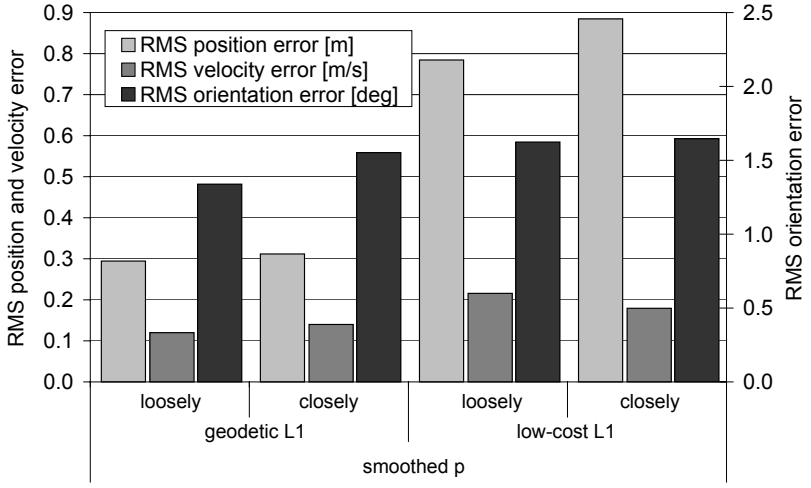

Fig. 4.5: Comparison between loosely and closely coupled approaches using carrier-phase smoothed pseudoranges. 3D position, velocity and orientation RMSE of 6 downhill runs (approximately 150000 samples).

Fig. 4.6 illustrates the rapid convergence of the orientation estimation after the start. Despite the large initial orientation error, the filter converges after a few seconds. In parallel, the bias terms converge as soon as the varying dynamics allow decorrelating them. Fast convergence of the filter parameters is crucial for sport applications of relatively short duration (e.g. alpine skiing).

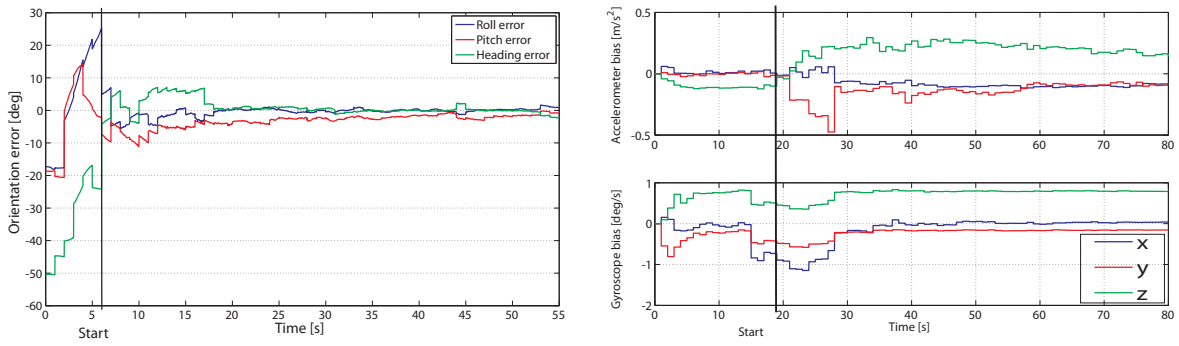

Fig. 4.6: Convergence of the orientation (left) and of the accelerometer and gyroscope biases (right) after the start.

4.2.3 GPS/MEMS-IMU Integration during Reduced Satellite Reception

Overall performance

The previous section has reported that the loosely and closely coupled approaches performed equally under reasonable satellite constellations (> 4 SVs). However, an accuracy improvement can be expected for the closely coupled strategy under partial satellite constellations [187, 224, 161, 225]. Such scenarios can be simulated by resampling GPS data sets and removing satellites observations over a variable period of time ($5 - 40$ s). In this section, two integration strategies are analyzed under such conditions in terms of position, velocity and orientation accuracies. The evaluation is based on the skiing experiment (section 4.1) and L1 GPS measurements from the geodetic receiver.

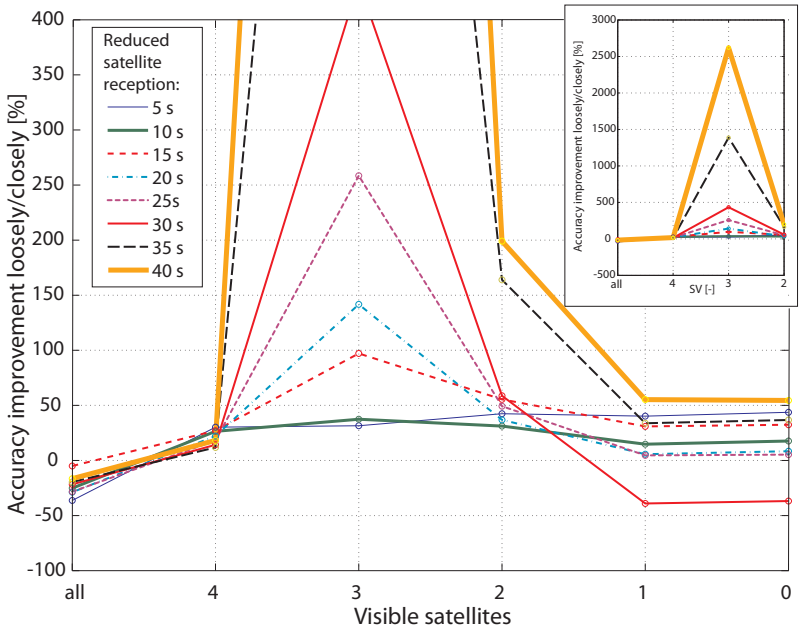

FIG. 4.7: Accuracy improvement of the closely coupled integration approach with respect to the loosely coupled approach as a function of the number of SVs and the number of considered satellites.

The overall accuracy improvement provided by the closely coupled integration approach with respect to the loosely coupled approach is computed for each data set based on:

$$\mathrm{RMSE}_{gain} = \begin{cases} \frac{\mathrm{RMSE}_l}{\mathrm{RMSE}_c} - 1 & \text{if } \frac{\mathrm{RMSE}_l}{\mathrm{RMSE}_c} > 1 \\ 1 - \frac{\mathrm{RMSE}_l}{\mathrm{RMSE}_c} & \text{if } \frac{\mathrm{RMSE}_l}{\mathrm{RMSE}_c} < 1 \end{cases} \tag{4.2.1}$$

where $RMSE$ is the root mean square error during the periods with partial satellite blockage. Index l denotes loosely coupled integration, index c closely coupled integration. This expression yields positive values when the closely coupled approach outperforms the loosely coupled integration.

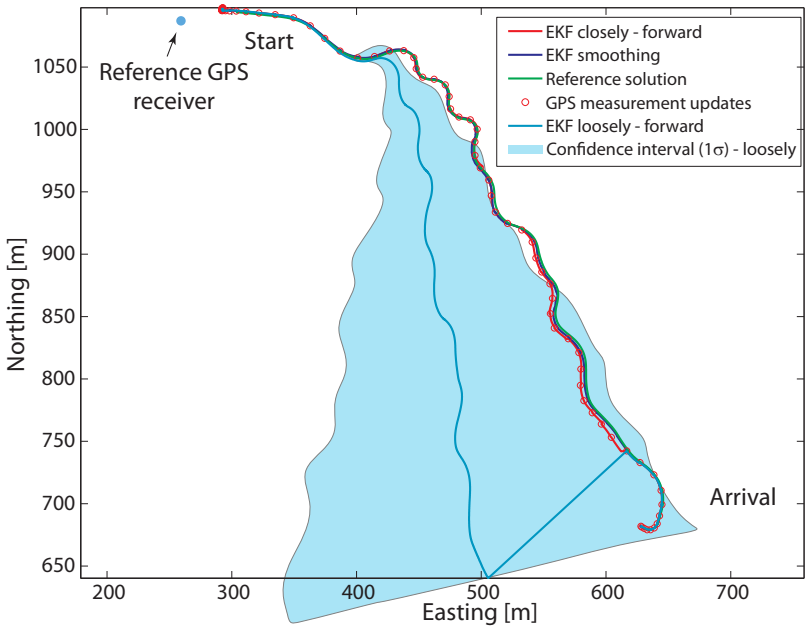

FIG. 4.8: Trajectory during 40 s of reduced satellite reception (3 satellites) applying a closely and a loosely coupled integration strategy.

The average improvement of the position, velocity, and orientation error is visualized in FIG. 4.7. It can be seen that the loosely coupled integration performs slightly better under complete satellite constellations (label "all" on the x-axis). At the critical number of 4 visible SVs, the performance of the closely coupled approach is marginally better (10 to 30%). With further decrease of tracked SVs, the improvement provided by the closely coupled approach increases and becomes maximum for 3 SVs and a GPS outage duration of 40 s. The trajectory depicted in FIG. 4.8 illustrates this behavior: The closely coupled solution follows very well the reference track whereas the loosely coupled solution diverges considerably. For fewer than 3 SVs, the improvement provided by the closely coupled integration is less important and the difference is again marginal for one tracked satellite.

Position and orientation accuracy

The improvement in position and orientation accuracy provided by the closely coupled integration scheme is analyzed for partial satellite constellations.

FIG. 4.9 shows the position errors for different durations of satellite tracking outages (10 s, 15 s, 20 s and 30 s). For outage times up to 15 s, the difference in performance between both approaches is marginal. The vertical component presents a peak at 4 satellites which is less dominant in the closely coupled approach. In such situations where no redundant satellites are available, the filter probably overweights the remaining pseudoranges with respect to the inertial solution. On the other hand, for outage times longer than 20 s the closely coupled approach outperforms the loosely coupled strategy, with a major improvement at 3 SVs. However, for cases with 3 or less satellites and reduced satellite reception longer than 30 s, the position error increases rapidly in correspondence to MEMS-inertial sensor characteristics.

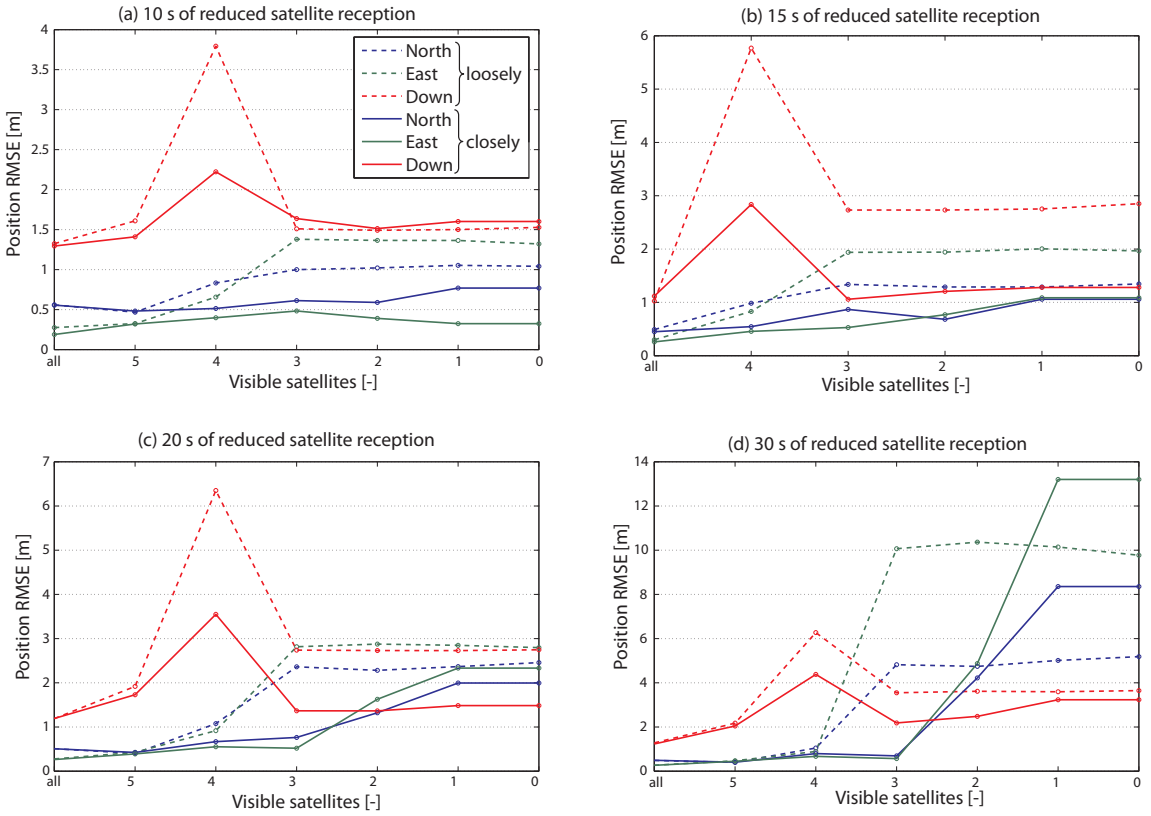

FIG. 4.9: Position RMSE during 10 s (a), 15 s (b), 20 s (c) and 30 s (d) of reduced satellite reception as a function of the number of satellites.

During such scenarios, neither approach is appropriate to satisfy accuracy requirements in sports (TAB. 2.1).

The evolution of the orientation errors is slower in time. Hence, the difference between the integration approaches becomes apparent only for larger outages (FIG. 4.10). There, the closely coupled strategy performs better. With this approach, the orientation error remains bounded and satisfactory results can be achieved even for only 2 SVs.

GPS outages up to 5 s are frequent in sport applications, whereas outages longer than 30 s are less frequent (e.g. in alpine skiing through satellite masking due to the changing surrounding). Indeed, most outages are less than 15 s. These investigations have revealed that the filter was capable of bridging typical outages without significant loss of navigation accuracy. Thus, MEMS-IMU measurements can be integrated with GPS to obtain sufficiently accurate results during GPS outages up to a few seconds in spite of the high dynamics like in ski racing.

The loosely coupled strategy provides similar performance at full or partial satellite constellation (more than 3 SVs) which confirms the findings in [161]. For 3 SVs and outages larger than 15 s the closely coupled approach is certainly better but this difference becomes negligible at 2 SVs and diminishes completely at 1 SV. This confirms the simulations presented by

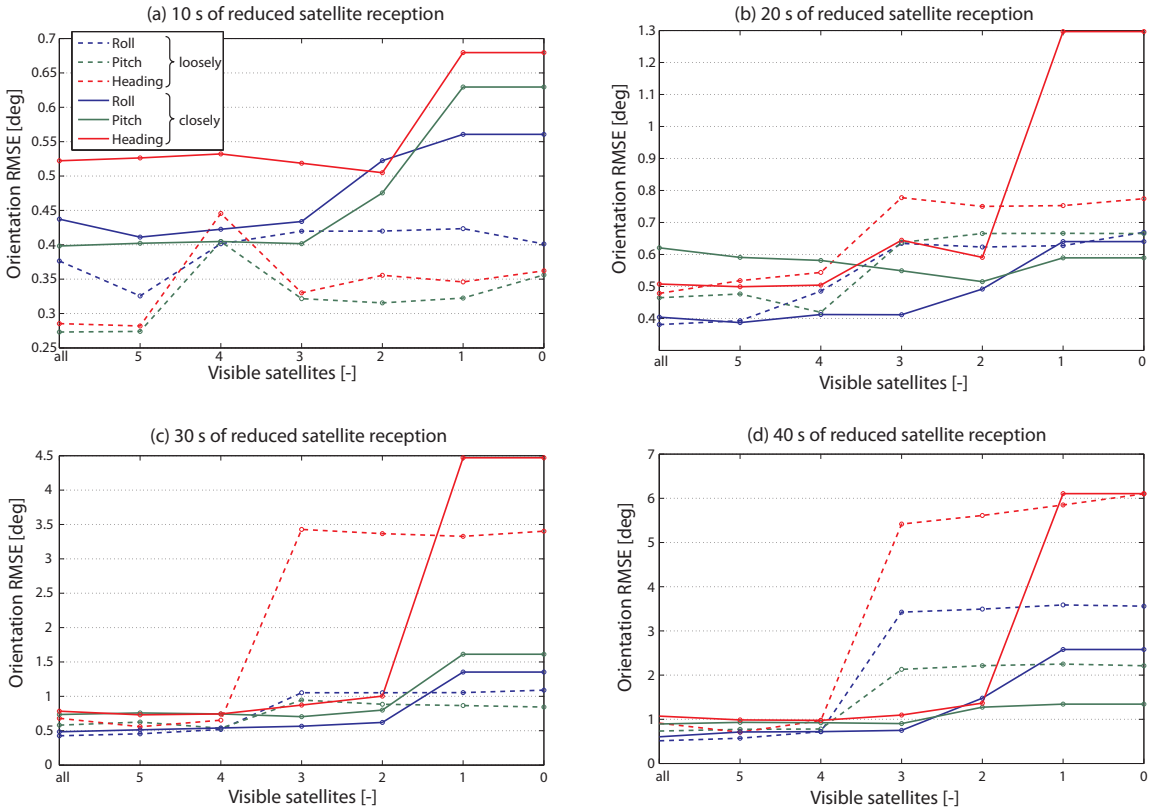

FIG. 4.10: Orientation RMSE during 10 s (a), 20 s (b), 30 s (c) and 40 s (d) of reduced satellite reception as a function of the number of satellites.

[187, 224]. Therefore, the closely coupled integration can provide better results under certain circumstances.

The analyzed data corresponds to a period of one hour during which the satellite geometry did not change significantly. Hence, no general conclusion for arbitrary satellite constellations is possible. However, the closely coupled strategy seems to possess important advantages in situations with reduced satellite reception and is therefore recommended.

4.2.4 Benefits of RTS Smoothing

Through backward smoothing, a large part of the random errors and drifts inherent to inertial navigation can be removed. FIG. 4.8 and 4.11 illustrate the navigation performance improvement by RTS smoothing. The trajectory starts to diverge between GPS updates when inertial measurements with remaining errors are integrated. At the GPS updates, the INS errors are calibrated. The drift due to inaccurate inertial error modeling decreases along the trajectory.

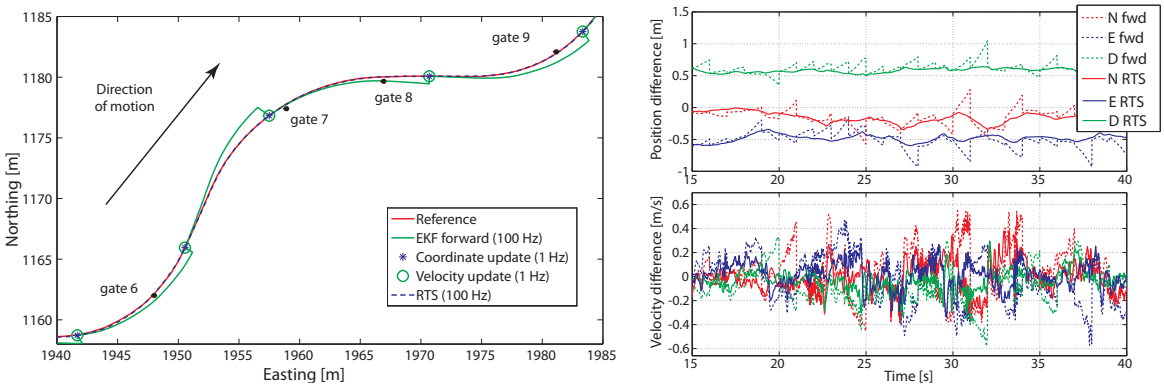

FIG. 4.11: Trajectory smoothing based on the RTS algorithm.

4.3 Benefits of UKF

This section assesses the performance of the EKF and SR-UKF. Indeed, theoretical considerations in section 3.4.2 revealed the suitability of the two approaches for sport applications. Therefore, the previously investigated trajectories were reprocessed using both methods and compared to the reference tracks.

4.3.1 Navigation Performance

TAB. 4.1 compares the RMSE and maximum errors between 6 reference trajectories and those obtained by EKF and SR-UKF integration of L1 GPS with MEMS-IMU. The differences of the RMSE are negligibly small (cm-level for position, 0.3 deg for orientation) and are mainly driven by differential GPS accuracy (with floating ambiguities). On the other hand, the maximum errors are larger for the SR-UKF, notably for the orientation. These maximum errors occur at the beginning or at the end of the run (FIG. 4.12). As soon as the filter parameters have converged the two filters provide identical results. These findings are confirmed by the studies presented in [225]: Loosely and closely coupled interpolation schemes and UKF have reported to calibrate MEMS-IMU with similar accuracies.

The covariance comparison gives also similar results for both filters. This is demonstrated by plotting the covariance of the orientation and the bias during a selected run in FIG. 4.13. The covariance decreases rapidly after the start of the skier (at $10s$).

4.3.2 Implementation Aspects

From the implementation point of view, the UKF approach sometimes encounters problems with the positive semi-definiteness of the $\mathbf{S}$ matrix after the Cholesky update [22]. Indeed, in the standard UKF, the covariance $\mathbf{P}$ is computed recursively. This requires calculating the matrix squareroot $\mathbf{S} \cdot \mathbf{S}^T = \mathbf{P}$ at each step (by Cholesky factorization). On the other hand, the Square-Root implementation of the UKF (SR-UKF) propagates $\mathbf{S}$ directly [203, 166]. Theoretically, this guarantees the positive semi-definiteness of the UKF during the covariance propagation. Practically, the positive semi-definiteness of the $\mathbf{S}$ matrix is occasionally still

TAB. 4.1: Comparison of the mean and maximum errors of the EKF and UKF for 6 runs.

		EKF	UKF	Difference
RMSE	N [m]	0.25	0.25	0.00
	E [m]	0.20	0.17	0.03
	h [m]	0.19	0.17	0.02
	rl [deg]	1.52	1.36	0.16
	pt [deg]	1.80	1.81	-0.01
	hd [deg]	2.04	1.94	0.10
Max. Error	N [m]	1.01	1.05	0.04
	E [m]	0.73	1.08	0.35
	h [m]	1.20	1.39	0.19
	rl [deg]	2.26	2.53	0.27
	pt [deg]	2.79	2.92	0.13
	hd [deg]	3.37	3.90	0.53

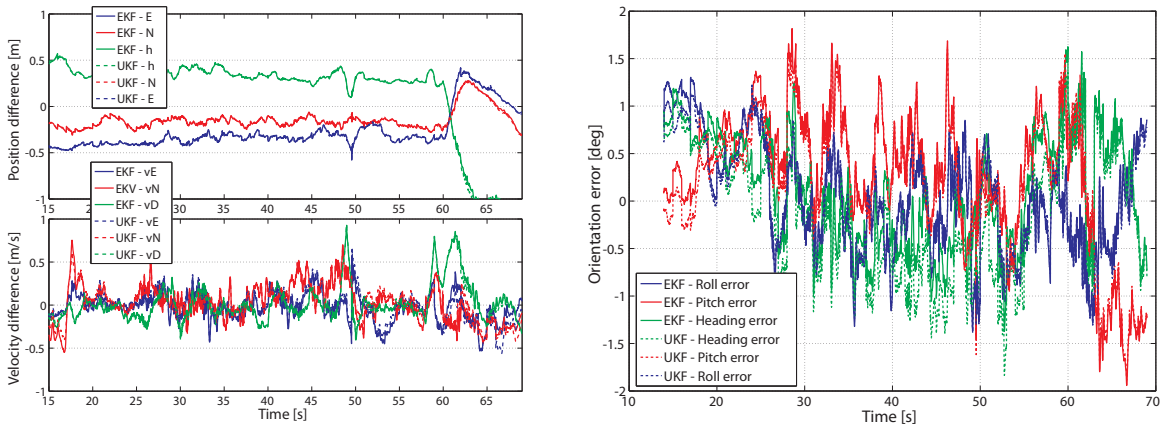

FIG. 4.12: Position, velocity (left) and orientation errors (right) of the smoothed EKF and SR-UKF solutions during run #11.

not met after the Cholesky update [22]. The Frobenius norm and the modified Cholesky factorization [114] can help to overcome this problem.

Furthermore, longer computational times were noticed with the SR-UKF implementation as compared to the EKF which confirms results presented by [180]. On the other hand, the previously mentioned references indicate that both algorithms are $O(n^3)$ [202, 205, 166, 96]. However, the observed differences might come from the choice of the programming language (*Matlab*, [101]) where the implementation of some functions (e.g. the matrix inversion) is highly optimized, whereas others are less (SP generation, update equations, covariance reconstruction). Additionally, the EKF system matrix $\mathbf{F}$ was derived analytically which reduces the computational load.

Considering the increased processing time and the encountered numerical instabilities, the SR-UKF approach seems to be less interesting for the sport application. On the other hand, the SR-UKF remains a straightforward approach for testing other (more complex) models

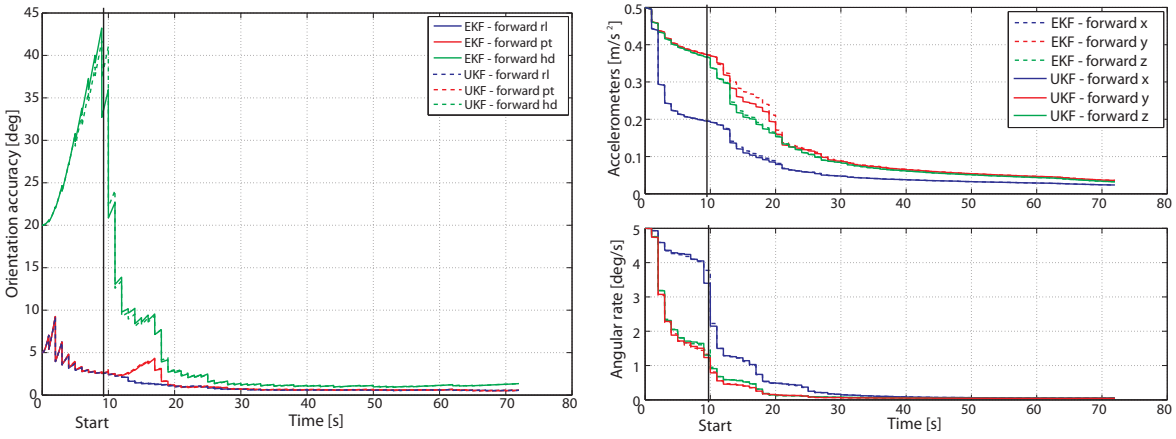

FIG. 4.13: Orientation (left) and bias covariance estimation (right) of the forward processed EKF and SR-UKF solutions during run #11.

(e.g. closely-coupled integration, hybridization with other sensors). Furthermore, it might provide better results than the EKF in the case of large initial attitude errors [37, 166] or under different dynamics as it was demonstrated in the studies [23, 22].

4.4 Magnetic Sensors

To evaluate the benefits of magnetic updates during the navigation process, magnetic observations were fed to the loosely coupled EKF based on relation 3.6.27. Dual-frequency GPS coordinates and velocities were input to limit the contribution of the GPS observation errors on this investigation.

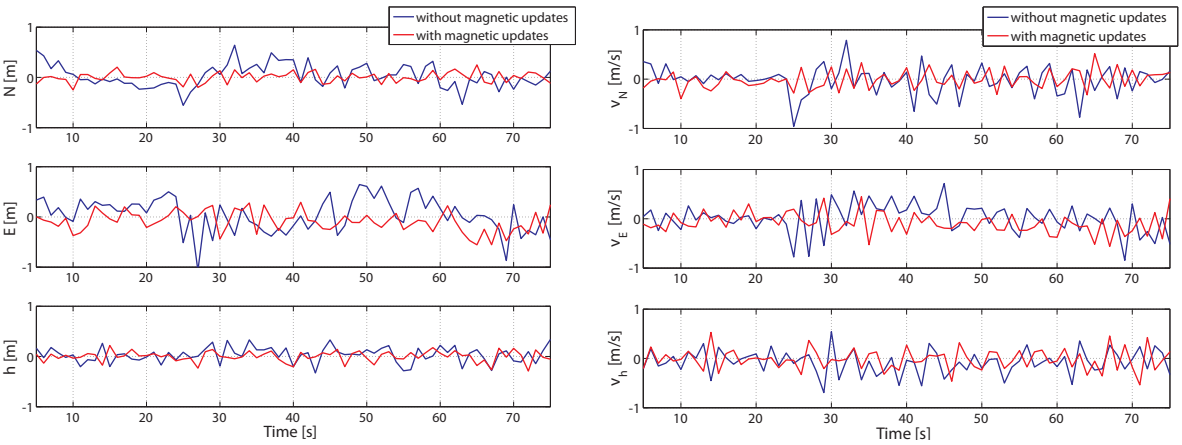

FIG. 4.14: Coordinate (left) and velocity (right) update innovations (run without GPS outages, forward filtering, with and without magnetic updates).

FIG. 4.14 depicts the coordinate and velocity innovations of a run processed in forward direction (< 1.0 m for the coordinate updates and < 1.0 m/s for the velocity updates). They

are efficiently reduced by the RTS smoothing algorithm (Fig. 4.11). However, no systematic improvement is realized by the application of magnetic updates.

Magnetic updates are useful for orientation estimation and potentially help to bridge the gaps in GPS positioning. A simulation with artificial satellite outages (Tab. 4.2) shows that the maximum orientation error is slightly reduced (less than 1 deg) by considering the magnetic observations. On the other hand, the magnetic updates do not improve the position and velocity estimation systematically (Tab. 4.2, Fig. 4.14). Reference [197] noted the sensitivity of magnetic sensors to high-frequency accelerations. This effect was also mentioned in study [221]. Nevertheless, these observations are indispensable during the sensor orientation initialization [171].

Tab. 4.2: Differences between the maximum position, velocity and orientation errors (with and without magnetic updates). Negative values indicate an improvement.

Difference	Position [cm]			Velocity [cm/s]			Orientation error [deg]		
	E	N	h	v_E	v_N	v_D	rl	pt	hd
GPS updates at 1 Hz	-0.2	0.5	1.7	-1.0	0.6	0.7	0.3	-1.3	-0.6
GPS outage of 5 s	-6.0	-0.6	-1.8	-3.8	-0.6	-1.8	0.3	-0.8	-0.6
GPS outage of 10 s	-7.0	-34.1	9.6	-1.8	-2.2	1.3	-0.1	-0.5	-0.8
GPS outage of 15 s	18.2	54.9	1.2	-0.8	8.2	3.6	0.4	-0.7	-1.0

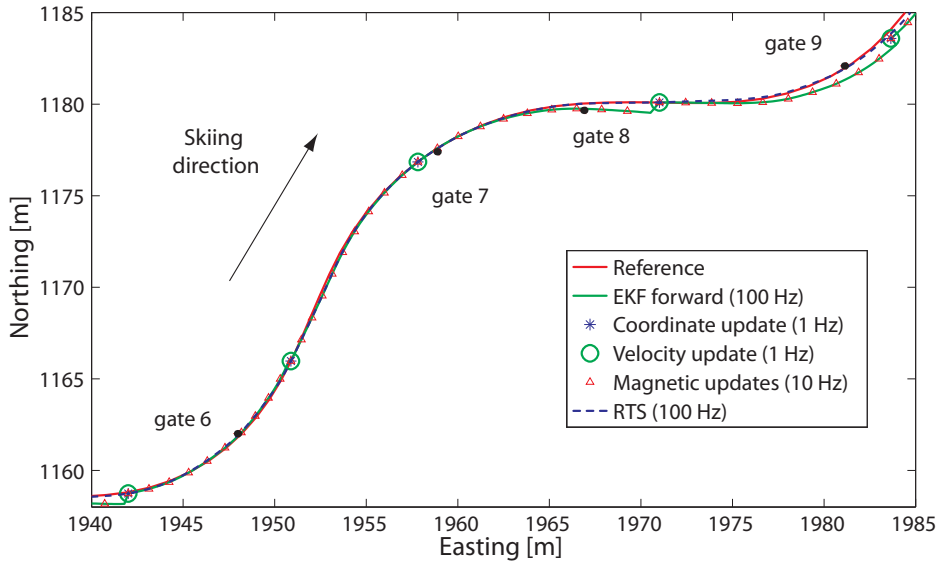

Fig. 4.15: Trajectory smoothing based on the RTS algorithm (with magnetic measurements).

4.5 Orientation Initialization

The initial alignment is a critical phase in GPS/MEMS-IMU integration. Two methods for the initialization of the orientation were previously introduced in section 3.6.2. The first algorithm is a modified coarse alignment approach where the gyroscope measurements are

replaced by magnetic measurements. The second method is a quaternion based approach using also accelerometer and magnetometer observations.

4.5.1 Evaluation based on Simulations

Firstly, the sensitivity of the algorithms to sensor biases is investigated. Indeed, it is important to verify whether the orientation error caused by typical accelerometer biases and magnetic disturbances can be tolerated. For this purpose, a synthetic set of inertial and magnetic measurements was generated. The measurement biases were alternatively added to each axis (Fig. 4.16). The accelerometer measurements were "fixed" at normal gravity and the magnetic measurements to the value of the Earth magnetic field at the position (46 °N, 7 °E, 1775 m) and time (2007).

Typical accelerometer biases encountered with the MEMS-type sensors amount to 0.2 m/s^2. Such biases cause maximum orientation errors of approximately 2 deg (Fig. 4.16, left). On the other hand, soft magnetic disturbances and magnetometer biases have a much larger impact on the initial orientation. Indeed, these errors can range up 0.2 T/T and cause orientation errors up to 20 deg (Fig. 4.16, right). Experience shows, however, that such errors are rapidly mitigated by the GPS updates and do not generate numerical instabilities in the KF. Hard magnetic disturbances (i.e. sign flipping or complete overmasking) induce variable orientation errors up to 50 deg which may cause filter divergence. Such cases can be provoked by the vicinity of other electronic accessories (e.g. computers) or metallic components of the sport equipment (e.g. in motorsports). In some cases the absolute value of the sensor bias can be reduced by sensor pre-calibration (chapter 5, [222]).

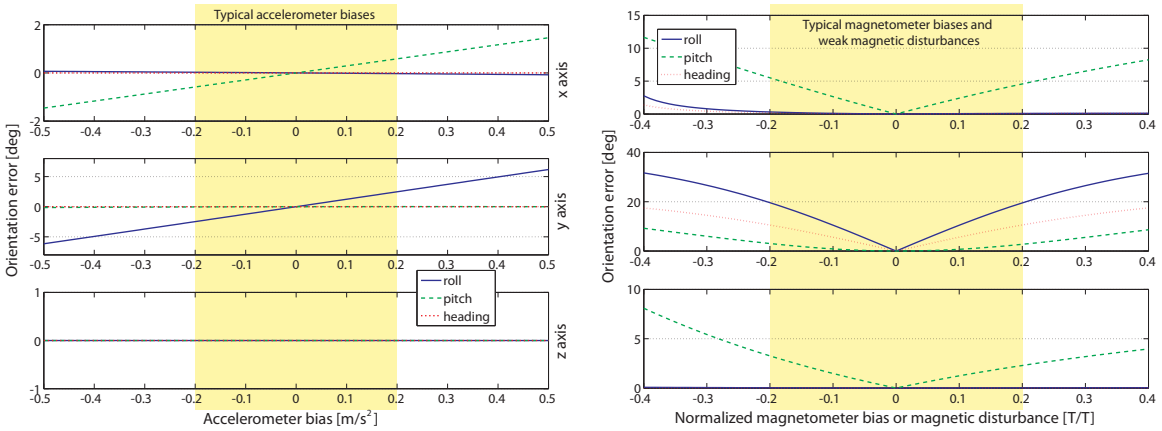

Fig. 4.16: Initial orientation error as a function of the initial accelerometer bias (left) and of the initial magnetometer bias or magnetic disturbance (right).

4.5.2 Experimental Evaluation

The limitations of both initialization algorithms with respect to the MEMS sensor error characteristics are also analyzed using the tactical-grade GPS/INS as reference. The errors of the modified coarse alignment and of the QUEST algorithm are illustrated in Fig. 4.17 for

one run. As depicted in the example, both algorithms converge rapidly after the start as soon as the dynamics increases and the inertial biases decorrelate from the orientation estimate [220]. The initial differences between the two solutions (< 0.5 deg) are negligible and have no impact on the filter convergence.

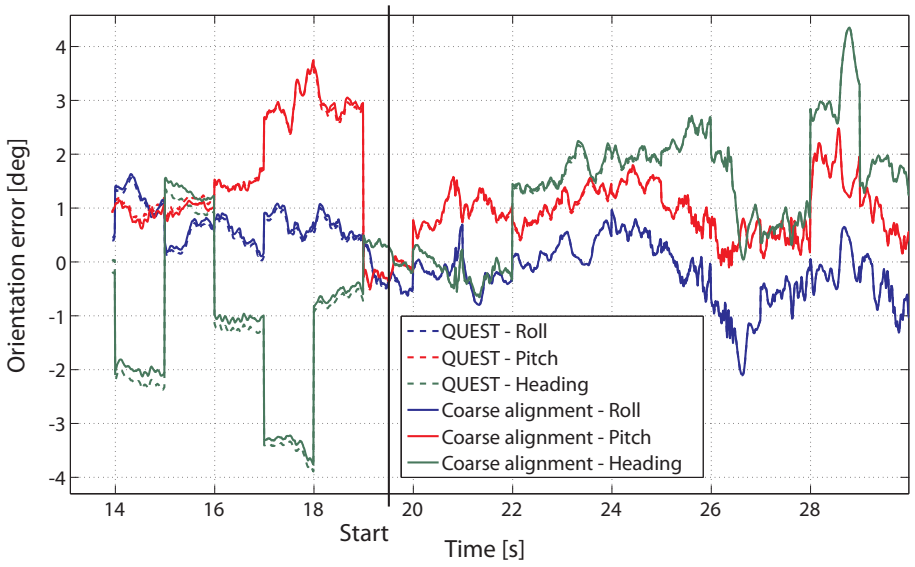

FIG. 4.17: Comparison of the coarse alignment and QUEST algorithm for the orientation initialization (run #11).

Chapter 5

MEMS-IMU Error Modeling

MEMS-type inertial and magnetic sensors are prone to very large and variable measurement errors. Although sensor calibration by the manufacturers (temperature, misalignments) removes its important part, the residual effect do not provide sufficiently accurate measurements for standalone inertial navigation. Therefore, permanent sensor error compensation during navigation becomes mandatory. Realistic estimation of the noise parameter in the inertial sensors is important for correct tuning of the KF. Moreover, the stochastic part of the inertial sensor errors is required for the simulations presented in section 6.6. For sensor calibration, turn tables and climatic chambers are used in industry. Ideally, the determination of the noise characteristics is also based on dynamic experiments with changing environmental conditions (e.g. temperature, pressure, vibrations). There, IMUs of higher quality can be used as reference.

In this chapter, the noise parameters are determined based on static and dynamic experiments. The MEMS sensor's output is compared to the reference signals provided by a higher-grade IMU. This information is used to verify the relevance of the proposed error model (section 3.1.2) and parameter estimation [222].

5.1 Static Evaluation by Allan Variance

The complexity of the observed errors is usually separated by terms of different time variations. Indeed, the origins of these terms is often linked to the oscillator environment (e.g. temperatures changes, vibrations) but they may also be internal (e.g. thermal noise). Several variance techniques have been developed for the analysis of these perturbations such as the Allan variance, the Hadamard variance or the total variance [76, 207, 208, 209]. The simplest of these methods is the Allan variance. This method was successfully applied to the modeling of the inertial sensor errors in [74, 35, 184, 228].

The Allan variance is a method where the root mean square random error is represented as a function of the averaging time. It was invented in 1966 by David Allan and was originally employed to study the stability of oscillators [2]. In 1998, the IEEE standard introduced this technique as a noise identification method [66]. This method can be used to determine the characteristics of the underlying random processes that perturb data. The Allan variance

considers five basic noise processes which can be expressed in the appropriate notation for inertial sensors (Fig. 5.1), namely [64]:

- The difference between the real analog value and the encoded digital value is called **quantization error**. This error is due to the bit resolution of the analog-to-digital converter, which is either rounded or truncated.
- **White noise** is a random process which is characterized by a flat PSD which means that every frequency is of equivalent importance in the random process.
- The **bias instability** originates from electronic or other sensors' components susceptible to random flickering [74].
- **Random walk** noise can be characterized by a trajectory consisting of taking successive random steps. This process is controlled by the differential equation defined in the relation 3.1.5.
- The error terms considered so far are all random processes. It is, however, useful to determine the behavior of the Allan variance under systematic (deterministic) effects. One such error is the **rate ramp**.

Moreover, a first-order Gauss-Markov process as well as a sinusoidal noise can be identified in the Allan variance plot [74, 35, 121]. In this work, the Allan variance is applied as a tool for modeling of inertial sensor errors.

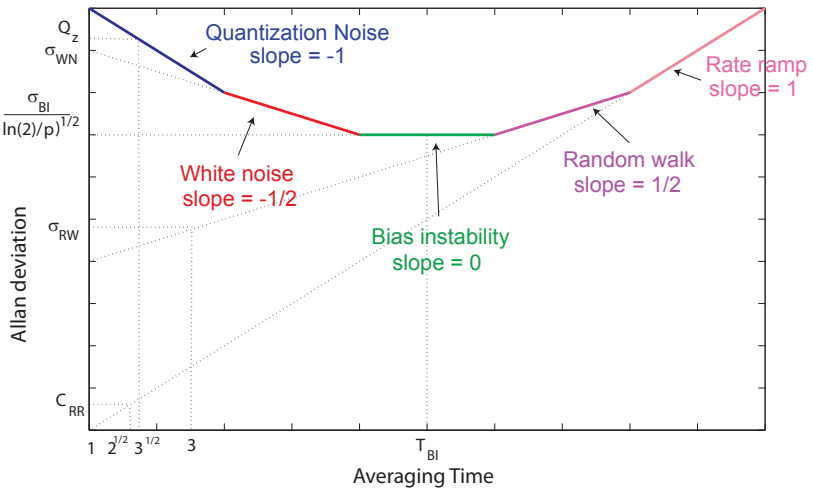

Fig. 5.1: Schematic sample representation of Allan variance.

5.2 Static Estimation of the Noise Parameters

In this section, the previously described parameters of the error model are estimated. After removal of the mean offset and scale-factor (trend) determined through parametric adjustment,

the stochastic component of the bias, the bias instability and the white noise are approximated using the Allan variance method.

Static experiments of three hours were conducted in three different environmental conditions (e.g. temperature, pressure). In order to provide inputs to the Allan variance analysis, the static measurements of the considered sensor (*Xsens MTi*) were recorded. These periods are considered long enough to give sufficiently significant results [64].

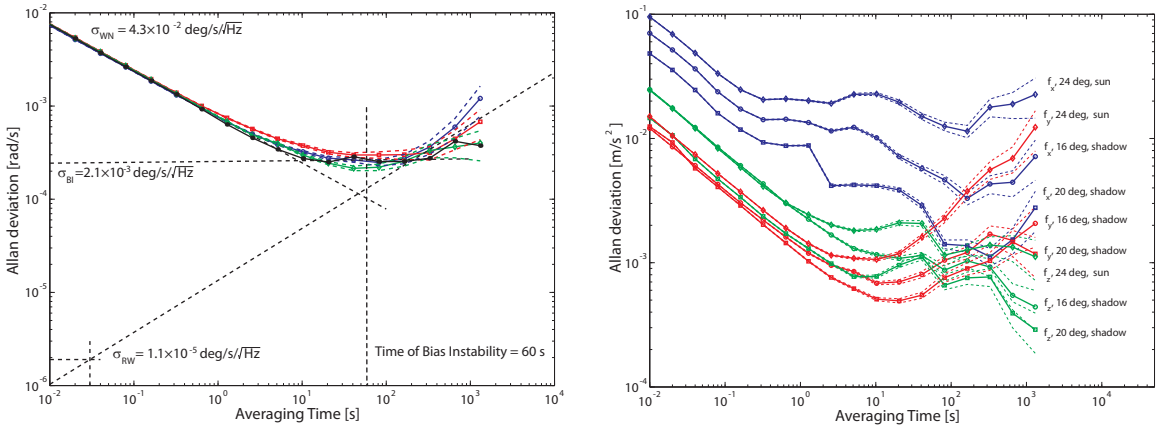

FIG. 5.2: Estimation of the static noise parameters for the gyroscopes (left) and Allan variance results for the accelerometers (right) of the *Xsens MTi*. The dotted lines indicate the standard deviations of the measurements.

TAB. 5.1: Noise estimates for *Xsens MTi* using Allan variance [64].

	White noise	Bias Instability		Random walk
	σ_{WN}	T_{BI}[s]	σ_{BI}	σ_{RW}
Gyroscopes [deg/s/$\sqrt{\text{Hz}}$]				
Gyro X, Y, Z	$4.3 \cdot 10^{-2}$	60	$2.1 \cdot 10^{-3}$	$1.1 \cdot 10^{-5}$
from manufacturer	$1.0 \cdot 10^{-2}$	–	–	–
Accelerometers [m/s^2/$\sqrt{\text{Hz}}$]				
Accelerometer X	$7.2 \cdot 10^{-3}$	0.6	$2.2 \cdot 10^{-3}$	$7.5 \cdot 10^{-6}$
Accelerometer Y	$1.3 \cdot 10^{-3}$	9	$1.2 \cdot 10^{-4}$	$1.3 \cdot 10^{-6}$
Accelerometer Z	$2.1 \cdot 10^{-3}$	35	$2.0 \cdot 10^{-4}$	–
from manufacturer	$2.0 \cdot 10^{-3}$	–	–	–

FIG. 5.2 illustrates that all gyroscopes have a similar behavior and that they are scarcely affected by variations in the environment. Unlike the gyroscopes, the accelerometers are affected by environmental variations and each sensor has a different behavior. As a result, the noise parameter of each sensor needs to be estimated individually. TAB. 5.1 summarizes the calibrated value and their corresponding accuracy [64]. The estimated values reveal an important variability of the error characteristics for each sensor axis. In addition, the experimentally obtained values are different from the specification of the manufacturer. Hence, employing calibrated parameters derived from experimental data could improve the tuning of the Kalman filter.

Ideally, the noise characteristics of the MEMS-IMU sensors would be estimated based on experiments in various environmental conditions and different dynamics. As the accuracy of the Allan variance decreases rapidly with increasing cluster size, the duration of the downhill skiing experiments was too short to retrieve numerical results.

5.3 Dynamic Error Model Investigation

To investigate the suitability of the MEMS error model as proposed in section 3.1.2, the raw data of 3 MEMS-IMUs (*Xsens MTi*) and a tactical-grade IMU (*Litton LN200*) were compared during a dozen of ski downhills of approximately 1 min duration (experimental system setup described in section 4.1).

5.3.1 Estimation of the Relative Alignment of the MEMS-IMU

Before a comparison between MEMS and reference IMU measurements can be performed, the physical misalignment between the two systems had to be determined. These were estimated by feeding the GPS/MEMS-IMU integration algorithm with the reference orientation angles provided by the reference solution using the following observation model [222, 215]:

$$\begin{aligned} h(\hat{\mathbf{x}}^-) &= (\mathbf{I}_3 + \mathbf{B}) \cdot \boldsymbol{\varphi}_{LN200} + \mathbf{w}_\varphi \\ \dot{\mathbf{B}} &= -\beta_B \cdot \mathbf{B} + \sqrt{2\sigma_B^2 \beta_B}\ \mathbf{w}_\varphi \end{aligned} \tag{5.3.1}$$

where $\mathbf{B}$ is the skew-symmetric form of the misalignment angles, $\boldsymbol{\varphi}_{LN200}$ are the orientation angles of the reference solution, $\mathbf{w}_\varphi$ the measurement noise and β_B the inverse of the correlation time T "fixed" to infinity. The accuracy of the misalignment angles is limited by the accuracy of the MEMS orientation determination and is estimated to 0.5 deg (1σ).

5.3.2 Estimation of the Reference Values for the Inertial Sensor Errors

With the reference signals corrected for the misalignment, the raw signals could be compared directly. From the observed differences, biases b and scale factors s were estimated through parameter adjustment of the following model, assuming that drifts can be neglected for data sets of short duration ($2 - 5$ min):

$$\ell_{LN200} - v = (1 - s) \cdot \ell_{MEMS} + b \tag{5.3.2}$$

During the static initialization, only biases could be computed. The absence of dynamics during this period did not permit to isolate scale factors. On the other hand, during the runs the signals decorrelated to a greater extent and the estimation of the scale factor became possible.

By comparing the biases estimated on the static portions before and after the runs and considering that the duration of the runs does not exceed one minute, the adjustment of drifts can be neglected. For longer data sets however, the correlation time could take into account the error drifts.

5.3.3 Error Model Analysis

Tab. 5.2 summarizes the results for a representative data set. When comparing the estimated mean biases with their standard deviations during static initialization, they often show to be irrelevant. This is further shown in Fig. 5.3 (left) and 5.5 (left). On the other hand, the biases observed during the run are statistically meaningful and better determined (Fig. 5.3 (right) and 5.5 (right)). The scale factors for the accelerometers are statistically significant (Fig. 5.4), whereas those for the gyroscopes proof to be insignificant (Fig. 5.6). However, the correlations between the accelerometer biases and scale factors remain large (0.9 for the "horizontal" axis, 0.3 for the "vertical" axis) which explains the difficulty to decorrelate the two error contributions.

Tab. 5.2: Estimated biases and scale factors during the static initialization and during a representative run. Shaded cells indicate statistically meaningless values.

Static Initialization	f_x[m/s^2]	f_y[m/s^2]	f_z[m/s^2]	ω_x[deg/s]	ω_y[deg/s]	ω_z[deg/s]
Bias	0.008	0.171	0.020	-0.11	0.51	1.38
Std. bias (1σ)	0.022	0.024	0.027	0.12	0.14	0.16
Downhill run	f_x[m/s^2]	f_y[m/s^2]	f_z[m/s^2]	ω_x[deg/s]	ω_y[deg/s]	ω_z[deg/s]
Bias	-0.049	0.039	-0.145	-0.21	0.38	1.39
Std. bias (1σ)	0.003	0.003	0.009	0.01	0.01	0.01
Scale factor [-]	0.0046	-0.0533	-0.0223	-0.0051	-0.0118	0.0004
Std. scale factor [-] (1σ)	0.0006	0.0009	0.0011	0.0212	0.0357	0.0250
Correlation [-]	0.93	0.32	0.98	0.31	0.43	0.14

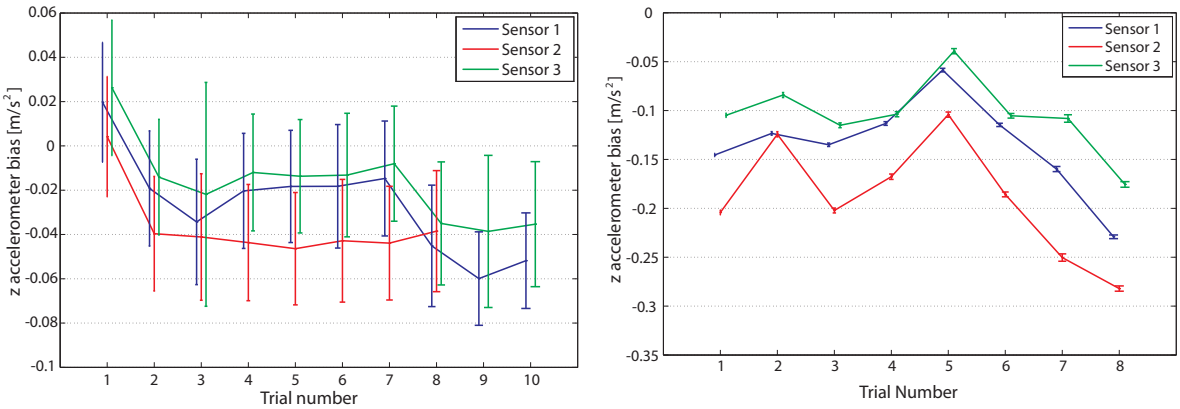

Fig. 5.3: Biases and standard deviations (1σ) observed during the static initialization (left) and dynamic phase (right) for the z-axis of 3 accelerometers.

Fig. 5.3 to 5.6 give examples of the estimated biases and scales factors for 3 MEMS-IMU sensors and 8-10 ski runs.

The accelerometer biases estimated during the static initialization have similar values for all runs (Fig. 5.3, left). However, the accelerometer biases and scale factors adjusted during the dynamic portion of the run vary considerably between the tracks (Fig. 5.3, right and Fig. 5.4).

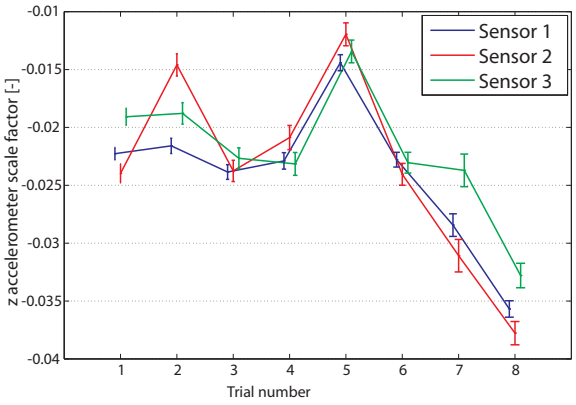

FIG. 5.4: Scale factors and standard deviations (1σ) observed for the z-axis of 3 accelerometers.

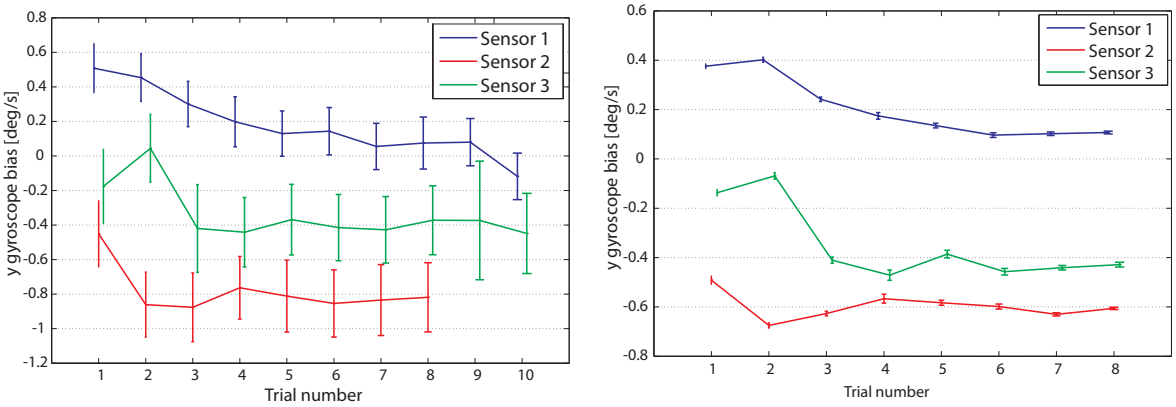

FIG. 5.5: Biases and standard deviations (1σ) observed during the static initialization (left) and dynamic phase (right) for the y-axis of 3 gyroscopes.

Scale factors and biases are highly correlated which can be seen in their temporal evolution. Indeed, a change in the bias (FIG. 5.3, right) causes a change of the scale factor (FIG. 5.4). Moreover, they seem to be correlated between MEMS-IMU sensors, i.e. the accelerometer biases of all 3 sensors increase during trial #5. This emphasizes the difficulty to separate biases and scale factors with statistical significance. Thus, the results of the accelerometer scale factors have to be interpreted with caution.

Considering the standard deviations of the gyroscope biases, the difference between the biases adjusted during the static initialization and during the dynamic portion is statistically irrelevant (TAB. 5.2). Unlike the accelerometer biases, the gyroscope biases converge to stable values with increasing experiment duration (FIG. 5.5, right). Moreover, the gyroscope scale factors vary much less between the trials than the accelerometer biases (FIG. 5.6). This may be explained by the observability of the gyroscope biases which is better than the observability of the accelerometer biases [227]. Furthermore, the sensor's temperature increases at the beginning of the experiment and becomes constant towards the end.

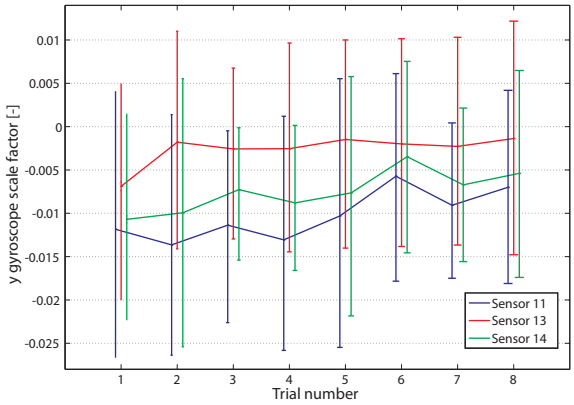

FIG. 5.6: Scale factors and standard deviations (1σ) observed for the y-axis of 3 gyroscopes.

5.3.4 Relevance to Kalman Filtering

The biases deduced from the raw static signals are now compared to those estimated by the EKF during the GPS/INS integration (FIG. 5.7). The comparison to their respective standard deviations shows that the obtained differences are statistically insignificant.

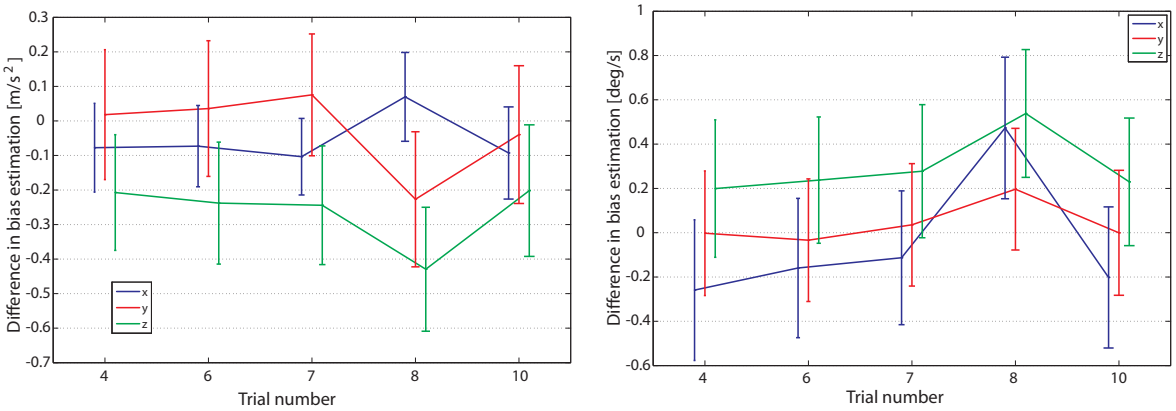

FIG. 5.7: Difference between the accelerometer (left) and gyroscope (right) biases estimated with the GPS/INS integration and those deduced from the raw data comparison during the run (MEMS sensor #1). The error bar indicates the standard deviation of the difference (1σ).

FIG. 5.7 shows that the biases estimated from the comparison of the raw signals are equivalent to those estimated by the GPS/INS integration based on EKF. However, which parameters provide the best navigation performance (position, velocity, orientation)? Would it be preferable to employ calibrated biases or scale factors? To answer these questions, the estimated biases and accelerometer scale factors obtained from the comparison to the reference signals were then fed back to the EKF. Either the biases estimated by the EKF or the calibrated biases from the raw data comparison were applied. The accelerometer scale factors were alternatively applied to the raw measurements. TAB. 5.3 illustrates the performance of the EKF

for one representative downhill run. Correcting the specific force measurements with the adjusted scale factors impacts the results only negligibly. The differences turn out to be below centimeter-level and of a few hundredths of a degree for the orientation. When applying the calibrated biases instead of estimating them with the EKF, the results are worse. Nevertheless, the differences are small (at the centimeter level and of the order of a few tenth of a degree) and therefore it can be claimed that the biases estimated by the EKF and those deduced from the comparison to the reference measurements are coherent. As listed in Tab. 5.3, applying the calibrated accelerometer scale factors does not improve the navigation quality. This is most likely due to the large correlation with the estimated biases. Hence, extending the MEMS error model by constant scale factors does not lead to improved navigation performance of the integrated system in the context of this application (downhill skiing).

Tab. 5.3: Accuracy of position and orientation as function of the applied biases and scale factors (run #10).

Estimate bias by GPS/INS integration		Yes	Yes	No	No
Apply calibrated biases		No	No	Yes	Yes
Apply calibrated accelerometer scale factors		No	Yes	No	Yes
RMSE	N [m]	0.36	0.35	0.46	0.46
	E [m]	0.39	0.39	0.45	0.45
	h [m]	0.42	0.43	1.36	1.36
	rl [deg]	0.87	0.95	2.67	2.68
	pt [deg]	0.56	0.53	3.95	3.92
	hd [deg]	0.70	0.91	1.11	1.10

5.4 Investigation of more Complex Error Models

The previous investigation showed that the simplified inertial error model was able to determine correctly the sensor biases. Furthermore, it was shown that other error terms (e.g. scale factors) could not be estimated at a statistically significant level. On the other hand, independent research with higher-grade IMUs [113, 112] indicated that more sophisticated error models, e.g. ARMA processes (Auto-Regressive and Moving Average), provided superior performance than that based on GM processes. Hence, it remains to be seen whether additional modeling might also bring benefits in the case of MEMS-type IMUs. For this reason, the MEMS-IMU signals were analyzed together with the reference signals based on Artificial Neural Networks (ANN).

An ANN was set up with a "log-sigmoid" activation function and a network configuration 1-4-4-1 (Fig. 5.8, [77, 232]). The network was trained for a MEMS-type IMU by means of reference inertial measurements presented in section 4.1 [63]. After training, the ANN was applied to the subsequent MEMS-IMU signals of the same downhill run. For the purpose of comparison, the MEMS-IMU signals were also corrected for a constant bias. Fig. 5.9 illustrates the residual measurement error of f_x computed with both modeling approaches. The RMSE and the standard deviation of the two solutions were computed and compared. Tab. 5.4 summarizes the improvement of the RMSE and its standard deviation when modeling the signal with ANN instead of subtracting a constant bias.

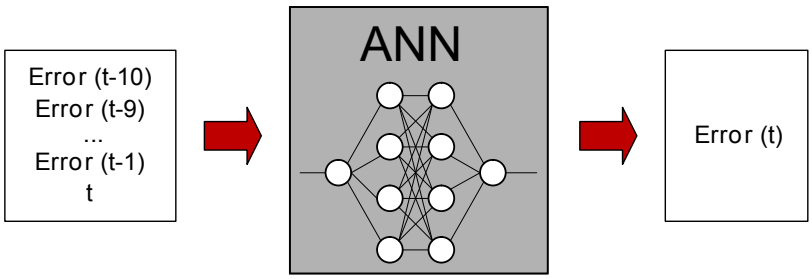

FIG. 5.8: ANN employed for inertial error estimation.

The RMSE does not show any systematic improvement. The average RMSE improves by 3% for trail #11, but worsens for trail #9 and #10 (-14% and -23%). On the other hand, the reduction of the standard deviation ($10 - 18\%$) indicates that the ANN is able to model part of the remaining systematic error in the MEMS-IMU data. Indeed, the presence of random walks is confirmed by the autocorrelation plots of the MEMS gyroscopes in FIG. 6.9.

TAB. 5.4: Error model improvement with ANN.

	Trial #9		Trial #10		Trial #11	
	RMSE	σ	RMSE	σ	RMSE	σ
f_x	-3%	-1%	-10%	-3%	-23%	-1%
f_y	52%	-26%	19%	19%	31%	-22%
f_z	-6%	-5%	-34%	-1%	-30%	-2%
ω_x	11%	-12%	23%	-17%	-34%	-15%
ω_y	-59%	-15%	61%	-18%	9%	-18%
ω_z	90%	-48%	79%	-42%	32%	-46%
Average	14%	-18%	23%	-10%	-3%	-17%

Based on this investigation, it would be premature, however, to conclude that more complex error models (like ANN) improve the error modeling for this particular application. Firstly, the ANN was trained with reference inertial signals which would not be available normally. It is questionable whether the ANN could be trained with the same efficiency with GPS observations. Indeed, section 5.3 has unveiled the difficulty to decorrelate the different error contributions in such a case. Secondly, when applying the parameters of the ANN to other runs, the signals were significantly deteriorated. This confirms the limitation of the ANN in cases where the systematic effects vary by their nature or due to the dynamics and environmental conditions (section 3.4.2).

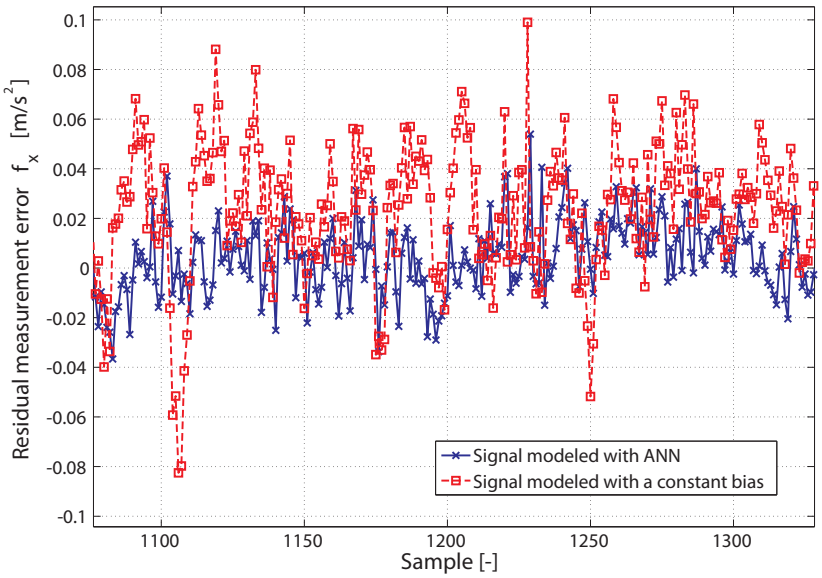

FIG. 5.9: Measurement errors after application of the ANN and the constant bias.

Chapter 6

Performance Improvement through Redundant IMUs

The investigations described previously reveal position accuracies ranging from few *cm* to half-meter accuracy depending on the quality of the employed GPS receiver. However, velocity and orientation accuracies have shown to be less sensitive to the quality of GPS observables. Hence, to improve the quality of these parameters, two possibilities can be envisaged: The first alternative consists of the integration of higher-grade IMUs which is impractical for sport applications (chapter 2). The second possibility targets at improving the navigation performance employing redundant sensors. While using redundant GPS receivers would not reduce the system's limitations inherent to satellite navigation (section 2.2.2), using redundant MEMS-IMU seems to be an ergonomically and economically viable alternative. Indeed, these devices can be highly miniaturized and hence it is possible to exploit numerous MEMS-IMU sensors for enhancing the navigation performance.

The IMU redundancy can improve the GPS/INS integration performance on several levels. Firstly, noise estimation can be achieved directly from the data and the stochastic parameters are hence closer to reality. Secondly, the noise level can be reduced and defective sensors, spurious signals and sensor malfunctioning can be detected and isolated. Furthermore, sensor error calibration (and hence orientation estimation) becomes conceivable even during uniform motion or static initialization. Due to the improved navigation accuracy, redundant IMUs bridge the gaps in the GPS data more effectively. Finally, more accurate orientation determination is expected with redundant IMU configurations.

Redundancy in inertial navigation has been investigated with higher-order IMUs [21]. Several authors have presented results for simulations and emulations, as well as theoretical derivations for MEMS-IMU, but - to the author's knowledge - the first experimental results using MEMS-type sensors have been openly published by [217, 6]. Based on simulations and theoretical derivations, reference [188] has found an accuracy improvement of 33% with MEMS-IMUs placed on a tetrahedron. Emulations with MEMS-SRIMU presented by [128] resulted in performance improvements of $20 - 34\%$.

The first part of this chapter presents the theoretical basis of IMU redundancy. It covers geometrical considerations about the spatial configurations of inertial sensors, as well as the theoretical basis of noise reduction achieved with sensor redundancy. Then, it presents an

algorithm that estimates the evolution of noise level during the processing. Furthermore, algorithms for the estimation of inertial sensor errors and the orientation during static initialization are introduced. In addition, the most commonly used Fault Detection and Isolation (FDI) algorithm, the parity space method, is tested. Finally, three algorithmic options for the integration of GPS data with redundant MEMS-IMUs are discussed. The second part of this chapter assesses the performance of the first two algorithms based on simulations and controlled experiments in skiing (orthogonally-redundant IMUs) and motorcycling (skew-redundant IMUs).

6.1 INS Redundancy Approaches in Inertial Navigation

Fig. 6.1 and Fig. 6.2 summarize different levels on which redundancy can be generated in inertial navigation [3].

- Redundancy at system level: Several GPS/INS components are formed and processed individually. Fault detection is applied on the resulting navigation solutions.

Fig. 6.1: Redundancy at system level.

- Redundancy on IMU or multi-IMU level. In the first geometry, individual IMUs are processed together or individually. Fault detection algorithms can be used before or after the navigation processing. In the second configuration, a multi-IMU sensor (e.g. SRIMU) is processed in one or multiple navigation processors. Fault detection is generally performed before the navigation process.

Fig. 6.2: Redundancy on IMU level (left) and on multi-IMU level (right).

System redundancy is not attractive for the sports application in terms of cost and size. However, inertial sensor redundancy can reduce measurement noise and improve navigation accuracy. Therefore, this research will focus on noise level estimation, detection and isolation of spurious signals or defective sensors. Finally, two geometries for IMU sensor redundancy will be highlighted (orthogonally and skew-redundant IMU).

6.2 Geometrical Arrangement of Redundant IMUs

Redundant IMUs have been used since early days of inertial technologies in safety critical operations such as in the control of civil, military or space aircrafts. Such applications require sensor redundancy to create fault-tolerant systems which are able to detect and isolate faulty sensors (i.e. FDI). If two sensors are placed collinear to each other, it is possible to detect a fault that occurs in either one of the sensors. To isolate the erroneous device at least three sensors are required. Traditionally, nine sensors were used in a three-dimensional system (three per axis).

Theoretically, any geometrical combination of inertial sensors is possible. In 1974, reference [185] proposed a first theory to optimally position any number of sensors. It also proved that less than nine sensors (four in theory) were required to isolate faults in a three-dimensional space. This theory essentially considers two situations: firstly, when sensors are equally spaced on a cone of half-angle α and, secondly, when one sensor is placed along the central cone axis while the remaining sensors are positioned equally around a cone of half-angle α. The optimal half-angle α corresponds to the configuration in which the variance is minimized (Fig. 6.3). Other configurations that have been considered are based on platonic solids [188]. Information filter [188] or the method of partial redundancies [64] can be applied to determine the optimal angle α as a function of the number and quality of sensors.

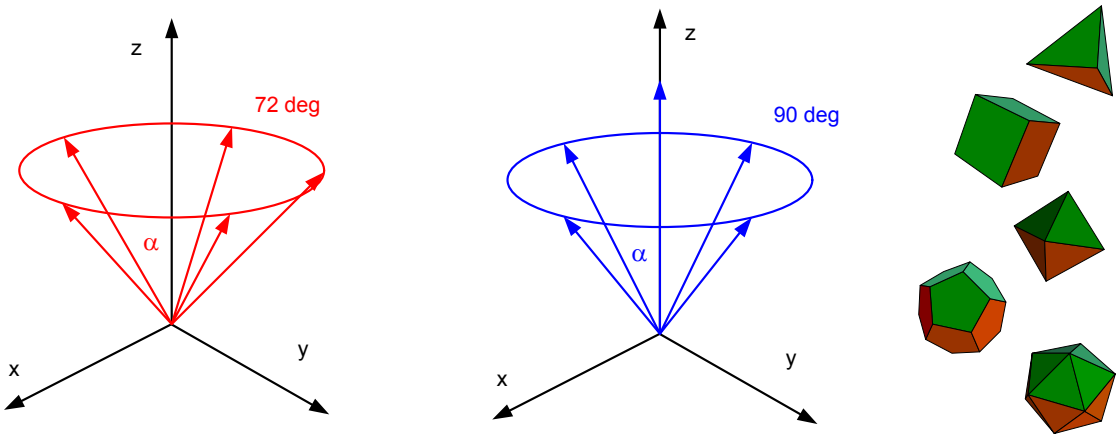

Fig. 6.3: Inertial sensors placed on a cone (left), on a cone and its axis (center) and platonic solids (right).

In practice, however, triads of MEMS-IMU sensors are available for modest cost. Hence, two configurations for redundant IMUs can be considered (Fig. 6.4):

- Orthogonally redundant IMUs.
- Skew redundant IMUs (SRIMUs).

Skew-redundant IMUs (SRIMUs) are composed of a redundant number of inertial sensors that are arranged according to a well-defined geometry [128, 185, 134]. Intuitively, they have

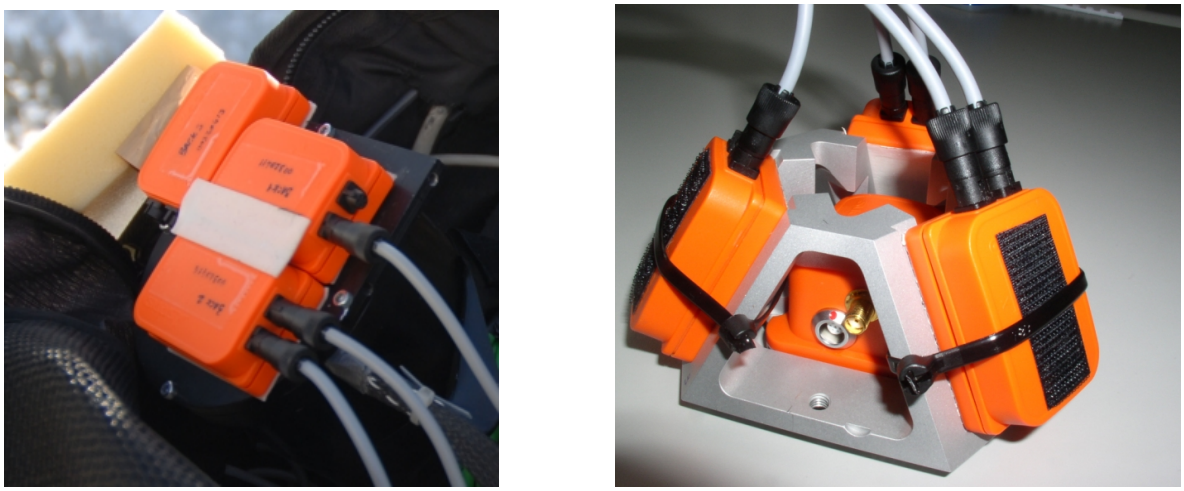

FIG. 6.4: Orthogonally-redundant (left) and skew-redundant IMUs (right).

a higher information volume and are thus preferable. Indeed, this strategy was adopted in [21, 188]. However, as far as sensor triads are employed, the orientation between triads is irrelevant with respect to the optimality of the information content [64]. Nonetheless, a sensor failure alters this conclusion and the triads' relative orientation becomes important. Therefore, the cone setup and the approach employing platonic solids are considered. The cone approach presents the advantage that the amount of redundancy of the vertical axis can be varied with respect to the redundancy of the horizontal plane by changing the cone's half-angle. This is an interesting option when IMUs are used together with GPS, because the vertical performance is reduced by a factor $2-3$ with respect to the horizontal plane due to the satellite geometry. However, the motion of athletes is complex and involves large rotations around all axes. Hence, the approach using platonic solids, e.g. a tetrahedron, seems to be appropriate.

6.3 Noise Reduction and Direct Noise Estimation

Combinations of redundant inertial sensors not only lower the measurement noise, but also offer the possibility to estimate its level during the processing with the help of adaptive filters. Indeed, the noise figures can evolve during the processing and adapt to particular situations (e.g. increased vibrations).

6.3.1 Noise Reduction

From n independent measurements $x_1, ..., x_n$ (with their respective variances $\sigma_{x1}, ..., \sigma_{xn}$), their best estimate $\hat{x}$ can be computed. Assuming homogeneous measurements (constant σ_{xi}), its variance $\sigma_{\hat{x}}$ can be derived as [235, 191]:

$$\sigma_{\hat{x}} = \sqrt{\sum_{i=1}^{n} w_i^2 \cdot \sigma_i} = \frac{\sigma_{xi}}{\sqrt{n}} \tag{6.3.1}$$

where the w_i are weighting factors.

According to equation 6.3.1, the noise affecting the best estimate $\hat{x}$ derived from measurements of 4 MEMS-IMU is supposed to be 2 times lower than the noise of the individual MEMS-IMU. Hence, the expected noise reduction for such configuration is of 50%.

Such theoretical reduction of the noise was verified by comparing the differences between the MEMS-IMU measurements and their best estimate to the reference measurements provided by a tactical-grade IMU (*LN200*). Thereafter, a parametric compensation was performed to remove systematic errors. Thus, the remaining differences were considered to be composed of white noise only. The averaged noise of the 4 MEMS-IMU gyros was estimated to 0.0194 rad/s, whereas the noise level of their best estimate amounts to 0.0101 rad/s. Hence, the experimental noise reduction is of approximately 48% which confirms the validity of the theoretical model. Fig. 6.5 illustrates these results graphically.

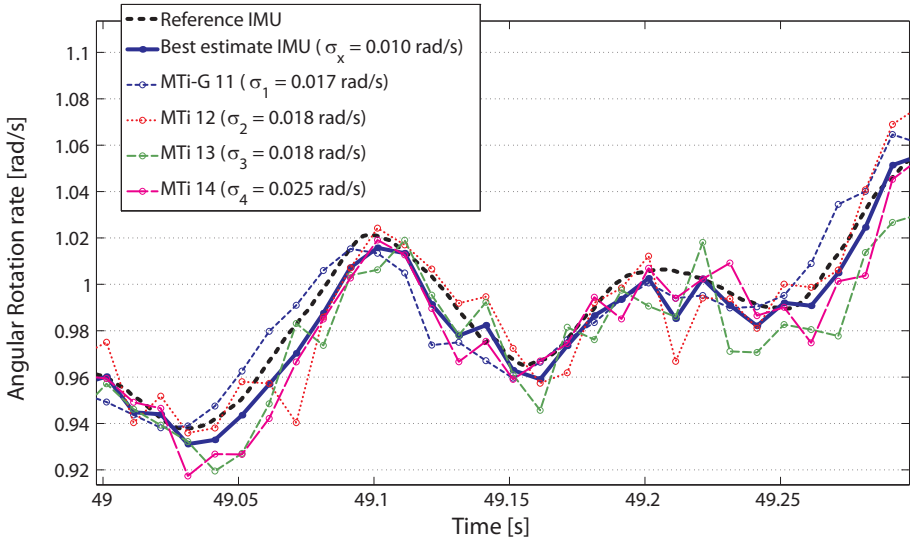

Fig. 6.5: Illustration of the angular rate measurements of 4 MEMS-IMUs in comparison to the reference measurements from a tactical-grade IMU.

6.3.2 Direct Noise Estimation

The use of multiple IMUs also offers the possibility to estimate the eventually varying noise level of the inertial data during the processing. The resulting adaptation of the stochastic parameters may improve the navigation performance and make the filter more stable. Moreover, it can improve the FDI performance which also depends on the correctness of the noise model. The algorithm proposed in this research is designed for a system setup composed of triads of inertial sensors and is presented in Appendix E.0.4. The reference noise level was estimated using the data of the tactical-grade IMU. The results are presented in Fig. 6.6. Hence, the algorithm provides results that are comparable to those obtained from the reference signal. It allows adapting the stochastic model of the KF during the processing.

The impact of correct noise estimation is further investigated by comparing the results of the GPS/INS integration with and without noise estimation. The orientation errors are slightly

reduced, approximatively 3% [64]. The other navigation states are only negligibly affected. However, the noise reduction might provide larger benefits when the noise level is expected to vary to a greater extent or when the noise-level input to the EKF substantially differs from reality. Furthermore, direct noise estimation reduces user interaction and user knowledge which is important which facilitates the automation of the processing. In addition, noise variations (especially from MEMS accelerometers, section 5.1) can be determined on-line.

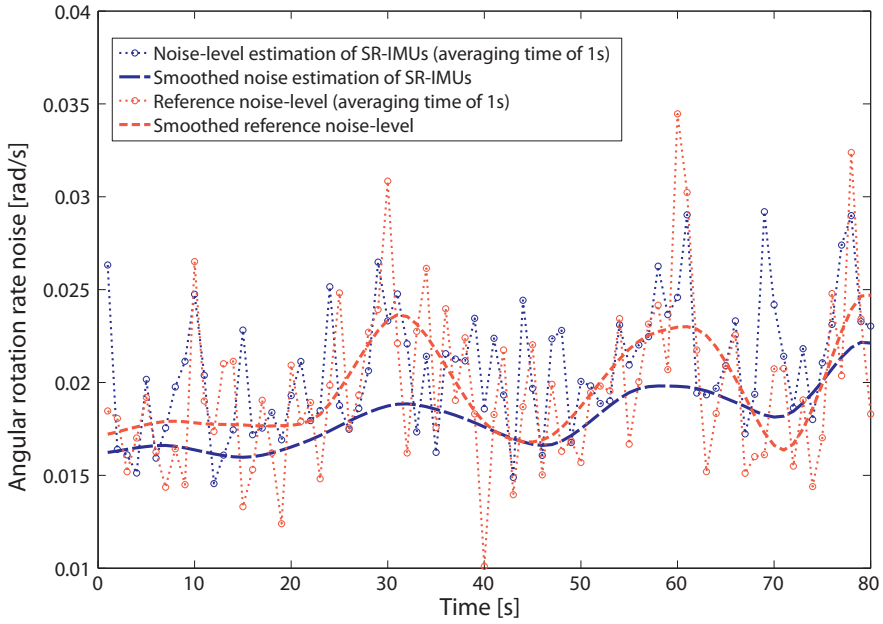

FIG. 6.6: Comparison between the noise-level estimates using SR-IMUs and the noise-level determined with the reference signals for a selected portion of the experiment.

6.4 Fault Detection and Isolation

FDI algorithms for inertial navigation were thoroughly investigated in the past. The most commonly used approach is the parity space method [61, 188, 48, 49, 185, 104], but other approaches such as artificial neural networks have also been examined [89]. The complexity of implementation of an efficient FDI system is increased when using MEMS-type IMUs. Indeed, their poor performance (i.e. noise density variations, large systematic measurement errors compared to the random errors) often creates false alarms as well as an increases the possibility of misdetection of faulty measurements [188]. In this non-safety critical application, the parity space method with MEMS-IMUs is investigated in the scope of increasing the navigation performance (e.g. prevention of gross errors, improving filter stability). The detailed algorithm is based on references [185, 64].

Decision Variable

The method performs composite statistical tests. Indeed, the fault detection can be viewed as a choice between two hypotheses concerning the absence or the presence of erroneous

measurements. The hypothesis test is based on a decision variable D that is compared to a threshold variable T. The decision variable D is computed as follows [185]:

$$\mathbf{v} = [\mathbf{I_M} - \mathbf{A} \cdot (\mathbf{A}^T \cdot \mathbf{A})^{-1} \cdot \mathbf{A}^T] \cdot \mathbf{z} \quad (6.4.1)$$

$$D = \mathbf{v}^T \cdot \mathbf{v} \quad (6.4.2)$$

where M is the number of measurements ($M = 12$ in the case of 4 sensor triads), $N = 3$ is the number of independent parameters, $\mathbf{A}$ the matrix which transforms the state space to the measurement space (equation 6.5.4), $\mathbf{z}$ represents the vector of measurements and $\mathbf{v}$ the residuals of the least squares adjustment.

Assessment of the Threshold

The threshold T can be obtained from:

$$T(p_{FA}, r, \sigma_n^2) = \sigma_n^2 \cdot Q^{-1}(p_{FA}|r) \quad (6.4.3)$$

where p_{FA} is the probability of false alarm, $r = M - N$ is the redundancy, $Q^{-1}(\chi^2|r) = 1 - P(\chi^2|r)$, $P(\chi^2|r)$ is the chi-square probability function, and σ_n^2 is the measurement noise level estimated by the previously discussed algorithm (0.1 rad/s/$\sqrt{\text{Hz}}$). Assuming a probability of false alarm of 5% ($p_{FA} = 0.05$), the threshold values for our system is $T_{0.05}(p_{FA} = 0.05) = 0.0155$ rad^2/s^2.

Now, the theoretical threshold is compared to an optimized threshold that minimizes the sum of the probability of false alarm and that of misdetection [42] while taking into account the reference measurements provided by the tactical-grade IMU. Assuming that all measurements with a difference exceeding a threshold of 3.5 σ_{diff} (variance of the difference vectors) are erroneous, the value of T is computed that minimizes the sum of false alarms and misdetections ($T = 0.0156$ rad^2/s^2). Thus, the theoretical threshold values computed with the parity space method and the empirical best threshold value are of the same order of magnitude.

Experimental Analysis

Fig. 6.7 presents the values of D and T and indicates when fault and correct measurements are detected successfully as well as the occurrence of misdetections and false alarms. The figure illustrates the difficulty of finding a good threshold value. Indeed, even with the best possible T value, approximately 76% of the faults are not detected. The Stanford plot in Fig. 6.8 highlights the important number of false alarms; the false-alarm-to-fault ratio is roughly 35%. The performance of the test is $1 - (p_{FA} + p_{MD}) = 96.4\%$. Regarding the performance of the isolation algorithm, 74.4% of faults are correctly isolated (Fig. 6.7). Considering a second threshold $T(p_{FA} = 0.01)$, an overall performance of 95.8% is reached.

Before applying the parity space method, the Gaussian assumption needs to be verified. Comparing the MEMS-IMU measurements to the reference measurements reveals quasi-Gaussian distribution (Fig. 6.9, [217]). However, the autocorrelation plots of the MEMS gyroscopes

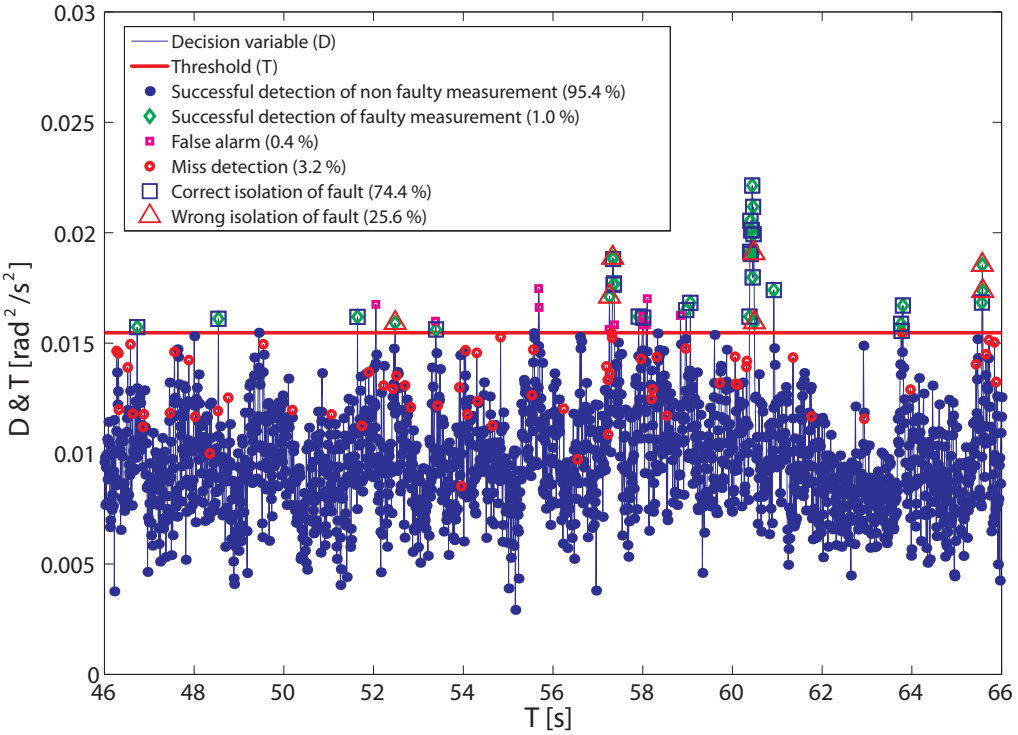

FIG. 6.7: Estimation of the best threshold for FDI and fault isolation.

reveal that a large proportion of the non-faulty noise measurement are composed of colored noise (FIG. 6.10). Indeed, the autocorrelations suggest that the errors are mainly composed of white noise and of random walk. Hence, the assumption of strictly Gaussian white noise errors in the parity space approach is not valid with MEMS-IMUs.

The presented investigation unveils the need for a more complex FDI model. One possibility would be to obtain a realistic T by training an artificial neural network with a large number of real or emulated measurements in which faults occurs frequently. Nevertheless, employing the FDI approach is considered a valuable addition to detect gross errors, enhance navigation performance and improve the EKF stability. As shown, the parity space method is capable of isolating an important part of the measurement errors and hence partially fulfills this objective.

6.5 System and Observation Model for the Redundant IMU Integration

The following sections review three mechanizations approaches described by [21]. Firstly, the inertial measurements are combined within the observation space to generate a synthetic set of observations that are then integrated by the standard GPS/INS algorithm. In the second approach, the mechanization equations are adapted to account for the redundant measure-

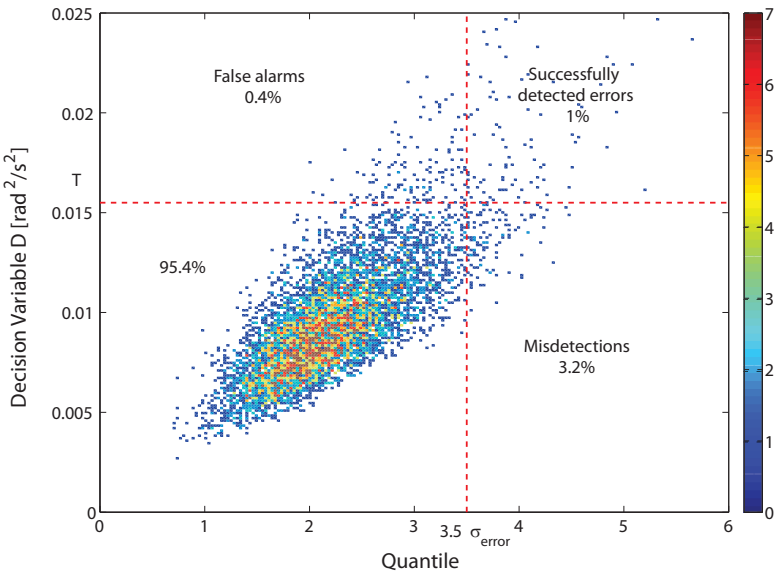

FIG. 6.8: Evaluation of the FDI performance ($p_{FA} = 5\%$).

ments. The third algorithm imposes geometrical constraints between the inertial sensors at the update stage.

6.5.1 Synthetic IMU Integration

In this approach, the redundant IMU data is merged into a synthetic set of measurements before being introduced to the GPS/INS algorithm based on the single IMU mechanization (FIG. 6.11). While fusing the IMU data, defective sensors can be detected and realistic noise and covariance terms can be estimated [21]. However, the "compound" biases estimated by the EKF cannot be back-projected to the individual sensors.

In a first step, synthetic measurements $\boldsymbol{\omega}^b$, $\mathbf{f}^b$ and $\mathbf{m}^b$ need to be generated from the individual measurements $\boldsymbol{\ell}_\omega^b$, $\boldsymbol{\ell}_f^b$ and $\boldsymbol{\ell}_m^b$.

$$\begin{aligned} \boldsymbol{\omega}^b &= \boldsymbol{\Pi}_\omega \, \boldsymbol{\ell}_\omega^b \\ \mathbf{f}^b &= \boldsymbol{\Pi}_f \, \boldsymbol{\ell}_f^b \\ \mathbf{m}^b &= \boldsymbol{\Pi}_m \, \boldsymbol{\ell}_m^b \end{aligned} \tag{6.5.1}$$

The above relation requires estimating the orthogonal projectors $\boldsymbol{\Pi}_\ell$ for the angular rates, $\boldsymbol{\Pi}_f$ for the linear accelerations and $\boldsymbol{\Pi}_m$ for the magnetic measurements.

$$\begin{aligned} \boldsymbol{\Pi}_\omega &= (\mathbf{A}_\omega^T \, \mathbf{P}_{\ell_\omega^b \boldsymbol{\ell}_\omega^b} \, \mathbf{A}_\omega)^{-1} \, \mathbf{A}_\omega^T \, \mathbf{P}_{\ell_\omega^b \boldsymbol{\ell}_\omega^b} \\ \boldsymbol{\Pi}_f &= (\mathbf{A}_f^T \, \mathbf{P}_{\ell_f^b \boldsymbol{\ell}_f^b} \, \mathbf{A}_f)^{-1} \, \mathbf{A}_f^T \, \mathbf{P}_{\ell_f^b \boldsymbol{\ell}_f^b} \\ \boldsymbol{\Pi}_m &= (\mathbf{A}_m^T \, \mathbf{P}_{\ell_m^b \boldsymbol{\ell}_m^b} \, \mathbf{A}_m)^{-1} \, \mathbf{A}_m^T \, \mathbf{P}_{\ell_m^b \boldsymbol{\ell}_m^b} \end{aligned} \tag{6.5.2}$$

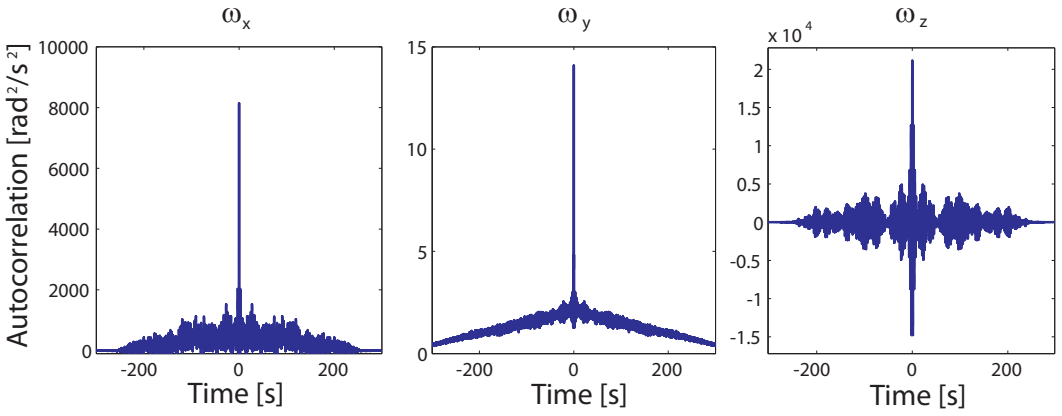

FIG. 6.9: Autocorrelation of errors of the MEMS gyros.

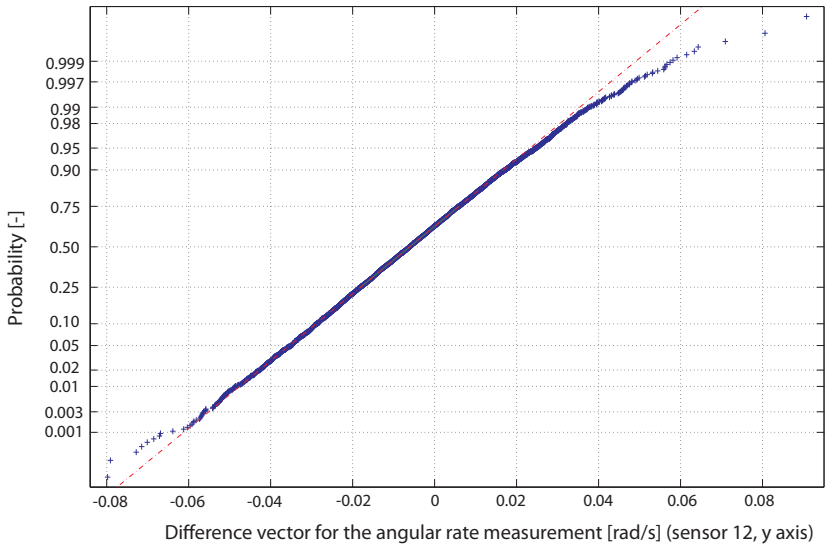

FIG. 6.10: Graphical assessment of the normality of the difference vector.

and their accuracy:

$$\begin{aligned}\mathbf{P}_{\omega^b\omega^b} &= \mathbf{A}_\omega^T\, \mathbf{P}_{\ell_\omega^b \ell_\omega^b}\, \mathbf{A}_\omega \\ \mathbf{P}_{f^b f^b} &= \mathbf{A}_f^T\, \mathbf{P}_{\ell_f^b \ell_f^b}\, \mathbf{A}_f \\ \mathbf{P}_{m^b m^b} &= \mathbf{A}_m^T\, \mathbf{P}_{\ell_m^b \ell_m^b}\, \mathbf{A}_m\end{aligned} \tag{6.5.3}$$

$\mathbf{A}_\omega$, $\mathbf{A}_f$ and $\mathbf{A}_m$ matrices transform the data from the actual sensor axes to the three orthogonal axes of the predefined body frame b. Their rows contain the direction cosine vectors of the angular rate sensor and accelerometer axes.

$$\mathbf{A}_\omega = \begin{bmatrix} \mathbf{R}_b^{b\omega 1} \\ \dots \\ \mathbf{R}_b^{b\omega i} \\ \dots \\ \mathbf{R}_b^{b\omega n} \end{bmatrix} \qquad \mathbf{A}_f = \begin{bmatrix} \mathbf{R}_b^{bf1} \\ \dots \\ \mathbf{R}_b^{bfi} \\ \dots \\ \mathbf{R}_b^{bfn} \end{bmatrix} \qquad \mathbf{A}_m = \begin{bmatrix} \mathbf{R}_b^{bm1} \\ \dots \\ \mathbf{R}_b^{bmi} \\ \dots \\ \mathbf{R}_b^{bmn} \end{bmatrix} \tag{6.5.4}$$

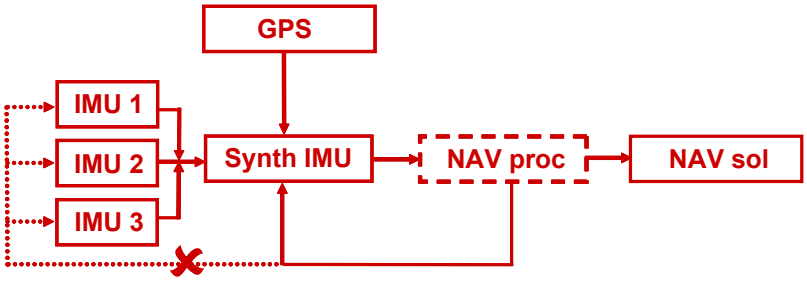

FIG. 6.11: Principle of mechanization based on a synthetic IMU.

$\mathbf{R}_b^{bi}$ is given by:

$$\mathbf{R}_{bi}^{b} = \mathbf{R}_3(\psi) \cdot \mathbf{R}_2(-\theta) \tag{6.5.5}$$

6.5.2 Extended IMU Mechanization

Similar to the synthetic approach, the extended mechanization also allows detecting defective sensors and estimating noise and covariance terms (FIG. 6.12). Moreover, this method permits modeling and estimation of the systematic errors separately for each sensor. However, pursuing this methodology requires the modification of GPS/INS software to accommodate the new expression of the mechanization equations.

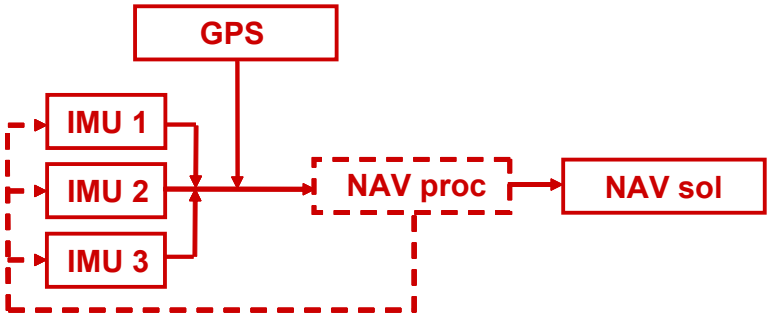

FIG. 6.12: Principle of mechanization based on an extended IMU mechanization.

To estimate individual sensor errors, the strapdown navigation equations C.1.7-C.1.20 need to be reviewed accordingly [21]. The velocity error model thus becomes:

$$\dot{\mathbf{v}}^n = \mathbf{\Pi}_f \mathbf{R}_b^n \boldsymbol{\ell}_f^b - (\boldsymbol{\omega}_{in}^n + \boldsymbol{\omega}_{ie}^n) \times \mathbf{v}^n + \mathbf{g}^n \tag{6.5.6}$$

where $\mathbf{\Pi}_f$ is defined by equation 6.5.2. The orientation error model is derived after modification of equation C.1.18.

$$\hat{\boldsymbol{\omega}}_{nb}^b = \mathbf{\Pi}_\omega \hat{\boldsymbol{\ell}}_\omega^b - \hat{\mathbf{R}}_n^b \hat{\boldsymbol{\omega}}_{in}^n \tag{6.5.7}$$

After differentiation, this leads to generalizations of equations C.1.13-C.1.20:

$$\begin{aligned}\delta\dot{\mathbf{v}}^n &= -(\mathbf{R}_b^n\mathbf{\Pi}_f\boldsymbol{\ell}_f^b)\times\boldsymbol{\epsilon}^n + \mathbf{R}_b^n\mathbf{\Pi}_f\delta\boldsymbol{\ell}_f^b - (\boldsymbol{\omega}_{in}^n+\boldsymbol{\omega}_{ie}^n)\times\delta\mathbf{v}^n - (\delta\boldsymbol{\omega}_{in}^n+\delta\boldsymbol{\omega}_{ie}^n)\times\mathbf{v}^n + \delta\mathbf{g}^n \\ \dot{\boldsymbol{\epsilon}}^n &= \mathbf{R}_b^n\mathbf{\Pi}_\omega\delta\boldsymbol{\ell}_\omega^b - \delta\boldsymbol{\omega}_{in}^n - \boldsymbol{\omega}_{in}^n\times\boldsymbol{\epsilon}^n\end{aligned} \tag{6.5.8}$$

The derivation of the system and observation model for the EKF is presented in Appendix E.0.5.

6.5.3 Geometrically-Constrained Mechanization

As for the extended mechanization, the geometrically constrained mechanization allows estimating the individual sensor errors. In this approach, multiple navigation solutions are computed (one for each IMU) and compared at regular time intervals (Fig. 6.13). This is, however, at the cost of increased computational effort and important modifications of the GPS/INS software. Furthermore, defective sensors can be detected and realistic noise terms estimated only if the constraints are imposed after each integration step.

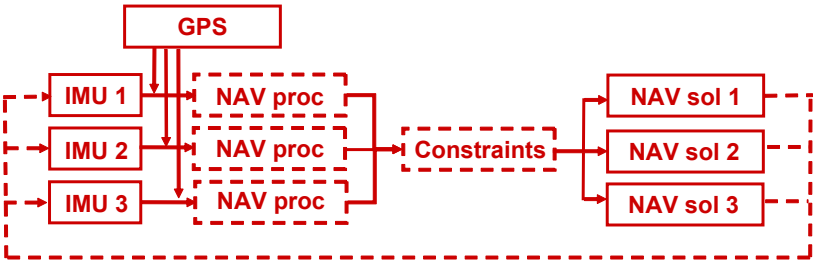

Fig. 6.13: Principle of mechanization based on a geometrically-constrained IMU mechanization.

Consider that two IMUs are employed. Both units are integrated using the standard IMU mechanization. The relative orientation between them (i.e. the relative orientation $\mathbf{R}_{b1}^{b2}$ and the lever arm $\mathbf{o}_{b1}^{b2}$) can be modeled and estimated as random constants supposing their direct determination is not sufficiently accurate [21].

$$\begin{aligned}\dot{\mathbf{R}}_{b1}^{b2} &= \mathbf{0_{3\times3}} \\ \dot{\mathbf{o}}_{b1}^{b2} &= \mathbf{0_{3\times1}}\end{aligned} \tag{6.5.9}$$

At predefined stages, the following observations can be added with a high weight.

$$\begin{aligned}\mathbf{R}_{b1}^n &= \mathbf{R}_{b2}^n\mathbf{R}_{b1}^{b2} \\ \mathbf{r}_1^n &= \mathbf{r}_2^n - \mathbf{R}_{b1}^n\mathbf{o}_{b2}^{b1} \\ \mathbf{v}_1^n &= \mathbf{v}_2^n - \mathbf{R}_{b1}^n\cdot(\mathbf{\Omega}_{ni}^{b1}+\mathbf{\Omega}_{ib}^{b1}+\mathbf{\Omega}^{b1}(\mathbf{b}_\omega))\cdot\mathbf{o}_{b2}^{b1}\end{aligned} \tag{6.5.10}$$

6.6 Navigation Performance Improvement

6.6.1 Algorithm Selection

The derivation of a synthetic IMU is the most straightforward approach as it does not require any modification of the standard GPS/INS algorithm. Unlike the extended and geometrically-constrained method, this approach does not allow to feedback sensor errors, which might yield less optimal navigation performance. On the other hand, the IMU error model investigation in chapter 5 has reported that the MEMS-IMU biases are relatively stable for the short trajectories encountered in some sports (e.g. lap, downhill). Furthermore, the same investigation has pointed out that the simplified error model was suitable for the considered application and sensors. The geometrically-constrained approach represents an interesting option for system calibration if the relative sensor geometry is insufficiently known. As mentioned, the computational effort is increased considerably compared to the first two approaches. In addition, it is more sensitive to sensor failures because defects can only be noticed at the update stage and the measurement faults can generally not be isolated.

In the sequel, the synthetic IMU approach will be compared to the approach based on extended IMU mechanization. The navigation performance improvement through the use of redundant MEMS-IMU is evaluated with experiments and orthogonally- and skew-redundant configurations. Furthermore, data sets consisting on varying numbers of IMU triads are emulated from real trajectories. The algorithms related to the emulation of the inertial measurements are presented in Appendix F.

6.6.2 Assessment Based on Experiments

Orthogonally-redundant configuration

In the skiing experiment, two redundant MEMS-IMU sensors (*Xsens MTi*) in orthogonal configuration are integrated at 100 Hz with the L1 and the L1/L2 DGPS solutions at 1 Hz (Fig. 6.4, left). The use of two MEMS-IMU reduces the noise level of the measurements by a factor of $\sqrt{2}$. In such configuration, measurement outliers can neither be detected nor identified. Nevertheless, an accuracy improvement was noticed for the orientation ($20-30\%$, Tab. 6.1) while the position and velocity states were not improved significantly. The performance improvement is similar for both integration approaches and equivalent with respect to the employment of single or dual-frequency differential processing.

Tab. 6.1: Orientation improvement with two orthogonally redundant MEMS-IMUs compared to the average performance of the single sensors.

	L1		L1/L2	
	Synthetic	Extended	Synthetic	Extended
rl	-37%	-24%	-43%	-20%
pt	-25%	-5%	-7%	8%
hd	-34%	-24%	-32%	-22%

The estimated synthetic biases represent approximately the average of the biases estimated after processing of the individual MEMS-IMUs (Fig. 6.14).

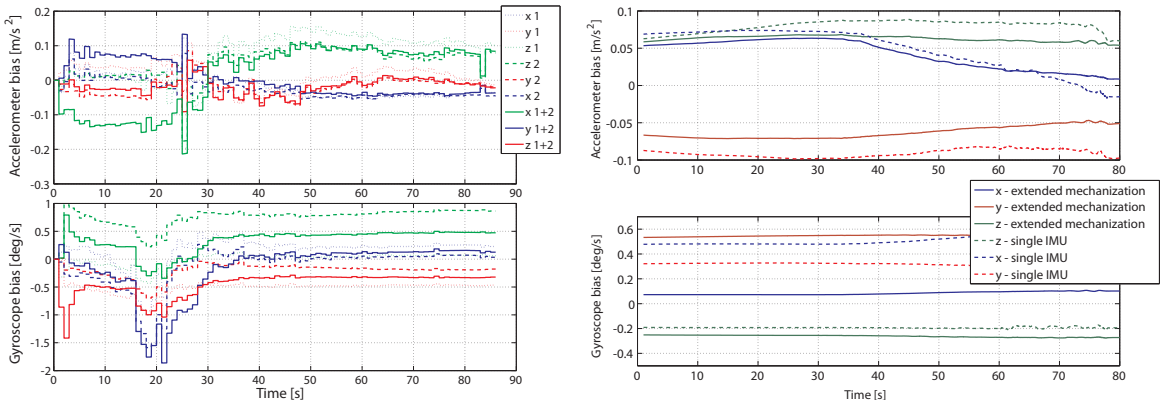

FIG. 6.14: Individually estimated biases compared to the synthetic IMU bias (left) and to the biases estimated by the extended mechanization (right).

Skew-redundant configuration

In a second experiment, a regular tetrahedron consisting of 4 MEMS-IMU was set up (FIG. 6.4, right). To investigate the performance of the multi-IMU system, it was fixed rigidly to a reference system consisting of a tactical-grade IMU (*Litton LN200*) and differential, dual-frequency GPS (*Javad Legacy*) [173]. The system was installed on a motorcycle (FIG. 6.15).

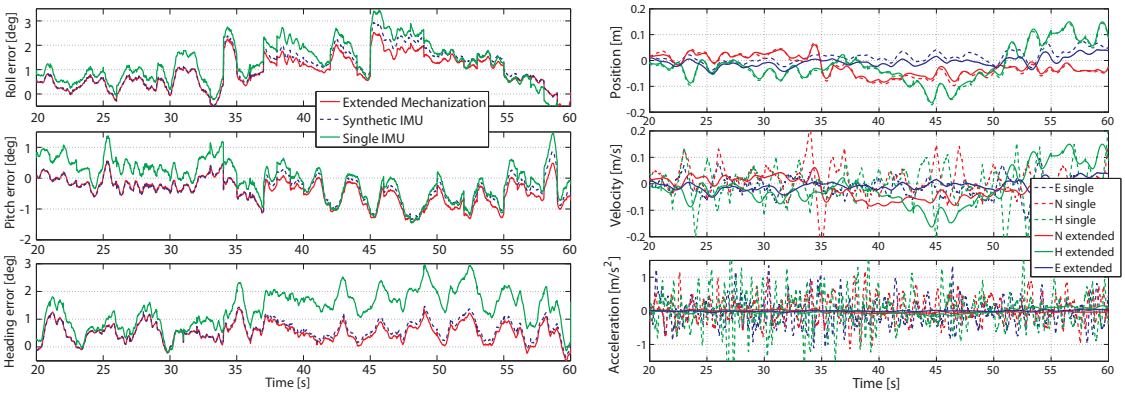

FIG. 6.15: Orientation error (left) and position, velocity and acceleration error (right) after integration of a single sensor (individual) and after extended mechanization.

As previously shown for this setup, the inertial measurement noise is reduced by a factor of 2 due to the measurement redundancy (FIG. 6.5, right). FIG. 6.16 summarizes the navigation performance of this particular GPS/MEMS-SRIMU system. The orientation accuracy of the system has now improved to less than 1deg. The experiment confirms previous findings where the velocity and orientation accuracies are almost invariant with respect to the accuracy of GPS aiding (e.g. L1 or L1/L2 differential code and carrier-phase). Furthermore, the acceleration is efficiently smoothed and improved. However, the "integrated" states (position and velocity) are less affected. The position accuracy is largely improved using dual-frequency GPS processing with ambiguity fixing, while hardly no improvement can be observed for

single-frequency GPS receivers. Indeed, the random part of the positioning error is reduced by a similar amount for single- and dual-frequency GPS processing. However, the systematic component for dual-frequency DGPS is much lower which explains the distinct accuracy enhancement.

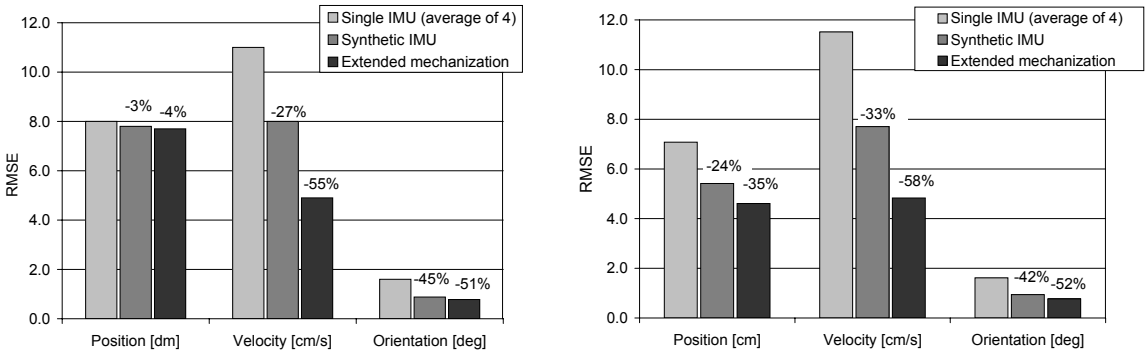

FIG. 6.16: RMSE of the tested MEMS-SRIMU system integrated with L1 DGPS (left) and L1/L2 DGPS (right).

FIG. 6.16 and TAB. 6.2 summarize the performance improvement of the GPS/MEMS-SRIMU system compared to the average accuracy of the solutions computed with the single MEMS-IMUs. An average improvement of 30% is obtained for the synthetic IMU approach. The extended mechanization performs slightly better than the synthetic approach (average improvement of 46%). This can be explained by the estimation of the individual biases and the FDI scheme that can run in parallel to the filter (rather than in cascade as in the synthetic IMU approach). However, the navigation performance is not improved by 100% as could be expected from the noise reduction. Indeed, residual correlations between the inertial measurements as well as the correlations between the filter states most likely limit the accuracy progression.

TAB. 6.2: Performance improvement of the average and maximum errors by the MEMS-SRIMUs compared to the performance of the individually integrated MEMS-IMU sensors.

RMSE		Maximum error	
Synthetic	Extended	Synthetic	Extended
-29%	-35%	-71%	-94%
-41%	-51%	-77%	-94%
-5%	-19%	-27%	-82%
-37%	-61%	-82%	-95%
-50%	-67%	-81%	-93%
-7%	-44%	-25%	-74%
-57%	-67%	-80%	-87%
-28%	-41%	-59%	-80%
-21%	-27%	-45%	-69%

TAB. 6.2 also recapitulates the performance enhancement with respect to the maximum errors. It is of 61% for the synthetic IMU approach and even more substantial for the extended

mechanization where the maximum errors are reduced by a factor of 2. FIG. 6.15 illustrates how the peaks of the orientation errors in the single MEMS-IMU/GPS integration are smoothed out by the extended mechanization.

6.6.3 Assessment Based on Emulation

In this section, a fictional system composed of one and ten MEMS-IMUs through the emulation of inertial measurements is studied. Position, velocity and orientation parameters computed with the reference system are assumed to represent the true motion, i.e. not affected by errors. The measurements are simulated along this "true" path. After adjusting the position and orientation parameters by cubic spline function, the latter are derivated with respect to time to compute specific force, angular rate and magnetic measurements (equation F.1.11). Then, the deterministic error terms assessed by parametric adjustment and the stochastic terms determined by the Allan variance method in chatper 5 are added. Finally, the emulated inertial measurements are integrated together with the dual-frequency DGPS solution. The resulting position, velocity and orientation errors are presented in FIG. 6.17 to 6.19 for both, the synthetic and extended mechanization approaches. The previously described experimental results are indicated as well.

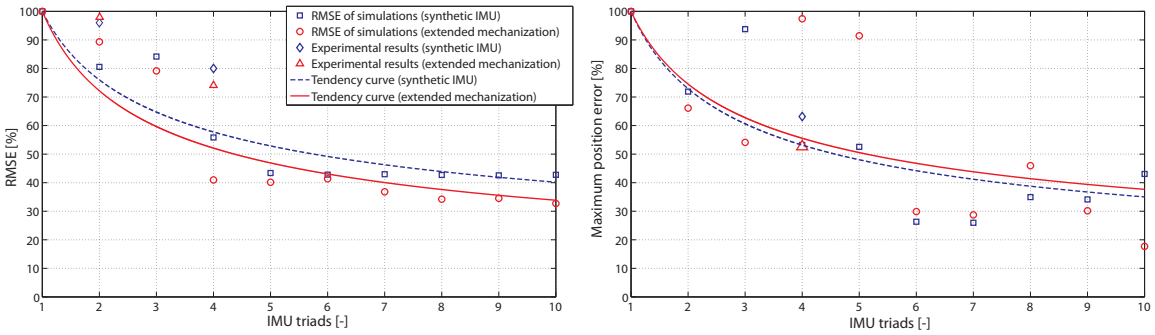

FIG. 6.17: Influence of the redundancy on the position error (left) and the maximum position error (right).

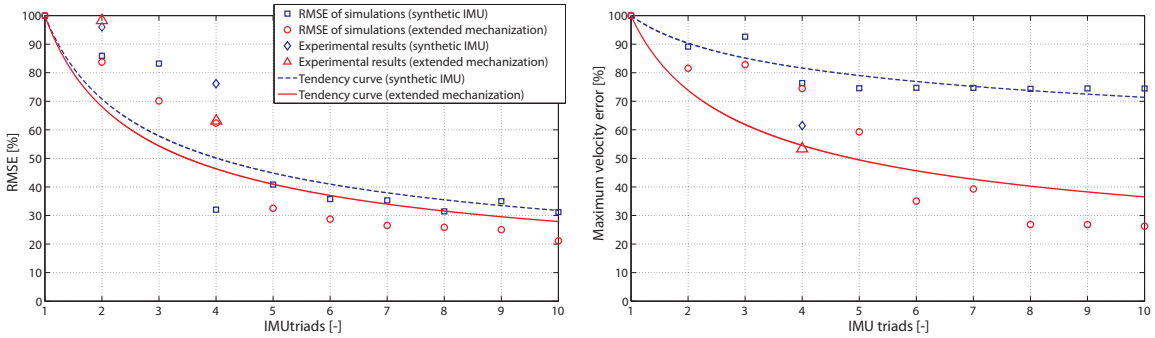

FIG. 6.18: Influence of the redundancy on the velocity error (left) and the maximum velocity error (right).

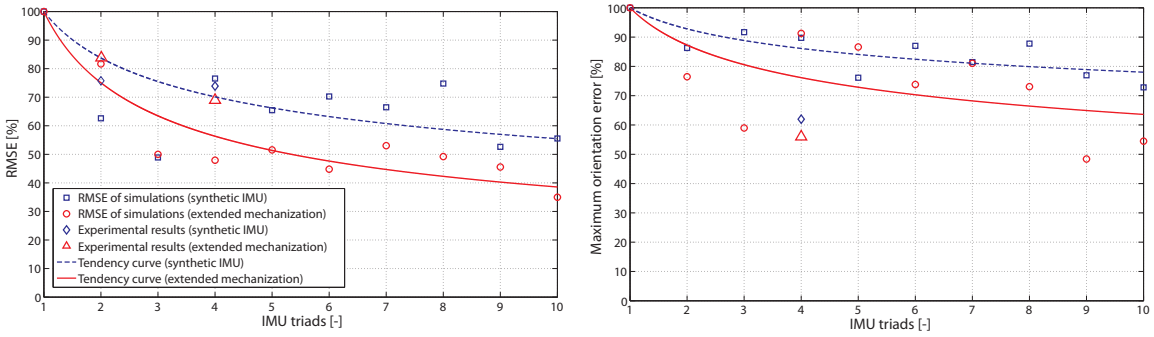

FIG. 6.19: Influence of the redundancy on the orientation error (left) and the maximum orientation error (right).

As expected, these results depict an inverse correlation between navigation errors and the number of IMUs. Furthermore, the curve tendencies appear to have a comparable form to the expected noise reduction ($\sqrt{n}$ where n is the number of triads). However, residual correlations between inertial measurements, as well as correlations between filter states, limit the reduction of navigation errors (i.e. errors in position, velocity and orientation) compared to the noise reduction. The extended mechanization is generally superior to the synthetic approach. Significant improvement is noticeable for both methods when the number of sensors exceeds five.

6.6.4 Notes on the Observability

When redundant IMUs are employed, the observability of the error states further decreases. The estimated synthetic biases represent the mean value of the individual estimates (i.e. similar to those depicted in FIG. 6.14). On the other hand, the biases estimated in the extended mechanization do not always follow their separate estimates (FIG. 6.14). The covariance analysis (FIG. 6.20) of the state vector reveals that the individual biases have small correlations (0.2-0.3) with the other terms and therefore do not explain the encountered differences. The explanation can be found through the study of the observability of the system. Indeed, a system composed of system matrix $\mathbf{F}$, observation matrix $\mathbf{H}$ and n states is observable if the observability matrix $\mathbf{O}$ has rank n [177].

$$\mathbf{O} = \begin{bmatrix} \mathbf{H} \\ \mathbf{H} \cdot \mathbf{F} \\ \dots \\ \mathbf{H} \cdot \mathbf{F}^{n-1} \end{bmatrix} \tag{6.6.1}$$

According to this approach, a single MEMS-IMU system is completely observable. Indeed, the observability matrix has rank 15 which corresponds to the number of states. However, the observability of the individual states depends essentially on the encountered dynamics. Indeed, orientation angles and bias terms are not completely observable under limited motion [227]. There is also a lack in observability when magnetic updates are performed at a higher rate than GPS updates. Actually, they only control the orientation but not the displacement.

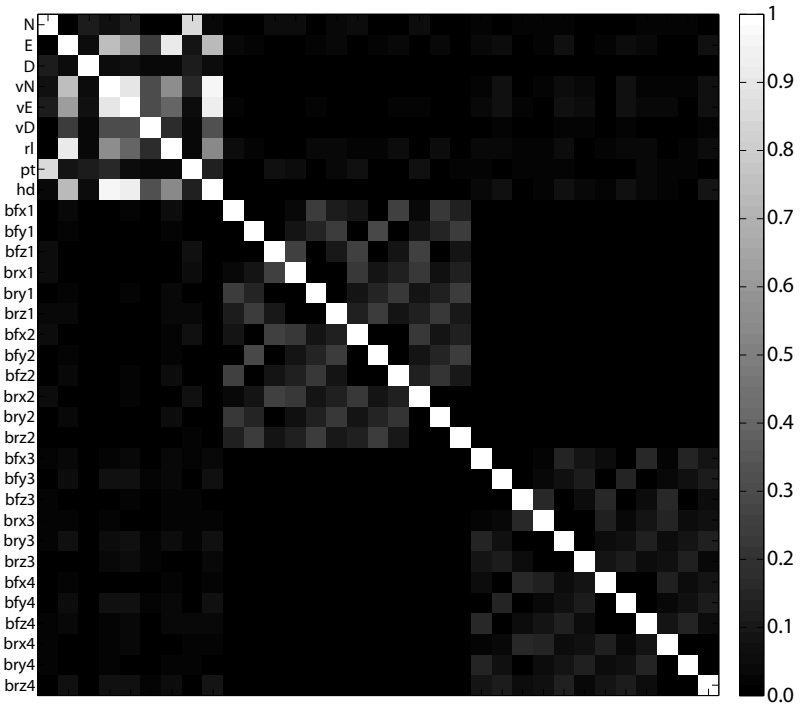

FIG. 6.20: State correlations in extended mechanization for 4 IMUs. Error state order: position (3), velocity (3), orientation (3), accelerometer biases (12), gyroscope biases (12). $bfx1$ is the abbreviation for the bias of accelerometer x of sensor #1.

On the other hand, the system has full rank if the magnetic updates are performed at the same frequency as GPS updates.

In the extended mechanization approach, the number of states increases to 33, but the rank of the observability matrix remains 15. Therefore, the observability of the sensor biases is reduced in favor of the navigation states (position, velocity and orientation). Indeed, the presented approach is not optimal for the observation of the actual bias states. The observability can be improved by constraining the inertial measurements $\boldsymbol{\ell}$ at the update stage by the following relations:

$$\hat{\boldsymbol{\ell}}_{f,bj} = \mathbf{R}_{bi}^{bj} \cdot \hat{\boldsymbol{\ell}}_{f,bi} \tag{6.6.2}$$

where $\hat{\boldsymbol{\ell}}_{f,bj}$ is the estimated inertial measurement in body frame bj. $\mathbf{R}_{bi}^{bj}$ is the rotation matrix between sensor i and sensor j given by relation 6.5.5.

The observation matrix $\mathbf{H}$ for 4 IMUs is extended to:

$$\mathbf{H} = \begin{bmatrix} \mathbf{0}_{12\times3} & \mathbf{0}_{12\times3} & \mathbf{0}_{12\times3} & \mathbf{R} & \mathbf{0}_{12\times12} \\ \mathbf{0}_{12\times3} & \mathbf{0}_{12\times3} & \mathbf{0}_{12\times3} & \mathbf{0}_{12\times12} & \mathbf{R} \end{bmatrix} \tag{6.6.3}$$

where

$$\mathbf{R} = \begin{bmatrix} \mathbf{0}_3 & \mathbf{R}_{b2}^{b1} & \mathbf{0}_3 & \mathbf{0}_3 \\ \mathbf{0}_3 & \mathbf{0}_3 & \mathbf{R}_{b3}^{b2} & \mathbf{0}_3 \\ \mathbf{0}_3 & \mathbf{0}_3 & \mathbf{0}_3 & \mathbf{R}_{b4}^{b3} \\ \mathbf{0}_3 & \mathbf{0}_3 & \mathbf{0}_3 & \mathbf{0}_3 \end{bmatrix} \tag{6.6.4}$$

6.6.5 Orientation Initialization and Inertial Error Estimation

The orientation initialization algorithms described in section 3.6.2 can be applied through the bias of a synthetic IMU (relations 6.5.1) or through least squares adjustment with the inertial and magnetic measurements. Assuming that the inertial and magnetic biases of all sensors are uncorrelated, the synthetic measurements become less and less affected by systematic (as well as random) errors with increasing sensor number. Thus, an enhanced orientation can be estimated (FIG. 6.21). Then, the initial bias terms for each sensor can be derived. Indeed, during static initialization or uniform motion ($\mathbf{a}^n \approx \mathbf{0}_3$), the accelerometer bias $\mathbf{b}_f$ and magnetic perturbation $\mathbf{b}_m$ can be derived from equations 6.5.1 thanks to the redundant measurements.

$$\begin{aligned} \mathbf{b}_f &= \mathbf{A}_f \cdot \mathbf{R}_n^b \cdot (\mathbf{g}^n - (2 \cdot \boldsymbol{\omega}_{ie}^n + \boldsymbol{\omega}_{en}^n) \cdot \mathbf{v}^n) + \boldsymbol{\ell}_f^b \\ \mathbf{b}_m &= \mathbf{A}_m \cdot \mathbf{R}_n^b \cdot \mathbf{h}^n + \boldsymbol{\ell}_m^b \end{aligned} \tag{6.6.5}$$

During static initialization ($\mathbf{v}^n = \mathbf{0}_3$), relation 6.6.5 simplifies further.

The computation of the gyro bias is less straightforward. $\mathbf{u}_b^b$ can be derived from relations F.1.1-F.1.5. Then, $\mathbf{b}_\omega$ becomes

$$\mathbf{b}_\omega = \mathbf{A}_\omega \cdot \frac{\mathbf{u}_b^b}{\Delta t} + \boldsymbol{\omega}_{ib}^b. \tag{6.6.6}$$

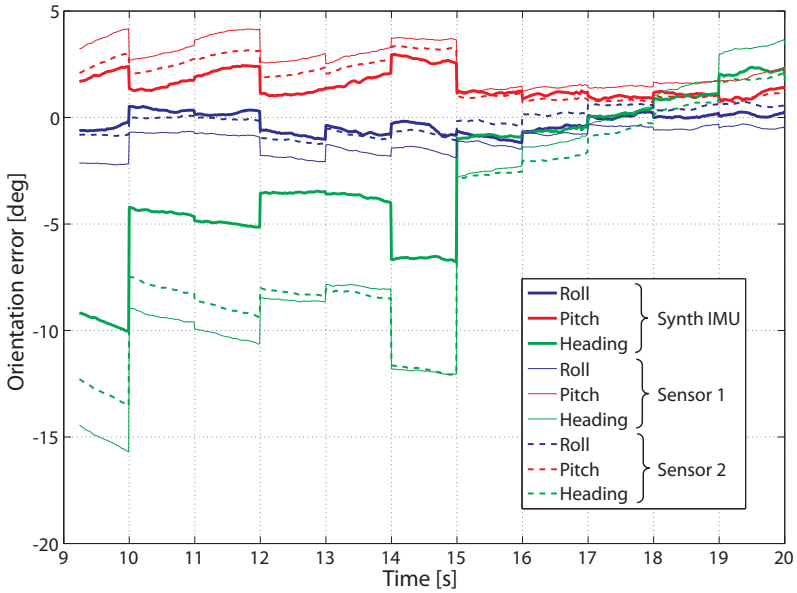

FIG. 6.21: Comparison of the orientation initialization of 2 single and a synthetic IMU.

Chapter 7

From Navigation to Performance Assessment in Sport

Trajectories determined by GPS and GPS/INS are characterized by a succession of discrete sample points (position, velocity and orientation). For convenient representation and efficient analysis, however, it is useful to represent trajectories as continuous curves. To compare trajectories, the positioning accuracy of the trajectories needs to be considered and may require additional filtering or trajectory matching steps. This chapter first outlines the developed trajectory modeling and comparison approaches. The methods are illustrated with concrete examples from performance assessment in sport. The second part presents two other examples for the exploitation of GPS/INS data in sports: application of GPS/INS for timing and derivation of additional information from the orientation estimates in alpine skiing and motorcycling.

7.1 Trajectory Modeling Approaches

Representing a trajectory by mathematical functions rather than by a set of discrete points creates a basis that is not only better suited for subsequent analysis (e.g. derivating curvilinear distance, curvature estimation) but can also contribute to data filtering. Indeed, GPS, and to a smaller account GPS/INS, trajectories are affected by noise of higher frequency and may also present residual outliers which need to be removed as well as data gaps (Fig. 7.1). Furthermore, sport professionals like to visualize trajectories as continuous curves and to resample data sets at arbitrary data rates for synchronization with other trajectory information (e.g. forces, heart rates).

7.1.1 Cubic Splines Smoothing

Cubic splines are piecewise polynomials of the third degree that fit between adjustment points. Thanks to their piecewise character, they can take local particularities of any data interval into account. Furthermore, they respect the continuity in position, velocity (first-order derivative) and acceleration (second-order derivative) on the right and left of the adjustment points.

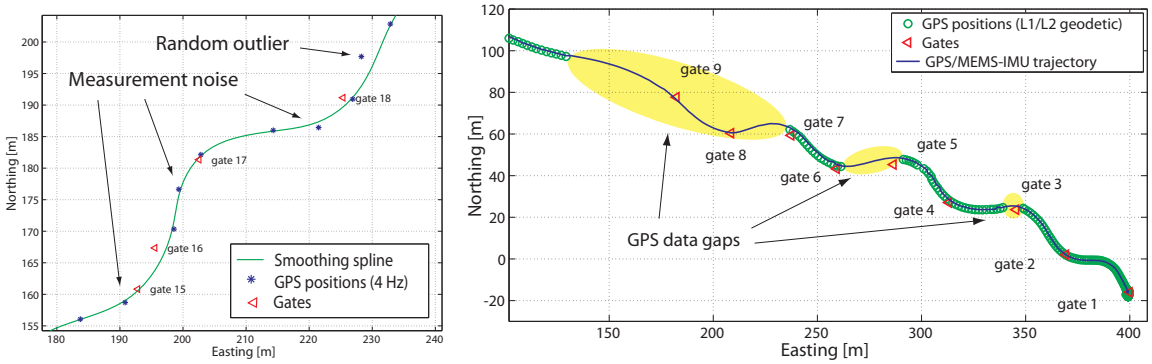

FIG. 7.1: Measurement noise, random outliers and data gaps in GPS data.

Reference [102] demonstrated that the spline function minimizes the second-order derivative, i.e. the acceleration and the velocity variation, for a set of given initial conditions. This corresponds to the physics of athlete's motion. Hence, cubic splines are particularly well adapted for trajectory interpolation in sport applications. This smoothing spline $f(x)$ minimizes the cost function J as:

$$
\begin{aligned}
J &= \lambda \sum_{k=1}^{N} w(j)\,[y(j) - f(x(j))]^2 + (1-\lambda) \int_{t_0}^{t_N} \lambda(t) \left[\frac{d^2}{dt^2} f(t)\right]^2 dt \\
f(t) &= \sum_{k\in\mathbb{Z}} g(k)\varphi(t-t_k) \\
\varphi(t-t_k) &= \sum_{i=1}^{n} (t-t_k)^{4-i} c_{ki}
\end{aligned}
\tag{7.1.1}
$$

The first quadratic term of expression 7.1.1 represents the error contribution of the approximation $f(t)$ with respect to the adjustment points $y(j)$. When the local weights $w(j)$ increase, the smoothing effect of the interpolation is reduced. The second term imposes a constraint on the smoothness of the approximation. If $\lambda = 0$, the spline corresponds to the least-squares fit of a straight line to the data points. On the other hand, if $\lambda = 1$, the spline becomes a natural cubic spline interpolant that follows the data. $\varphi(t-t_k)$ represents the polynomial piecewise basis and $g(k)$ their associated coefficients. Smoothing splines minimize the cost function J as a function of the smoothing parameter λ. A detailed description of the spline algorithm can be found in [29, 28].

Through the definition of an appropriate weighting function $w(j)$, references [97, 171] have developed an effective method representing trajectories derived from dual-frequency differential GPS (FIG. 7.2). Small weights are attributed to the points during transition periods where carrier-phase ambiguities are fixed and float ($ntrans$). Such strong de-weighting avoids discontinuities in the modeled trajectory due to sudden drops of accuracy while relying on the movement prediction due to athlete's inertia. For other transition epochs, $w(j)$ is linearly increasing in time from w_{trans} to the final value of w_{float}, which is the value of $w(j)$ for epochs of float ambiguities outside the transition periods. This method has proven to be effective in filtering the dual-frequency GPS trajectory for sudden jumps due to abrupt changes in satellite constellation or in the measurement accuracy (FIG. 7.3).

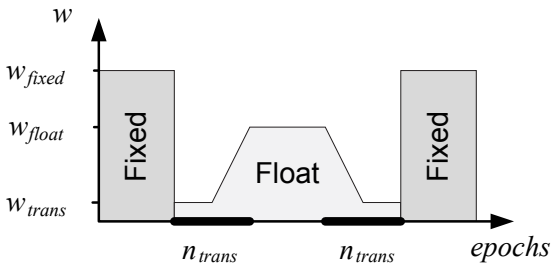

FIG. 7.2: Weighting function associated to dual-frequency GPS trajectories.

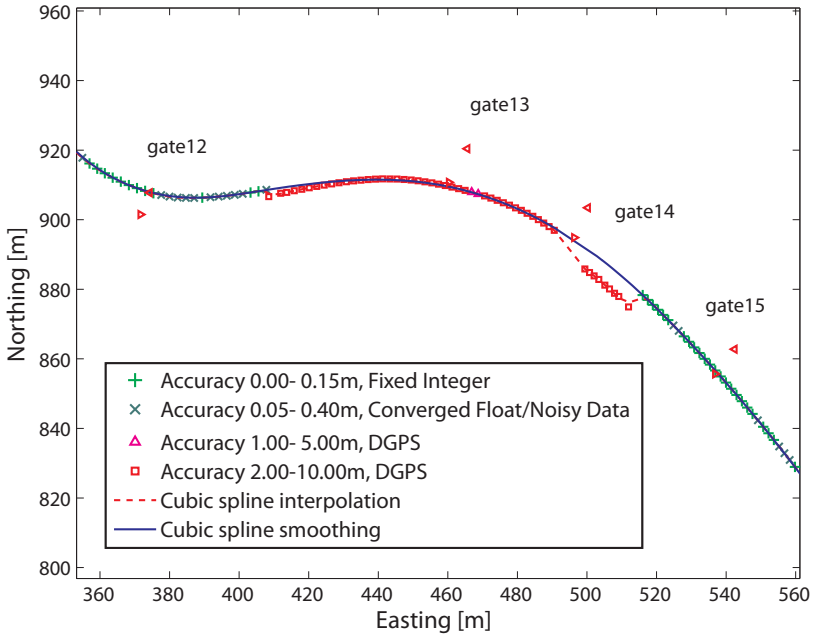

FIG. 7.3: GPS trajectory with changing accuracy and ambiguity status.

However, the previously described method becomes less adequate for differential GPS positioning using single-frequency data. Indeed, carrier-phase ambiguities can rarely be resolved with L1 DGPS, especially with low-cost receivers under dynamic conditions. As shown in section 4.2.1, L1 DGPS offers reduced accuracy in positioning, but not necessary in velocity estimates. Outliers in position are more frequent than with dual-frequency trajectory. To make matters worse, other distinctive information is absent (e.g. number of visible satellites, DOP) or inaccessible, like the stochastic parameters related to the tracking performance in low-cost receivers (e.g. Phase Lock Loop). For these reasons, the spline smoothing is found to be ineffective for single-frequency data.

7.1.2 Additional Kalman Filtering

In the case of poor positioning but acceptable velocity accuracy, Kalman filtering of position and velocity results provides an alternative solution for additional trajectory smoothing. As

for GPS processing (equation 3.4.3), a constant velocity model was implemented for state propagation.

$$\begin{aligned}(\mathbf{v}^n)_{k+1} &= (\mathbf{v}^n)_k \\ (\mathbf{r}_e^n)_{k+1} &= (\mathbf{r}_e^n)_k + \mathbf{D}^{-1} \cdot (\mathbf{v}^n)_k \cdot \Delta t\end{aligned} \tag{7.1.2}$$

Other models based on more sophisticated state prediction may improve the navigation solution, but have not been investigated. EKF and SPKF were implemented and provided equivalent results. Particle filtering has been investigated by study [105] with similar results as for the KF. However, their increased computational complexity and the difficulties related to the Sampling Importance Re-sampling (SIR, [65]) render this approach less effective than KF. After filtering, the trajectory is interpolated by cubic splines for convenient analysis.

FIG. 7.4 illustrates trajectory reconstruction by KF with subsequent spline interpolation using single-frequency GPS derived positions of poor accuracy. The simple spline smoothing without additional Kalman prefiltering is also shown for comparison. It can be seen that the trajectory based on cubic spline smoothing of the GPS positions does not pass gates 5 to 7. On the other hand, the Kalman filtered trajectory respects the ground truth (represented by the gates) much better thanks to the accuracy of the provided velocity estimates.

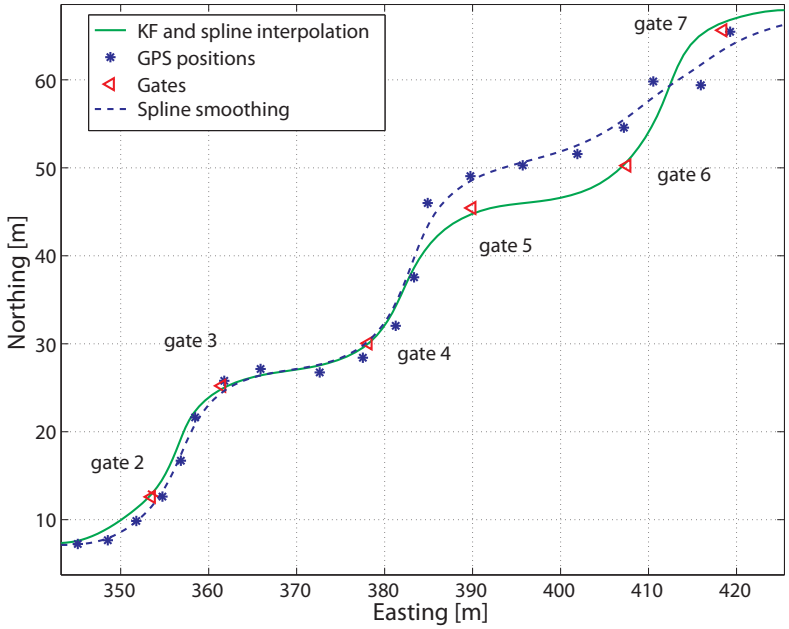

FIG. 7.4: L1 DGPS trajectory modeled with smoothing splines and KF.

7.1.3 Limitations of Trajectory Modeling

Interpolation and smoothing with cubic splines does not guarantee exact reproduction of adjustment points and therefore can introduce additional interpolation errors. Accordingly, such an approach should be used cautiously on data of uniform accuracy. The additional KF and spline interpolation reduce efficiently the high frequency noise in the trajectory data.

However, they cannot remove systematic errors, e.g. constant position offsets in L1 DGPS (Fig. 7.5). Such systematic effects need to be considered for comparison between trajectories or visualization with respect to reference points (e.g. gates, street boundaries).

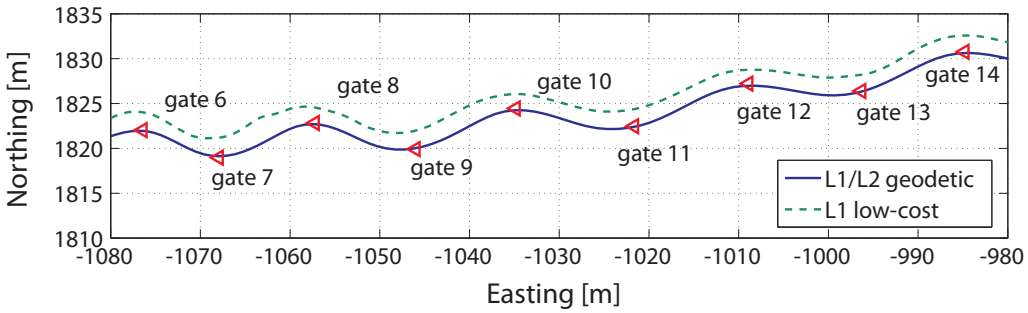

Fig. 7.5: Two sets of L1 DGPS trajectories showing a constant position offset.

7.2 Trajectory Matching

7.2.1 Problem Definition

Systematic errors in the position domain originate mainly by the limited performance of phase-smoothed code DGPS. If such (GPS or GPS/MEMS-IMU) trajectories are to be compared, analyzed or visualized, this effect must be mitigated. Fig. 7.6 illustrates a case where the trajectory is systematically displaced. The offset trajectory does not cross the gates correctly. Therefore, the velocity comparison will be distorted. The example shows that the comparison of trajectories with poor positioning accuracy only becomes conceivable after trajectory matching and correction. This section describes two trajectory matching approaches, presents experimental results and points out risks related to such operations.

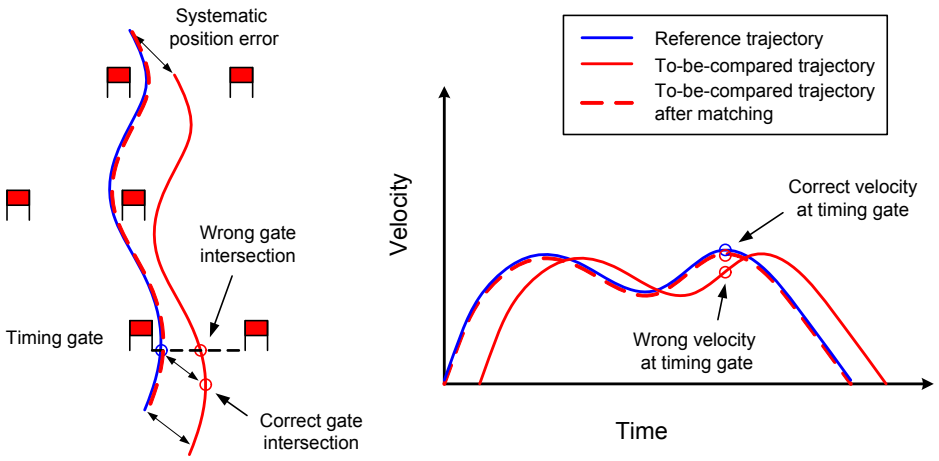

Fig. 7.6: Trajectory matching where a curve is affected by a systematic position error.

7.2.2 Extension of Cubic Spline Smoothing

The smoothing spline expression 7.1.1 can be extended by an additional term representing the closeness of the polynomial fit with respect to external geometrical constraints **K** as:

$$\begin{aligned} J &= \sum_{k=1}^{N} w(j)\left[\mathbf{y}(j) - \mathbf{f}(x(j))\right]^2 + \lambda_1 \int_{t_0}^{t_N} \lambda(t)\left[\frac{d^2}{dt^2}\mathbf{f}(t)\right]^2 dt + \lambda_2 \int_{t_0}^{t_N} w(\mathbf{f}(t))dt \\ \mathbf{f}(t) &= \sum_{k\in\mathbb{Z}} \mathbf{g}(k)\varphi(t-t_k) \\ w(\mathbf{f}(t)) &= \sum_{k\in\mathbb{Z}} \mathbf{G}(k)\theta(\mathbf{f}(t)-\mathbf{K}) \\ \varphi(t-t_k) &= \sum_{i=1}^{n} (t-t_k)^{4-i} c_{ki} \end{aligned} \tag{7.2.1}$$

where the first two terms correspond to the cubic spline expression (equation 7.1.1). $w(\mathbf{f}(t))$ takes into account external constraints **K** which are related to the measurements $x(j)$ through the relation θ. **G** defines their respective weight. The equation system becomes multi-dimensional. In contrast to relation 7.1.1, the system does no longer consist of linear equations. Therefore, no simple solution for **G** can be found. Furthermore, expressing geometrical constraints **K** and their associated weights **G** is difficult. The success of such operation depends on the relative geometry of the trajectory and the gates (section 7.2.5). As several trajectory points might be affected by the geometrical constraints, more sophisticated adjustment methods might be required (e.g. dynamic networks [20]).

7.2.3 Eigenvector Approach for Feature-Based Correspondence

Reference [164] proposes an eigenvector approach for establishing a correspondence between two sets of points. The approach was developed for computer vision, but can be adapted to trajectory matching.

First, consider two trajectories with easting and northing coordinates. A proximity matrix **H** is computed for each trajectory.

$$\mathbf{H} = e^{-\frac{r_{i,j}^2}{2\cdot\sigma^2}} \tag{7.2.2}$$

where $r_{i,j} = \|x_i - x_j\|$. σ controls the interaction between features. A large value of σ will allow more possibilities for correspondences.

Next, the eigenvalue decomposition of **H** is computed.

$$\mathbf{H} = \mathbf{V}\mathbf{D}\mathbf{V}^T \tag{7.2.3}$$

The diagonal matrix **D** contains the (positive) eigenvalues along its diagonal in decreasing size. The modal matrix **V** is orthogonal and has the eigenvectors **e** as its column vectors. Each

row of $\mathbf{V}$ can then be thought of as a feature vector $\mathbf{f}$ containing the n modal coordinates of feature i.

$$\mathbf{V} = \left[\begin{array}{c|c|c} \mathbf{e}_1 & ... & \mathbf{e}_n \end{array} \right] = \left[\begin{array}{c|c|c} \mathbf{f}_1 & ... & \mathbf{f}_n \end{array} \right]^T \tag{7.2.4}$$

The final stage is to correlate the two sets of feature vectors yielding the association matrix $\mathbf{Z}$.

$$z_{i,j} = \|\mathbf{f}_i - \mathbf{f}_j\|^2 \tag{7.2.5}$$

$z_{i,j}$ reflects the confidence in the match between x_i and x_j, As the trajectories have different numbers of points, their number of modes will differ. Therefore, the least significant modes (corresponding to the smallest eigenvalues) are truncated.

The algorithm allows detecting correspondences of rotated, translated and distorted features. However, the sign of each eigenvector is not unique. This disadvantage can be overcome by a sign correction [163] or by considering only the most important modes (i.e. those corresponding to the largest eigenvalues) [39]. Furthermore, the value of σ significantly influences the number of correspondences detected by the algorithm. Generally, with increasing values of σ, more correspondences can be found [39].

Once the correspondences between the trajectories are correctly evaluated, the trajectories can be matched. To do so, a 2D Helmert transformation [78] can be applied estimating a rotation (ω) and translation (ΔE, ΔN) between two trajectories or trajectory segments. As the scale of the GPS trajectories is sufficiently stable, no scaling factor between the two trajectories is estimated.

$$\begin{bmatrix} E_1 \\ N_1 \end{bmatrix} = \begin{bmatrix} \cos\omega & \sin\omega \\ -\sin\omega & \cos\omega \end{bmatrix} \begin{bmatrix} E_2 \\ N_2 \end{bmatrix} + \begin{bmatrix} \Delta E \\ \Delta N \end{bmatrix} \tag{7.2.6}$$

After compensation, the statistical significance of the rotation can be estimated. Indeed, if $\omega > 3 \cdot \sigma_\omega$, the rotation is considered to be statistically meaningless at a threshold of 99,7% and a second computation without estimation of the rotation may be performed.

7.2.4 Position Accuracy Improvement through Trajectory Matching

The eigenvector approach has been implemented for the matching of two trajectories. The easting and northing coordinates that are employed in the matching algorithm can be selected according to various schemes:

- A first approach matches all the trajectory points (Fig. 7.7). The size of the **H** and **Z** matrices as well as the computation time are important. This approach assumes that the translation and rotation are identical for the entire trajectory. However, this is usually not true as the satellite constellation may vary during the trajectory duration.
- In a second strategy, the trajectory is delimited (e.g. by timing gates, Fig. 7.8) and independent Helmert parameters are estimated for each trajectory segment. The size of the **H** and of the **Z** matrices is reduced accordingly.

- Thirdly, only characteristic points of the trajectory (points of maximum curvature, inflection points, Fig. 7.9) are retained for the matching. The curvature parameter can be derived from GPS and GPS/INS trajectory (Appendix G.1). Again, the computation complexity is reduced thanks to the reduced number of points. This approach can also be applied to trajectory segments.

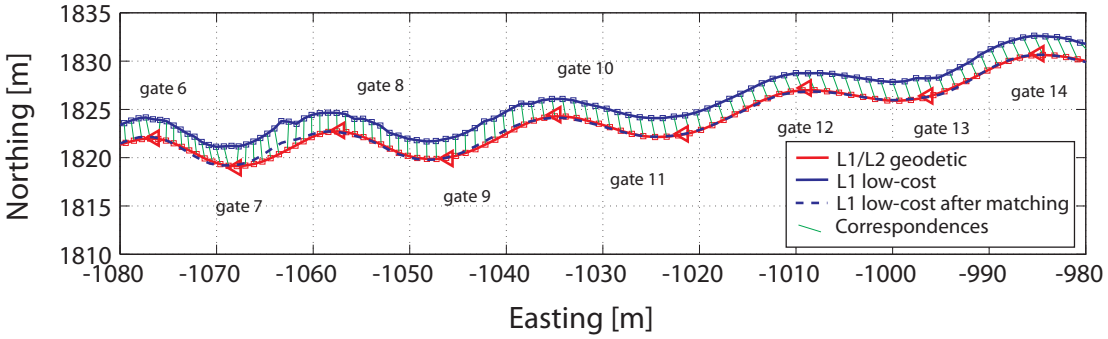

Fig. 7.7: Matching correspondences of the entire trajectory.

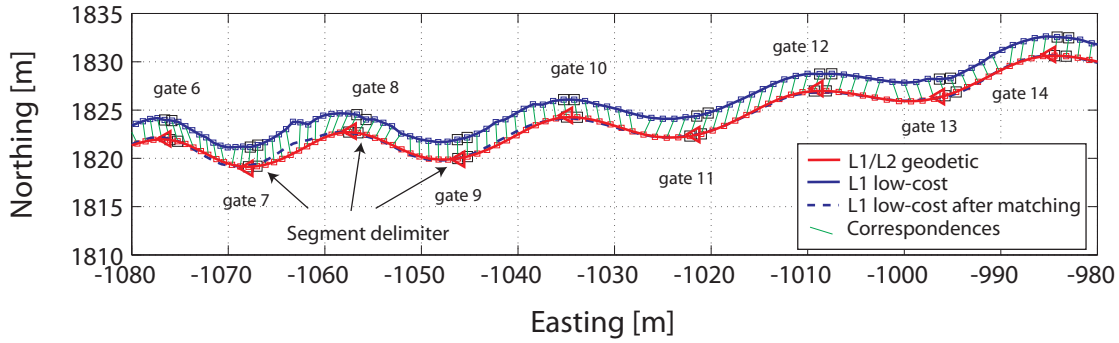

Fig. 7.8: Matching correspondences of the trajectory by segments.

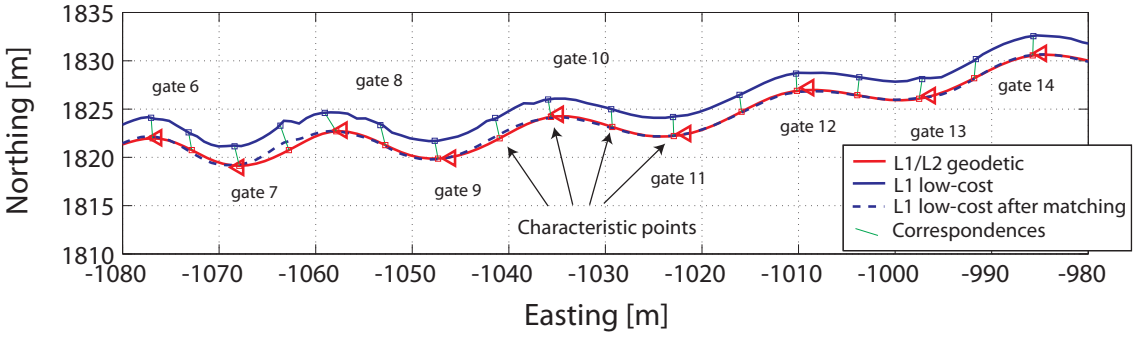

Fig. 7.9: Matching correspondences of the trajectory by characteristic points.

Fig. 7.7 to 7.9 present the correspondences calculated between two trajectories introduced in Fig. 7.5. The evolution of the differences in position between the two tracks is illustrated in 7.10. Tab. 7.1 summarizes the translation values computed by the three approaches. Rotation angles were found to be statistically insignificant in this case. The average offset computed on the entire trajectory indicates that the main part of the systematic offset in the north direction was removed thanks to the matching algorithm. The east coordinate error is less important in this case and is not well estimated. The altitude correction can be also applied after successful finding of the correspondences.

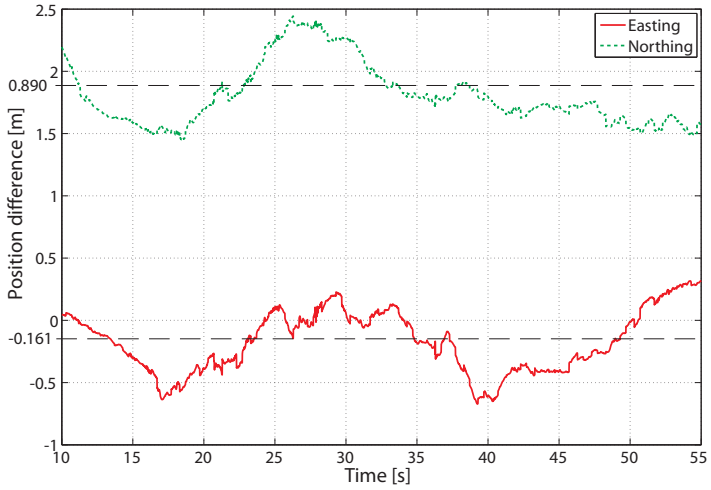

Fig. 7.10: Evolution of the position difference.

Tab. 7.1: Performance Comparison of three matching algorithms. The "average offset" corresponds to the mean offset between the L1 and L1/L2 trajectories.

	Easting [m]	Northing [m]	Altitude [m]	Rotation [–]	Correspondences [found/possible]
Entire trajectory	-0.310	1.881	-1.338	-	178/190
Segment	0.084	1.876	-1.410	-	180/182
Characteristic points	-0.019	1.927	-1.386	-	31/31
Trajectory to gates	-0.618	1.884	-1.611	-	100/151
Average offset	-0.161	1.890	-1.386	-	-

All three approaches match trajectories mutually. However, the boundary constraints cannot be taken into account as in the case of geometrically constrained smoothing splines. Hence, the trajectory comparison is facilitated after matching, but its topological correctness can not be guaranteed. For this reason, the trajectories are preferably matched to a reference trajectory that respects the "ground truth" (as is the case of the examples in Fig. 7.7 to 7.9). Such an "ideal" curve can be obtained from previous trials or synthetically designed based on experience. Fig. 7.11 illustrates results of the trajectory matching, where the reference trajectory was generated interpolating the trajectory gates with a a cubic spline.

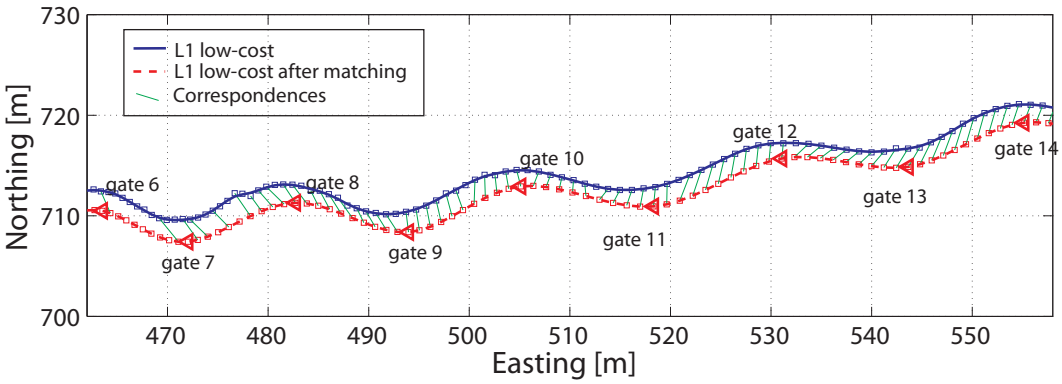

FIG. 7.11: Matching correspondences of the trajectory to the gates.

7.2.5 Risk Related to Trajectory Matching

Different trajectories on the same track may originate not only from systematic errors in positioning but also reflect the reality of distinct choices. Indeed, 7.12 illustrates two geometrically identical trajectories where athlete B anticipates the turns whereas athlete A chooses a direct path. Matching these trajectories would time-distort the information related to the performance evaluation. In such a case, the geometry of the trajectory and of the local boundaries does not allow expressing a unique condition. Moreover, the approach based on constrained smoothing splines is not applicable. Hence, the methodology of trajectory matching must be applied after careful evaluation of the position errors, the trajectories' geometry and the available boundary constraints.

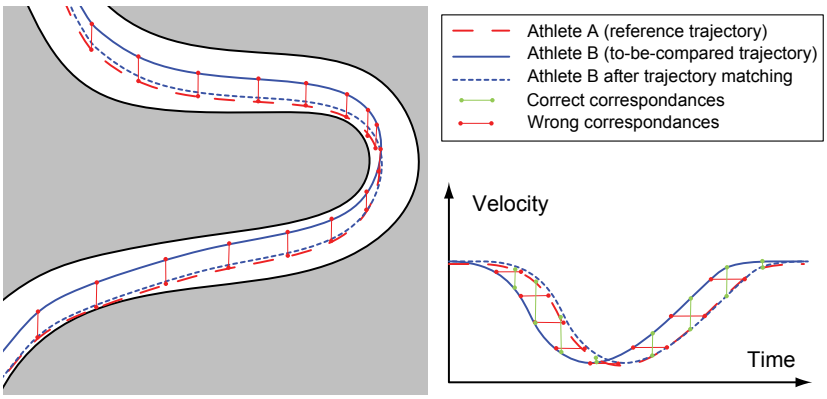

FIG. 7.12: Risk related to trajectory matching.

7.3 Trajectory Comparison

The evaluation of trajectories may include the comparison of timing splits, their shape, velocities, and orientation. Relative timing splits - whether between real or virtual gates - can be studied once the trajectories are reconstructed.

7.3.1 Spatial Trajectory Comparison Approach

Problem definition

The analysis of the athletic performance trajectories is often based on datasets that were recorded at different times. This situation occurs, for example, in downhill skiing competitions or training in which skiers make sequential (not simultaneous) runs. Such trajectories cannot be compared by considering only the differences in coordinates or velocities recorded at the same instant in time (as could be done for real-time comparison between two competitors). Fig. 7.13 (left) depicts the position of two athletes sampled at the same time interval. Obviously, athlete A is faster than B (the sampling points of athlete B are closer to each other). Their velocity profiles with respect to the time from the start are given in Fig. 7.13 (right). An accurate explanation could not be given for the substandard performance of athlete B based on the simple time- or distance-based comparison. Indeed, the temporal profiles can be considered as trajectories with a common frame but which are affected by a drift. Thus, it is not very useful to compare them directly. A better approach is to compare the tracks spatially in increments smaller than the gate crossings.

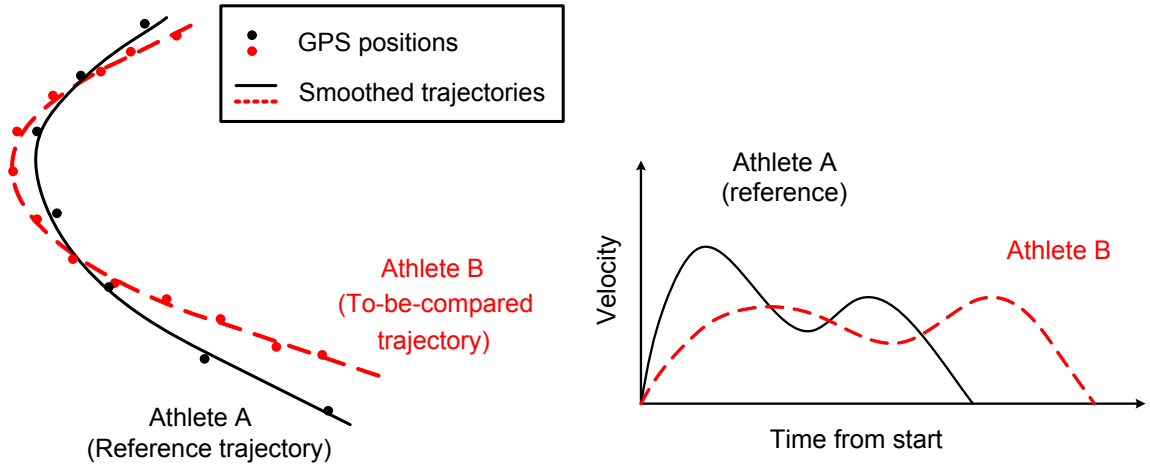

Fig. 7.13: Trajectory and velocity evaluation based on distance or time comparison.

The easiest approach to compare two trajectories spatially is to identify the points which are closest (Euclidean distance) to each other on either curve. However, this method does not ensure a rigorous comparison between several trajectories because the sampling points are not located on a common cross-section of the track. To make matters worse, this error increases if the sampling rate is small and the velocities are high. In addition, intermediate times for real or virtual gates cannot be assessed by this approach.

Proposed approach

To compare trajectories, the GPS or GPS/INS datasets are first matched to the ground truth and modeled as continuous curves (section 7.1.1). Then, a reference trajectory is selected (e.g. the faster athlete, the mathematical model of an optimal course). The comparison is achieved

by intersecting equitemporal planes that are perpendicular to the reference track with all the to-be-compared trajectories. FIG. 7.14 (left) shows a simplified schematic of a reference trajectory and a single trajectory that will be compared to it. Based on the intersection time of both trajectories with the plane, the differences between the athletes are computed. Of course, the coordinate differences between the trajectories are of utmost importance, but also any other attributes attached to the trajectories can be compared in a straightforward manner (e.g. elapsed time, velocities, accelerations, heart rates). Additional splits and (virtual) gates can be easily computed and interposed between the timing cells or gates. Thanks to this approach, the performance can be evaluated at any preselected time or distance interval.

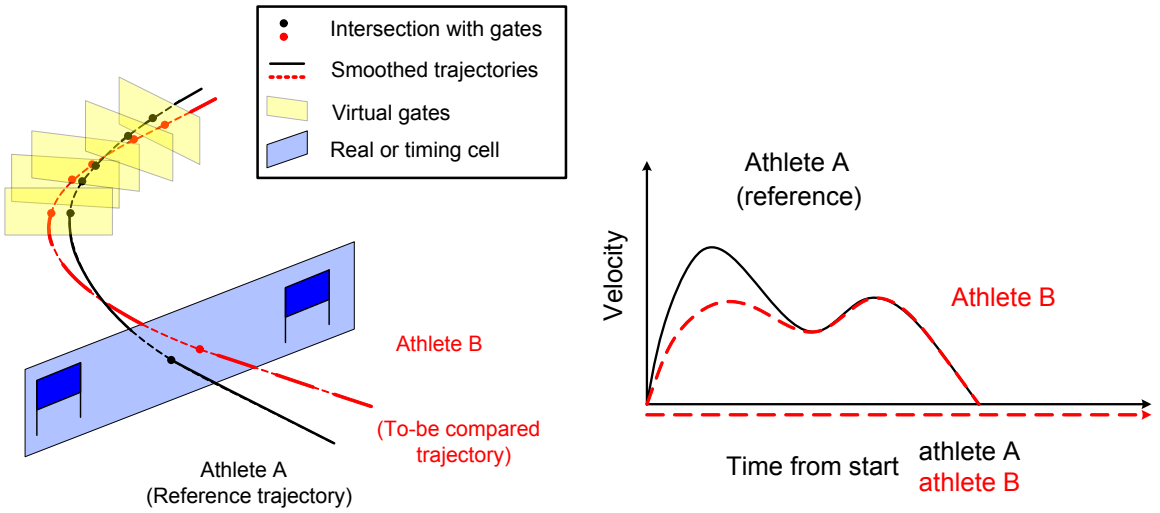

FIG. 7.14: Principle of spatial trajectory comparison. The rectangles represent the plane spanned by a set of real or virtual gates (left). Velocity comparison derived from spatial trajectory comparison (right).

Expressing the vertical plane to a reference trajectory as:

$$a \cdot E + b \cdot N + c \cdot h + d = 0 \tag{7.3.1}$$

where a, b, c and d are the parameters of the plane (FIG. 7.15, right), the normal vector to the plane is given by:

$$\begin{bmatrix} a \\ b \\ c \end{bmatrix} = \begin{bmatrix} v_E \\ v_N \\ v_h \end{bmatrix} \tag{7.3.2}$$

Taking the difference between the two following expressions, d is eliminated and the intersection point of trajectory B with the plane $[E_B N_B h_B]$ is determined iteratively.

$$\left.\begin{array}{l} a \cdot E_A + b \cdot N_A + c \cdot h_A + d = 0 \\ a \cdot E_B + b \cdot N_B + c \cdot h_B + d = 0 \end{array}\right\} \rightarrow a \cdot (E_A - E_B) + b \cdot (N_A - N_B) + c \cdot (h_A - h_B) = 0 \tag{7.3.3}$$

If the intersection with a real gate is sought (FIG. 7.15, left), the following equation system needs to be solved supposing a vertical plane ($c = 0$).

$$\left.\begin{array}{l} a \cdot E_R + b \cdot N_R + d = 0 \\ a \cdot E_L + b \cdot N_L + d = 0 \\ a \cdot E_P + b \cdot N_P + d = 0 \end{array}\right\} \rightarrow -(E_L - E_R) \cdot N_P + (N_L - N_R) \cdot E_P + N_R \cdot E_L - N_L \cdot E_R = 0 \quad (7.3.4)$$

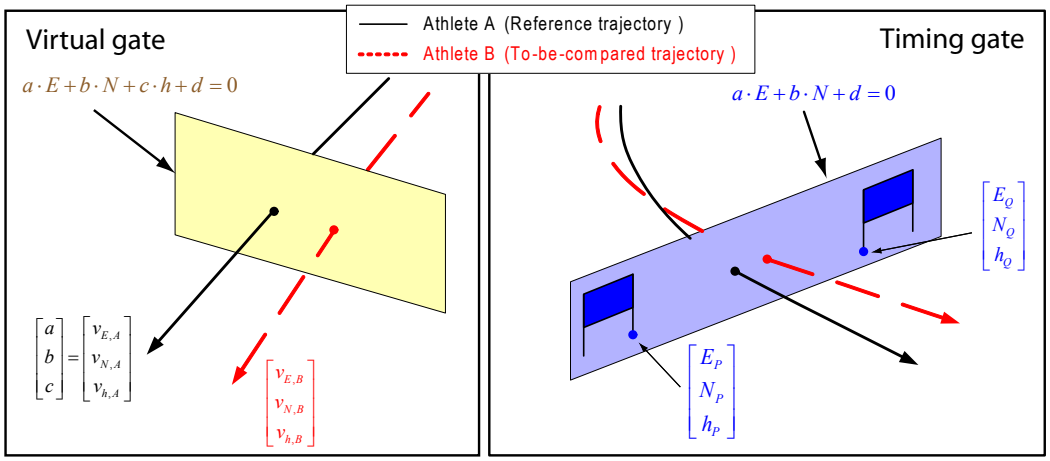

FIG. 7.15: Gate intersection.

Once the intersection time is computed, any parameter related to this period (e.g. velocity, heart-rate) can be compared. The orientation comparison is less straightforward because the orientation angles do not belong to a vector space [135]. The orientation differences between two trajectories can be determined based on the following relation:

$$\mathbf{R}_{b1}^{n} = (\mathbf{I} - \Delta\mathbf{R}_{b}^{n}) \cdot \mathbf{R}_{b2}^{n} \quad (7.3.5)$$

where $\mathbf{R}_{b1}^{n}$ is the reference orientation and $\mathbf{R}_{b2}^{n}$ the to-be-compared orientation. $\Delta\mathbf{R}_{b}^{n}$ is the skew-symmetric matrix with the orientation differences.

The given example on spatial comparison clearly illustrates the superior performance of athlete A in the first section of the track (FIG. 7.14, right). In the second section, the performance is identical for both contenders, as indicated by the overlapping trajectory lines. Alternatively, the abscissa could indicate the distance from the start and highlight different sections on the track (sectors, intermediates, gates, etc.).

7.3.2 Methodology for Trajectory Comparison

FIG. 7.16 summarizes the methodology for trajectory comparison. GPS or GPS/MEMS-IMU trajectories with post-processed dual-frequency GPS data can be compared after cubic spline smoothing (section 7.1.1). On the other hand, single-frequency GPS trajectories require special treatment because of their limited position accuracy. L1 DGPS trajectories may necessitate additional Kalman filtering (section 7.1.2). Both, single-frequency GPS and GPS/MEMS-IMU trajectories, need then to be matched to avoid biased comparisons. Reference trajectories

are adjusted to boundary constraints, if they were measured. Finally, the other trajectories are matched and compared to the adjusted reference trajectory (section 7.2).

The presented methodology has already found its commercial adaptation in a software package dedicated to the performance analysis in sports (Fig. 7.17, [198]).

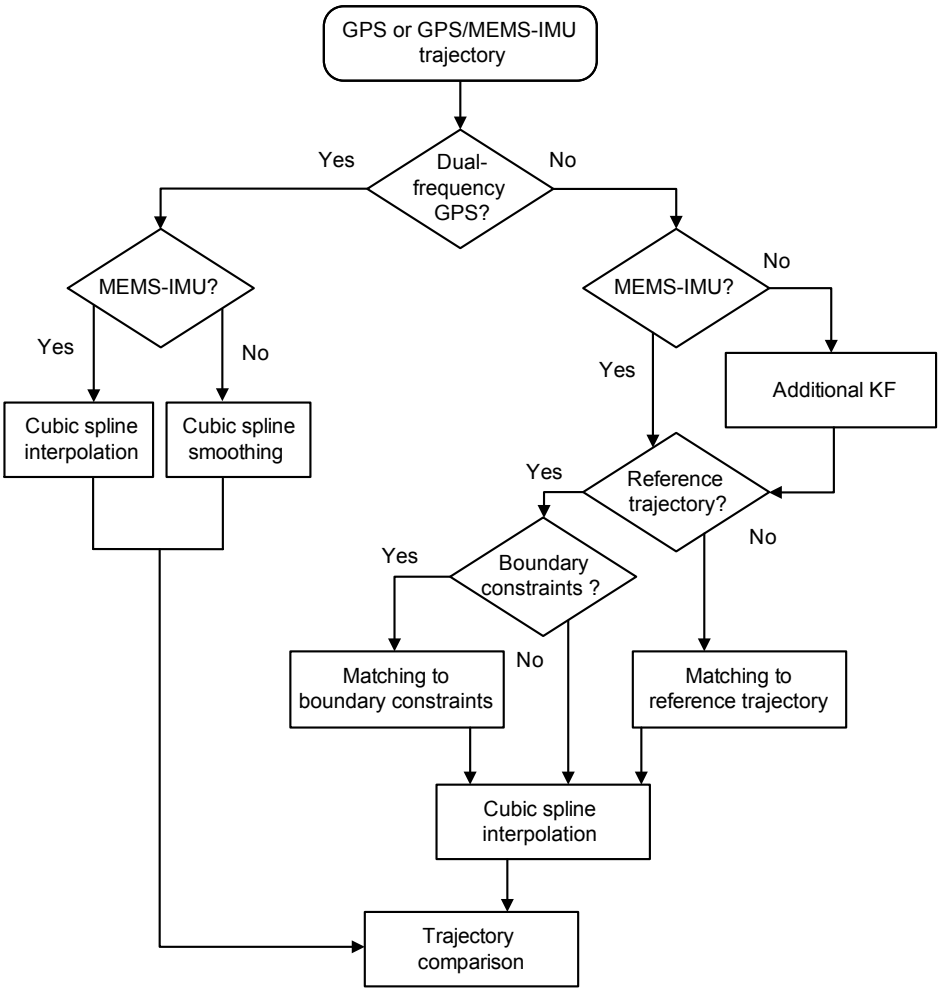

Fig. 7.16: Methodology for trajectory comparison.

7.3.3 Alternative Methods for Trajectory Comparison

Even though the presented strategy for trajectory comparison is rigorous, it suffers from some drawbacks. Firstly, it is a two-step solution consisting of a trajectory determination followed by the comparison. Some knowledge of the first step is ignored in the second (e.g. correlations between the states). Hence, the method is numerically not optimal. Secondly, the intersection of the to-be-compared trajectory with the plane perpendicular to the reference trajectory is computationally expensive. Therefore, two other methods were explored, but did not yet lead to efficient alternatives. For the sake of completeness, they are presented in the sequel.

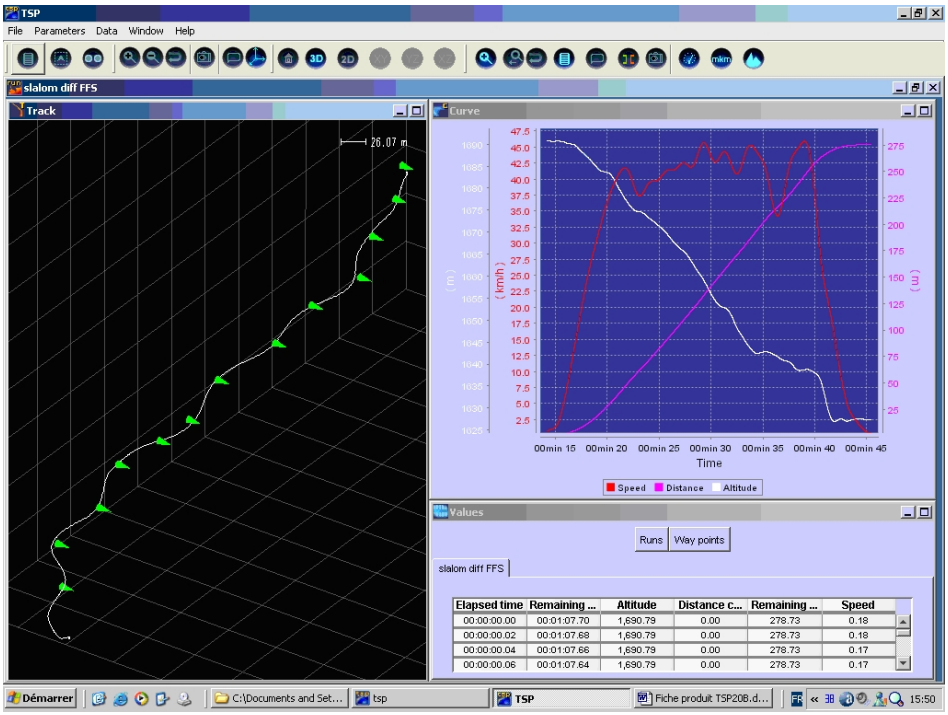

FIG. 7.17: GPS chronometry displayed on the user interface of the commercial trajectory analysis software [198]. The screen on the left displays a trajectory modeled from positioning data logged in a ski course. The screen on the right shows speed (red line), distance traveled (pink line), and altitude (white line) along various sections of the course. The table gives the numerical data and allows performing gate-to-gate comparisons.

Point distribution models

Studies [144, 145] present a model based on Point Distribution Models (PDMs) to qualify robot performance. The PDM corresponds to the representation of the trajectories by a set of chosen points transformed from the trajectory space to the space of deformation modes. To determine whether two sets of trajectories are similar, a Principal Component Analysis (PCA) and Linear Discriminant Analysis (LDA) can be performed.

A PCA has been applied to 10 runs of alpine skiing where 8 runs were recorded by a professional skier (section 4.1) and two runs by an amateur (FIG. 7.18-7.19). The trajectory cluster corresponding to the professional skier is quite compact which is certainly related to his technical abilities. The difference between the amateur and the professional skier is clearly visible for run 2, where the amateur made a technical fault at the lower part of the track (around gate 6).

A second example described in section 7.4 compares two pairs of skis based on 10 downhills. As FIG. 7.20 depicts, there is no statistically meaningful difference between the two pairs of ski. Indeed, the difference is smaller than the variance of the two clusters which corresponds to the investigation presented in section 7.4.

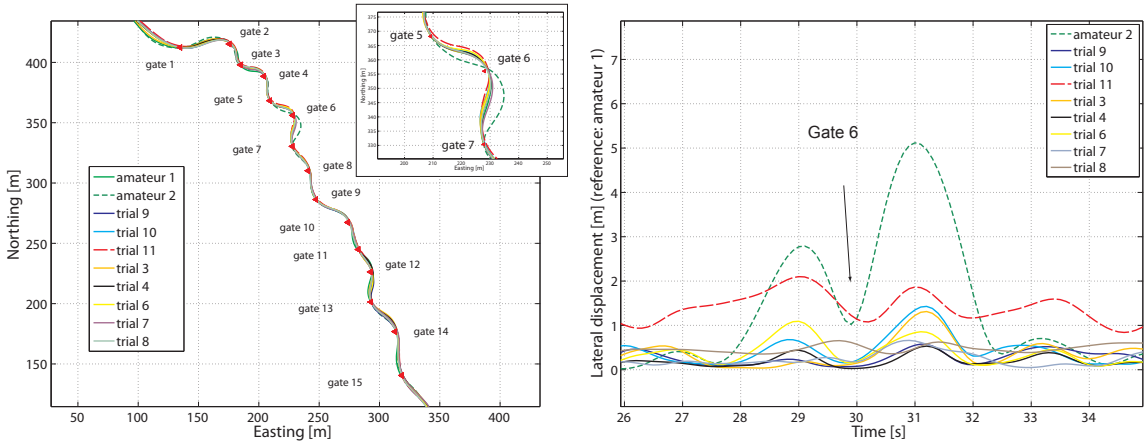

FIG. 7.18: The 10 downhills analyzed in the PCA. The lateral displacements quantifiy the technical error of the amateur skier on his second run (around gate 6).

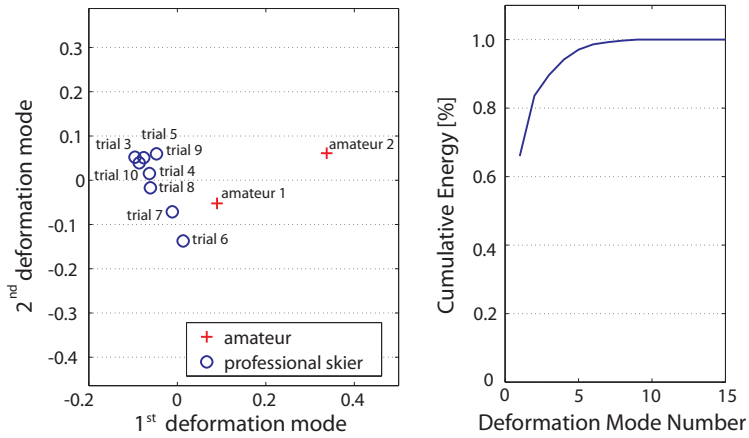

FIG. 7.19: The two principal modes of behavior of 10 downhills. More than 80% of the energy is contained in the first two deformation modes (right). The first deformation mode clearly isolates the run where the amateur skier made an error near gate 6.

Unlike the PCA, the LDA focuses on the maximum difference between clusters, optimizes the ratio between inter-cluster and intra-cluster variance. If the affiliation of trajectories to a group (cluster) is known, this method might provide statistically concluding results.

Time-dependent networks

References [44, 45] focus on analyzing the behavior of the route selection by identifying the path a person would take to go from one location to another. Discrete choice models capture correlations that allow the modeler to control the trade-off between the simplicity of the model and the level of realism. The key concept of capturing correlation is called a subnetwork. The importance and originality of this approach lies in the possibility to capture the most important correlation without considerably increasing the model complexity. Unfortunately,

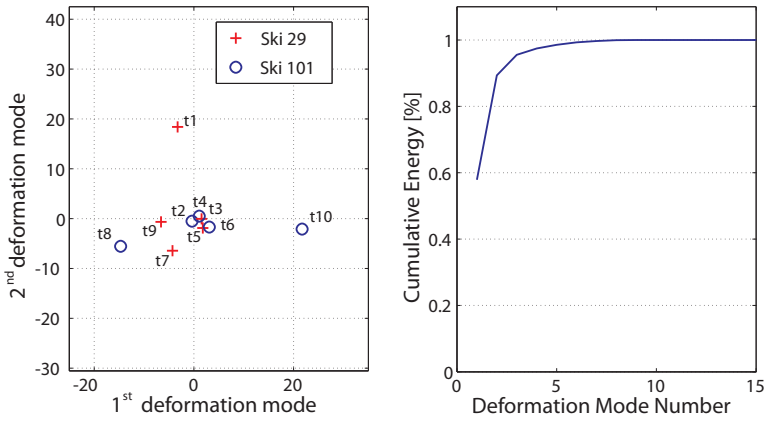

FIG. 7.20: Comparison of ski 29 and 101 with a PCA.

this method does not allow extracting directly quantitative information about trajectory differences.

7.3.4 Visualization Aspects

The visualization of the trajectories and that of compared parameters is critical when addressing sport professionals.

To simplify the comparison, metric coordinates are first computed in a local Transverse Mercator projection. This map projection guarantees negligible distortions for the scale of the networks considered in sports (rarely $>$ 10 km) [175] and allows expressing metric coordinates of small values which are more easy to interpret.

The experience shows that the interpretation of trajectory parameters with respect to time is difficult. Indeed, the evaluation is facilitated if these parameters are illustrated on the trajectory itself and eventually with respect to known ground features. Section 7.6.1 presents a case related to the evaluation of drifting tires. FIG. 7.30 (right) reports the evolution of the slipping angle as a function of time. It is difficult to interpret these values without the relation to the track geometry. Therefore, FIG. 7.29 represents the slipping angle as a function of their location which allows pertinent conclusions about the tires and the technique of the driver, i.e. that the motorcycle is inclined even on the straight parts of the curve and this inclination is compensated by lateral acceleration (FIG. 7.30, left).

Another important aspect for correct interpretation is the indication of statistical significance. The varying navigation state accuracies are assessed by introducing a quality indicator. In one dimension, the quality indicator is a confidence interval (e.g. $x \pm \sigma_x$). In 2D, the standard deviation σ_d of the coordinate difference d between two trajectories A and B computed by error propagation based on the accuracies of both trajectories ($\sigma_{E,A}$, $\sigma_{N,A}$, $\sigma_{E,B}$, $\sigma_{N,B}$, FIG. 7.21) is:

$$\sigma_d = \frac{1}{d}\sqrt{\Delta E^2 \cdot (\sigma_{E,A}^2 + \sigma_{N,A}^2) + \Delta N^2 \cdot (\sigma_{E,B}^2 + \sigma_{N,B}^2)} \tag{7.3.6}$$

Based on this indicator, correct conclusions about the significance of the performance differences can be made. This is illustrated by two trajectories compared in FIG. 7.21. The

trajectories's position can be considered as different only at sections with no overlap between the "snakes" formed around the trajectory by the quality indicators. The accuracy can be used to clearly highlight when the observed phenomenon is statistically meaningful, as illustrated in Fig. 7.22 (dotted line around the trajectory).

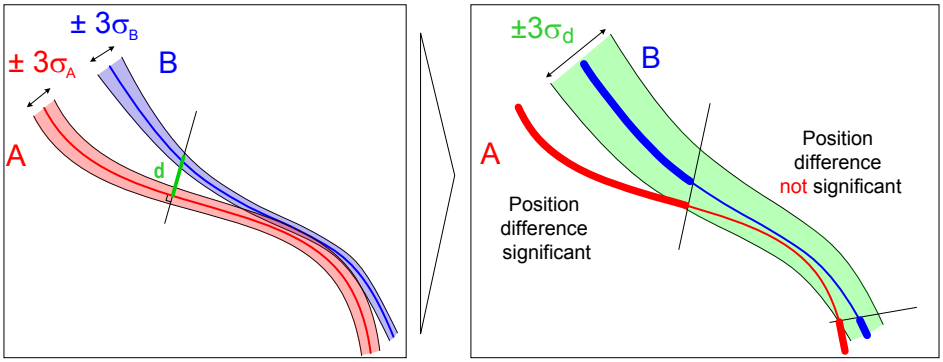

Fig. 7.21: Trajectory comparison methodology based on accuracy indicators: Trajectories B is significantly different from trajectory A if it does not overlap the buffer of $\pm 3\sigma_d$ around trajectory B.

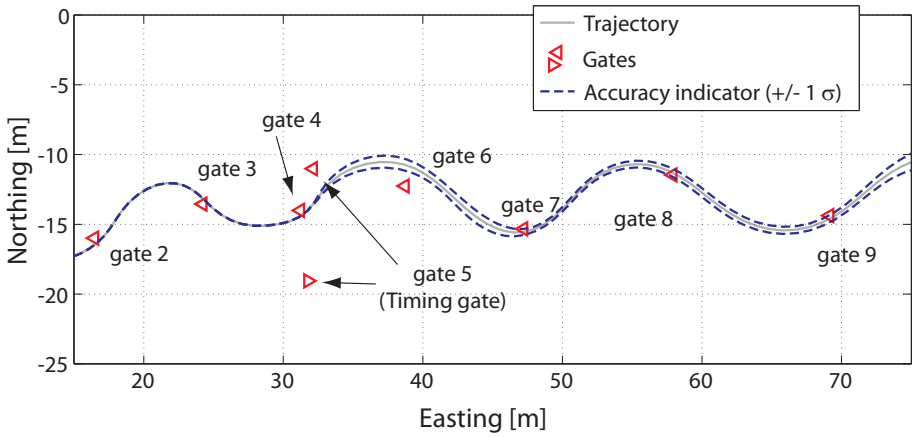

Fig. 7.22: GPS/MEMS-IMU trajectory with accuracy indicator (1σ). Satellite masking decreased the positioning accuracy near gate 6, but the INS helped to bridge the GPS gaps efficiently.

Another use of accuracy indicators is demonstrated in Fig. 7.23. There, the velocity profiles of two runs in a giant slalom are depicted and their respective differences augmented by a quality indicator ($\pm\sigma$). Gate intersections are plotted to provide an external reference. The data presented here was collected by a skier equipped with a low-cost L1 GPS receiver and a triple-axis MEMS-IMU. Based on this figure, the performance of the skier during the two runs can be evaluated gate by gate, but only at moments where such difference is marked as significant (shaded areas).

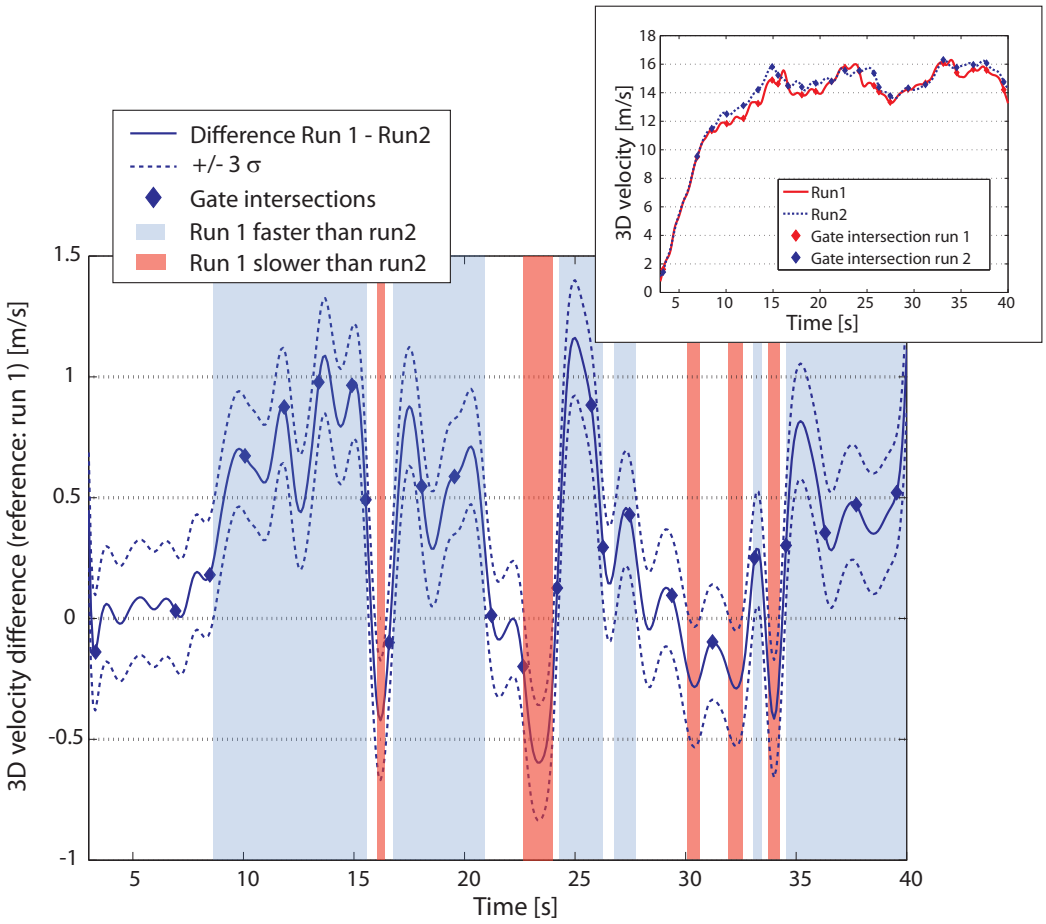

FIG. 7.23: Velocity comparison based on the spatial comparison algorithms and illustration of the accuracy indicator. The shaded areas indicate where the skiers' velocity difference was significant.

7.4 Position-Based Chronometry

A frequently asked question in the sports domain is the accuracy of position-based chronometry compared to the traditional approach based on timing cells. Contrary to the traditional discrete character of chronometry with timing cells, the timing based on GPS or GPS/MEMS-IMU trajectories is continuous. This fact has several advantages.

- Comparisons can be made over smaller sections, e.g. between two gates.
- It can include topological aspects such as finding an ideal line by comparing different tracks.
- Other parameters related to a defined section of the track (e.g. heart rate, velocity) can be compared.
- While timing cells provide only discrete measurements, trajectory-based timing provides a flexible approach that is independent of the skier's posture.

The theoretical accuracy of timing derived from trajectories can be deduced from the following basic relation:

$$\Delta t = \frac{\Delta x}{v} \tag{7.4.1}$$

Hence, considering a speed v of 80 km/h and a relatively large (differential) positioning error Δx of 0.4 m leads to a timing error Δt of 1.8/100 s.

The following investigation, undertaken in collaboration with TracEdge and the German ski federation (DSV), demonstrates the feasibility of GPS chronometry and illustrates its advantages over the traditional approach [218]. A professional downhill skier was equipped with an L1/L2 GPS receiver (*Javad Legacy*). He performed 10 super-G-like runs alternating two pairs of skis (Number 29 and 101). Three timing splits were measured (start, intermediate, and arrival) using a professional timing system. The timing gate locations were determined in post-processing based on L1/L2 measurements with sub-decimeter accuracy.

The purpose of the test was twofold.

1. Determine the faster ski (for DSV).
2. Compare the accuracy of position-based chronometry to the traditional approach based on timing cells.

Intersecting the GPS trajectories with the timing gates as depicted in Fig. 7.15 (page 109) allows determining intermediates based on positioning which can then be compared to those of the timing cells (Tab. 7.2).

To answer the question about the faster ski, the average split of the two skis is computed. The difference between the average splits $(29 - 101)$ amounts to $5 - 8/100$ s with a standard deviation of $27 - 74/100$ s (Tab. 7.2). As the standard deviation is much larger than the average difference, there is no statistical proof that ski 101 is faster than ski 29. To reach a conclusion about the faster ski, the test setup has to be reviewed.

Secondly, the accuracy of position-based chronometry is assessed. The difference between the individual splits derived by positioning and splits derived from timing cells is $2 - 7/100$ s with a standard deviation of $5 - 8/100$ s. In addition, the standard deviation of the time differences between the two sets of skis is similar for both methods (Tab. 7.2). Hence, both methods provide similar accuracies and lead to the same conclusion about the performance difference of the two skis.

A constant time difference between the two timing methods can be explained by the accuracy of the gate coordinates. However, the varying differences are caused by numerous factors.

- Firstly, the carrier-phase ambiguities could only be fixed during the first five runs due to adverse satellite signal reception conditions (northern exposure, slope bounded by woods). This explains the somewhat larger differences during the last five runs with floating ambiguities. Indeed, the varying accuracy of GPS positioning with float ambiguities is a major source of error: A positioning error of 50 cm at 60 km/h results in a timing error of 3/100 s. The experience, however, shows that the splits derived from L1 GPS data are only negligibly noisier than those derived from L1/L2 data because the relative position errors vary slowly.

- Secondly, the fact that the GPS antenna is placed on the helmet whereas the timing cells are intersected by the skier's feet or hands is a potential source of error: A longitudinal change in position of the skier's head with respect to his feet of 20 cm will cause a timing error of 1.2/100 s. However, if he intersects the split with his hands, the difference could become significant and might explain certain differences.

Unfortunately, the chronometry system based on the timing cells used in the test was not certified, and, therefore, no assertion about its timing accuracy can be made. Nevertheless, the timing accuracies achieved with both methods are equivalent. This demonstrates that position-based chronometry is an interesting alternative offering additional flexibility for evaluating the performance. Indeed, many virtual splits can be introduced without extra cost. This allows refining the evaluation of the skis depending on the slope, wind or snow conditions.

TAB. 7.2: Comparison between traditional and GPS chronometry.

	Start-Intermediate			**Start-Arrival**			Ambiguity
Ski	Cell [s]	GPS [s]	Diff. [1/100 s]	Cell [s]	GPS [s]	Diff. [1/100 s]	status
29	16.54	16.62	-8	36.73	36.76	-3	90% fixed
101	16.62	16.70	-8	36.75	36.78	-3	90% fixed
29	16.70	16.75	-5	36.68	36.72	-4	90% fixed
101	16.40	16.48	-8	36.39	36.42	-3	90% fixed
29	16.61	16.67	-6	36.66	36.68	-2	90% fixed
101	16.44	16.56	-13	36.44	36.51	-6	Float
29	16.58	16.59	-1	36.82	36.71	12	Float
101	16.45	16.44	1	36.55	36.45	9	Float
29	16.75	16.92	-17	37.45	37.61	-15	Float
101	17.00	17.10	-10	37.90	37.91	0	Float
Average splits [s]							
29	16.63	16.71		36.87	36.9		
101	16.58	16.66		36.81	36.81		
Standard deviation of the average splits [1/100 s]							
29	9	13		33	40		
101	25	27		63	63		
Time difference ski 29-101 [1/100 s]							
	5	5		6	8		
Standard deviation of the time difference ski 29-101 [1/100 s]							
	27	30		71	74		
Average time difference GPS-Cell [1/100 s]							
			-7			-2	
Standard deviation difference time GPS-Cell [1/100 s]							
			5			8	

7.5 Orientation Related Assessment - Skiing

For the development and performance analysis of some sport equipment or the evaluation of the athlete's technique, sport professionals rely on the knowledge about its orientation with respect to the direction of motion. In alpine skiing, the determination of accurate orientations of a ski is the prerequisite for analyzing acting forces. The latter needs to be decomposed with respect to the terrain to analyze potential and kinetic energies, as well as joint loading and energy transfers during a turn. Moreover, the edging and skidding angles can be assessed in relation to the technique of a skier.

Data from GPS/MEMS-IMU provide a new possibility to obtain such information more accurately and faster in comparison to optical methods (section 2.2.1). For a complete investigation, both skis need to be equipped with GPS antennas and MEMS-IMU sensors to recover the position and orientation parameters (Fig. 7.24). Based on the slope information derived from a digital terrain model $\mathbf{R}_n^{slope}$, the orientation of the sensor with respect to the ski $\mathbf{R}_{ski}^b$ and the sensor orientation from the GPS/MEMS-IMU integration $\mathbf{R}_b^n$, the orientation of the ski with respect to the slope $\mathbf{R}_{ski}^{slope}$ can be computed.

$$\mathbf{R}_{ski}^{slope} = \mathbf{R}_n^{slope} \cdot \mathbf{R}_b^n \cdot \mathbf{R}_{ski}^b \tag{7.5.1}$$

The local referential (x_{slope}, y_{slope}, z_{slope}) is defined as follows (Fig. 7.24): the xy-plane represents the local surface with the x-axis aligned to the maximum slope of the terrain. The heading is the angle between this fall line (x_{slope}) and the direction of the ski (x_{ski}). The roll describes the edging angle of the ski.

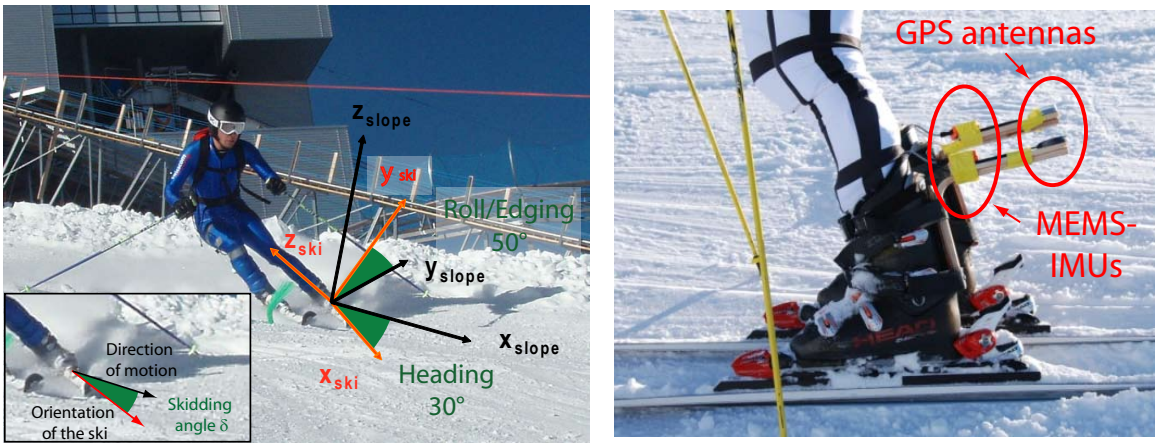

Fig. 7.24: Definition of the reference frames and illustration of the heading and roll (edging) angles in alpine skiing.

The zoom on the two turns illustrated in Fig. 7.25 allows studying the technique of the athlete.

- During the turn initiation ①, the ski is flat (Roll angle $\phi = 0$ deg).
- The steering phase of the turn ② lasts until the ski's orientation reaches the fall line (Heading angle $\psi = 0$ deg). During this phase, the roll (edging) angle increases gradually and reaches its maximum (approximately 50 deg).

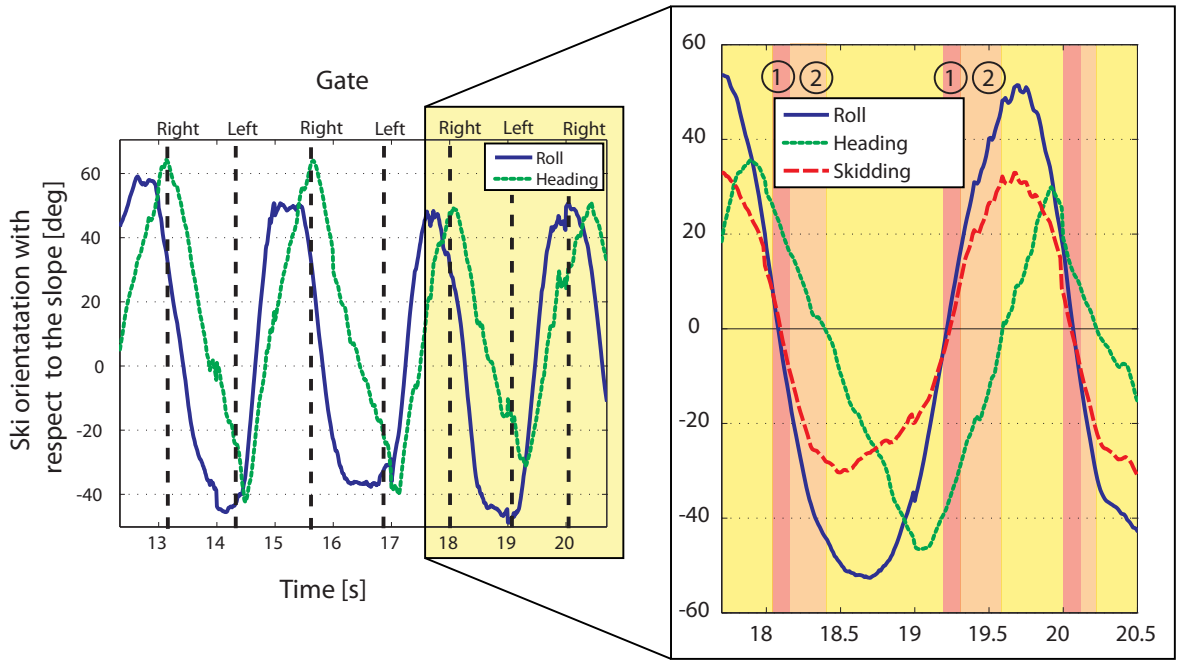

FIG. 7.25: Illustration of the roll (edging), heading and skidding angles during two turns.

The skidding of the skis can be obtained by analyzing their orientation with respect to the velocity vector also obtained by GPS/MEMS-IMU. First, the direction of the trajectory α can be derived from the velocity components v_N and v_E (FIG. 7.24).

$$\tan(\alpha) = \frac{v_N}{v_E} \tag{7.5.2}$$

Furthermore, the GPS/INS integration yields the heading ψ of the ski. Combining the two variables provides the skidding angles of the ski $\delta = \psi - \alpha$. In this example, the skidding angle is zero at the initiation and increases during the first phase of the curve (FIG. 7.25). To study the carving and slipping phases of a turn, it is interesting to display the skidding angles with respect to the trajectory (FIG. 7.26[1]). The left figure illustrates a trajectory where the athlete anticipated the curves by sliding, whereas on the right figure he carved the curves as properly as possible. The images of FIG. 7.27 underline the different technique of the athlete.

7.6 Orientation Related Assessment - Motorcycling

The accurate knowledge of position, velocity and orientation data is important for different aspects of motorcycling. In the sequel, innovative approaches with the GPS/MEMS-IMU system are described for this application. The following investigation is based on the experimental setup described in section 4.1 (FIG. 7.28).

[1]reproduced with the agreement of Swiss Federal Institute for Snow and Avalanche Research Davos (SLF)

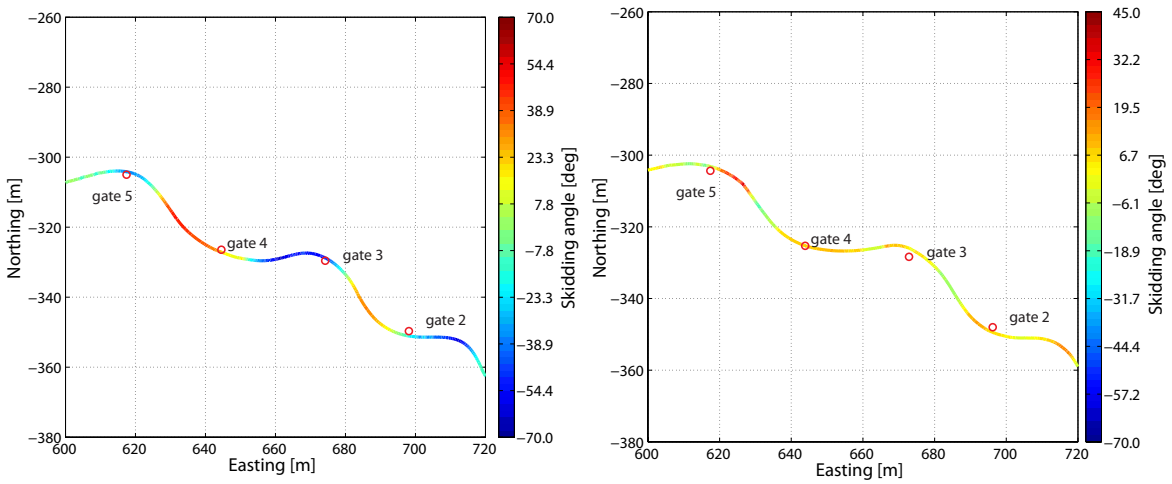

FIG. 7.26: Skidding angles of a run where the turns were anticipated with drifting (left) and of a run where the curves were carved as properly as possible (right).

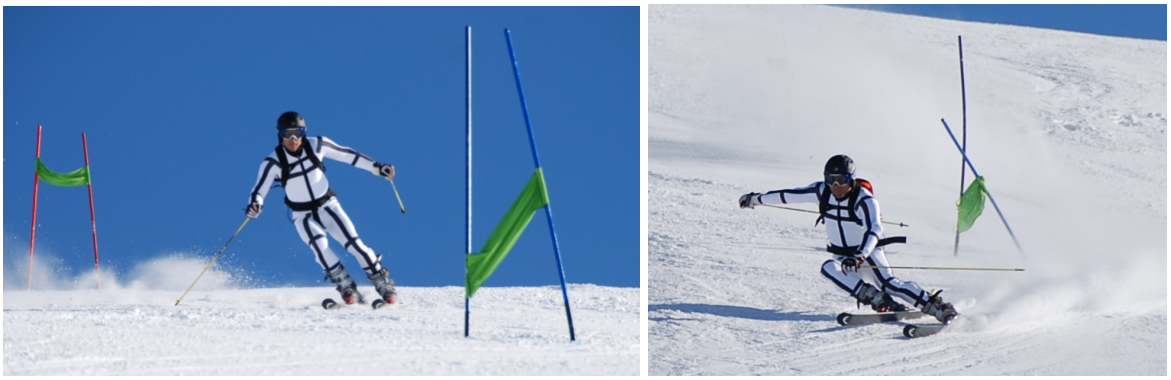

FIG. 7.27: Drifting (left) and carving (right).

7.6.1 Reference Frame Aspects

Similarly to the skiing experiment, the core information is provided from GPS/MEMS-IMU. Related to that are the derived quantities (i.e. accelerations, tire slips) visualized with respect to the parameters related to the motorcycle, e.g. torque or throttle (FIG. 7.30). FIG. 7.29 gives an example where the lateral slipping of the back wheel of the motorbike is visualized on two turns of the track.

When studying the motorcycle performance, various parameters are determined in different reference frames, e.g. in the reference frame fixed to the motorcycle (abbreviated with *moto*) and in the reference frame fixed to the track (abbreviation *track*, FIG. 7.28). Measurements (e.g. force or torque) can be converted between the two frames considering the rotation matrix $\mathbf{R}_b^n$ which expresses the orientation of the MEMS-IMU (body frame b) with respect to the navigation frame n (which is estimated in the GPS/MEMS-IMU integration), the slope of the

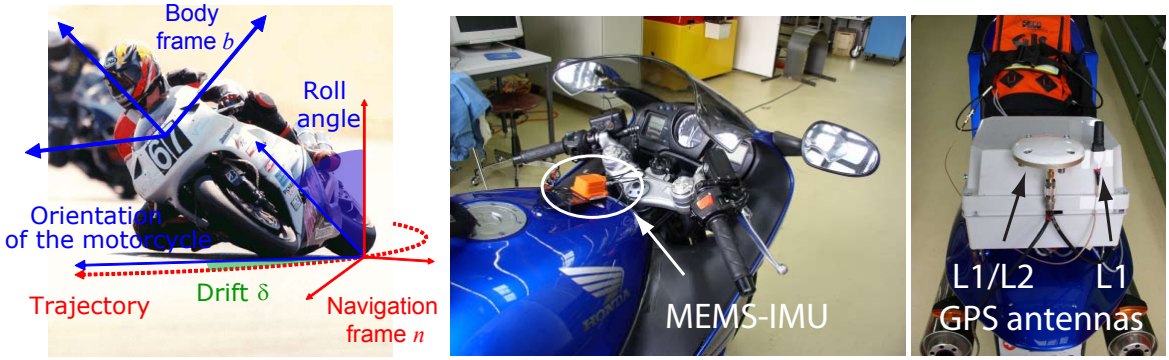

FIG. 7.28: GPS/MEMS-IMU system setup.

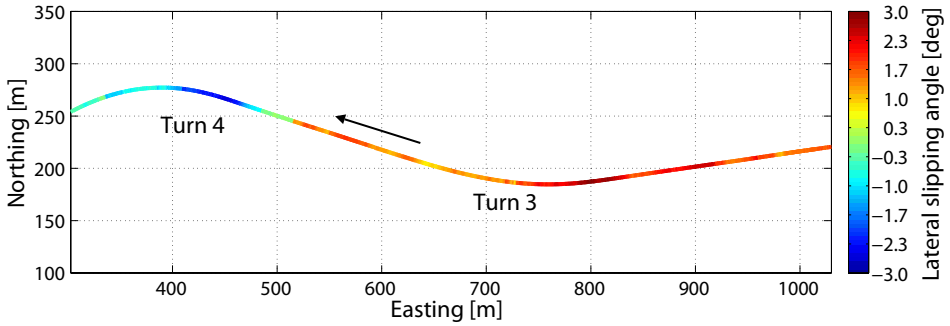

FIG. 7.29: Lateral slipping angles visualized on the GPS/MEMS-IMU derived trajectory.

track $\mathbf{R}_n^{track}$ (derived from a terrain model) and the misalignment of the MEMS-IMU with respect to the motorcycle $\mathbf{R}_{moto}^b$.

$$\mathbf{x}^{track} = \mathbf{R}_n^{track} \cdot \mathbf{R}_b^n \cdot \mathbf{R}_{moto}^b \cdot \mathbf{x}^{moto} \tag{7.6.1}$$

where $\mathbf{x}$ stands for observations in either frame.

7.6.2 Computation of the Lateral Slipping of Tires

The lateral slipping of tires can be observed directly with the use of GPS/INS derived results (section 7.5). FIG. 7.30 illustrates the estimated slipping angle with respect to the throttle and the traction/braking torque at the rear wheel respectively. The corresponding roll angle and the lateral acceleration are plotted as well (FIG. 7.30, left). The confidence level of the slipping angle ($1\sigma \approx 1$ deg) highlights the accuracy of the estimated slipping (FIG. 7.30, right). The presented experiment was conducted in winter and therefore the experienced dynamics were small. Nevertheless, statistically significant drifts were observed during the turns. The determined lateral acceleration is consistent with the roll angle. It can be noted that the motorcyclist was inclined even on a great portion of the straight lines contrary to his subjective feeling (FIG. 7.29). As revealed by FIG. 7.30, this inclination was compensated by the lateral acceleration.

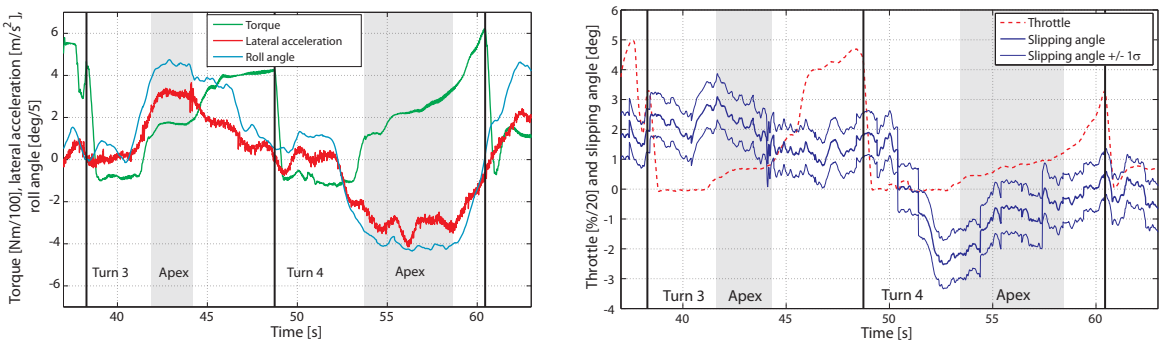

FIG. 7.30: Motorbike trajectory analysis: Torque, lateral accelerations, throttle and slipping angles with accuracy indicator (1σ). The black vertical lines indicate the beginning of the turns.

7.6.3 Evaluation of the Tire Characteristics

The "magic formula tire model" defined by [129] provides a mathematical expression from which forces and moments acting longitudinally or laterally from the road on the tire can be related to its slipping (FIG. 7.31).

$$\begin{aligned} Y(X) &= y(x) + \Delta y \\ x &= X + \Delta x \\ y(x) &= D \cdot \sin(C \cdot \arctan(B \cdot x - E \cdot (B \cdot x - \arctan(B \cdot x)))) \end{aligned} \tag{7.6.2}$$

where

- X represents the lateral slipping angle δ or the longitudinal slipping κ (equation 7.6.3).
- Y stands for the lateral force F_y, the aligning torque M_z or longitudinal force F_x.
- B, C, D, E, Δx and Δy are constant coefficients.

The constant coefficients are usually determined by laboratory experiments (on a drum). The GPS/MEMS-IMU system permits the calibration of these deterministic parameters in situ. First, force and torque measurements need to be referenced with respect to the road. This becomes possible due to the orientation determined by GPS/INS. The lateral slipping angle computed from GPS/INS needs only to be corrected for the steering of the front wheel, the tire radius variation due to speed, load and roll angle as well as the suspension pitch. The latter can be measured directly by means of linear potentiometers. The determination of the longitudinal slipping requires the knowledge of the longitudinal velocity of the motorbike (v_{sx} obtained from GPS/INS) and that the tire at the contact patch (v_x measured by means of digital speed sensors after compensation for the tire radius variation).

$$\kappa = -\frac{v_{sx}}{v_x} \tag{7.6.3}$$

Hence, the combination of all these measurements permits evaluating tires directly in the field. This calibration reflects the actual characteristics of the surface (e.g. temperature, roughness)

and therefore refines laboratory findings. The peak value of Y is often situated at approximately 10 deg of slipping and slipping angles up to 30 deg can be modeled. In this range, the accuracy of the slipping angles accounts therefore for $3 - 10\%$ of the error, whereas the torque and force measurements can be determined with an accuracy of $5\% \cdot Y$.

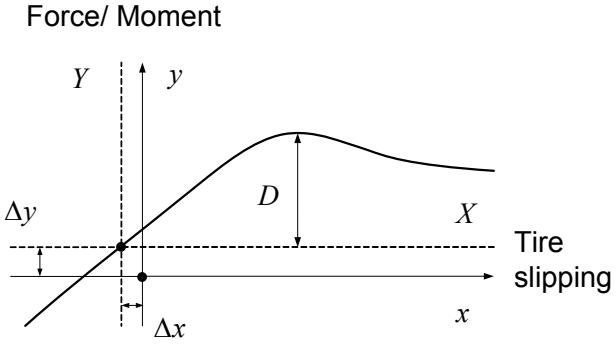

FIG. 7.31: Explanation of the coefficients of the "magic formula tire model" (equation 7.6.2).

7.6.4 Other Perspectives

Orientation determination also provides the essential data for the analysis of vibrations of a motorcycle. Indeed, the study of tire-related vibrations is today very important in motorbike racing. The so-called "chattering" vibrations may appear at the curves' entry, apex or exit and enforce the rider to reduce its speed. Currently, the evaluation of chattering is largely based on (subjective) driver information. This feeling is important, but it needs to be refined by means of numerical and experimental approaches [32]. One approach consists in using hybrid eigenvector bases to perform a modal synthesis [158, 157]. The vibratory behavior of a given tire is depending on two external parameters: ground load (vertical) and roll angle. To build the modal basis, a modal analysis is carried out in laboratory and provides the eigenfrequencies and eigenmodes for discrete values of these parameters. Then, vibration measurements are realized on the track and dedicated software is applied to identify the frequencies where chattering exists (rider data). The hybrid model is then used to reduce or cancel the chattering vibrations.

The efficiency of such a predictive model depends on the quality of experimental data. The use of the low-cost L1 GPS/MEMS-IMU system combined with a force measurement unit (body reference frame) allows determining accurate roll angles and evaluating the vertical force in the local reference frame. These two parameters are required for the definition of the precise dynamic conditions under which the vibrations appear.

Chapter 8

Conclusions and Perspectives

8.1 Conclusions

This research aimed at developing methods for performance analysis in sports based on trajectories derived from low-cost GPS and INS. Several aspects and algorithms have been presented and investigated by means of simulations and experimental testing. This section highlights the major findings. Firstly, the developed GPS/INS integration algorithms and their navigation performance are summarized. Secondly, the trajectory analysis strategy is recapitulated. Finally, recommendations for the selection of GPS/INS systems for different sport disciplines are given.

Methods and System Performance

The developed approach focuses on strapdown inertial navigation with light-weight and low-cost MEMS-type inertial sensors. In this approach, the inertial errors are mitigated through loose or close coupling with external GPS measurements. As MEMS-IMUs are subject to large systematic errors, a simplified error model was suggested and investigated. Furthermore, methods based on redundant MEMS-IMUs aiming at improving the orientation accuracy were evaluated. These methods and their performance are outlined in this section.

Integration algorithm. Extended and unscented Kalman filters have been identified as the most appropriate GPS/INS integration methods for the sport application because of their rapid convergence and reasonable computational complexity. Unlike the EKF, the UKF does not require the linearization of the system model for state and covariance propagation. Experiments revealed that the performance of both filter types was numerically equivalent. On the other hand, the UKF implementation tends to be computationally more expensive and numerically less stable than the EKF.

Inertial error model. The suitability of the proposed, simplified inertial error model was evaluated through a comparison of raw measurements between the tactical-grade reference IMU and the MEMS-IMU. It has been demonstrated that the numerous MEMS-IMU errors sources cannot be decorrelated effectively. The simplified approach allows appropriate modeling of the quickly evolving inertial sensor errors. Indeed, the differences between the

biases based on raw signal comparison and those estimated by the KF has been proven to be statistically insignificant.

As the conventional alignment methods used in GPS/INS are not applicable because of the sensor characteristics of the MEMS-IMU sensors, two alternatives were proposed. The first method is a modified coarse alignment algorithm where the sensing of the Earth's rotation rate is replaced by the measurement of the Earth's magnetic field. The second approach is a quaternion estimation method, also based on accelerometer and magnetometer measurements. Even though the performance of the two methods is satisfactory, the latter is preferred because of the absence of numerical singularities.

System performance. The loosely and closely coupled GPS/MEMS-IMU integration algorithms have been evaluated under reasonable satellite constellations (> 4 SVs). Under such conditions, the loosely coupled integration strategy provides slightly increased performance over the closely coupled approach, however the difference is marginal. The position accuracy is mainly driven by the precision of differential GPS ranging from dm accuracy for dual-frequency DGPS to 0.7 m with single-frequency DGPS and low-cost receivers. On the other hand, the velocity and orientation accuracy (0.2 m/s and 1-2 deg respectively) are less affected by the choice of receiver hardware, and they are hardly influenced by the MEMS-IMU integration approach.

Both, loosely and closely coupled integration schemes, were analyzed under less favorable satellite constellations (≤ 4 SVs) with single-frequency DGPS from geodetic receivers. For constellations consisting of 3 SVs, the closely coupled approach clearly outperforms the loosely coupled method and allows maintaining a submetric position accuracy during up to 30 s of reduced satellite signal reception. For the orientation, good results can be achieved even with only 2 SVs and via closely coupled integration. However, for satellite outages longer than 20 s with less than 2 SVs in view, the navigation errors are dominated by the inertial sensor errors and exceed the accuracy requirements for sports applications.

Inertial redundancy. A wide range of position accuracies can be covered depending on the GPS processing strategy and receiver quality. Hence, for applications with high position accuracy demands, dual-frequency receivers are recommended if cost and ergonomics are not obstacles. To improve the orientation accuracy, other approaches are required. A system of redundant IMUs provides an economically and ergonomically viable solution to improve navigation performance. Simulations and experiments have demonstrated that the orientation performance can be improved by $30 - 50\%$ with 4 sensors in skew-symmetric configuration. In addition, the following recommendations regarding the integration of redundant inertial sensors are given.

- Two integration approaches have been investigated: an algorithm based on a synthetic IMU, where the observations are fused into a compound set of measurements, and an extended mechanization approach, where the state vector is increased by individual biases per sensor. The second method is found to be more optimal for system calibration because the error characteristics of the individual sensors are considered separately. Furthermore, fault detection and direct noise estimation can be performed within this integration procedure whereas the synthetic approach requires cascade processing.
- Inertial error estimation is feasible even during static inertial alignment or during uniform motion, which enhances also the estimation of the initial orientation.

- Employing redundant IMUs enables direct noise estimation. Hence, less prior knowledge about the sensor characteristics and the dynamics is required.

Methodology for Trajectory Analysis in Sports

Trajectory modeling. For visualization convenience and for synchronization with other performance-relevant measurements, trajectories are modeled as continuous curves. As the quality of the GPS positioning varies with the receiver hardware and processing algorithms, a flexible approach for trajectory modeling was proposed. Dual-frequency GPS positions and velocities are conveniently smoothed by cubic splines. On the contrary, trajectories from single-frequency (and especially low-cost) GPS receivers are preferably preprocessed by additional Kalman filtering. Indeed, making use of the superior accuracy of the velocity measurements, the position quality can be increased. In addition, a matching algorithm was proposed that mitigates to a certain extent the systematic effects remaining in single-frequency GPS positioning. It is based on feature-based correspondence. Furthermore, the inclusion of accuracy indicators is indispensable to evaluate the significance of the performance parameters because it allows taking into account the varying navigation state accuracies.

Trajectory comparison. Besides the analysis of individual trajectories, the comparison of numerous trajectories is of utmost importance for sport applications. For this purpose, a spatial comparison method was introduced where equitemporal planes perpendicular to a reference track intersect with the other trajectories. Two main advantages of this method were highlighted.

- The performance can be evaluated at any preselected time or distance interval. Additional splits and (virtual) gates can be easily computed and interposed between the timing cells or gates. Thus, this approach presents an interesting alternative to traditional timing methods.
- Not only coordinate differences between the trajectories can be determined, but also any other attributes attached to the trajectories can be compared in a straightforward manner (e.g. elapsed time, velocities, accelerations, heart rates).

Trajectory-derived parameters. Besides the analysis of position, velocity and orientation, GPS/INS trajectories allow retrieving additional parameters for performance evaluation. For instance by comparing the trajectory of the ski to its orientation, its skidding angles can be derived. Combining this data with a digital terrain model allows determining the heading and edging of the skis. Similarly, the lateral slipping angles can be computed in motorcycling. The knowledge about the orientation of the motorbike is further required to correctly exploit torque and force measurements and to study the vibratory behavior of the pneumatics.

Recommendations

Three categories of sport applications, that rely on accurate trajectory determination, were identified: trajectory comparison, material testing and development, as well as motion analysis and rehabilitation. The choice of the adopted GPS/MEMS-IMU integration approach

eventually depends on the targeted application. Indeed, the cm to dm level for position accuracy is crucial only for few applications, namely those related to timing (material testing) and those disciplines where small trajectory differences are important. Therefore, the use of dual-frequency GPS receivers is reserved to few sport applications with higher accuracy needs and larger budgets. On the other hand, redundant MEMS-IMUs can be exploited when improved orientation estimation is required. Tab. 8.1 summarizes recommendations for the use of GPS/INS systems for the identified sport applications.

Tab. 8.1: Recommendations for trajectory determination in sports.

Trajectory comparison	
- Post-mission	L1 DGPS/MEMS-IMU
- Real time (e.g. TV broadcasting)	L1 GPS
- Chronometry	L1/L2 DGPS, evtl. coupled to MEMS-IMU
Material testing and development	
- Tire development, ski testing	L1 or L1/L2 DGPS/MEMS-IMU, evtl. SR-IMU
- Vibrations	L1 DGPS/MEMS-IMU at 400 Hz, evtl. SR-IMU
- Gliding and aerodynamic properties	L1 or L1/L2 DGPS/MEMS-IMU
Motion analysis and rehabilitation	
- Evaluation of the athlete's motion	L1 DGPS/MEMS-IMU (at lumbar #1)
- Energy transfer	L1 DGPS/MEMS-IMU (at lumbar #1)

8.2 Perspectives

During the development of this work, new research challenges have emerged that are worth further investigations.

GPS/MEMS-IMU integration automation. For a wider use, the GPS/MEMS-IMU systems need to be further automated. Unfortunately, optimal GPS processing and GPS/INS integration are far from being self-acting methods and require a lot of experience about the employed sensors and the mechanisms of the algorithms. Hence, future research should focus on the following aspects:

- Post-processing of GPS data is certainly more optimal for performance assessment because more sophisticated models can be exploited, e.g. for ambiguity resolution or cycle-slip detection. On the other hand, most GPS receivers offer real-time differential processing. If the communication setup can be effectively automated, this alternative can save user interaction at the cost of (slightly) reduced navigation performance.
- Separating position and velocity estimation during the processing makes more effective use of all available satellite measurements [41, 40]. In such a processing scheme, the accuracy of the velocity estimates and the relative positioning are potentially improved.
- Currently, the system initialization is performed on manually selected, static periods at the beginning or at the end of the runs. This phase can be automated by selecting static sections, or periods with constant orientation and speed. Likewise, static periods

during the sport performance should be recognized to perform re-initializations of the system. Knowledge about these intervals can then be considered in adaptive KF [111].

Inertial redundancy. Redundant IMUs are already used in many fields (e.g. aviation, robotics, virtual reality). In addition, the extension of this concept to MEMS-IMUs could be attractive to a wide range of applications (e.g. reliable low-cost navigation systems, airborne mapping, pedestrian navigation). The closer investigation of the following aspects could improve the navigation performance when using redundant (MEMS-)IMUs.

- Although the extended mechanization approach performs slightly better than the numerically less optimal synthetic IMU, it was reported that the estimated biases do not always correspond to the physical biases. This problem might be explained by the reduced observability of the system and might be overcome by geometrically constraining the inertial measurements. However, this hypothesis needs further investigation to assess the entire potential of the extended mechanization.
- The presented fault detection and identification approach based on the commonly used parity space method is unacceptable in case of redundant MEMS-IMUs for safety-critical applications. Thus, new methods need to be developed.

Performance evaluation in sports. The proposed trajectory modeling and comparison algorithms provide accurate results. However, it is a cascade approach and hence sub-optimal. Indeed, some information from GPS/INS processing is not introduced into the trajectory comparison algorithm. In addition, ground constraints and reference trajectories would ideally be integrated already during the GPS/INS integration.

The contribution of GPS/INS has been highlighted in skiing and motorcycling. However, trajectory determination, analysis and comparison can be of interest to many more disciplines:

- GPS-only applications limit the study of the performance during the different phases of a stroke (drive and recovery). Thanks to the high measurement frequency of the MEMS-IMUs, a profound analysis of the effectiveness of the strokes in rowing becomes conceivable.
- For the development of boats, its drifting could be evaluated with a GPS/INS system. Another interesting topic is the detection of false-starts in sailing. Indeed, today this is mainly done visually with limited accuracy (estimated to 1 m by professional referees). The generalized use of the low-cost GPS/INS system would reduce the subjectivity of this procedure.
- As soon as the system is capable of providing real-time results, it will provide interesting topics for the media. Displaying not only position and velocity, but also orientations of the athlete or equipment will enhance the appreciation of the sport performance. An experiment has been conducted at EPFL for the “Patrouille des Glaciers” which is an off-track skiing race in the Swiss Alps. Several teams have been equipped with low-cost GPS. Their performance was visualized on Internet and in the arrival area. Not only position was displayed, but also physiological measurements like heart rate, oxygen saturation of hemoglobin and SpO2 [133].

- Other developments at EPFL target the reconstruction of the body motion based on measurements of artificial magnetic fields [110] and MEMS-IMUs. In this context, the GPS/INS could provide the basic information about the trajectory and absolute orientation which will be completed by the relative motion of the human body.
- Energy transfer computations in sports are complex because they require the determination of the center of gravity of athletes. Reference [174] has shown that the lumbar point rather than the center of mass can be employed for the determination of kinetic and potential energies in running. Evaluating an anatomic point is experimentally easier and can be achieved e.g. with GPS/INS. Similar investigations are currently ongoing for downhill skiing and could be envisaged for other disciplines.

Bibliography

[1] W. Abdel-Hamid, T. Abdelazim, N. El-Sheimy, and G. Lachapelle. **Improvement of MEMS-IMU/GPS Performance Using Fuzzy Modeling**. *GPS Solutions*, 10(1):1–11, 2006.

[2] D.W. Allan. **Statistics of Atomic Frequency Standards**. *IEEE*, 54(2):221–230, 1966.

[3] D.J. Allerton and H. Jia. **A Review of Multisensor Fusion Methodologies for Aircraft Navigation Systems**. *The Journal of Navigation*, 58(3):405–417, 2005.

[4] Applanix. **PosProc**. Version 2.1.

[5] K.-H. Bae and D. Lichti. **Edge and Tree Detection from Three-Dimensional Unorganised Point Clouds from Terrestrial Laser Scanners**. In *Proceedings of the* 12^{th} *Australian Remote Sensing and Photogrammetry Conference, Fremantle, Australia*, 2004.

[6] J.B. Bancroft, G. Lachapelle, M.E. Cannon, and M. Petovello. **Twin IMU-HSGPS Integration for Pedestrian Navigation**. In *Proceedings of the ION GNSS, Savannah, GA, USA*, 2008.

[7] I.Y. Bar-Itzhack. **REQUEST – A New Recursive Algorithm for Attitude Determination**. In *Proceedings of the ION NTM, Santa Monica, CA, USA*, 1996.

[8] C. Barelle, A. Ruby, and M. Tavernier. **Cliqang: Un outil d'analyse cinématique simple et fonctionnel. Application au saut à ski**. In *Proceedings of the IXème Congrès International des Chercheurs en Activités Physiques et Sportives, Valence, France*, 2001.

[9] T. Beran, R.B. Langley, S.B. Bisnath, and L. Serrano. **High-Accuracy Point Positioning with Low-Cost GPS Receivers: How Good Can It Get?** In *Proceedings of the ION GNSS 2005, Long Beach, CA, USA*, 2005.

[10] Th. Blumenbach. ***GPS-Anwendungen in der Sportwissenschaft, Entwicklung eines Messverfahrens für das Skispringen***. PhD thesis, TU Dresden, 2005.

[11] Th. Blumenbach. ***Satellitennavigation - Anwendungen in der Sportwissenschaft***. Köln: Sport und Buch Strauss GmbH, 2005.

[12] S. Botton, F. Duquenne, Y. Egels, M. Even, and W. Pascal. ***GPS – localisation et navigation***. Hermes, 1997.

[13] M. S. Braasch. **Performance comparison of multipath mitigating receiver architectures**. In *Proceedings of the IEEE Aerospace Conference, Big Sky, MT, USA*, 2001.

[14] M. Brodie, A. Walmsley, and W. Page. **Fusion Motion Capture: A Prototype System Using Inertial Measurement Units and GPS for Biomechanical Analysis of Ski Racing**. *Sport Technology*, 1(1):17–28, 2008.

[15] A.M. Bruton, C.L. Glennie, and K.P. Schwarz. **Differentiation for High Precision GPS Velocity and Acceleration Determination**. *GPS Solutions*, 2(4):4–21, 1999.

[16] F. Burri. **Etude numérique pour l'optimisation d'ailerons de kitesurf**. Master's thesis, EPFL, 2006.

[17] M. Chansarkar. **Neural Networks in GPS Navigation**. *GPS Solutions*, 4(2):14–18, 2000.

[18] D.J. Cho, C. Park, and S.J. Lee. **An Assisted GPS Acquisition Method using L2 Civil Signal in Weak Signal Environment**. *Journal of Global Positioning Systems*, 3(1-2):25–31, 2004.

[19] Codamotion. http://www.codamotion.com/.

[20] I. Colomina and M. Blàzquez. **A Unified Approach to Static and Dynamic Modeling in Photogrammetry and Remote Sensing**. In *Proceedings of the XX^{th} ISPRS Congress, Istanbul, Turkey*, 2004.

[21] I. Colomina, M. Giménez, J.J. Rosales, M. Wis, A. Gómez, and P. Miguelsanz. **Redundant IMUs for Precise Trajectory Determination**. In *Proceedings of the XX^{th} ISPRS Congress, Istanbul, Turkey, Working Group I/5*, 2004.

[22] V. Constantin. **Intégration GPS/MEMS-IMU basée sur un filtre de Kalman "sigma-point"**. Master's thesis, EPFL, 2007.

[23] V. Constantin, A. Waegli, and J. Skaloud. **Le filtre de Kalman "unscented" – outil performant en géodésie cinématique**. *Géomatique Suisse*, 1:12–17, 2008.

[24] S. Corazza, L. Mündermann, A.M. Chaudhari, T. Demattio, C. Cobelli, and T.P. Andriacchi. **A Markerless Motion Capture System to Study Musculoskeletal Biomechanics: Visual Hull and Simulated Annealing Approach**. *Annals of biomedical engineering*, 34(6):1019–1029, 2006.

[25] N. Coulmy. ***Contribution at the energetic and kinematic motion analysis in cross-country skiing. Application to three disciplines in nordic skiing : cross-country skiing, biathlon, nordic combined. Comparative analysis of two 3D motion analysis systems using a stick human model and a volumic human model and application to case studies in cross-country skiing***. PhD thesis, Université de Grenoble 1, Saint-Martin-d'Hères, France, 2000.

[26] T. Creel, A.J. Dorsey, P.J. Mendicki, J. Little, R.G. Mach, and B.A. Renfro. **New, Improved GPS: the Legacy Accuracy Improvement Initiative**. *GPS World*, March 2006, 2006.

[27] Dartfish. http://www.dartfish.com/.

[28] C. De Boor. ***A Practical Guide to Splines***. Applied mathematical sciences, New York: Springer-Verlag, 2001.

[29] P. Dierckx. ***Curve and Surface Fitting with Splines***. New York: Oxford University Press Inc., 1993.

[30] M. Do, S. Ayer, and M. Vetterli. **Invariant Image Retrieval using Wavelet Maxima Moment**. In *Proceedings of the* 3^{rd} *International Conference on Visual Information Systems, Amsterdam, The Netherlands*, 1999.

[31] S. Ducret, P. Ribot, R. Vargiolu, J. Lawrence, and A. Midol. ***Analysis of Downhill Ski Performance using GPS and Grounding Force Recording***, pages 56–67. Science and Skiing III, 2005.

[32] M. Duvernier, P. Fraysse, V. Bomblain, and E. Dormegnie. **Tyre Modelling for NVH Engineering in ADAMS**. In *Proceedings of the* 1^{st} *MSC.ADAMS European User Conference*, 2002.

[33] B. Eisfeller, M. Irsigler, and T. Pany. **Code and Carrier Phase Tracking Performance of a Future Galileo RTK Receiver**. In *Proceedings of the European Navigation Conference ENC-GNSS 2002, Copenhagen, Denmark*, 2002.

[34] B. Eisfeller, C. Tiberius, T. Pany, and G. Heinrichs. **Real-Time Kinematic in the Light of GPS Modernisation and Galileo**. *Galileo's World*, Autumn 2002:28–34, 2002.

[35] N. El-Sheimy, H. Hou, and X. Niu. **Analysis and Modeling of Inertial Sensors Using Allan Variance**. *IEEE Transactions on Instrumentation and Measurement*, 57(1):140–149, 2008.

[36] N. El-Sheimy and X. Niu. **The Promise of MEMS to the Navigation Community**. *InsideGNSS*, March/April 2007, 2007.

[37] N. El-Sheimy, E.-H. Shin, and X. Niu. **Kalman Filter Face-Off**. *Inside GNSS*, March 2006, 2006.

[38] P. Enge. **GPS Modernization: Capabilities of the New Civil Signals**. In *Australian International Aerospace Congress*, 2003.

[39] S. Epiney. **Modélisation de la trajectoire pour l'analyse de performances sportives**. Project de semestre, EPFL, 2007.

[40] J.L. Farrell. ***GNSS Aided Navigation and Tracking: Inertially Augmented or Autonomous***. American Literacy Press, 2007.

[41] J.L. Farrell. **Don't Dump That Data!: Thorough Use of GNSS Measurements**. *InsideGNSS*, Fall 2008, 2008.

[42] S. Feng, W.Y. Ochieng, D. Walsh, and R. Ioannides. **A Measurement Domain Receiver Autonomous Integrity Monitoring Algorithm**. *GPS Solutions*, 10(2):85–96, 2006.

[43] Fédération Aéronautique Internationale FIA. ***Guidelines for the Use of GPS in Ballooning Competitions***, 2004.

[44] E. Frejinger. ***Route Choice Analysis : Data, Models, Algorithms and Applications***. PhD thesis, EPFL, 2008.

[45] E. Frejinger and M. Bierlaire. **Capturing Correlation with Subnetworks in Route Choice Models**. In *Proceedings of the* 11^{th} *International Conference on Travel Behavior Research, Kyoto, Japan*, 2006.

[46] FRWD. http://www.frwd.com/.

[47] M. Gad-el Hak. ***The MEMS Handbook***, volume 2.1-15. Taylor and Francis edition, 2006.

[48] E. Gai, J.V. Harrison, and K.C. Daly. **Generalized Likelihood Test for FDI in Redundant Sensor Configurations**. *Journal of Guidance and Control*, 2(1):9–17, 1979.

[49] E. Gai, J.V. Harrison, and K.C. Daly. **Performance of Two Redundant Sensor Configurations**. *IEEE Transactions on Aerospace and Electronic Systems*, 15(3):405–413, 1979.

[50] Galileo. **Mission High Level Definition**, 2002.

[51] Galileo. **Mission Requirements Document**, 2002.

[52] Garmin. http://www.garmin.com/.

[53] L. Ge, S. Han, and Ch. Rizos. **Multipath Mitigation of Continuous GPS Measurements Using an Adaptive Filter**. *GPS Solutions*, 4(2):19–30, 2000.

[54] A. Gelb. ***Applied Optimal Estimation***. The M.I.T. Press, 1994.

[55] G. Gibbons. **GPS and Galileo: Prospects for Building the Next Generation of Global Navigation Satellite Systems**. *Journal of Global Positioning Systems*, 3(1-2), 2004.

[56] P.T. Gibbs and H.H. Asada. **Wearable Conductive Fiber Sensors for Multi-Axis Human Joint Angle Measurements**. *Journal of NeuroEngineering and Rehabilitation*, 2(7), 2005.

[57] S. Godha and M.E. Cannon. **GPS/MEMS INS Integrated System for Navigation in Urban Areas**. *GPS Solutions*, 11(3):193–203, 2007.

[58] S. Gölnitz. **Die Unbestechlichen - Speedmessung mit GPS**. *Surf*, 6(40-4), 2003.

[59] Compe GPS. http://www.compegps.com.

[60] M.S. Grewal and A.P. Andrews. ***Kalman Filtering, Theory and Practice***. Prentice Hall, 1993.

[61] R. Grover Brown. **A Baseline GPS RAIM Scheme and a Note on the Equivalence of three RAIM Methods**. *The Journal of Navigation*, 39(3):301–316, 1992.

[62] S. Gruenig. **Analyse de courses de ski grâce à l'utilisation de mesures accélérométriques et de GPS**. Master's thesis, EPFL, 2000.

[63] S. Guerrier. **Application of Artificial Neural Networks in GPS/MEMS-IMU Integration**. Project de semestre, EPFL, 2007.

[64] S. Guerrier. **Integration of Skew-Redundant MEMS-IMU with GPS for Improved Navigation Performance**. Master's thesis, EPFL, 2008.

[65] F. Gustafsson, F. Gunnarsson, N. Bergman, U. Forssell, J. Jansson, R. Karlsson, and P.-J. Nordlund. **Particle Filters for Positioning, Navigation and Tracking**. *IEEE Transactions on Signal Processing*, 50(2):425–437, 2002.

[66] Gyro, Accelerometer Panel of the IEEE Aerospace, and USA Electronic Systems Society. **IEEE 1293 Standard Specification Format Guide and Test Procedure for Linear, Single-Axis, Non-gyroscopic Accelerometers**, 1999.

[67] R. Hatch. **The Synergism of GPS Code and Carrier Measurements**. In *Proceedings of the 3^{rd} International Geodetic Symposium on Satellite Doppler Positioning, Las Cruces, NM, USA*, 1982.

[68] R. Hatch, J. Jung, P. Enge, and B. Pervan. **Civilian GPS: The Benefits of Three Frequencies**. *GPS Solutions*, 3(4):1–9, 2000.

[69] G. Hein. **From GPS and GLONASS via EGNOS to Galileo Positioning and Navigation in the Third Millennium**. *GPS Solutions*, 3(4):39–47, 2000.

[70] G. Hein, J. Godet, J.-L. Issler, J.-C. Martin, Ph. Erhard, R. Lucas, and T. Pratt. **Status of Galileo Frequency and Signal Design**. In *Proceedings of the ION GPS 2002, Portland, OR, USA*, 2002.

[71] G. Hein, M. Irsigler, J. Rodriguez, and T. Pany. **Performance of Galileo L1 Signal Candidates**. In *Proceedings of the European Navigation Conference ENC-GNSS 2004, Rotterdam, The Netherlands*, 2004.

[72] C.J. Hernando, R. Roldán, and M. Aguilera. **On the Evaluation of EGNOS User Performances versus Mission Navigation Requirements**. In *Proceedings of the ENC-GNSS 2008, Toulouse, France*, 2008.

[73] Ch. Hide, T. Moore, and M. Smith. **Adaptive Kalman Filtering for Low Cost INS/GPS**. In *Proceedings of the ION GPS 2002, Portland, OR, USA*, 2002.

[74] H. Hou. **Modeling Inertial Sensors Errors using Allan Variance**. Master's thesis, Geomatics Engineering, University of Calgary, 2004.

[75] J. How, N. Pohlman, and C.-W. Park. **GPS Estimation Algorithms for Precise Velocity, Slip and Race-Track Position Measurements**. In *Proceedings of the SAE Motorsports Engineering Conference and Exhibition*, 2002.

[76] D.A. Howe, R.L. Beard, A. Greenhall, F. Vernotte, W.J. Riley, and T.K. Peppler. **Enhancements to GPS Operations and Clock Evaluations Using "Total" Hadamard Deviation**. *IEEE Transactions on Ultrasonics, Ferroelectrics and Frequency Control*, 52, 2005.

[77] Y.H. Hu. ***Handbook of Neural Network Signal Processing***. CRC Press, Inc., 2000.

[78] L. Huguenin and B. Merminod. **Estimation avancée – Transformations de coordonnées: Généralités et similitudes 2-D**, 2002. Polycopié, EPFL.

[79] D. Ineichen, E. Brockmann, and S. Schaer. **Enhancing the Swiss Permanent GPS Network (AGNES) for GLONASS**. In *Subcommission for the European Reference Frame (EUREF), London, UK*, 2007.

[80] J.-L. Issler, G.W. Hein, J.-C. Martin, Ph. Erhard, R. Lucas-Rodriguez, and T. Pratt. **Galileo Frequency and Signal Design**. *GPS World*, Juli 2003, 2003.

[81] C. Jekeli. ***Inertial Navigation Systems with Geodetic Applications***. Walter de Gruyter, Berlin, 2001.

[82] S.J. Julier. **The Scaled Unscented Transformation**. *Proceedings of the American Control Conference*, 6:4555–4559, 2002.

[83] S.J. Julier. **The Spherical Simplex Unscented Transformation**. In *Proceedings of the IEEE American Control Conference, Denver, CO, UK*, 2003.

[84] S.J. Julier and J.K. Uhlmann. **A General Method for Approximating Nonlinear Transformations of Probability Distributions**. Technical report, Department of Engineering Science, University of Oxford, 1996.

[85] R.E. Kalman. **A New Approach to Linear Filtering and Prediction Problems**. *Transactions of the ASME-Journal of Basic Engineering*, 82(Series D):35–45, 1960.

[86] T. Kitasuka, T. Nakanishi, and A. Fukuda. **Design of WiPS: WLAN-Based Indoor Positioning System**. *Korea Multimedia Society*, 7(4):15–29, 2003.

[87] V. Klimov, V. Persev, S. Revnivykh, V. Mitrikas, V. Kossenko, V. Zvonar, V. Dvorkin, E. Andruschak, and A. Tyulyakov. **GLONASS Status, Performance and Perspectives**. In *Proceedings of the ION GNSS 2005, Long Beach, CA, USA*, 2005.

[88] P. Krenn. **GPS Applikationen im Sport**. Master's thesis, TU Graz, 2008.

[89] U. Krogmann. **Artificial Neural Networks for Inertial Sensor Fault Diagnosis**. In *Proceedings of the Symposium of Gyro Technology*, Stuttgart, Germany, 1995.

[90] Q. Ladetto. ***Capteurs et algorithmes pour la localisation autonome en mode pédestre***. PhD thesis, EPFL, 2002.

[91] R.B. Langley. **Smaller and Smaller: The Evolution of the GPS Receiver**. *GPS World*, April 2000, 2000.

[92] M. Lehmann. **Réalisation d'un serveur de corrections GPS accessible par GPRS**. Master's thesis, EPFL, 2005.

[93] A. Lehtinen. **Doppler Positioning with GPS**. Master's thesis, Tampere University of Technology, Finland, 2008.

[94] A. Leick. ***GPS Satellite Surveying***. John Wiley & Sons, 2^{nd} edition, 1995.

[95] Y. Li, A. Dempster, B. Li, J. Wang, and C. Rizos. **A Low-Cost Attitude Heading Reference System by Combination of GPS and Magnetometers and MEMS Inertial Sensors for Mobile Applications**. *Journal of Global Positioning Systems*, 5(1-2):90–97, 2006.

[96] Y. Li, J. Wang, C. Rizos, P. Mumford, and W. Ding. **Low-Cost Tightly Coupled GPS/INS Integration based on a Nonlinear Kalman Filtering Design**. In *Proceedings of the ION NTM, Monterey, CA, USA*, 2006.

[97] Ph. Limpach. **Trajectographie de courses de ski avec GPS**. Master's thesis, EPFL, 2003.

[98] Spoat live tracking. http://www.prosoftconsult.at/spoat/.

[99] H.J. Luinge and P.H. Veltink. **Inclination Measurement of Human Movement Using a 3-D Accelerometer With Autocalibration**. *IEEE Transactions on Neural Systems and Rehabilitation Engineering*, 12(1):112–121, 2004.

[100] H.J. Luinge and P.H. Veltink. **Measuring Orientation of Human Body Segments using Miniature Gyroscopes and Accelerometers**. *Medical and Biological Engineering and Computing*, 43(2):273–282, 2005.

[101] Mathworks. **Matlab**. Version 7.3.0.

[102] R.J.Y. McLeod and M.L. Baart. ***Geometry and Interpolation of Curves and Surfaces***. Cambridge University Press, Cambridge, 1998.

[103] J.S. Meditch. ***Stochastic Optimal Linear Estimation and Control***. McGraw-Hill, New York, 1969.

[104] A. Medvedev. **Fault Detection and Isolation by a Continuous Parity Space Method**. *Automatica*, 31(7):1039–1044, 1995.

[105] C. Meichtry. **Trajectory Modeling from GPS Data Applied in Ski**. Master's thesis, EPFL, 2006.

[106] B. Merminod and J. Skaloud. **DGPS-Calibrated Accelerometric System for Dynamic Sports Events**. In *Proceedings of the ION GPS 2000, Salt Lake City, UT, USA*, 2000.

[107] S. Meyer. **Etude des signatures de vitesse et d'accélération du skieur lors de virages définis de slalom**. Master's thesis, Université de Neuchâtel, 2008.

[108] F. Michahelles, E. Crameri, and B. Schiele. **Design, Implementation and Testing of a Wearable Sensing System for Professional Downhill Skiing in Cooperation with Trainers**. In 2^{nd} *International Forum on Applied Wearable Computing (IFAWC 2005), Zurich, Switzerland*, 2005.

[109] F. Michahelles and B. Schiele. **Sensing and Monitoring Professional Skiers**. *Pervasive Computing, IEEE*, 4(3):40–45, 2005.

[110] Polhemus MINUTEMAN. http://www.polhemus.com/.

[111] A.H. Mohamed and K.P. Schwarz. **Adaptive Kalman Filtering for INS/GPS**. *Journal of Geodesy*, 73:193–203, 1999.

[112] S. Nasser and N. El-Sheimy. **A Combined Algorithm of improving INS Rrror Modeling and Sensor Measurements for Accurate INS/GPS Navigation**. *GPS solutions*, 10:29–39, 2006.

[113] S. Nasser and N. El-Sheimy. **INS Error Model Improvement for Enhanced INS/GPS Navigation During GPS Signal Blockage Periods**. *Survey Review*, 38(308), 2006.

[114] J. Nocedal and S.J. Wright. ***Numerical Optimization***. Springer Verlag, New York, 1999.

[115] A. Noureldin, A. El-Shafie, and M.R. Taha. **Optimizing Neuro-Fuzzy Modules for Data Fusion of Vehicular Navigation Systems using Temporal Cross-Validation**. *Engineering Applications of Artificial Intelligence*, 20(1):49–61, 2007.

[116] Novatel. **GrafNav**. Version 7.6.

[117] J. Oaks, M.M. Largay, W.G. Reid, and J.A. Buisson. **Comparative Analysis of GPS Clock Performance Using Both Code-Phase and Carrier-Derived Pseudorange Observations**. In *Proceedings of the* 36^{th} *Annual Precise Time and Time Interval (PTTI) Meeting, Reston, VA, USA*, 2004.

[118] J. Oaks, K. Senior, M.M. Largay, and R. Beard. **NRL Analysis of GPS On-Orbit Clocks**. In *Proceedings of the Frequency Control Symposium and Exposition*, 2005.

[119] D. O'Brien. **Radio Freedom**. *New Scientist*, 2444, 2004.

[120] M. O'Donnel, T. Watson, J. Fisher, S. Simpson, G. Brodin, D. Walsh, and E. Bryant. **Galileo Performance: GPS Interoperability and discriminators for Urban and Indoor Environments**. *GPS World*, June 2003, 2003.

[121] The Institute of Electrical and Electronics Engineers Inc. **IEEE 1554 Recommended Practice for Inertial Sensor Test Equipment, Instrumentation, Data Acquisition and Analysis**, 2005.

[122] World Magnetic Model of the United States National Geospatial-Intelligence Agency. http://www.ngdc.noaa.gov/geomag/WMM/DoDWMM.shtml.

[123] K. O'Keefe. **Availability and Reliability Advantages of GPS/Galileo Integration**. In *Proceedings of the ION GPS 2001, Salt Lake City, UT, USA*, 2001.

[124] I. Oppermann, L. Stoica, A. Rabbachin, Z. Shelby, and J. Haapola. **UWB Wireless Sensor Networks: UWEN – A Practical Example**. *IEEE Radio Communications*, 2004.

[125] G. Opshaug and P. Enge. **GPS and UWB for Indoor Navigation**. In *Proceedings of the ION GPS 2001, Salt Lake City, UT, USA*, 2001.

[126] G. Opshaug and P. Enge. **Integrated GPS and UWB Navigation System**. In *Proceedings of the IEEE UWB Science and Technology (UWBST) Conference, Baltimore, MD, USA*, 2002.

[127] Organicmotion. http://www.organicmotion.com/.

[128] A. Osman, B. Wright, S. Nassar, A. Noureldin, and N. El-Sheimy. **Multi-Sensor Inertial Navigation Systems Employing Skewed Redundant Inertial Sensors**. In *Proceedings of the ION GNSS 2006, Fort Worth, TX, USA*, 2006.

[129] H.B. Pacejka and E. Bakker. **The Magic Formula Tyre Model**. *Vehicle System Dynamics – International Journal of Vehicle Mechanics and Mobility*, 21:1–18, 1992.

[130] M.E. Parés. **On the Development of an IMU Simulator**. Master's thesis, Universitat Politècnica de Catalunya, Spain, 2008.

[131] M.E. Parés, J.J. Rosales, and I. Colomina. **Yet another IMU Simulator: Validation and Applications**. In *Proceedings of Eurocow 2008, Castelldefels, Spain*, 2008.

[132] B.W. Parkinson and J.J. Spilker. ***Global Positioning System: Theory and Application***. American Institute of Aeronautics and Astronautics, 1996.

[133] La patrouille des Glaciers 2008. http://polypdg.epfl.ch/.

[134] A.J. Pejsa. **Optimum Skewed Redundant Inertial Navigators**. *AIAA Journal*, 12:899–902, 1974.

[135] X. Pennec. **Computing the Mean of Geometric Features: Application to the Mean Rotation**. Unité de recherche INRIA Sophia Antipolis, Rapport de recherche no. 3371, 1998.

[136] O. Perrin, M. Scaramuzza, Th. Buchanan, S. Soley, P.-Y. Gilliron, and A. Waegli. **Challenging EGNOS in the Swiss Alps**. In *Proceedings of the European Navigation Conference ENC-GNSS 2003, Graz, Austria*, 2003.

[137] S. Pittet, V. Renaudin, Merminod. B., and M. Kasser. **UWB and MEMS Based Indoor Navigation**. *Royal Journal of Navigation*, 61(03):369–384, 2008.

[138] I. Planovsky and J. Hefty. **GPS Antenna Phase Center Position: Precision, Accuracy and Time Variability**. In *Proceedings of the EGS XXVII General Assembly, Nice, France*, 2002.

[139] Polar. http://www.polar.fi/.

[140] S. Revnivykh. **Status and Development of GLONASS**. In *Proceedings of the ION GPS/GNSS 2003, Portland, OR, USA*, 2003.

[141] S. Revnivykh. **GLONASS Program Update**. In *Proceedings of the ION GNSS 2008, Savannah, GA, USA*, 2008.

[142] S. Revnivykh. **GLONASS Status and Progress**. In *Proceedings of the ION GNSS 2008, Savannah, GA, USA*, 2008.

[143] J.G. Richards. **The Measurement of Human Motion: A Comparison of Commercially Available Systems**. *Human Movement Science*, 18(5):589–602, 1999.

[144] P. Roduit. ***Trajectory Analysis using Point Distribution Models: Algorithms, Performance Evaluation, and Experimental Validation using Mobile Robots***. PhD thesis, EPFL, 2008.

[145] P. Roduit, A. Martinoli, and J. Jacot. **A Quantitative Method for Comparing Trajectories of Mobile Robots using Point Distribution Models**. In *Proceedings of the IEEE/RSJ International Conference on Intelligent Robots and Systems, San Diego, CA, USA*, 2007.

[146] D. Roetenberg, H.J. Luinge, C.T.M. Baten, and P.H. Veltink. **Compensation of Magnetic Disturbances Improves Inertial and Magnetic Sensing of Human Body Segment Orientation**. *IEEE Transactions on Neural Systems and Rehabilitation Engineering*, 13(3):395–405, 2005.

[147] J.J. Rosales and I. Colomina. **A Flexible Approach for the Numerical Solution of the INS Mechanization Equations**. In *Proceedings of the VI Setmana Geomàtica de Barcelona, Spain*, 2005.

[148] S. Ryan and G. Lachapelle. **Augmentation of DGNSS with Dynamic Constraints for Marine Navigation**. In *Proceedings of the ION GPS 1999, Nashville, TN, USA*, 1999.

[149] S. Ryan and G. Lachapelle. **Impact of GPS/Galileo Integration on Marine Navigation**. In *Proceedings of the IAIN World Congress – ION Annual Meeting 2000*, 2000.

[150] S. Ryan, M. Petovello, and G. Lachapelle. **Augmentation of GPS for Ship Navigation in Constricted Waterways**. In *Proceedings of the ION NTM, Long Beach, CA, USA*, 1998.

[151] NRCtech SA. http://www.nrctech.ch.

[152] C. Satirapod and P. Homniam. **GPS Precise Point Positioning Software for Ground Control Point Establishment in Remote Sensing Applications**. *Journal of Surveying Engineering (ASCE)*, 132(1):11–14, 2006.

[153] P.G. Savage. **Strapdown Inertial Navigation Integration Algorithm Design Part 1: Attitude Algorithms**. *Journal of Guidance, Control and Dynamics*, 21(1):19–28, 1998.

[154] Ph. Schaer, J. Skaloud, and Ph. Tomé. **Towards In-Flight Quality Assessment of Airborne Laser Scanning**. In *Proceedings of the XXI ISPRS Congress, Beijing, China*, 2008.

[155] S. Schaer. ***Mapping and Predicting the Earth's Ionosphere Using the Global Positioning System***. PhD thesis, Astronomical Institute, University of Berne, Switzerland, 1999.

[156] A. Scheidegger. **Energy Management Optimization for a Solar Vehicle**. Master's thesis, EPFL, 2004.

[157] A. Schorderet. ***Synthèse modale et problème inverse en dynamique des structures***. PhD thesis, EPFL, 1997.

[158] A. Schorderet and Th. Gmür. **Structural Dynamics Optimization based on a Hybrid Inverse Synthesis Method using a Quadratic Approximation**. *ASME Transactions : Journal of Vibration and Acoustics*, 126(2):253–259, 2004.

[159] M.D. Schuster and S.D. Oh. **Three-Axis Attitude Determination from Vector Observations**. *Journal of Guidance and Control*, 4(1):70–77, 1981.

[160] K.P. Schwarz and N. El-Sheimy. **Future Positioning and Navigation Technologies**. Study report for Batelle, Columbus Division and Topographic Engineering Center, Fort Belvoir, VA, USA, 1999.

[161] K.P. Schwarz, M. Wei, and M. Van Gelderen. **Aided Versus Embedded – A Comparison of two Approaches to GPS/INS Integration**. In *Proceedings of the IEEE PLANS 1994, Las Vegas, NV, USA*, 1994.

[162] C. Seynat, A. Kealy, and K. Zhang. **A Performance Analysis of Future Global Navigation Satellite Systems**. *Journal of Global Positioning Systems*, 3(1-2):232–241, 2004.

[163] L. Shapiro. **Towards a vision-based motion framework**. Technical report, Oxford University, 1991.

[164] L.S. Shapiro and M. Brady. **Feature-Based Correspondence: an Eigenvector Approach**. *Image Vision Computing*, 10(5):283 – 288, 1992.

[165] X. Shen and Y. Gao. **Kinematic Processing Analysis of Carrier Phase based Precise Point Positioning**. In *Proceedings of FIG XXII International Congress, Washington DC, USA*, 2002.

[166] E.-H. Shin. ***Estimation Techniques for Low-Cost Inertial Navigation***. PhD thesis, UCGE Report Number 20219, 2005.

[167] A. Simsky and F. Boon. **New Standalone GPS Navigation Algorithms**. *European Journal of Navigation*, 1(2):34–40, 2003.

[168] J. Skaloud and H. Gontran. **Techniques GPS-RTK appliquées à la trajectographie**. *XYZ*, 99(2e semestre 2004), 2004.

[169] J. Skaloud, H. Gontran, and B. Merminod. **GSM-Distributed RTK for Precise Analysis of Speed Skiing**. In *Proceedings of the 8^{th} European Navigation Conference ENC-GNSS 2004, Rotterdam, The Netherlands*, 2004.

[170] J. Skaloud and K. Legat. **Navigation Techniques**. Lecture notes EPFL, 2007.

[171] J. Skaloud and Ph. Limpach. **Synergy of CP-DGPS, Accelerometry and Magnetic Sensors for Precise Trajectography in Ski Racing**. In *Proceedings of the ION GPS/GNSS 2003, Portland, OR, USA*, 2003.

[172] J. Skaloud and B. Merminod. **DGPS-Calibrated Accelerometric System for Dynamic Sports Events**. In *Proceedings of the ION GPS, Salt Lake City, UT, USA*, 2000.

[173] J. Skaloud, J. Vallet, K. Keller, G. Veyssiére, and O. Kölbl. **An Eye for Landscapes – Rapid Aerial Mapping with Handheld Sensors**. *GPS World*, May 2006, 2006.

[174] J. Slawinski, V. Billat, J.-P. Koralsztein, and M. Tavernier. **Use of Lumbar Point for the Estimation of Potential and Kinetic Mechanical Power in Running**. *Journal of applied Biomechanics*, 20:324–331, 2004.

[175] J. P. Snyder. ***Map Projections – A Working Manual***. U.S. Geological Survey Professional Paper 1395. United States Government Printing Office, Washington, D.C., 1987.

[176] A. Somieski, E. Favey, and C. Bürgi. **Precise Point Positioning with Single-Frequency Mass Market Receivers**. In *Proceedings of the ION GNSS 2008, Savannah, GA, USA*, 2008.

[177] B. Southall, B. F. Buxtony, and J.A. Marchant. **Controllability and Observability: Tools for Kalman Filter Design**. In *British Machine Vision Conference 1998, Southampton, UK*, 1998.

[178] Virtual Spectator. http://www.virtualspectator.co.nz.

[179] Sportvision. http://www.sportvision.com/.

[180] M. St-Pierre and D. Gingras. **Comparison between the Unscented Kalman Filter and the Extended Kalman Filter for the Position Estimation Module of an Integrated Navigation Information System**. In *Proceedings of the IEEE Intelligent Vehicles Symposium, Parma, Italy*, 2004.

[181] T. Stansell, R. Fontana, and W. Cheung. **The Modernized L2 Civil Signal**. *GPS World*, September 2001, 2001.

[182] O. Staub. ***Electrically Small Antennas***. PhD thesis, EPFL, 2000.

[183] G. Strang and K. Borre. ***Linear Algebra, Geodesy and GPS***. Wellesley-Cambridge Press, 1997.

[184] J.M. Strus, M. Kirkpatrick, and J.W. Sinko. **Development of a High Accuracy Pointing System for Maneuvering Platforms**. *InsideGNSS*, March/April 2008, 2008.

[185] M.A. Sturza. **Navigation System Integrity Monitoring Using Redundant Measurements**. *Journal of the Institute of Navigation*, 35(4):69–87, 1988.

[186] S. Sukkarieh. ***Low Cost, High Integrity, Aided Inertial Navigation Systems for Autonomous Land Vehicles***. PhD thesis, University of Sydney, Australia, 2000.

[187] S. Sukkarieh and M. George. **Tightly Coupled INS/GPS with Bias Estimation for UAV Applications**. In *Proceedings of the Australian Conference on Robotics and Automation, Sydney, Australia*, 2005.

[188] S. Sukkarieh, P. Gibbens, B. Brocholsky, K. Willis, and H.F. Durrant-Whyte. **A Low-Cost Redundant Inertial Measurement Unit for Unmanned Air Vehicles**. *The International Journal of Robotics Research*, 19(11):1089–1103, 2000.

[189] M. Supej, O. Kugovnik, and B. Nemec. ***Energy Principle used for Estimating the Quality of a Racing Ski Turn***, pages 216–227. Science and Skiing III, 2005.

[190] Tiempo. http://www.tiempo-ic.com/.

[191] D.H. Titterton and J.L. Weston. ***Strapdown Inertial Navigation Technology***. Peter Peregrinus Ltd, 1997.

[192] R. Toda, N. Takeda, T. Murakoshi, S. Nakamura, and M. Esashiy. **Electrostatically Levitated Spherical 3-Axis Accelerometer**. In *Proceedings of the* 15^{th} *IEEE international conference*, 2002.

[193] Ph. Tomé. ***Integration of Inertial and Satellite Navigation Systems for Aircraft Attitude Determination***. PhD thesis, University of Porto, Portugal, 2002.

[194] Ph. Tomé and O. Yalak. **Improvement of Orientation Estimation in Pedestrian Navigation by Compensation of Magnetic Disturbances**. *ION Journal of Navigation*, 55(3):179–190, 2008.

[195] F. Toran-Marti and J. Ventura-Traveset. **The ESA EGNOS Project: The First Step of the European Contribution to the Global Navigation Satellite System (GNSS)**. Technical report, GNSS-1 Project Office, 2004.

[196] F. Toran-Marti, J. Ventura-Traveset, E. Gonzalez, M. Toledo, A. Catalina, C. Barredo, and A. Salonico. **Position via Internet: SISNeT catches GPS in Urban Canyons**. *GPS World*, April 2004, 2004.

[197] D. Törnqvist. ***Statistical Fault Detection with Applications to IMU Disturbances***. PhD thesis, Linköping, Sweden, 2006.

[198] TracEdge. http://www.tracedge.com/.

[199] Trip tracker. http://www.ttsm.com/.

[200] TracTrac. http://www.tractrac.com/.

[201] USA-EU. **Agreement on the Promotion, Provision and Use of Galileo and GPS Satellite-Based Navigation Systems and related Applications**, 2004. 21. Juli 2004.

[202] R. Van der Merwe. ***Sigma-Point Kalman Filters for Probabilistic Inference in Dynamic State-Space Models***. PhD thesis, OGI School of Science and Engineering at Oregon Health and Science University, 2004.

[203] R. Van der Merwe and E.A. Wan. **The Unscented Kalman Filter for Nonlinear Estimation**. In *Proceedings of IEEE Symposium 2000, Lake Louise, AB, USA*, 2000.

[204] R. Van der Merwe and E.A. Wan. **Efficient Derivative-Free Kalman Filters for Inline Learning**. In *Proceedings of the European Symposium on Artificial Neural Networks 2001, Bruges, Belgium*, 2001.

[205] R. Van der Merwe, E.A. Wan, and S.J. Julier. **Sigma-Point Kalman Filter for Nonlinear Estimation and Sensor-Fusion – Applications to Integrated Navigation**. In *Proceedings of the AIAA Guidance, Navigation, and Control Conference and Exhibit, Providence, RI, USA*, 2004.

[206] A. J. Van Dierendonck and M. S. Braasch. **Evaluation of GNSS receiver correlation processing techniques for multipath and noise mitigation**. In *Proceedings of the ION NTM, Long Beach, CA, USA*, 1997.

[207] F. Vernotte, E. Lantz, and J.J. Gagnepain. **Oscillator Noise Analysis: Multivariance Measurement**. *IEEE Transactions on Instrumentation and Measurement*, 42(2):342–350, 1993.

[208] F. Vernotte, E. Lantz, J. Groslambert, and J.J. Gagnepain. **A new Multi-Variance Method for the Oscillator Noise Analysis**. In *Proceedings of the Frequency Control Symposium*, 1999.

[209] F. Vernotte and G. Zalamansky. **A Bayesian Method for Oscillator Stability Analysis**. *IEEE Transactions on Ultrasonics, Ferroelectrics and Frequency Control*, 46(6):1545–1550, 1999.

[210] Vicon. http://www.vicon.com/.

[211] S. Vieilledent. **Comparaison de systèmes d'analyse du mouvement 3D**. Technical report, Institut National du Sport – Laboratoire Mouvement, Action et Performance, 2002.

[212] The vLink ™Racing Computer. http://www.advancedracingcomputers.com/vlink.html.

[213] U. Vollath. **The Factorized Multi-Carrier Ambiguity Resolution (FAMCAR) Approach for Efficient Carrier-Phase Ambiguity Estimation**. In *Proceedings of the ION GNSS 2004, Long Beach, CA, USA*, 2004.

[214] A. Waegli. **Analyse de données dynamiques pour l'aviation civile dans le cadre du projet EGNOS**. Master's thesis, EPFL, 2003.

[215] A. Waegli, J.-M. Bonnaz, and J. Skaloud. **L'analyse de performance sportive à l'aide d'un système GPS/INS low-cost: évaluation de capteurs inertiels de type MEMS**. *Revue XYZ*, (113 – 4ème trimestre 2007):19–24, 2007.

[216] A. Waegli and P.-Y. Gilliéron. **Le Concept d'intégrité d'EGNOS**. *Géomatique Suisse*, 11, 2003.

[217] A. Waegli, S. Guerrier, and J. Skaloud. **Redundant MEMS-IMU integrated with GPS for Performance Assessment in Sports**. In *Proceedings of the IEEE/ION PLANS 2008, Monterey, CA, USA*, 2008.

[218] A. Waegli, F. Meyer, S. Ducret, J. Skaloud, and R. Pesty. ***Assessment of Timing and Performance Based on Trajectories from low-cost GPS/INS Positioning***, pages 556–564. Science and Skiing IV, 2007.

[219] A. Waegli, A. Schorderet, Ch. Prongué, and J. Skaloud. ***Accurate Trajectory and Orientation of a Motorcycle derived from Low-Cost Satellite and Inertial Measurement Systems***, pages 223–230. The Engineering of Sport 7, 2008.

[220] A. Waegli and J. Skaloud. **Assessment of GPS/MEMS-IMU Integration Performance in Ski Racing**. In *Proceedings of ENC-GNSS 2007 (TimeNav'07), Geneva, Switzerland*, 2007.

[221] A. Waegli and J. Skaloud. **Turning Point: Trajectory Analysis for Skiers**. *InsideGNSS*, Spring 2007, 2007.

[222] A. Waegli, J. Skaloud, Ph. Tomé, and J.-M. Bonnaz. **Assessment of the Integration Strategy between GPS and Body-Worn MEMS Sensors with Application to Sports**. In *Proceedings of the ION GNSS 2007, Fort Worth, TX, USA*, 2007.

[223] G. Wahba. **A Least Squares Estimate of Spacecraft Attitude**. *SIAM Review*, 7(3):409, 1965.

[224] M. Wei and K.P. Schwarz. **Testing a Decentralized Filter for GPS/INS Integration**. In *Proceedings of the IEEE PLANS 1990, Las Vegas, NV, USA*, 1990.

[225] J. Wendel, J. Metzger, R. Moenikes, A. Maier, and G.F. Trommer. **A Performance Comparison of Tightly Coupled GPS/INS Navigation Systems Based on Extended and Sigma Point Kalman Filters**. In *Proceedings of the ION GNSS, Long Beach, CA, USA*, 2005.

[226] R. Williams, Th. Delaney, E. Nelson, J. Gratton, J. Laurent, and B. Heath. **Speeds Associated With Skiing and Snowboarding**. *Wilderness and Environmental Medicine*, 18(2):102–105, 2007.

[227] S. Winkler and P. Vörsmann. **Multi-Sensor Data Fusion for Small Autonomous Unmanned Aircraft**. *European Journal of Navigation*, 5(2):32–41, 2007.

[228] Z. Xiang and D. Gebre-Egziabher. **Modeling and Bounding Low Cost Inertial Sensors Errors**. In *Proceedings of the IEEE/ION PLANS 2008, Monterey, CA, USA*, 2008.

[229] Y. Yang. ***Tightly Coupled MEMS INS/GPS Integration with INS Aided Receiver Tracking Loops***. PhD thesis, UCGE Report, 2007.

[230] Y. Yang and W. Gao. **An Optimal Adaptive Kalman Filter**. *Journal of Geodesy*, 80(4):177–183, 2006.

[231] Y. Yang, R.R. Hatch, and R.T. Sharpe. **GPS Multipath Mitigation in Measurement Domain and its Applications for High Accuracy Navigation**. In *Proceedings of the ION GNSS 2004, Long Beach, CA, USA*, 2004.

[232] G. Yegnanarayana. ***Artificial Neural Networks***. Prentic-Hall of India, New Delhi, 2005.

[233] K. Zhang, R. Deakin, R. Grenfell, Y. Li, J. Zhang, W.N. Cameron, and D.M. Silcock. **GNSS for Sports - Sailing and Rowing Perspectives**. *Journal of Global Positioning Systems*, 3(1-2):280–289, 2004.

[234] K. Zhang, R. Grenfell, R. Deakin, Y. Li, Z. Jason, A. Hahn, Ch. Gore, and T. Rice. **Towards a Low-Cost, High Output Rate, Real-Time GPS Rowing Coaching and Training System**. In *Proceedings of the ION GPS/GNSS 2003, Portland, OR, USA*, 2003.

[235] N.F. Zhang. **The Uncertainty Associated with the Weighted Means of Measurement Data**. *Metrologia*, 43:195–204, 2006.

[236] R. Zhu and Z. Zhou. **A Real-Time Articulated Human Motion Tracking Using Tri-Axis Inertial/Magnetic Sensors Package**. *IEEE Transactions on Neural Systems and Rehabilitation Engineering*, 12(2):295–302, 2004.

[237] A. Zinoviev. **Using GLONASS in Combined GNSS Receivers: Current Status**. In *Proceedings of the ION GNSS 2005, Long Beach, CA, USA*, 2005.

Appendix A

Extended Kalman Filter Algorithm

Fig. A.1 summarizes the equations and operations of the GPS/INS integration with an EKF [85, 191, 81]. The MEMS-IMU measurements are propagated over time and updated by GPS measurements at predefined epochs. The state prediction corresponds to the strapdown inertial navigation described in section 3.6.3. The mathematical derivation of the covariance prediction and the update stage is described in Appendix C. The filter initialization is detailed in section 3.6.2.

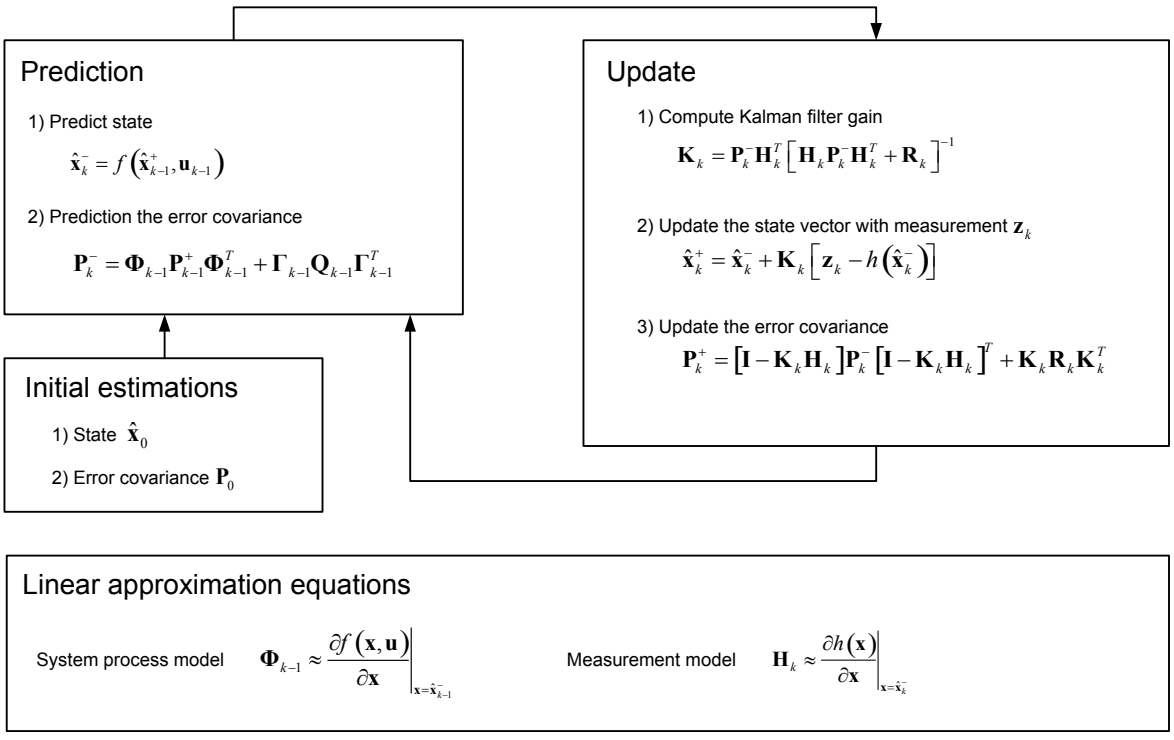

Fig. A.1: Extended Kalman filter algorithm.

Appendix B

Unscented Kalman Filter Algorithm

B.1 Algorithm

This section details the scaled UKF algorithm described in [166]. A non-linear system process with non-additive noise is assumed.

$$\mathbf{x}_{k+1} = f(\mathbf{x}_k^a) = f(\mathbf{x}_k, \mathbf{w}_k) \tag{B.1.1}$$
$$\mathbf{Q}_k = E(\mathbf{w}_k \mathbf{w}_k^T) \tag{B.1.2}$$

By augmenting the state $\mathbf{x}$ by the noise vector $\mathbf{w}$, the effect of the noise on the covariance propagation can be described naturally. As a result, the derivation presented in C.2.2 is no longer required.

$$\mathbf{x}^a = \begin{bmatrix} \mathbf{x} \\ \mathbf{w} \end{bmatrix} \tag{B.1.3}$$
$$\mathbf{P}^a = \begin{bmatrix} \mathbf{P} & \mathbf{0} \\ \mathbf{0} & \mathbf{Q}_k \end{bmatrix} \tag{B.1.4}$$

where superscript a indicates the augmented state. Thus, the system model with non-additive noise can be written as:

$$\mathbf{x}_{k+1} = f(\mathbf{x}_k^a) \equiv f(\mathbf{x}_k, \mathbf{w}_k) \tag{B.1.5}$$
$$\mathbf{Q}_k = E(\mathbf{w}_k, \mathbf{w}_k) \tag{B.1.6}$$

B.2 Initialization

The unscented transformation is required to generate the sigma points (SP) of the UKF. First, the state vector and the covariance matrix need to be initialized.

$$\hat{\mathbf{x}}_{0|0}^a = \begin{bmatrix} \mathbf{x}_0 \\ \mathbf{0} \end{bmatrix} \quad \mathbf{P}_{0|0}^a = \begin{bmatrix} \mathbf{P}_0 & \mathbf{0} \\ \mathbf{0} & \mathbf{Q}_0 \end{bmatrix} \tag{B.2.1}$$

In the second step, the $p = n + 2$ SPs and weights that capture the mean and variance in a n-dimensional space are generated [82]. w_0 needs to be selected within $0 \leq w_0 \leq 1$. $w_0 = 0.5$ seems to be an appropriate choice. The other $n + 1$ weights are computed with:

$$w_i = \frac{1 - w_0}{n + 1} \tag{B.2.2}$$

Then, the spherical simplex SPs can be derived by the subsequently described iterative process. Let $\mathbf{X}_{u,i}^{j}$ be the i^{th} SP in a j-dimensional space. The first points capturing the mean and covariance in a one-dimensional space are found to be:

$$\begin{aligned} w_1 &= w_2 = \frac{1 - w_0}{2} \\ \left\{\mathbf{X}_{u,0}^{1}, \mathbf{X}_{u,1}^{1}, \mathbf{X}_{u,2}^{1}\right\} &= \left\{0, -\frac{1}{\sqrt{2w_1}}, \frac{1}{\sqrt{2w_1}}\right\} \end{aligned} \tag{B.2.3}$$

Respecting the mean and covariance condition, the following SPs for the two-dimensional case can be determined by:

$$\left\{\mathbf{X}_{u,0}^{2}, \mathbf{X}_{u,1}^{2}, \mathbf{X}_{u,2}^{2}, \mathbf{X}_{u,3}^{2}\right\} = \left\{\begin{bmatrix} 0 \\ 0 \end{bmatrix}, \begin{bmatrix} -\frac{1}{\sqrt{2w_1}} \\ -\frac{1}{\sqrt{6w_1}} \end{bmatrix}, \begin{bmatrix} \frac{1}{\sqrt{2w_1}} \\ -\frac{1}{\sqrt{6w_1}} \end{bmatrix}, \begin{bmatrix} 0 \\ \frac{2}{\sqrt{6w_1}} \end{bmatrix}\right\} \tag{B.2.4}$$

FIG. B.1 illustrates the generation of SPs in the one- and two dimensional space.

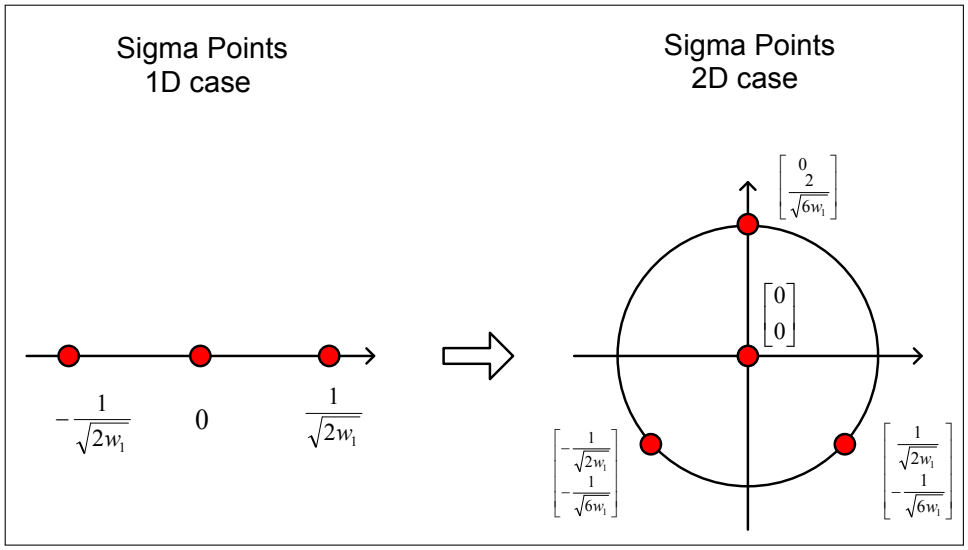

FIG. B.1: Sigma point generation illustrated in the one- and two-dimensional space.

For $j = 2$ to n, the vector sequence can be expanded as follows:

For $i = 0$:

$$\mathbf{X}_{u,0}^{j} = \begin{bmatrix} \mathbf{X}_{u,0}^{j-1} \\ 0 \end{bmatrix} = \mathbf{0}_{n \times 1} \tag{B.2.5}$$

For $i = 1$ to j:

$$\mathbf{X}_{u,i}^{j} = \begin{bmatrix} \mathbf{X}_{u,i}^{j-1} \\ -\frac{1}{\sqrt{j(j+1)w_1}} \end{bmatrix} \tag{B.2.6}$$

For $i = j + 1$:

$$\mathbf{X}_{u,i}^{j} = \begin{bmatrix} \mathbf{0}_{(j-1)\times 1} \\ \frac{j}{\sqrt{j(j+1)w_1}} \end{bmatrix} \tag{B.2.7}$$

This leads to a vector sequence of $n+2$ SPs of dimension $n \times 1$. An increase of one dimension in the state space adds a new SP and increases their dimension by one element.

After computing the SPs, their weights for mean (index m, equation B.2.8) and covariance (index c, equation B.2.9) have to be determined.

$$w_i^m = \begin{cases} \frac{w_0 - 1}{\alpha^2} + 1 & \text{for } i = 0 \text{ with } 10^{-4} \leq \alpha \leq 1, \\ \frac{w_i}{\alpha^2} & \text{for } i \neq 0. \end{cases} \tag{B.2.8}$$

$$w_i^c = \begin{cases} \frac{w_0 - 1}{\alpha^2} + 2 + \beta - \alpha^2 & \text{for } i = 0, \\ \frac{w_i}{\alpha^2} & \text{for } i \neq 0. \end{cases} \tag{B.2.9}$$

α may be chosen in the interval $10^{-4} \leq \alpha \leq 1$, whereas $\beta = 2$ is optimal for Gaussian distributions.

Cholesky factorization is applied to obtain the square root matrix $\mathbf{S}_{0|0}^a$ such that $\mathbf{S}_{0|0}^a \cdot \mathbf{S}_{0|0}^{T^a} = \mathbf{P}_{0|0}^a$. Then, the scaled SPs are computed as follows:

$$\mathbf{X}_{i,0|0}^a = \hat{\mathbf{x}}_{0|0}^a + \alpha \cdot \mathbf{S}_{0|0}^a \cdot \mathbf{X}_{u,i}^a \tag{B.2.10}$$

B.3 Prediction

The SPs are first transformed through the system model.

$$\mathbf{X}_{i,k|k-1} = f(\mathbf{X}_{i,k-1|k-1}^a) \tag{B.3.1}$$

f is defined in section 3.6.3 and equations 3.6.7 (orientation prediction), 3.6.12 (velocity prediction), 3.6.17 (position prediction), as well as equation 3.6.19 (extra states prediction).

Then, the mean and covariance is computed based on the propagated SPs $\mathbf{X}_{i,k|k-1}$.

$$\hat{\mathbf{x}}_k^- = \sum_{i=0}^{p-1} w_i^m \mathbf{X}_{i,k|k-1} \tag{B.3.2}$$

$$\mathbf{P}_k^- = \sum_{i=0}^{p-1} w_i^c \Delta\mathbf{X}_{i,k|k-1} \Delta\mathbf{X}_{i,k|k-1}^T \tag{B.3.3}$$

where $\Delta\mathbf{X}_{i,k|k-1} = \mathbf{X}_{i,k|k-1} - \hat{\mathbf{x}}_k^-$.

Special treatments are required when averaging position and orientation because they do not belong to a vector space. In the position domain, the position of each of the SPs $\mathbf{X}_{i,k|k-1}$ can be transformed to the e-frame where the position weighted mean is given by:

$$\hat{\mathbf{r}}^e_{k|k-1} = \sum_{i=0}^{p-1} w_i^m \cdot \mathbf{r}^e_{i,k|k-1} \tag{B.3.4}$$

The weighted average of the quaternions can be computed based on various algorithms.

- Weighted average [22].
- Spherical linear interpolation [22].
- Convergence algorithm [166].

The three algorithms have been investigated in [22]. For large covariances, the spherical linear interpolation algorithm and the convergence algorithm outperform the weighted average. However, the weighted average algorithm is the fastest algorithm and it provides sufficiently accurate results for decreasing covariances.

Then, the state and covariance are augmented.

$$\hat{\mathbf{x}}^a_{k|k-1} = \begin{bmatrix} \mathbf{x}_k^- \\ \mathbf{0} \end{bmatrix} \quad \mathbf{P}^a_{k|k-1} = \begin{bmatrix} \mathbf{P}_k^- & \mathbf{0} \\ \mathbf{0} & \mathbf{Q}_k \end{bmatrix} \tag{B.3.5}$$

Finally, the SPs are updated applying a Cholesky factorization to the new covariance matrix $\mathbf{P}^{a-}_{k|k-1}$ such that $\mathbf{S}^{a-}_{k|k-1} \cdot \mathbf{S}^{Ta-}_{k|k-1} = \mathbf{P}^-_{k|k-1}$.

$$\mathbf{X}^a_{i,k|k-1} = \hat{\mathbf{x}}^{a-}_{k-1} + \alpha \cdot \mathbf{S}^{a-}_{k|k-1} \cdot \mathbf{X}^a_{u,i} \tag{B.3.6}$$

B.4 Measurement Update

Firstly, the SPs are transformed through the measurement model.

$$\mathbf{Z}_{i,k|k-1} = h(\mathbf{X}_{i,k|k-1}) \tag{B.4.1}$$

The measurement models derived for the EKF are applied (section 3.6.4): Equation 3.6.21 for position updates, equation 3.6.23 for velocity updates and equation 3.6.27 for magnetic measurement updates.

[166] applies a special treatment to the position updates in order to avoid an ill-conditioned covariance matrix as position is expressed in terms of the geodetic latitude and longitude. Further evaluation is necessary in order to justify this approach.

The predicted measurements are then derived from the transformed SPs.

$$\hat{\mathbf{z}}_k^- = \sum_{i=0}^{p-1} w_i^m \cdot \mathbf{Z}_{i,k|k-1} \tag{B.4.2}$$

The covariance between the states and the measurements $P_{xz,k}$ as well as the covariance of the innovation sequence $P_{zz,k}$ is given by:

$$P_{xz,k} = \sum_{i=0}^{p-1} w_i^c \cdot \Delta\mathbf{X}_{i,k|k-1} \cdot \Delta\mathbf{Z}_{i,k|k-1}^T \tag{B.4.3}$$

$$P_{zz,k} = \sum_{i=0}^{p-1} w_i^c \cdot \Delta\mathbf{Z}_{i,k|k-1} \cdot \Delta\mathbf{Z}_{i,k|k-1}^T + \mathbf{R}_k \tag{B.4.4}$$

where $\Delta\mathbf{Z}_{i,k|k-1} = \mathbf{Z}_{i,k|k-1} - \hat{\mathbf{z}}_k^-$.

The following update equations are similar to the EKF approach: Compute the gain matrix $\mathbf{K}_k$, the innovations and update the covariance matrix $\mathbf{P}_k^+$:

$$\mathbf{K}_k = \mathbf{P}_{xz,k} \cdot \mathbf{P}_{zz,k}^{-1} \tag{B.4.5}$$

$$\hat{\mathbf{x}}_k^+ = \hat{\mathbf{x}}_k^- + \mathbf{K}_k \cdot (\mathbf{z}_k - \hat{\mathbf{z}}_k^-) \tag{B.4.6}$$

$$\mathbf{P}_k^+ = \mathbf{P}_k^- + \mathbf{K}_k \cdot \mathbf{P}_{zz,k} \cdot \mathbf{K}_k^T \tag{B.4.7}$$

Finally, $\mathbf{S}_k^{a+}$ can be computed by applying Cholesky factorization to $\mathbf{P}_k^{a+}$ to update the scaled SPs.

$$\mathbf{X}_{i,k|k}^a = \hat{\mathbf{x}}_k^{a+} + \alpha \cdot \mathbf{S}_k^{a+} \cdot \mathbf{X}_{u,i}^a \tag{B.4.8}$$

Appendix C

GPS/INS Navigation State Error Models and Covariance Prediction for EKF

C.1 Error Model Derivation

C.1.1 Position Errors Model

In the local-level mechanization, the position can be represented in geographic coordinates $\mathbf{r}^n = [\varphi\ \lambda\ h]^T$. Its derivation can be expressed introducing the velocity vector $\mathbf{v}^n = [v_N\ v_E\ v_D]^T$.

$$\dot{\mathbf{r}}^n = \mathbf{D}^{-1} \cdot \mathbf{v}^n \tag{C.1.1}$$

Equation C.1.1 can be transformed as follows:

$$\mathbf{v}^n = \mathbf{D} \cdot \dot{\mathbf{r}}^n \tag{C.1.2}$$

Linearizing equation C.1.2 leads to:

$$\delta\mathbf{v}^n = \mathbf{D} \cdot \delta\dot{\mathbf{r}}^n + \delta\mathbf{D} \cdot \dot{\mathbf{r}}^n \tag{C.1.3}$$

where

$$\delta\mathbf{D} \cdot \dot{r}^n = \left(\frac{\partial \mathbf{D}}{\partial \varphi}\delta\varphi + \frac{\partial \mathbf{D}}{\partial \lambda}\delta\lambda + \frac{\partial \mathbf{D}}{\partial h}\delta h \right) \cdot \dot{\mathbf{r}}^n = \mathbf{D}_r \cdot \delta\mathbf{r}^n \tag{C.1.4}$$

and

$$\mathbf{D}_r = \begin{bmatrix} 0 & 0 & \dot{\varphi} \\ -\dot{\lambda}(R+h)\sin\varphi & 0 & \dot{\lambda}\cos\varphi \\ 0 & 0 & 0 \end{bmatrix} \tag{C.1.5}$$

Substituting equation C.1.4 into equation C.1.3 leads to the error equation for the position.

$$\delta\dot{\mathbf{r}}^n = \mathbf{D}^{-1} \cdot \delta\mathbf{v}^n - \mathbf{D}^{-1} \cdot \mathbf{D}_r \cdot \delta\mathbf{r}^n \tag{C.1.6}$$

C.1.2 Velocity Errors Model

The navigation equation in the n-frame for the velocity is expressed in function of the specific force measurements $\mathbf{f}^n$, the gravity vector $\mathbf{g}^n$, the gyroscope measurements $\mathbf{\Omega}_{in}^n$, the Earth rotation $\mathbf{\Omega}_{ie}^n$ and the velocity $\mathbf{v}^n$.

$$\dot{\mathbf{v}}^n = \mathbf{f}^n - (\boldsymbol{\omega}_{in}^n + \boldsymbol{\omega}_{ie}^n) \times \mathbf{v}^n + \mathbf{g}^n \tag{C.1.7}$$

The estimated specific force term $\hat{\mathbf{f}}^n$ can be expressed introducing the direction cosine matrix $\mathbf{R}_b^n$ and the orientation errors $\mathbf{E}^n$.

$$\hat{\mathbf{f}}^n = \hat{\mathbf{R}}_b^n \hat{\mathbf{f}}^b = (\mathbf{I} - \mathbf{E}^n) \cdot \mathbf{R}_b^n \cdot (\mathbf{f}^b - \delta\mathbf{f}^b) \tag{C.1.8}$$

where the true orientation $\mathbf{R}_b^n$ is related to the estimated orientation $\hat{\mathbf{R}}_b^n$ and the orientation errors $\mathbf{E}^n$ defined by equation C.1.10 as follows:

$$\hat{\mathbf{R}}_b^n = (\mathbf{I} - \mathbf{E}^n) \cdot \mathbf{R}_b^n \tag{C.1.9}$$

$\mathbf{E}^n$ is the skew-symmetric matrix representing the misalignment errors.

$$\mathbf{E}^n = [\boldsymbol{\epsilon}^n]\times = \begin{bmatrix} 0 & -\epsilon_D & \epsilon_E \\ \epsilon_D & 0 & -\epsilon_N \\ -\epsilon_E & \epsilon_N & 0 \end{bmatrix} \tag{C.1.10}$$

Linearizing equation C.1.8, $\delta\mathbf{f}^n$ can be expressed as:

$$\delta\mathbf{f}^n = \mathbf{f}^n - \hat{\mathbf{f}}^n = \mathbf{R}_b^n \cdot \delta\mathbf{f}^b - \mathbf{f}^n \times \boldsymbol{\epsilon}^n \tag{C.1.11}$$

Setting $\hat{\boldsymbol{\omega}}_{in}^n = \boldsymbol{\omega}_{in}^n$ - $\delta\boldsymbol{\omega}_{in}^n$, $\hat{\boldsymbol{\omega}}_{ie}^n = \boldsymbol{\omega}_{ie}^n$ - $\delta\boldsymbol{\omega}_{ie}^n$ and neglecting second-order effects, the linearization of equation C.1.7 leads to:

$$\delta\dot{\mathbf{v}}^n = -\mathbf{f}^n \times \boldsymbol{\epsilon}^n + \mathbf{R}_b^n \delta\mathbf{f}^b - (\boldsymbol{\omega}_{in}^n + \boldsymbol{\omega}_{ie}^n) \times \delta\mathbf{v}^n - (\delta\boldsymbol{\omega}_{in}^n + \delta\boldsymbol{\omega}_{ie}^n) \times \mathbf{v}^n + \delta\mathbf{g}^n + \frac{\partial \mathbf{g}}{\partial \mathbf{x}} \delta\mathbf{x} \tag{C.1.12}$$

where $\delta\mathbf{g}^n$ is the error in the gravity term. $\frac{\partial \mathbf{g}}{\partial \mathbf{x}} \delta\mathbf{x}$ is the change of gravity due to an error in position and can be safely neglected when working with MEMS-IMU sensors and when updating the state vector frequently.

$$\delta\dot{\mathbf{v}}^n = -\mathbf{f}^n \times \boldsymbol{\epsilon}^n + \mathbf{R}_b^n \delta\mathbf{f}^b - (\boldsymbol{\omega}_{in}^n + \boldsymbol{\omega}_{ie}^n) \times \delta\mathbf{v}^n - (\delta\boldsymbol{\omega}_{in}^n + \delta\boldsymbol{\omega}_{ie}^n) \times \mathbf{v}^n + \delta\mathbf{g}^n \tag{C.1.13}$$

C.1.3 Orientation Errors Model

The time derivative of equation C.1.9 leads to:

$$\dot{\hat{\mathbf{R}}}_b^n = \dot{\mathbf{R}}_b^n - \dot{\mathbf{E}}^n \mathbf{R}_b^n - \mathbf{E}^n \dot{\mathbf{R}}_b^n \tag{C.1.14}$$

The rate of change of the $\mathbf{R}_b^n$ can be expressed in terms of the orientation errors.

$$\hat{\dot{\mathbf{R}}}_b^n = \hat{\mathbf{R}}_b^n \hat{\mathbf{\Omega}}_{nb}^b \tag{C.1.15}$$

Introducing equation C.1.9 and setting $\hat{\mathbf{\Omega}}_{nb}^b = \mathbf{\Omega}_{nb}^b - \delta\mathbf{\Omega}_{nb}^n$, equation C.1.15 leads to:

$$\hat{\dot{\mathbf{R}}}_b^n = (\mathbf{I} - \mathbf{E}^n)\mathbf{R}_b^n(\mathbf{\Omega}_{nb}^b - \delta\mathbf{\Omega}_{nb}^n) \tag{C.1.16}$$

Comparing equation C.1.14 and C.1.16 and neglecting second-order effects, the following expression for $\dot{\boldsymbol{\epsilon}}^n$ can be expressed in vector form:

$$\dot{\boldsymbol{\epsilon}}^n = \mathbf{R}_b^n \delta\boldsymbol{\omega}_{nb}^b \tag{C.1.17}$$

Thus, the orientation errors are directly proportional to the errors of the body frame rate of change of the angular velocity. $\delta\boldsymbol{\omega}_{nb}^b$ can be determined by subtracting the angular velocity of the navigation-level frame with respect to the inertial frame from the absolute angular velocity measured by the gyroscopes.

$$\hat{\boldsymbol{\omega}}_{nb}^b = \hat{\boldsymbol{\omega}}_{ib}^b - \hat{\mathbf{R}}_n^b \hat{\boldsymbol{\omega}}_{in}^n \tag{C.1.18}$$

After some modifications and neglecting second-order effects, linearizing $\delta\boldsymbol{\omega}_{nb}^b$ becomes:

$$\delta\boldsymbol{\omega}_{nb}^b = \boldsymbol{\omega}_{ib}^b - \mathbf{R}_n^b \boldsymbol{\omega}_{in}^n + \hat{\mathbf{R}}_n^b \mathbf{E}^n \omega_{in}^n \tag{C.1.19}$$

Substituting C.1.19 into C.1.17 leads to the error equation for the orientation.

$$\dot{\boldsymbol{\epsilon}}^n = \mathbf{R}_b^n \delta\boldsymbol{\omega}_{ib}^b - \delta\boldsymbol{\omega}_{in}^n - \boldsymbol{\omega}_{in}^n \times \boldsymbol{\epsilon}^n \tag{C.1.20}$$

C.2 Covariance Prediction

C.2.1 System Matrix

The state covariance matrix propagates as:

$$\tilde{\mathbf{P}}_k = \mathbf{\Phi}_{k-1}\hat{\mathbf{P}}_{k-1}\mathbf{\Phi}_{k-1}^T + \mathbf{\Gamma}_{k-1}\mathbf{Q}_{k-1}\mathbf{\Gamma}_{k-1}^T \tag{C.2.1}$$

The transition matrix $\mathbf{\Phi}$ can be computed based on the system matrix $\mathbf{F}$.

$$\begin{aligned}\mathbf{\Phi} &= e^{\mathbf{F}\Delta t} \\ &\approx \mathbf{I} + \mathbf{F}\Delta t + \frac{(\mathbf{F}\Delta t)^2}{2!} + \frac{(\mathbf{F}\Delta t)^3}{3!}\end{aligned} \tag{C.2.2}$$

where

$$\Delta t = t_{k+1} - t_k \tag{C.2.3}$$

The system matrix $\mathbf{F}$ can be expressed as follows:

$$\mathbf{F} = \left[\begin{array}{c|ccc} & \mathbf{0}_{3\times3} & \mathbf{0}_{3\times3} & \\ \mathbf{F}_{main} & \mathbf{R}_b^n & \mathbf{0}_{3\times3} & \mathbf{0}_{9\times3} \\ & \mathbf{0}_{3\times3} & \mathbf{R}_b^n & \\ \hline \mathbf{0}_{3\times9} & -\beta_f \cdot \mathbf{I}_{3\times3} & \mathbf{0}_{3\times3} & \mathbf{0}_{3\times3} \\ \mathbf{0}_{3\times9} & \mathbf{0}_{3\times3} & -\beta_\omega \cdot \mathbf{I}_{3\times3} & \mathbf{0}_{3\times3} \\ \mathbf{0}_{3\times9} & \mathbf{0}_{3\times3} & \mathbf{0}_{3\times3} & -\beta_{d_m} \cdot \mathbf{I}_{3\times3} \end{array}\right] \tag{C.2.4}$$

where $\mathbf{F}_{main}$ is defined as follows:

$$\mathbf{F}_{main} = \begin{bmatrix} \mathbf{F}_{11} & \mathbf{F}_{12} & \mathbf{F}_{13} \\ \mathbf{F}_{21} & \mathbf{F}_{22} & \mathbf{F}_{23} \\ \mathbf{F}_{31} & \mathbf{F}_{32} & \mathbf{F}_{33} \end{bmatrix} \tag{C.2.5}$$

Based on equation C.1.6, $\mathbf{F}_{11}$, $\mathbf{F}_{12}$ and $\mathbf{F}_{13}$ can be derived.

$$\mathbf{F}_{11} = -\mathbf{D}^{-1}\mathbf{D}_r = \begin{bmatrix} 0 & 0 & -\frac{\dot{\varphi}}{R+h} \\ \dot{\lambda}\tan(\varphi) & 0 & -\frac{\dot{\lambda}}{R+h} \\ 0 & 0 & 0 \end{bmatrix} \tag{C.2.6}$$

$$\mathbf{F}_{12} = \mathbf{D}^{-1} \tag{C.2.7}$$

$$\mathbf{F}_{13} = \mathbf{0}_{3\times3} \tag{C.2.8}$$

The derivation of the velocity terms is more complex. First, two components of equation C.1.13 have to be computed. Set:

$$\boldsymbol{\Omega} = \boldsymbol{\omega}_{in}^n + \boldsymbol{\omega}_{ie}^n = \boldsymbol{\omega}_{en}^n + 2\boldsymbol{\omega}_{ie}^n = \begin{bmatrix} (2\Omega_E + \dot{\lambda})\cos\varphi \\ -\dot{\varphi} \\ -(2\Omega_E + \dot{\lambda})\sin\varphi \end{bmatrix} \tag{C.2.9}$$

Note that at $v = 20$ m/s:

$$\boldsymbol{\omega}_{en}^n = \begin{bmatrix} 0 \\ -3\cdot10^{-6} \\ 3\cdot10^{-6} \end{bmatrix} \frac{\text{rad}}{\text{s}} < \boldsymbol{\omega}_{ie}^n = \begin{bmatrix} 0 \\ 5\cdot10^{-5} \\ -5\cdot10^{-5} \end{bmatrix} \frac{\text{rad}}{\text{s}} \tag{C.2.10}$$

Derivating equation C.2.9 with respect to position leads to:

$$\frac{\partial\boldsymbol{\Omega}}{\partial\mathbf{r}} = \begin{bmatrix} -2\Omega_E\sin\varphi & 0 & -\frac{v_E}{(R+h)^2} \\ 0 & 0 & \frac{v_N}{(R+h)^2} \\ -2\Omega_E\cos\varphi - \frac{\dot{\lambda}}{\cos\varphi} & 0 & -\frac{v_E}{(R+h)^2}\tan\varphi \end{bmatrix} \tag{C.2.11}$$

Derivating equation C.2.9 with respect to velocity leads to:

$$\frac{\partial\boldsymbol{\Omega}}{\partial\mathbf{v}} = \begin{bmatrix} 0 & \frac{1}{R+h} & 0 \\ -\frac{1}{R+h} & 0 & 0 \\ 0 & \frac{\tan\varphi}{R+h} & 0 \end{bmatrix} \tag{C.2.12}$$

Now, compute $\delta\boldsymbol{\Omega} \times \mathbf{v}^n$:

$$\begin{aligned}\delta\boldsymbol{\Omega} \times \mathbf{v}^n &= -\mathbf{v}^n \times \delta\boldsymbol{\Omega} = [-\mathbf{v}^n] \times (\frac{\partial\boldsymbol{\Omega}}{\partial\mathbf{r}}\delta\mathbf{r} + \frac{\partial\boldsymbol{\Omega}}{\partial\mathbf{v}}\delta\mathbf{v}) \\ &= \begin{bmatrix} -v_E(2\Omega_E\cos\varphi + \frac{v_E}{(R+h)\cos^2\varphi}) & 0 & \frac{v_E^2}{(R+h)^2}\tan\varphi - \frac{v_D v_N}{(R+h)^2} \\ 2\Omega_E(v_N\cos\varphi - v_D\sin\varphi) + \frac{v_E v_N}{(R+h)\cos^2\varphi} & 0 & -\frac{v_E}{(R+h)^2\cos\varphi}(v_N\sin\varphi + v_D\cos\varphi) \\ 2\Omega_E v_E\sin\varphi & 0 & \frac{v_E^2}{(R+h)^2} + \frac{v_N^2}{(R+h)^2} \end{bmatrix}\delta\mathbf{r} \\ &+ \begin{bmatrix} \frac{v_D}{R+h} & \frac{v_E}{(R+h)}\tan\varphi & 0 \\ 0 & \frac{v_D}{R+h} + \frac{v_N}{R+h}\sin\varphi & 0 \\ -\frac{v_N}{R+h} & -\frac{v_E v_N}{(R+h)} & 0 \end{bmatrix}\delta\mathbf{v}\end{aligned} \tag{C.2.13}$$

Evaluate $\boldsymbol{\Omega} \times \delta\mathbf{v}^n$:

$$\boldsymbol{\Omega} \times \delta\mathbf{v}^n = \begin{bmatrix} 0 & -2(\Omega_E + \frac{v_E}{(R+h)\cos\varphi})\sin\varphi & 2\frac{v_N}{R+h} \\ 2\left(\Omega_E + \frac{v_E}{(R+h)\cos\varphi}\right)\sin\varphi & 0 & 2\left(\Omega_E\cos\varphi + \frac{v_E}{(R+h)}\right) \\ -2\frac{v_N}{R+h} & -2\left(\Omega_E + \frac{v_E}{(R+h)\cos\varphi}\right)\cos\varphi & 0 \end{bmatrix}\delta\mathbf{v} \tag{C.2.14}$$

Based on equation C.1.13, the velocity terms of the system matrix can be determined.

$$\mathbf{F}_{21} = \begin{bmatrix} -v_E\left(2\Omega_E\cos\varphi + \frac{\dot\lambda}{\cos\varphi}\right) & 0 & \frac{\dot\lambda\sin\varphi}{(R+h)}v_E - \frac{\dot\varphi}{(R+h)}v_D \\ 2\Omega_E(v_N\cos\varphi - v_D\sin\varphi) + \frac{\dot\lambda}{\cos\varphi}v_N & 0 & -\frac{\dot\lambda}{(R+h)}(v_N\sin\varphi + v_D\cos\varphi) \\ 2\Omega_E v_E\sin\varphi + \frac{\partial g_0(\varphi,h)}{\partial\varphi} & 0 & \frac{\dot\lambda\cos\varphi}{(R+h)}v_E + \frac{\dot\varphi}{(R+h)}v_N - \frac{2g}{R} + \frac{6}{R^2}h \end{bmatrix} \tag{C.2.15}$$

$$\mathbf{F}_{22} = \begin{bmatrix} \frac{v_D}{R+h} & -2(\Omega_E + \dot\lambda)\sin\varphi & \dot\varphi \\ (2\Omega_E + \dot\lambda)\sin\varphi & \frac{v_D + v_N\tan\varphi}{R+h} & (2\Omega_E + \dot\lambda)\cos\varphi \\ -2\dot\varphi & -2(\Omega_E + \dot\lambda)\cos\varphi & 0 \end{bmatrix} \tag{C.2.16}$$

$$\mathbf{F}_{23} = -[\mathbf{f}^n\times] = -\left[\mathbf{R}_b^n\mathbf{f}^b\times\right] = \begin{bmatrix} 0 & f_D & -f_E \\ -f_D & 0 & f_N \\ f_E & -f_N & 0 \end{bmatrix} \tag{C.2.17}$$

Note: The term $\frac{6}{R^2}h$ can be safely neglected.

Based on equation C.1.20, the velocity terms of the system matrix become:

$$\mathbf{F}_{31} = \begin{bmatrix} \Omega_E\sin\varphi & 0 & \frac{\dot\lambda\cos\varphi}{(R+h)} \\ 0 & 0 & -\frac{\dot\varphi}{(R+h)} \\ \Omega_E\cos\varphi + \frac{\dot\lambda}{\cos\varphi} & 0 & -\frac{\dot\lambda\sin\varphi}{(R+h)} \end{bmatrix} \tag{C.2.18}$$

$$\mathbf{F}_{32} = \begin{bmatrix} 0 & -\frac{1}{R+h} & 0 \\ \frac{1}{R+h} & 0 & 0 \\ 0 & \frac{\tan\varphi}{R+h} & 0 \end{bmatrix} \tag{C.2.19}$$

$$\mathbf{F}_{33} = -[\boldsymbol{\omega}_{in}^{n}]\times = \begin{bmatrix} 0 & -(\Omega_E + \dot{\lambda})\sin\varphi & \dot{\varphi} \\ (\Omega_E + \dot{\lambda})\sin\varphi & 0 & (\Omega_E + \dot{\lambda})\cos\varphi \\ -\dot{\varphi} & -(\Omega_E + \dot{\lambda})\cos\varphi & 0 \end{bmatrix} \tag{C.2.20}$$

C.2.2 System Noise Model

The gamma matrix is given by:

$$\boldsymbol{\Gamma} = \left[\begin{array}{c|cc|ccc} & \mathbf{0}_{3\times3} & \mathbf{0}_{3\times3} & & & \\ \mathbf{I}_{9\times9} & -\mathbf{R}_b^n & \mathbf{0}_{3\times3} & \multicolumn{3}{c}{\mathbf{0}_{9\times9}} \\ & \mathbf{0}_{3\times3} & -\mathbf{R}_b^n & & & \\ \hline & & & \sqrt{2\beta_{f^b}}\cdot\mathbf{I}_{3\times3} & & \\ \mathbf{0}_{9\times9} & \multicolumn{2}{c|}{\mathbf{0}_{9\times6}} & & \sqrt{2\beta_{\omega}}\cdot\mathbf{I}_{3\times3} & \\ & & & & & \sqrt{2\beta_{d_m}}\cdot\mathbf{I}_{3\times3} \end{array}\right] \tag{C.2.21}$$

$\mathbf{Q}_k$ is given by:

$$\mathbf{Q}_k = |\Delta t| \cdot diag(\sigma_r^2 \;\; \sigma_v^2 \;\; \sigma_\epsilon^2 \;\; \sigma_f^2 \;\; \sigma_\omega^2 \;\; \sigma_{w_{f^b}}^2 \;\; \sigma_{w_{b_\omega}}^2 \;\; \sigma_{w_{d_m}}^2) \tag{C.2.22}$$

The system noise matrix $\mathbf{Q}_{ww}$ can then be integrated from:

$$\begin{aligned} \mathbf{Q}_{ww} &= \int_0^{\Delta t} \boldsymbol{\phi}(t)\cdot\boldsymbol{\Gamma}\cdot\mathbf{Q}_k\cdot\boldsymbol{\Gamma}^T\cdot\boldsymbol{\phi}(t)^T dt \\ &\approx \int_0^{\Delta t} (\mathbf{I}+\mathbf{F}(t)\cdot\Delta t)\cdot\boldsymbol{\Gamma}\cdot\mathbf{Q}_k\cdot\boldsymbol{\Gamma}^T\cdot(\mathbf{I}+\mathbf{F}(t)\cdot\Delta t)^T dt \end{aligned} \tag{C.2.23}$$

Neglecting higher order terms ($\geq O(\Delta t^2)$, [60]), $\mathbf{Q}_{ww}$ becomes:

$$\mathbf{Q}_{ww} \approx \boldsymbol{\Gamma}\cdot\mathbf{Q}_k\cdot\boldsymbol{\Gamma}\cdot\Delta t \tag{C.2.24}$$

This simplification avoids the integration of $\mathbf{F}$ and seems appropriate knowing that the choice of the noise parameters of $\mathbf{Q}_k$ is arbitrary and essentially based on the experience.

C.3 Measurement Model Derivation

C.3.1 Loosely Coupled Integration

At epochs where position, velocity and magnetometer observations are sufficiently accurate, the measurement matrix and its covariance matrix have the following form:

$$\mathbf{H} = \begin{bmatrix} \mathbf{H}_r \\ \mathbf{H}_v \\ \mathbf{H}_m \end{bmatrix} \tag{C.3.1}$$

$$\mathbf{R} = \begin{bmatrix} \mathbf{R}_r & & \\ & \mathbf{R}_v & \\ & & \mathbf{R}_m \end{bmatrix} \tag{C.3.2}$$

where $\mathbf{H}_r$, $\mathbf{H}_v$, $\mathbf{H}_m$ are the measurement matrices for position, velocity and magnetometer observations and $\mathbf{R}_r$, $\mathbf{R}_v$, $\mathbf{R}_m$ the corresponding covariance matrices. Their derivation is developed in the sections C.3.1 and C.3.3.

GPS coordinate updates

Linearizing equation 3.6.21 leads to:

$$\mathbf{H}_r = \left[\begin{array}{c|c|c|c|c} \mathbf{I}_{3\times3} + \delta(\mathbf{D}^{-1})\mathbf{o}^n & \mathbf{0}_{3\times3} & -\mathbf{D}^{-1}\mathbf{O}^n & \mathbf{0}_{3\times9} \end{array} \right] \tag{C.3.3}$$

where $\mathbf{O}^n = [\mathbf{o}^n\times] = [\mathbf{R}_b^n \cdot \mathbf{o}^b\times]$ and where

$$\delta(\mathbf{D}^{-1})\mathbf{o}^n = \begin{bmatrix} 0 & 0 & -\frac{a_N}{(R+h)^2} \\ \frac{a_E \tan\varphi}{(R+h)\cos\varphi} & 0 & -\frac{a_E}{(R+h)^2\cos\varphi} \\ 0 & 0 & 0 \end{bmatrix} \tag{C.3.4}$$

The covariance matrix is given by:

$$\mathbf{R}_r = \begin{bmatrix} (\frac{\sigma_{r_N}}{R+h})^2 & 0 & 0 \\ 0 & (\frac{\sigma_{r_E}}{(R+h)\cos\varphi})^2 & 0 \\ 0 & 0 & \sigma_{r_D}^2 \end{bmatrix} \tag{C.3.5}$$

GPS velocity updates

Setting $\boldsymbol{\omega}_{nb}^n = \mathbf{R}_b^n\boldsymbol{\omega}_{ib}^b - \boldsymbol{\omega}_{in}^n$, equation 3.6.23 can be derivated to find:

$$\mathbf{H}_v = \left[\begin{array}{c|c|c|c|c|c} \mathbf{O}^n\mathbf{D}_1 & \mathbf{I}_{3\times3} + \mathbf{O}^n\mathbf{D}_2 & \mathbf{O}^n(\boldsymbol{\Omega}_{in}^n + 2\boldsymbol{\Omega}_{nb}^b) & \mathbf{0}_{3\times3} & -\mathbf{O}^n\mathbf{R}_b^n & \mathbf{0}_{3\times3} \end{array} \right] \tag{C.3.6}$$

where

$$\mathbf{D}_1 = \frac{\partial\boldsymbol{\omega}_{in}^n}{\partial\mathbf{r}} = \begin{bmatrix} -\Omega_E\sin\varphi & 0 & -\frac{v_E}{(R+h)^2} \\ 0 & 0 & \frac{v_N}{(R+h)^2} \\ -(\Omega_E\cos\varphi + \frac{v_E}{R+h}) & 0 & \frac{v_E\tan\varphi}{(R+h)^2} \end{bmatrix} \tag{C.3.7}$$

$$\mathbf{D}_2 = \frac{\partial\boldsymbol{\omega}_{in}^n}{\partial\mathbf{v}} = \begin{bmatrix} 0 & \frac{1}{R+h} & 0 \\ -\frac{1}{R+h} & 0 & 0 \\ 0 & -\frac{\tan\varphi}{R+h} & 0 \end{bmatrix} \tag{C.3.8}$$

The covariance matrix is given by:

$$\mathbf{R}_v = \begin{bmatrix} \sigma_{vN}^2 & 0 & 0 \\ 0 & \sigma_{vE}^2 & 0 \\ 0 & 0 & \sigma_{vD}^2 \end{bmatrix} \tag{C.3.9}$$

C.3.2 Closely Coupled Integration

The measurement matrix has the following form:

$$\mathbf{H} = \begin{bmatrix} \mathbf{H}_{DDp} \\ \mathbf{H}_{DD\dot{\phi}} \\ \mathbf{H}_m \end{bmatrix} \tag{C.3.10}$$

The covariance matrix becomes:

$$\mathbf{R} = \begin{bmatrix} \mathbf{R}_{DDp} & & \\ & \mathbf{R}_{DD\dot{\phi}} & \\ & & \mathbf{R}_m \end{bmatrix} \tag{C.3.11}$$

The derivation of $\mathbf{H}_{DDp,NED}$, $\mathbf{H}_{DD\dot{\phi},NED}$, $\mathbf{H}_m$ and the covariance terms is presented in the sections C.3.2 and C.3.3.

GPS double-differenced pseudorange updates

After accounting for the lever-arm effect defined in equation 3.6.21, the measurement matrix for the first expression of equation 3.3.13 $\mathbf{H}_{DD,ECEF}$ can by derivated in the e-frame as follows:

$$(\nabla\Delta p^{zs}_{Li,mr} - \nabla\Delta\rho^{zs-}_{mr}) - v^{zs}_{mr} = \mathbf{H}_{DD,ECEF} \begin{bmatrix} \partial x \\ \partial y \\ \partial z \end{bmatrix} \tag{C.3.12}$$

where

$$\mathbf{H}_{DD,ECEF} = \begin{bmatrix} \frac{\Delta x^z}{\rho^{z-}_r} - \frac{\Delta x^s}{\rho^{s-}_r} & \frac{\Delta y^z}{\rho^{z-}_r} - \frac{\Delta y^s}{\rho^{s-}_r} & \frac{\Delta z^z}{\rho^{z-}_r} - \frac{\Delta z^s}{\rho^{s-}_r} \end{bmatrix} \tag{C.3.13}$$

with a size of $\mathbf{H}_{DD,ECEF}$ is $[nsat - 1 \times 3]$. Then, $\mathbf{H}_{DDp}$ yields:

$$\mathbf{H}_{DDp} = \mathbf{H}_{DD,ECEF} \cdot \mathbf{H}_f \cdot \mathbf{H}_r \tag{C.3.14}$$

where $\mathbf{H}_f$ is the derivative of the transformation function from curvilinear to cartesian coordinates with respect to the position $\mathbf{r}^n$. $\mathbf{H}_r$ is given by equation C.3.3.

The measurement covariance matrix can be derived by double error propagation:

$$\mathbf{R}_{DDp} = \mathbf{F}_{\nabla\Delta p,\Delta p} \cdot \mathbf{F}_{\Delta p,p} \cdot \mathbf{R}_p \cdot \mathbf{F}^T_{\Delta p,p} \cdot \mathbf{F}^T_{\nabla\Delta p,\Delta p} \tag{C.3.15}$$

where

$$\mathbf{F}_{\nabla\Delta p,\Delta p} = \left[\begin{array}{c|c} \mathbf{I}_{nsat} & -\mathbf{I}_{nsat} \end{array} \right] \tag{C.3.16}$$

and

$$\mathbf{F}_{\Delta p,p} = \left[\begin{array}{c|c} \begin{matrix} 1 \\ 1 \\ 1 \\ 1 \\ 1 \end{matrix} & -\mathbf{I}_{nsat-1} \end{array} \right] \tag{C.3.17}$$

and where $nsat$ is the number of satellite measurements retained for the computation.

GPS double-differenced Doppler updates

The system matrix $\mathbf{H}_{DD\dot{\phi},ECEF}$ can be expressed in the e-frame as follows:

$$(\nabla\Delta\dot{p}^{zs}_{mr} - \nabla\Delta\dot{\rho}^{s,i-}_{mr}) - v^{zs} = \mathbf{H}_{DD\dot{\phi},ECEF} \begin{bmatrix} \partial x \\ \partial y \\ \partial z \\ \partial \dot{x} \\ \partial \dot{y} \\ \partial \dot{z} \end{bmatrix} \tag{C.3.18}$$

with

$$\mathbf{H}_{DD\dot{p},ECEF} = \begin{bmatrix} a^{zs}_{mr} & b^{zs}_{mr} & c^{zs}_{mr} & d^{zs}_{mr} & e^{zs}_{mr} & f^{zs}_{mr} \end{bmatrix} \tag{C.3.19}$$

where m indicates the master receiver, r the rover receiver, s an arbitrary satellite number and z the reference satellite. The coefficients a^{zs}_{mr}, b^{zs}_{mr}, c^{zs}_{mr}, d^{zs}_{mr}, e^{zs}_{mr}, f^{zs}_{mr} are given by:

$$a^{zs}_{mr} = \begin{bmatrix} \frac{1}{\rho^{z-}_r} - \frac{(\Delta x^{z-})^2}{(\rho^{z-}_r)^3} & -\frac{\Delta x^{z-}\Delta y^{z-}}{(\rho^{z-}_r)^3} & -\frac{\Delta x^{z-}\Delta z^{z-}}{(\rho^{z-}_r)^3} \end{bmatrix} \begin{bmatrix} \Delta\dot{x}^{z-} \\ \Delta\dot{y}^{z-} \\ \Delta\dot{z}^{z-} \end{bmatrix} \tag{C.3.20}$$

$$- \begin{bmatrix} \frac{1}{\rho^{s-}_r} - \frac{(\Delta x^{s-})^2}{(\rho^{s-}_r)^3} & -\frac{\Delta x^{s-}\Delta y^{s-}}{(\rho^{s-}_r)^3} & -\frac{\Delta x^{s-}\Delta z^{s-}}{(\rho^{s-}_r)^3} \end{bmatrix} \begin{bmatrix} \Delta\dot{x}^{s-} \\ \Delta\dot{y}^{s-} \\ \Delta\dot{z}^{s-} \end{bmatrix} \tag{C.3.21}$$

$$b^{zs}_{mr} = \begin{bmatrix} -\frac{\Delta x^{z-}\Delta y^{z-}}{(\rho^{z-}_r)^3} & \frac{1}{\rho^{z-}_r} - \frac{(\Delta y^{z-})^2}{(\rho^{z-}_r)^3} & -\frac{\Delta y^{z-}\Delta z^{z-}}{(\rho^{z-}_r)^3} \end{bmatrix} \begin{bmatrix} \Delta\dot{x}^{z-} \\ \Delta\dot{y}^{z-} \\ \Delta\dot{z}^{z-} \end{bmatrix} \tag{C.3.22}$$

$$- \begin{bmatrix} \frac{\Delta x^{s-}\Delta y^{s-}}{(\rho^{s-}_r)^3} & \frac{1}{\rho^{s-}_r} - \frac{(\Delta y^{s-})^2}{(\rho^{s-}_r)^3} & -\frac{\Delta y^{s-}\Delta z^{s-}}{(\rho^{s-}_r)^3} \end{bmatrix} \begin{bmatrix} \Delta\dot{x}^{s-} \\ \Delta\dot{y}^{s-} \\ \Delta\dot{z}^{s-} \end{bmatrix} \tag{C.3.23}$$

$$c^{zs}_{mr} = \begin{bmatrix} -\frac{\Delta x^{z-}\Delta z^{z-}}{(\rho^{z-}_r)^3} & -\frac{\Delta x^{z-}\Delta z^{z-}}{(\rho^{z-}_r)^3} & \frac{1}{\rho^{z-}_r} - \frac{(\Delta z^{z-})^2}{(\rho^{z-}_r)^3} \end{bmatrix} \begin{bmatrix} \Delta\dot{x}^{z-} \\ \Delta\dot{y}^{z-} \\ \Delta\dot{z}^{z-} \end{bmatrix} \tag{C.3.24}$$

$$- \begin{bmatrix} -\frac{\Delta x^{s-}\Delta z^{s-}}{(\rho^{s-}_r)^3} & -\frac{\Delta x^{s-}\Delta z^{s-}}{(\rho^{s-}_r)^3} & \frac{1}{\rho^{s-}_r} - \frac{(\Delta z^{s-})^2}{(\rho^{s-}_r)^3} \end{bmatrix} \begin{bmatrix} \Delta\dot{x}^{s-} \\ \Delta\dot{y}^{s-} \\ \Delta\dot{z}^{s-} \end{bmatrix} \tag{C.3.25}$$

$$d^{zs}_{mr} = \frac{\Delta x^{z-}}{\rho^{z-}_r} - \frac{\Delta x^{s-}}{\rho^{s-}_r} \tag{C.3.26}$$

$$e^{zs}_{mr} = \frac{\Delta y^{z-}}{\rho^{z-}_r} - \frac{\Delta y^{s-}}{\rho^{s-}_r} \tag{C.3.27}$$

$$f^{zs}_{mr} = \frac{\Delta z^{z-}}{\rho^{z-}_r} - \frac{\Delta z^{s-}}{\rho^{s-}_r} \tag{C.3.28}$$

The size of $\mathbf{H}_{DD\dot{p},ECEF}$ is $[nsat - 1 \times 3]$. $\mathbf{H}_{DD\dot{p}}$ can be derived accounting for the rotation $\mathbf{R}^n_e$ from the Earth fixed reference frame to the NED frame. $\mathbf{H}_v$ is given by equation C.3.6.

$$\mathbf{H}_{DD\dot{p}} = \mathbf{H}_{DD\dot{p},ECEF} \cdot \mathbf{H}_{R^n_e} \cdot \mathbf{H}_v \tag{C.3.29}$$

The measurement covariance matrix can be obtained similarly to $\mathbf{R}_{DD}$ (equation C.3.15). Unlike for the pseudorange measurements, no correlations between the measurements to the same satellite are introduced because only phase differences are measured.

C.3.3 Magnetic Updates

Derivating equation 3.6.27 leads to:

$$\mathbf{H}_m = \left[\begin{array}{c|c|c|c|c} \mathbf{0}_{3\times3} & \mathbf{0}_{3\times3} & \mathbf{R}_n^b[\mathbf{h}^n]\times & \mathbf{0}_{3\times6} & -\mathbf{I}_{3\times3} \end{array} \right] \tag{C.3.30}$$

The covariance matrix is given by:

$$\mathbf{R}_m = \sigma_m \cdot \mathbf{I}_{3\times3} \tag{C.3.31}$$

Appendix D

System Performance

TAB. D.1: Position and velocity RMSE of differential GPS solutions for 6 downhill runs (approximately 150000 samples). The right column indicates the estimated accuracy of the reference trajectories.

	Geodetic L1/L2	Geodetic L1		Low-cost L1		Reference
	Fixed (95%)	Float	Smoothed p	Float	Smoothed p	Accuracy
N [m]	0.027	0.301	0.344	0.304	0.577	0.05
E [m]	0.021	0.161	0.146	0.301	0.405	0.05
h [m]	0.020	0.294	0.504	0.644	0.980	0.05
v_N [m/s]	0.105	0.105	0.117	0.208	0.136	0.02
v_E [m/s]	0.115	0.115	0.118	0.189	0.108	0.02
v_D [m/s]	0.141	0.141	0.152	0.350	0.194	0.02

TAB. D.2: Position, velocity and orientation RMSE of 6 downhill runs based on the loosely coupled approach (approximately 150000 samples).

	Geodetic L1/L2	Geodetic L1		Low-cost L1	
	Fixed (95%)	Float	Smoothed p	Float	Smoothed p
N [m]	0.132	0.245	0.323	0.570	0.570
E [m]	0.066	0.203	0.159	0.497	0.624
h [m]	0.044	0.187	0.401	1.358	1.159
v_N [m/s]	0.076	0.117	0.122	0.156	0.186
v_E [m/s]	0.066	0.107	0.152	0.140	0.157
v_D [m/s]	0.049	0.069	0.086	0.188	0.304
rl [deg]	1.14	1.52	0.66	1.71	0.56
pt [deg]	1.15	1.80	0.64	1.95	0.73
hd [deg]	1.75	2.04	2.72	2.62	3.58

TAB. D.3: Position, velocity and orientation RMSE of 6 downhill runs based on the loosely and the closely coupled approach and carrier-phase smoothed pseudoranges (approximately 150000 samples).

	Geodetic L1		Low-cost L1		Reference
	Loosely	Closely	Loosely	Closely	Accuracy
N [m]	0.323	0.313	0.570	0.657	0.05
E [m]	0.159	0.180	0.624	0.657	0.05
h [m]	0.401	0.442	1.159	1.340	0.05
v_N [m/s]	0.122	0.136	0.186	0.163	0.02
v_E [m/s]	0.152	0.144	0.157	0.158	0.02
v_D [m/s]	0.086	0.140	0.304	0.218	0.02
rl [deg]	0.66	0.51	0.56	0.91	0.01
pt [deg]	0.64	0.58	0.73	0.96	0.01
hd [deg]	2.72	3.57	3.58	3.08	0.03

Appendix E

GPS/INS Mechanization with Redundant IMUs

E.0.4 Direct Noise Estimation

The algorithm proposed below is designed for a system setup composed of triads of inertial sensors [64].

Firstly, the norms which are less sensitive to the orientation of the inertial (and magnetic) measurements are computed at each instant k and for every sensor i.

$$\bar{\ell}_i(k) = \sqrt{\ell_{xi}^2(k) + \ell_{yi}^2(k) + \ell_{zi}^2(k)} \tag{E.0.1}$$

where $i = 1, ..., n$ and n being the number of sensor triads. Squared differences are then computed to form the $\mathbf{d}$ matrices.

$$\mathbf{d}_{\bar{\ell}}(n,k) = \begin{bmatrix} (\bar{\ell}_1(k) - \frac{\sum_{j=2}^{n} \bar{\ell}_j(k)}{n-1})^2 \\ \dots \\ (\bar{\ell}_n(k) - \frac{\sum_{j=1}^{n-1} \bar{\ell}_j(k)}{n-1})^2 \end{bmatrix} \tag{E.0.2}$$

An averaging time T (typically a few seconds) is chosen (Fig. E.1). Assuming all sensors' errors to be uncorrelated and identical, the noise is directly estimated.

$$\sigma_\ell(k,T) = \sqrt{\frac{1}{n}\int_{k-T}^{k+T} (\sum_{i=1}^{n} \mathbf{d}_{\bar{\ell}}(i,k)) \cdot dt} \tag{E.0.3}$$

E.0.5 Generalized Extended Kalman Filter Implementation

The following modifications to the standard GPS/INS mechanization have to be made. For the orientation propagation, equation 3.6.9 has to be modified as:

$$\mathbf{u}_b^b \approx \mathbf{\Pi}_\omega(\boldsymbol{\ell}_\omega^b)_k \cdot (t_{k+1} - t_k) \tag{E.0.4}$$

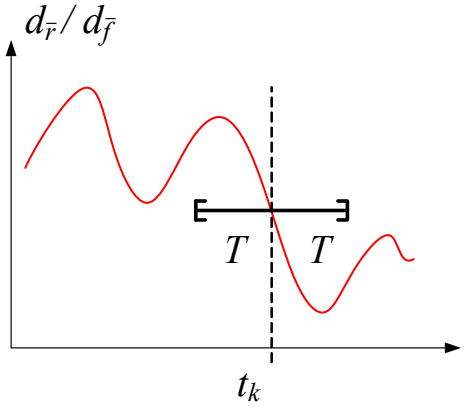

FIG. E.1: Schematic representation of the averaging window.

The accelerometer measurements are integrated in the velocity strapdown equation 3.6.12 and equation 3.6.14.

$$(\Delta \mathbf{v}_f^n)_{k+1} \approx (\mathbf{R}_b^n)_{k+1|k} \mathbf{\Pi}_f \cdot (\boldsymbol{\ell}_f^b)_k \cdot \Delta t \tag{E.0.5}$$

The generalized system matrix $\mathbf{F}$ can be expressed as follows (m gyroscopes, n accelerometer and magnetometer p):

$$\mathbf{F} = \left[\begin{array}{c|ccc} \mathbf{F}_{main} & \begin{array}{c}\mathbf{0}_{3\times m}\\ \mathbf{R}_b^n \cdot \mathbf{\Pi}_f \\ \mathbf{0}_{3\times m}\end{array} & \begin{array}{c}\mathbf{0}_{3\times n}\\ \mathbf{0}_{3\times n} \\ \mathbf{R}_b^n \cdot \mathbf{\Pi}_\omega\end{array} & \mathbf{0}_{9\times p} \\ \hline \mathbf{0}_{m\times 9} & -\beta_f \cdot \mathbf{I}_{m\times m} & \mathbf{0}_{m\times n} & \mathbf{0}_{m\times k} \\ \mathbf{0}_{n\times 9} & \mathbf{0}_{n\times m} & -\beta_\omega \cdot \mathbf{I}_{n\times n} & \mathbf{0}_{n\times k} \\ \mathbf{0}_{k\times 9} & \mathbf{0}_{k\times m} & \mathbf{0}_{k\times n} & -\beta_{d_m} \cdot \mathbf{I}_{k\times k} \end{array}\right] \tag{E.0.6}$$

The gamma matrix $\mathbf{\Gamma}$ becomes:

$$\mathbf{\Gamma} = \left[\begin{array}{c|cc|c} \mathbf{I}_{9\times 9} & \begin{array}{c}\mathbf{0}_{3\times 3}\\ -\mathbf{R}_b^n \cdot \mathbf{\Pi}_f \\ \mathbf{0}_{3\times 3}\end{array} & \begin{array}{c}\mathbf{0}_{3\times 3}\\ \mathbf{0}_{3\times 3} \\ -\mathbf{R}_b^n \cdot \mathbf{\Pi}_\omega\end{array} & \mathbf{0}_{(m+n+k)\times(m+n+k)} \\ \hline \mathbf{0}_{(m+n+k)\times 9} & \multicolumn{2}{c|}{\mathbf{0}_{(m+n+k)\times 6}} & \begin{array}{ccc}\sqrt{2\beta_{f^b}} \cdot \mathbf{I}_m & & \\ & \sqrt{2\beta_\omega} \cdot \mathbf{I}_n & \\ & & \sqrt{2\beta_{d_m}} \cdot \mathbf{I}_k\end{array} \end{array}\right] \tag{E.0.7}$$

The generalized position update model (equation C.3.3) is given by:

$$\mathbf{H}_r = \left[\begin{array}{c|c|c|c|c} \mathbf{I}_{3\times 3} + \delta(\mathbf{D}^{-1})\mathbf{o}^n & \mathbf{0}_{3\times 3} & -\mathbf{D}^{-1}\mathbf{O}^n & \mathbf{0}_{3\times(m+n+k)} \end{array}\right] \tag{E.0.8}$$

The generalized velocity update model (equation C.3.6) is given by:

$$\mathbf{H}_v = \left[\begin{array}{c|c|c|c|c|c} \mathbf{O}^n\mathbf{D}_1 & \mathbf{I}_{3\times 3} + \mathbf{O}^n\mathbf{D}_2 & \mathbf{O}^n(\mathbf{\Omega}_{in}^n + 2\mathbf{\Omega}_{nb}^b) & \mathbf{0}_{3\times m} & -\mathbf{O}^n\mathbf{R}_b^n \cdot \mathbf{\Pi}_\omega & \mathbf{0}_{3\times k} \end{array}\right] \tag{E.0.9}$$

The magnetic error model (equation 3.6.27) becomes:

$$\mathbf{h}_m(\hat{x}_k^-) = \mathbf{\Pi}_m \mathbf{R}_n^b[\mathbf{h}^n] \times \boldsymbol{\epsilon}^n - \mathbf{d}_m + \mathbf{w}_m \tag{E.0.10}$$

which leads to:

$$\mathbf{H}_m = \left[\begin{array}{c|c|c|c|c} \mathbf{0}_{3\times3} & \mathbf{0}_{3\times3} & \mathbf{R}_n^b[\mathbf{h}^n]\times & \mathbf{0}_{3\times(m+n)} & -\mathbf{I}_{k\times k} \end{array} \right] \tag{E.0.11}$$

Appendix F

Simulation of GPS and MEMS-IMU Data

The purpose of this simulation is to analyse the capability of the EKF to model biases (and scale factors) and to test its robustness against various error sources (e.g. bad GPS coordinates, high measurement noise).

F.1 Measurement Simulation

F.1.1 Gyroscope Measurements

The strapdown equation for the orientation term can be expressed in the following way (equation 3.6.7):

$$(\mathbf{q}_b^n)_{k+1|k+1} = (\mathbf{q}_n^n)_{k+1|k} \cdot (\mathbf{q}_b^n)_{k|k} \cdot (\mathbf{q}_b^b)_{k|k+1} \tag{F.1.1}$$

It follows that:

$$(\mathbf{q}_b^b)_{k|k+1} = (\mathbf{q}_n^b)_{k|k} \cdot (\mathbf{q}_n^n)_{k|k+1} \cdot (\mathbf{q}_b^n)_{k+1|k+1} \tag{F.1.2}$$

where $(\mathbf{q}_n^b)_{k|k} = (\mathbf{q}_b^n)_{k|k}^c$, $(\mathbf{q}_n^n)_{k|k+1} = (\mathbf{q}_n^n)_{k+1|k}^c$ and where $(\mathbf{q}_n^n)_{k+1|k}$ is defined by equation 3.6.10. c indicates the complex conjugate of the corresponding quaternion. The $\mathbf{q}_b^b$ quaternion is defined as a function of the rotation vector $\mathbf{u}$:

$$(\mathbf{q}_b^b)_{k|k+1} = \begin{bmatrix} \cos(\frac{\|\mathbf{u}_b^b\|}{2}) \\ \frac{\mathbf{u}_b^b}{\|\mathbf{u}_b^b\|} \sin(\frac{\|\mathbf{u}_b^b\|}{2}) \end{bmatrix} \tag{F.1.3}$$

Thus:

$$\left\|\mathbf{u}_b^b\right\| = 2 \cdot \arccos(\mathbf{q}_b^b(1)) \tag{F.1.4}$$

This leads to:

$$\mathbf{u}_b^b = \frac{1}{\sin(\frac{\|\mathbf{u}_b^b\|}{2})} \left\|\mathbf{u}_b^b\right\| \cdot \mathbf{q}_b^b(2:4) \tag{F.1.5}$$

and

$$\boldsymbol{\omega}_{ib}^b = \frac{\mathbf{u}_b^b}{\Delta t} \tag{F.1.6}$$

Redundant measurements can be generated by rotating $\boldsymbol{\omega}_{ib}^b$ to frame b_i:

$$\boldsymbol{\omega}_{i,bi}^{bi} = \boldsymbol{R}_b^{bi}\boldsymbol{\omega}_{ib}^b \tag{F.1.7}$$

where

$$\boldsymbol{R}_{bi}^b = \mathbf{R}_3(\psi) \cdot \mathbf{R}_2(-\theta) \tag{F.1.8}$$

F.1.2 Specific Force Measurements

The strapdown equation for the velocity term can be expressed in the following way:

$$\begin{aligned}(\mathbf{v}^n)_{k+1} =& (\mathbf{v}^n)_k + ((\mathbf{g}^n)_k - (2(\boldsymbol{\omega}_{ie}^n)_k + (\boldsymbol{\omega}_{en}^n)_k) \times (\mathbf{v}^n)_k) \cdot (t_{k+1} - t_k) \\ &+ (\mathbf{R}_b^n)_{k|k} \cdot (\mathbf{f}^b)_k \cdot (t_{k+1} - t_k)\end{aligned} \tag{F.1.9}$$

The time differential of $\mathbf{v}^n$ can be derived.

$$\begin{aligned}(\dot{\mathbf{v}^n})_{k+1} &= \frac{(\mathbf{v}^n)_{k+1} - (\mathbf{v}^n)_k}{t_{k+1} - t_k} \\ &= (\mathbf{g}^n - (2\boldsymbol{\omega}_{ie}^n + \boldsymbol{\omega}_{en}^n) \times (\mathbf{v}^n)_k) + (\boldsymbol{R}_b^n)_{k|k} \cdot (\mathbf{f}^b)_k\end{aligned} \tag{F.1.10}$$

Setting $\dot{\mathbf{v}}^n = \mathbf{a}^n$ (the "local" acceleration vector), $\mathbf{f}_b$ can be found transforming equation F.1.10:

$$(\mathbf{f}^b)_k = (\mathbf{R}_n^b)_{k|k} \cdot (\mathbf{a}^n - \mathbf{g}^n + (2 \cdot \boldsymbol{\omega}_{ie}^n + \boldsymbol{\omega}_{en}^n) \times (\mathbf{v}^n)_k) \tag{F.1.11}$$

Redundant accelerometer measurements can be generated as described in equation F.1.7.

F.1.3 Magnetometer Measurements

The magnetometer measurements are modeled based on a model of the Earth's magnetic field (expressed as $\mathbf{h}^n$).

$$\mathbf{h}^b = \mathbf{R}_n^b \cdot \mathbf{h}^n \tag{F.1.12}$$

Redundant magnetometer measurements can be generated according to equation F.1.7.

F.1.4 Error Simulation

Biases and white noise are applied to the simulated measurement as defined in section 3.1.

$$\begin{aligned} \mathbf{f}^b &= \hat{\mathbf{f}}^b - \mathbf{b}_{f^b} - \mathbf{w}_{f^b} \\ \boldsymbol{\omega} &= \hat{\boldsymbol{\omega}} - \mathbf{b}_\omega - \mathbf{w}_\omega \\ \mathbf{h} &= \hat{\mathbf{h}} - \mathbf{d}_m - \mathbf{w}_m \end{aligned} \tag{F.1.13}$$

where

$\mathbf{f}^b$	modeled specific force
$\hat{\mathbf{f}}^b$	true specific force
$\mathbf{b}_{f^b}$	accelerometer bias
$\mathbf{w}_{f^b}$	measurement (white) noise
$\boldsymbol{\omega}$	modeled angular rate
$\hat{\boldsymbol{\omega}}$	true angular rate
$\mathbf{b}_\omega$	bias of the angular rate measurements
$\mathbf{w}_\omega$	measurement (white) noise
$\mathbf{h}$	modeled magnetic field
$\hat{\mathbf{h}}$	true magnetic field measurement
$\mathbf{d}_m$	magnetic disturbance
$\mathbf{w}_m$	measurement (white) noise

Appendix G

Trajectory Matching

G.1 Curvature

The curvature can be estimated form the horizontal velocity (v_E, v_N) and acceleration terms (a_E, a_N).

$$c_{2D} = \frac{v_E \cdot a_N - v_N \cdot a_E}{(v_E^2 - v_N^2)^{\frac{3}{2}}} \tag{G.1.1}$$

The normal vector to a trajectory can be derived from the eigenvector of the covariance vector [5].

$$Cov(x, y) = E\left[(x - \mu_x)(y - \mu_y)^T\right] \tag{G.1.2}$$

The normal vector $\mathbf{n}$ corresponds to the eigenvector with the largest eigenvalue, while the tangent vector corresponds to smallest eigenvalue. Then, the curvature can be derived through

$$c_{2D} = \frac{1}{2k+1} \sum_{j=-k}^{k} \|\mathbf{n}(t) - \mathbf{n}(t-k)\| \tag{G.1.3}$$

where $\mathbf{n}(t)$ it the normal vector at time t and its j^{th} neighborhood points. k is the number of neighborhood points that are considered.

G.2 Helmert Transformation

The functional model of the Helmert transformation is given by:

$$\begin{aligned} w_E &= \cos\omega \cdot E_2 + \sin\omega \cdot N_2 + \Delta E - E_1 \\ w_N &= -\sin\omega \cdot E_2 + \cos\omega \cdot N_2 + \Delta N - N_1 \end{aligned} \tag{G.2.1}$$

where E and N are the coordinates in the first (index 1) or second (index 2) coordinate system. ω is the rotation between the two systems, while ΔE and ΔN are the translation with respect to east and north. w_E and w_N represent the misclosure terms of the Helmert transformation in east and north direction.